

Implementation of the DAQ software for the ALTI module in the ATLAS TileCal and the search for new physics in the four lepton final state

---

A thesis submitted to the Faculty of Science, University of the Witwatersrand in fulfillment of the requirements for the degree of:
Doctor of Philosophy in Physics

Author: **Humphry Tlou**

Supervisor: Prof. Bruce Mellado
Co-Supervisor: Dr. Xifeng Ruan
CERN Advisor: Dr. Henric Wilkens

Institute for Collider Particle Physics
School of Physics, Faculty of Science
University of the Witwatersrand

2023

Declaration

I declare that this thesis is a result of my own work, except where explicit reference is made to the work of others. It is being submitted for the Degree of Doctor of Philosophy at the University of the Witwatersrand, Johannesburg. It has not been submitted before for any qualification or examination at any other University.

Related research output: Journals

- H. Tlou. Implementation of the DAQ software in the ALTI Module of the ATLAS TileCal. Published in: J.Phys.Conf.Ser. 1690 (2020) 1, 012055. Contribution to: ICPPA 2020, the 5^{th} International Conference on Particle Physics and Astrophysics held at MEPhI 5-9 October 2020, Moscow, Russian Federation. Available online: https://iopscience.iop.org/article/10.1088/1742-6596/1690/1/012055/pdf
- H. Tlou, on behalf of the ATLAS Tile Calorimeter System. Integration and Commissioning of the ATLAS Tile Demonstrator Module for Run 3. Published in: 2022 *JINST* 17 C11010. Contribution to: TWEPP 2022, Topical Workshop on Electronics for Particle Physics, 19-23 September 2022; Bergen, Norway. Available online: https://iopscience.iop.org/article/10.1088/1748-0221/17/11/C11010/pdf
- J. Abdallah *et al.* Study of energy response and resolution of the ATLAS Tile Calorimeter to hadrons of energies from 16 to 30 GeV. *Eur. Phys. J. C*, 81(6):549, 2021. Available online: https://arxiv.org/pdf/2102.04088.pdf
- H. Tlou, A. Fadol, B. Mellado, O. Mtintsilana and X. Ruan. Search for heavy resonances in the $\ell^+\ell^-\ell^+\ell^-$ final state in association with missing transverse energy using pp collisions at $\sqrt{s} = 13$ TeV with the ATLAS detector, to be submitted by the ATLAS collaboration to *JHEP*.

Proceedings

- H. Tlou and B. Mellado. Integration of the ALTI module in the ATLAS Tile Calorimeter system, in The Proceedings of SAIP2021, the 66^{th} Annual Conference of the South African Institute of Physics, edited by Prof. Aletta Prinsloo, (UJ), pp. 497 - 502. ISBN: 978-0-620-97693-0. Available online: http://saip.org.za/Proceedings/Track%20F/81.pdf
- H. Tlou, A. Fadol, B. Mellado, O. Mtintsilana and X. Ruan. Search for heavy resonances in the $\ell^+\ell^-\ell^+\ell^-$ final state in association with missing transverse energy using pp collisions at $\sqrt{s} = 13$ TeV with the ATLAS detector, in The Proceedings of SAIP2021, the 66^{th} Annual Conference of the South African Institute of Physics, edited by Prof. Aletta Prinsloo, (UJ), pp. 126 - 131. ISBN: 978-0-620-97693-0. Available online: http://saip.org.za/Proceedings/Track%20B/20.pdf
- O. Mtintsilana, H. Tlou, A. Fadol, B. Mellado and X. Ruan. Search for a heavy pseudo-scalar decaying into a Z boson and another heavy scalar boson leading to four lepton final states in pp collisions at $\sqrt{s} = 13$ TeV with the ATLAS detector, in The Proceedings of SAIP2021, the 66^{th} Annual Conference of the South African Institute of Physics, edited by Prof. Aletta Prinsloo, (UJ), pp. 145 - 150. ISBN: 978-0-620-97693-0. Available online: http://saip.org.za/Proceedings/Track%20B/23.pdf
- H. Tlou and B. Mellado. Upgrade of ATLAS Tile Calorimeter TTC system for Phase-II test-beam campaigns, in The Proceedings of SAIP2022, the 67^{th} Annual Conference of the South African Institute of Physics, edited by Prof. Aletta Prinsloo, (UJ), pp. 523 - 527. ISBN: 978-0-6397-4426-1. Available online: https://events.saip.org.za/event/225/attachments/3393/4897/SAIP%202022%20Proceedings%20978-0-6397-4426-1.pdf

ORCiD: 0000-0002-4934-1661
Scopus Author ID: 57195434522
INSPIRE HEP Author Identifier: H.Tlou.1



Humphry Tlou, **13^{th} of June 2023 in Johannesburg.**

Abstract

The discovery of the Standard Model (SM) Higgs boson in 2012 presents new challenges and opportunities for the Large Hadron Collider (LHC) experiments. After a long period of operation, the LHC experiments needed to maintain and upgrade their detectors in order to continue and conduct research beyond the SM. As part of the upgrades, the Tile Calorimeter (TileCal) participated in Phase-I of the upgrades (December 2018 - March 2022). TileCal, the central hadronic calorimeter ($|\eta| < 1.7$) of the ATLAS experiment uses a set of Trigger and Data Acquisition (TDAQ) software to readout, transport and store physics data resulting from collisions at the LHC. In preparation for the Phase-I upgrades, the ATLAS Local Trigger Interface (ALTI) module was designed for the ATLAS experiment at CERN for TDAQ purposes. It is a 6U VME electronics board, which is a part of the Timing, Trigger and Control (TTC) system. It integrates the functionalities of four legacy modules, currently used in the experiment: Local Trigger Processor, Local Trigger Processor interface, TTC VME bus interface and the TTC emitter. The ALTI module provides the interface between the Level-1 Central Trigger Processor and the TTC optical broadcasting network to the front-end electronics of each of the ATLAS sub-detectors. This thesis discusses the development, validation and integration of the TileCal specific ALTI software in the TileCal online software by the author. A set of ALTI boards were installed in the back-end electronics of the sub-detector and fully validated for the ATLAS detector at CERN. Performance testing and maintenance of the ALTI modules and software were performed during the second half of the upgrade period, in preparation for Run 3 (2022–2025) data-taking period. The thesis also discusses the search for the presence of a new heavy resonance produced via gluon-gluon fusion and decaying to the four-lepton (4ℓ) final state, in association with missing transverse energy ($E_{\mathrm{T}}^{\mathrm{miss}}$), with $\ell = e$, μ (where ℓ is the lepton, e is the electron and μ is the muon). The search uses 2015–2018 proton-proton collision data at

$\sqrt{s} = 13\,\text{TeV}$, corresponding to an integrated luminosity of $139\,\text{fb}^{-1}$, collected by the ATLAS detector. The data are interpreted in terms of two models, firstly the $R \to SH \to 4\ell + E_{\text{T}}^{\text{miss}}$, where R is a scalar boson, which decays to two lighter scalar bosons (S and H). The S decays to a pair of neutrinos and the H decays into 4ℓ, through ZZ bosons. The second model is the $A \to Z(\nu\nu)H(ZZ) \to 4\ell + X$, where A is considered to be a CP-odd scalar which decays to a CP-even scalar H and the Z boson. The Z boson decays to X, which can be a pair of neutrinos or jets, and the H decays to the 4ℓ final state.

This thesis is dedicated to my loving family and friends.

For their endless love and support

Acknowledgements

The research work was conducted at CERN in Geneva, Switzerland between 2019 and 2022 under the ATLAS TileCal group and the HDBS-HBSM Working Group. The research was carried out while pursuing a PhD at the University of the Witwatersrand in Johannesburg, South Africa, with support from the National Research Foundation and the Department of Science and Innovation through the SA-CERN consortium. The financial assistance of SAINTS, iThemba LABS NRF, through the PhD SA-CERN Excellence Scholarship, towards this research work is hereby acknowledged. The 2021 ATLAS PhD Grant, funded by CERN & Society Foundation, and the Bank Lombard Odier & Co Ltd is also acknowledged. The ATLAS PhD Grant was established by former ATLAS spokespersons Fabiola Gianotti and Peter Jenni. The financial assistance has given me an opportunity to participate and contribute to the advancement of science and technology while based at CERN. Thanks to Peter Jenni for constantly checking in on me during coffee breaks and sharing his knowledge and wisdom.

I am grateful to acknowledge and express my appreciation to the individuals who have provided significant support to me not only during my research work but throughout my doctoral program. I would like to extend my deepest gratitude to Dr. Henric Wilkens, my project advisor at CERN, for his valuable guidance, unwavering interest, and encouragement throughout all phases of the TileCal project. Without his continuous optimism concerning this work, enthusiasm, encouragement and support, this project would not have been a success. It was an honour to have discussions and gain the expertise from Oleg Solovyanov and Jalal Abdallah about the TDAQ system. I am grateful to have been given the role of maintaining the TDAQ infrastructure throughout my studies. I had great fun working with Andrey Ryzhov. Truly, a great friend, on and off the field of work. When it came to DCS issues, Filipe Martins was always happy to assist. I gained invaluable experience by actively participating in the TileCal activities,

where I took the roles of Tile Test Beam shifter, ATLAS Calo/Fwd Shifter, Tile DAQ expert, Tile DCS expert, Data Quality and Monitoring team leader, and Tile Run Coordinator throughout my six years at CERN. I also participated in detector maintenance work for TileCal in P1 and test beam, where I enjoyed working with Irakli Minashvili, Stanislav Nemecek and other colleagues. I am grateful to Prof. Bruce Mellado, my supervisor, for his continuous support and encouragement throughout the project. His determination and conviction have motivated me to always strive for the best. I would also like to express my gratitude to my co-supervisor, Dr. Xifeng Ruan, for the opportunity to work together. Our conversations extended beyond technical aspects and encompassed the broader societal and industrial implications of our research.

During my stay at CERN, I also met a lot of people of different nationalities and ethnic groups. I worked with some of these people and what a great experience it has been. Many thanks to the School of Physics and the Institute for Collider Particle Physics at the University of the Witwatersrand, the TileCal community, the ATLAS TDAQ experts: Markus Joos, Andrei Kazarov, Antoine Marzin, and the ATLAS collaboration. Also not forgetting my restaurant 1 *"R1"* friends: Mamadou (*"Shaka Zulu!"*, it's how we greeted each other), Lulzim, Rose and others, they hosted us with love and it always felt great to have conversations filled with laughter and be able to share life experiences with them. The administration people, bus drivers, cleaners and guards made CERN a warm and a conducive environment to work in. Last but not least, I would like to thank my family and friends for their endless love and support throughout this hugely rewarding and enriching process.

Contents

Declaration i

Abstract iii

Dedication v

Acknowledgements vi

List of Figures xii

List of Tables xxv

Nomenclature xxx

1 Introduction and theoretical background 1

1.1 Introduction . . . 1
1.2 The Standard Model of elementary particles . . . 3
1.2.1 Elementary particles and their interaction . . . 3
1.2.2 Gauge symmetries . . . 6
1.2.3 Quantum electrodynamics . . . 6
1.2.4 Quantum chromodynamics . . . 7
1.2.5 Electroweak Theory . . . 8
1.2.6 Spontaneous symmetry breaking and the Higgs mechanism 9
1.2.7 The Higgs boson mass measurements . . . 10
1.3 The SM Higgs boson at the LHC . . . 11
1.3.1 Proton-proton collisions . . . 11
1.3.2 Production modes . . . 13
1.3.3 Decay channels . . . 16
1.4 Physics beyond the Standard Model . . . 18

1.4.1 Multilepton anomalies and the 2HDM+S model 19

2 CERN, LHC and the ATLAS experiment **27**
2.1 CERN 27
2.2 The Large Hadron Collider 27
2.2.1 Particle production rate 30
2.2.2 LHC experiments 31
2.3 The ATLAS experiment 32
2.3.1 Inner Detector 35
2.3.2 Calorimeters 36
2.3.3 Muon Spectrometer 39
2.3.4 The Trigger and Data Acquisition System 40
2.4 The Tile Calorimeter electronics 42
2.4.1 Front-End Electronics 43
2.4.2 Back-End Electronics 44

3 TileCal Online Software **49**
3.1 Online software 49
3.1.1 Partition 51
3.2 Tile online software 53
3.2.1 TileCal run types 54
3.3 TDAQ software release and versioning 55
3.4 TDAQ software organization and build systems 56
3.5 Diagnostics and Verification System 57

4 Implementation of the DAQ software and integration of the ALTI Module in the TileCal **61**
4.1 Introduction 61
4.2 ALTI hardware 62
4.3 ALTI software 72
4.3.1 Low-level and high-level software 72
4.3.2 OKS configuration 73
4.4 The TileCal test bench setup 81
4.4.1 TileCal low-level software 85
4.4.2 Eventviewer 85
4.5 Integration of the ALTI module in the TileCal system 86
4.5.1 Installation of ALTI modules 87

4.5.2 Calibrations and DVS results . . . 90
4.5.3 Pilot Run results with the ALTI system . . . 94
4.5.4 Run 3 data-taking results . . . 96
4.6 TTC system upgrade for the TileCal Phase-II test beam campaigns 98
4.6.1 TileCal Phase-II upgrade electronics . . . 99
4.6.2 Test beam setup . . . 100
4.6.3 Integration of the ALTI module . . . 104
4.6.4 Performance and test beam results . . . 107

5 Object reconstruction and identification with ATLAS 110
5.1 Tracks . . . 110
5.2 Vertices . . . 113
5.3 Leptons . . . 114
5.3.1 Electrons . . . 114
5.3.2 Muons . . . 118
5.4 Jets . . . 121
5.5 Missing transverse momentum . . . 122
5.6 Overlap removal . . . 122

6 The search for heavy resonances in the 4ℓ final state in association with $E_{\mathrm{T}}^{\mathrm{miss}}$ 124
6.1 Introduction . . . 124
6.2 Data and Monte Carlo simulation . . . 126
6.3 Event selection . . . 131
6.4 Analysis strategy . . . 135
6.4.1 Signal optimisation . . . 136
6.4.2 Signal acceptance . . . 147
6.5 Signal and background parametrisation . . . 147
6.5.1 Signal modelling . . . 147
6.5.2 Background modelling . . . 152
6.6 Systematic uncertainties . . . 155
6.6.1 Experimental systematic uncertainties . . . 156
6.6.2 Theoretical systematic uncertainties . . . 156
6.7 Statistical procedure and results . . . 159
6.7.1 Statistical procedure . . . 159
6.7.2 Results . . . 161

7 Conclusions **168**

Appendices **170**

A Integration of the ALTI Module in the TileCal **171**
A.1 ALTI modules installed in P1 TTC crates 171
A.2 Schematics for Laser, physics and CIS runs at the TB area 172

B The search for heavy resonances in the 4ℓ final state in association with $E_{\mathrm{T}}^{\mathrm{miss}}$ **174**
B.1 S mass scan with different energy gaps 174
B.2 Object vs Event based $E_{\mathrm{T}}^{\mathrm{miss}}$ significance in signal optimisation . . 174
B.3 Cut-flows and signal acceptances 178
B.4 Background estimation 182
B.5 Kinematic distributions 187
B.6 Signal modelling 190
B.7 Background modelling 199
B.8 Systematic uncertainties 203
B.8.1 Experimental systematic uncertainties 204
B.8.2 Systematic uncertainties on background shapes modelling . 207
B.9 Shape uncertainties 214
B.10 Systematic uncertainty breakdown 218
B.10.1 Systematic uncertainties on the normalisation of the $m_{4\ell}$ distribution 222
B.11 Effect of ZZ background normalisation on the upper limits 223

Bibliography **227**

List of Figures

1.1 A summary of the SM elementary particles (twelve fermions and five fundamental bosons) and their properties. 4

1.2 The Higgs potential $V(\Phi)$ for $\mu^2 < 0$ and $\lambda > 0$, where the energy density is a function of the $Re(\Phi)$ and $Im(\Phi)$ values. 9

1.3 The figure shows the $m_{4\ell}$ distribution for the selected Higgs boson candidates at $\sqrt{s} = 13\,\text{TeV}$ by the ATLAS and CMS collaborations. For the ATLAS collaboration, the observed and expected $m_{4\ell}$ distributions for an integrated luminosity of $139\,\text{fb}^{-1}$ are presented in (a), where the data points with error bars are compared to background processes in red, yellow, and violet. The signal expectation for a Standard Model (SM) Higgs boson with a mass of $m_H = 125\,\text{GeV}$ is also shown in blue [13]. The CMS collaboration presents its results for the $m_{4\ell}$ distribution in the low-mass region for an integrated luminosity of $137\,\text{fb}^{-1}$ at $\sqrt{s}$ =13 TeV in (b), where the data points with error bars are compared to background processes in blue and green. The anticipated signal for a SM Higgs boson with a mass of $m_H = 125\,\text{GeV}$ is depicted in magenta [14]. . 11

1.4 Summary of Higgs boson mass measurements from ATLAS and CMS independent analyses, as well as the combined analysis shown here. The uncertainties are given as systematic (magenta bands), statistical (yellow bands), and the total (black error bars). The (red) vertical line and corresponding (gray) band represent the combined measurement's central value and total uncertainty, respectively [15]. 12

1.5 An illustration of a hadron-hadron collision [16]. 13

1.6 Feynman diagrams for the Higgs boson production modes at the LHC: (a) gluon-gluon fusion, (b) vector boson fusion, (c) associated production with a vector boson and (d) associated production with a pair of heavy quarks. 15
1.7 Cross-sections of the SM Higgs boson with $m_H = 125\,\text{GeV}$ as a function of the center-of-mass energy $\sqrt{s}$ in (a) and in (b) the cross sections as a function of the Higgs mass at $\sqrt{s} = 13\,\text{TeV}$ [24]. . . . 15
1.8 LO Feynman diagrams of the Higgs boson decay channels for the $H \to b\bar{b}$, $H \to \tau\tau$, and $H \to \mu\mu$ (upper left); $H \to ZZ$ and $H \to WW$ (upper right); and $H \to \gamma\gamma$ (lower) channels. 17
1.9 The Higgs boson decay branching ratios and their theoretical uncertainties (bands) as a function of the Higgs boson mass [24]. . . 18
1.10 The Feynman diagrams depicting the production (a) and decay (b,c,d) of the heavy scalar boson H. 21
1.11 The impact of the effective decay process $H \to h\chi\chi$ on the Higgs p_{T} spectrum. Under the BSM hypothesis of $gg \to H \to h\chi\chi$ (solid lines), the spectrum is distorted with respect to the SM prediction (dashed line) (a). A comparative view of the Higgs p_{T} spectrum as described by the S-mediated interaction (solid lines) and the effective $H \to h\chi\chi$ interaction (dashed line) (b) [1]. 22
1.12 Feynman diagrams of the production of the Higgs boson in association with DM: (a) the decay of a heavy scalar H through the effective quartic $\lambda_{Hh\chi\chi}$ vertex and (b) due to the additional scalar S under a replacement of $\lambda_{Hh\chi\chi}$ with λ_{HhS} and $\lambda_{S\chi\chi}$ [1]. 23
1.13 The negative 2 times the logarithm of the profile likelihood ratios for each of the individual fit results considered in this article, overlaid with that of their combination. The significance of a result is calculated as the square root of the point which intersects the y-axis (that is, the SM-only hypothesis where $(\beta_g = 0)$) [50]. . . . 26

2.1 The LEP [51] was situated in a tunnel underground between year 1989 and 2000, and the tunnel now houses the LHC [52]. 28
2.2 An illustration of the CERN's accelerator complex [53]. 29
2.3 The LHC will go through several long shutdown periods before constant nominal luminosity [54]. 30
2.4 The four main experiments at the LHC. 31

2.5 Overview of the ATLAS experiment. Energetic particles collide at the experiment's center. Tracking detectors (dark grey), calorimeters (grey and orange), and the muon system (blue) record the resulting particles. The magnets generate magnetic fields essential for measuring charged particle momenta. Image sourced from [63]. 33
2.6 A cross-sectional representation of the ATLAS detector, illustrating how each subdetector contributes to particle identification and tracking. 34
2.7 The ATLAS uses a right handed coordinate system (a). Central regions approach $\eta_{det} = 0$, while $|\eta_{det}| \gg 0$ for forward regions (b). 35
2.8 The ATLAS ID is depicted in (a). A blow-up diagram of the ID sub-detectors is illustrated in (b) with layers of the IBL, pixels, SCT, and TRT. A charged particle track is indicated by the red line. 36
2.9 The calorimeters of the ATLAS detector [64] consist of an inner liquid argon EM calorimeter (depicted in orange), which is surrounded by the TileCal. Several forward calorimeters surround the beam pipe, covering an angular range of -5 $< \eta <$ 5. 37
2.10 The ATLAS EM calorimeter consists of liquid argon cells separated by lead inserted between them. These liquid argon cells are responsible for measuring the deposited charge from electromagnetic showers. [66]. 38
2.11 TileCal detector is divided into three barrels and four partitions (a). Schematic diagram of the TileCal wedge module (b) [67]. 39
2.12 Segmentation in depth and $|\eta|$ of the Tile Calorimeter modules in the central and extended barrels. The central barrel has a coverage up to $|\eta| < 1.0$. The extended barrel covers the region $0.8 < |\eta| < 1.7$ [55]. 40
2.13 This is a general overview of the TDAQ system [68]. 41
2.14 The TileCal barrels comprise 256 modules, containing drawers with FE electronics. The cross-section displays the electronics within the drawer. Scintillating tiles are connected to PMTs via WLS fibres for light transmission [78]. 42
2.15 The TileCal BE electronics signal chain. 43

2.16 In Point 1, the TileCal BE read-out electronics are partitioned into four crates labelled EBA, LBA, LBC and EBC, which correspond to the colours of the TileCal detector barrels shown in Figure 2.11(a). The TTC and ROD VME modules in the crates are represented diagrammatically in panel (b). 44
2.17 One of the P1 TTC crate housing different modules (a). The ROD crate housing eight ROD modules, TBM and a SBC (b). 45
2.18 Diagrammatic representation of TileCal DCS hierarchal system used in Run 2 [82]. 46
2.19 A diagram illustrating the sequence of signal readout in the calibration systems of TileCal [86]. 48

3.1 A depiction of the Configuration Databases: architecture, management and access [70]. 51
3.2 The IGUI of the Tile175 partition. 52
3.3 The RCD schematic diagram. The RCD handles the TileCal BE hardware operation, with one RCD application running in each TTC and ROD crate [91]. 53
3.4 A visual overview of the TDAQ software organization, where the TileCal and other sub-detector software projects are constructed using the tdaq project. The tdaq project, in turn, is developed based on the dqm-common and tdaq-common projects. 57
3.5 A diagrammatic representation is shown for the Tile Online software release packages, which consist of twenty-nine packages, with the majority dependent on the TileConfiguration package. 59
3.6 CIS HG DVS test result from IGUI. The test result shows that there are problems in the amplitude of channel 3. Log files show that the pulse amplitude, width and phase were incorrect in 100 events, and thus the channel is color coded red for bad. 60
3.7 Plots showing results from DVS pedestal test for both high and low gain. Results show that noise levels are within acceptable levels for this module (EBC52). 60

4.1 The four legacy TTC modules (LTPi, LTP, TTCvi and TTCex) will be replaced by the ALTI module (a). ALTI module (b). . . . 62
4.2 ALTI functional block diagram. 63
4.3 ALTI firmware block diagram. 64

4.4 ALTI clock source paths and distribution. 65
4.5 TTC B-channel data format. 69
4.6 Pattern generator block diagram. 71
4.7 TTC decoder 80
4.8 B175 test bench (a). On top is the ROD crate with one ROD module, a TBM and a SBC. At the bottom is the TTC crate (b). 81
4.9 The ALTI module inserted in the TTC crate of a test-bench at CERN. 82
4.10 The schematic diagram of the ALTI configuration for B175 standalone runs. 82
4.11 A screenshot of the execution of the *testAltiQuickBoot* command to load the firmware. The ALTI module is detected in slot 6 and the latest firmware is loaded. 83
4.12 OKS Data Editor showing the ALTI classes and the TileB175_ALTI2 object. 84
4.13 Pattern generator for the B175 test bench. 84
4.14 TileTTC class provides an interface between the TTCvi and the ALTI class. 85
4.15 The Tile175 eventviewer showing CIS run results. Results show 7 samples that form a Gaussian distribution. In the absence of a pulse, only the pedestal is shown. 86
4.16 ALTI modules with new optical fibres, ready to be installed in the TTC crates of the BE electronics. 87
4.17 The TileCal TTC crates are located above the read-out driver crates in the BE electronics (a). ALTI modules were installed in the TTC crates of LBA, LBC, EBA, EBC and the Laser crate (b). 88
4.18 Pattern generator 88
4.19 The schematic diagram of the ALTI configuration for P1 standalone runs. 89
4.20 The schematic diagram of the ALTI configuration for P1 physics runs. 90
4.21 Laser calibration test results in TileCal. 91
4.22 CIS calibration results showing the Amp/Q plots. 92
4.23 CIS calibration results showing the time plots. 92
4.24 Pedestal calibration test results in TileCal. 93
4.25 Pedestal calibration test results in TileCal. 93

4.26 The CIS DVS test taken for one read-out module in good working condition, shows a good reconstructed pulse of the ADC counts against time, for seven samples per channel (a). The pedestal DVS test shows the RMS ADC counts against the channel number and the electronics noise level is below the threshold for all read-out channels (b). 94
4.27 a view of a few event displays from the pilot run is shown on VP1 (a) and the ATLANTIS display (b). 95
4.28 a view of the Atlantis display (a) and pulse shape for EBC13 D6 Tile cell PMTs (b). 96
4.29 Event display of a collision event displayed by Atlantis. 96
4.30 Event display of a collision event displayed by VP1. 97
4.31 TileCal hybrid Demonstrator Minidrawer. 99
4.32 Sketch of the TileCal Phase-II upgrade readout electronics. The left side of the sketch (magenta) are the on-detector electronics and the right side (red) are the off-detector electronics. 100
4.33 Beam elements and the scanning table in the test beam setup. . . 101
4.34 Schematic diagram of the FE and BE electronics in the test beam setup. 102
4.35 Beam elements and the scanning table in the test beam setup. . . 103
4.36 ALTI installed in the TTC crate at test beam area. 104
4.37 The schematic of the ALTI configuration at test beam area for all run types. 105
4.38 Three pattern generator files used at the test beam setup. File for pedestal and CIS runs (a). File for laser runs (b). File for physics runs (c). 106
4.39 The test beam eventviewer for a laser run. Results show 15 samples that form a Gaussian distribution. In the absence of a pulse, only the pedestal is shown. 106
4.40 Results from DVS pedestal test for high frequency noise in both high and low gain. Results show that noise levels are within acceptable levels for the LBC01 module. 107
4.41 LBC01 CIS HG DVS test result from IGUI. The test results indicate that there is a deviation in the amplitude, width or phase of channel 6, hence the channel is flagged red for bad, to trigger further investigation. 108

4.42 Test of the pulse shape in the PMT. The test also checks if the histogram is not empty (a). The total TileCal event energy measured in pCs (b). 108
4.43 Layer A7 cell response in LBC02 module, exposed to 108 GeV muon beam (a). Layer A7 cell's PMT energy response correlation plot (b). 109

5.1 Track reconstruction showing the *inside-out* and the *outside-in* approaches. 111
5.2 Illustration of reconstructed vertices showing the primary vertex and the secondary vertex. 113
5.3 Illustration of an electron (in red) traversing through the detector [123]. It first traverses the tracking system (Pixel, SCT and TRT) and enters the EM calorimeter. 115
5.4 Combined muon reconstruction requires the combination of tracks from the ID and MS. The ATLAS software provides four complementary types of reconstructed muons: Combined, Segment-tagged, Calorimeter-tagged and Extrapolated muons. 119

6.1 Feynman diagrams represent the production of heavy bosons via gloun-fusion (a) $R \to SH \to 4\ell + E_{\mathrm{T}}^{\mathrm{miss}}$ and (b) $A \to Z(\nu\nu)H(ZZ) \to 4\ell + X$ models. 126
6.2 The luminosity-weighted distribution of the mean number of interactions per crossing for pp collision data collected by the ATLAS experiment in the period between 2015 - 2018 at the LHC. 127
6.3 2D plots showing the energy gap of the (a) $R \to SH \to 4\ell + E_{\mathrm{T}}^{\mathrm{miss}}$ and (b) $A \to Z(\to X)H(\to 4\ell)$ and $A \to Z(\to 2\ell)H(\to 2\ell)$ models. The energy gap is represented by the z-axis as $m_R - m_H$ or $m_A - m_H$. 130
6.4 The cross-section of the $A \to Z(\nu\nu)H(ZZ) \to 4\ell + X$ calculated using the 2HDM with different $\tan(\beta)$ and $\cos(\beta - \alpha)$ assumptions. 131
6.5 Distribution for the $R \to SH \to 4\ell + E_{\mathrm{T}}^{\mathrm{miss}}$ signal compared to the different background components of the (a) Number of central jets, (b) Number of b-tagged jets. Each signal is normalised to the total number of the background. 139

6.6 2D scan of the $p_{\mathrm{T}}^{4\ell}$ and $E_{\mathrm{T}}^{\mathrm{miss}}$ significance for the $R \to SH \to 4\ell + E_{\mathrm{T}}^{\mathrm{miss}}$ signal in the zero central jets region. The z-axis shows the significance calculated using $s/\sqrt{b}$ (top) and $s/\sqrt{s+b}$ (bottom). The High-$E_{\mathrm{T}}^{\mathrm{miss}}$ scans are shown in (a) and (c), and Low-$E_{\mathrm{T}}^{\mathrm{miss}}$ in (b) and (d). 140

6.7 Distribution for the $R \to SH \to 4\ell + E_{\mathrm{T}}^{\mathrm{miss}}$ signal compared to the different background components of the (a) Four-lepton invariant mass, (b) Four-lepton transverse momentum, (c) Missing transverse energy and (d) $E_{\mathrm{T}}^{\mathrm{miss}}$ significance. Each signal is normalised to the total number of background to obtain a better comparison to the background. 141

6.8 Distribution for the $A \to Z(\nu\nu)H(ZZ) \to 4\ell + X$ signal compared to the different background components of (a) Number of central jets and (b) Number of b-tagged jets. Each signal is normalised to the total number of SM backgrounds. 142

6.9 Distribution for the $A \to Z(\to X)H(\to 4\ell)$ signal comparing to the different background components of the (a) Four-lepton invariant mass, (b) Four-lepton transverse momentum, (c) Missing transverse energy and (d) $E_{\mathrm{T}}^{\mathrm{miss}}$ significance. Each signal is normalised to the total number of the background. 144

6.10 Distribution for the $A \to Z(\to X)H(\to 4\ell)$ signal comparing to the different background components of the (a) Di-jet transverse momentum, (b) Di-jet invariant mass and (c) Di-jet $\Delta\eta$. Each signal is normalised to the total number of background. 145

6.11 Diagram illustrates the categorisation scheme for $A \to Z(\nu\nu)H(ZZ) \to 4\ell + X$ and $R \to SH \to 4\ell + E_{\mathrm{T}}^{\mathrm{miss}}$ optimisation. Eight orthogonal categories are developed for the $A \to Z(\nu\nu)H(ZZ) \to 4\ell + X$ signal and four for $R \to SH \to 4\ell + E_{\mathrm{T}}^{\mathrm{miss}}$ signal. 146

6.12 The invariant mass of the four leptons of the interpolated $A \to Z(\to X)H(\to 4\ell)$ signal shape with H mass fixed to 500 GeV and A mass varied by 10 GeV. The blue, green and cyan histogram are the original histograms used in the input for different categories. . 150

6.13 The invariant mass of the four leptons of the interpolated $A \to Z(\to X)H(\to 4\ell)$ signal shape with A mass fixed to 500 GeV and H mass varied by 10 GeV. 151

6.14 The 4ℓ invariant mass distributions for the analytical function fit to $qqZZ$ background in different signal regions. 153
6.15 The 4ℓ invariant mass distributions for the analytical function fit to the $qqZZ$ background in different signal regions. 155
6.16 The shape uncertainties as a function of the $m_{4\ell}$ of the HOEW correction for the $qqZZ$ background in different signal regions. . . 158
6.17 The Pre-fit and Post-fit results of the $m_{4\ell}$ distributions for the $A \to Z(\nu\nu)H(ZZ) \to 4\ell + X$ signal with $(m_A, m_H) = (460, 320)$ GeV. A blue arrow indicates that the ratio is off-scale. 163
6.18 The Pre-fit and Post-fit results of the $m_{4\ell}$ distributions for the $R \to SH \to 4\ell + E_{\mathrm{T}}^{\mathrm{miss}}$ signal with $(m_R, m_H) = (420, 250)$ GeV. A blue arrow indicates that the ratio is off-scale. 163
6.19 Best fit values of the signal strength modifiers μ with their 68% expected confidence intervals (error bars). 164
6.20 The impact of nuisance parameters on (a) $A \to Z(\nu\nu)H(ZZ) \to 4\ell + X$ signal sensitivity (σ_{AZH}) and (b) $R \to SH \to 4\ell + E_{\mathrm{T}}^{\mathrm{miss}}$ (σ_{RSH}), are performed for different mass hypotheses. (a) shows $(m_A, m_H) = (320, 220)$ and (b) shows $(m_R, m_H) = (390, 220)$. . . 165
6.21 The (a) expected and (b) observed upper limits at 95% confidence level on the $\sigma(gg \to A) \times \mathrm{BR}(A \to ZH) \times \mathrm{BR}(H \to ZZ \to 4\ell) \times \mathrm{A} \times \mathrm{E}$ on (m_H, m_A) planes. 166
6.22 The expected and observed 1D upper limits at 95% confidence level on the $\sigma(gg \to A) \times \mathrm{BR}(A \to ZH) \times \mathrm{BR}(H \to ZZ \to 4\ell) \times \mathrm{A} \times \mathrm{E}$ for different m_A mass while fixing m_H to be 500 and 520 GeV for $A \to Z(\nu\nu)H(ZZ) \to 4\ell + X$. 166
6.23 The (a) expected and (b) observed upper limits at 95% confidence level on the $\sigma(gg \to R) \times \mathrm{BR}(R \to SH) \times \mathrm{BR}(H \to ZZ \to 4\ell) \times \mathrm{A} \times \mathrm{E}$ on (m_H, m_R) planes. 167
6.24 The expected and observed 1D upper limits at 95% confidence level on the $\sigma(gg \to R) \times \mathrm{BR}(R \to SH) \times \mathrm{BR}(H \to ZZ \to 4\ell) \times \mathrm{A} \times \mathrm{E}$ for different m_R mass while fixing m_H to be 220 and 250 GeV for the $R \to SH \to 4\ell + E_{\mathrm{T}}^{\mathrm{miss}}$ model. 167

A.1 Four TTC partitions. 171
A.2 Schematic of the laser runs at test beam. 172
A.3 Schematic of the physics runs at test beam. 173

A.4 Schematic of the CIS runs at test beam. 173

B.1 The missing transverse energy of the four-lepton system at particle level of the $R \to SH \to 4\ell + E_{\mathrm{T}}^{\mathrm{miss}}$ signal for different m_S values. . 175
B.2 The transverse momentum of the four-lepton system at particle level of the $R \to SH \to 4\ell + E_{\mathrm{T}}^{\mathrm{miss}}$ signal for different m_S values. . 175
B.3 2D scan of the $p_{\mathrm{T}}^{4\ell}$ and $E_{\mathrm{T}}^{\mathrm{miss}}$ significance for the $R \to SH \to 4\ell + E_{\mathrm{T}}^{\mathrm{miss}}$ signal. The Event-based $E_{\mathrm{T}}^{\mathrm{miss}}$ significance is shown in (a) and (b) and Object-based $E_{\mathrm{T}}^{\mathrm{miss}}$ significance in (c) and (d) for High- and Low-$E_{\mathrm{T}}^{\mathrm{miss}}$ of the zero central jet. 176
B.4 Two-dimensional scan of the $p_{\mathrm{T}}^{4\ell}$ and $E_{\mathrm{T}}^{\mathrm{miss}}$ significance for the $R \to SH \to 4\ell + E_{\mathrm{T}}^{\mathrm{miss}}$ signal. The Event-based $E_{\mathrm{T}}^{\mathrm{miss}}$ significance is shown in (a) and (b), and Object-based $E_{\mathrm{T}}^{\mathrm{miss}}$ significance in (c) and (d) for High- and Low-$E_{\mathrm{T}}^{\mathrm{miss}}$ of the one central jet. 177
B.5 2D scan of the $p_{\mathrm{T}}^{4\ell}$ and $E_{\mathrm{T}}^{\mathrm{miss}}$ significance for the $R \to SH \to 4\ell + E_{\mathrm{T}}^{\mathrm{miss}}$ signal in the zero central jets region. The High-$E_{\mathrm{T}}^{\mathrm{miss}}$ scans are shown in (a) and (c), and Low-$E_{\mathrm{T}}^{\mathrm{miss}}$ on (b) and (d). . . 178
B.6 Kinematic distributions of the (a) number of central jets, (b) number of b-tagged jets and (c) di-jet invariant mass. The data at integrated luminosity of 139 fb^{-1} are compared to the SM prediction in the control region of $80 < m_{4\ell} < 170\,\mathrm{GeV}$. 183
B.7 Kinematic distributions of (a) the $m_{4\ell}$, (b) $p_T^{4\ell}$, (c) $\eta^{4\ell}$, and (d) $y^{4\ell}$. The data at integrated luminosity of 139 fb^{-1} are compared to the SM prediction in the control region of $80 < m_{4\ell} < 170\,\mathrm{GeV}$. 185
B.8 Non-discriminative kinematic distributions of the (a) $N_{\mathrm{jets}}^{\mathrm{Central}}$, (b) $N_{b\text{-jets}}$, (c) $\eta^{4\ell}$, and (d) $y^{4\ell}$. The data corresponding to an integrated luminosity of 139 fb^{-1}, are compared to the SM prediction in the $m_{4\ell} > 200\,\mathrm{GeV}$ region. 187
B.9 Kinematic distributions of (a) the m_{Z_1}, (b), m_{Z_2} and (c) $E_{\mathrm{T}}^{\mathrm{miss}}$ significance. The date at integrated luminosity of 139 fb^{-1} are compared to the SM prediction in the control region of $80 < m_{4\ell} < 170\,\mathrm{GeV}$. 188
B.10 Kinematic distributions of (a) the $p_{\mathrm{T}}^{\ell_1}$, (b) $p_{\mathrm{T}}^{\ell_2}$, (c) $p_{\mathrm{T}}^{\ell_3}$, and (d) $p_{\mathrm{T}}^{\ell_4}$. The date at integrated luminosity of 139 fb^{-1} are compared to the SM prediction in the control region of $80 < m_{4\ell} < 170\,\mathrm{GeV}$. 189

B.11 Distributions of the four-lepton invariant mass for fitting the $\mathcal{CB}+\mathcal{G}$ PDF of equation B.2 to $R \to SH \to 4\ell + E_{\mathrm{T}}^{\mathrm{miss}}$ signal with $m_H = 220\,\mathrm{GeV}$ and different m_R masses. The fit is performed using MC simulation with statistics equivalent to integrated luminosity of $139\,\mathrm{fb}^{-1}$. The ratio plot in each figure shows the pull distribution. The plots are shown for the High-$E_{\mathrm{T}}^{\mathrm{miss}}$ and $N_{\mathrm{jets}}^{\mathrm{Central}} \geq 1$ signal region. 193

B.12 The invariant mass of the four leptons of the interpolated $A \to Z(\to 2\ell)H(\to 2\ell + X)$ signal shape with H mass fixed to 250 GeV and A mass varied by 10 GeV. Because the signal doesn't peak on the H mass, a few mass points ($N = 25$) are shown as an example to get a better view of the interpolated samples. The blue, green and cyan histogram are the original histograms used in the input for different categories. 194

B.13 The invariant mass of the four leptons of the interpolated $A \to Z(\to 2\ell)H(\to 2\ell + X)$ signal shape with A mass fixed to 500 GeV and H mass varied by 10 GeV. 195

B.14 The invariant mass of the four leptons of the $A \to ZH \to 4\ell + X$ for all the signal regions with varies mass points. 196

B.15 The invariant mass of the four leptons of the interpolated $R \to SH \to 4\ell + E_{\mathrm{T}}^{\mathrm{miss}}$ signal shape with H mass fixed to 500 GeV and R mass varied by 10 GeV. The blue, green and cyan histogram are the original histograms used in the input for different categories. . 197

B.16 The invariant mass of the four leptons of the interpolated $R \to SH \to 4\ell + E_{\mathrm{T}}^{\mathrm{miss}}$ signal shape with R mass fixed to 500 GeV and H mass varied by 10 GeV. 198

B.17 The four-lepton invariant mass distributions for the analytical function fit to $ggZZ$ background in different signal regions. 199

B.18 The four-lepton invariant mass distributions for the analytical function fit to VVV background in different signal regions. 200

B.19 The four-lepton invariant mass distributions for the analytical function fit to others ($qqZZ$(EW), $t\bar{t}V$, $t\bar{t}$ and WZ) background in different signal regions. 201

B.20 Systematic uncertainties on the $A \to Z(\to X)H(\to 4\ell)$ shape (top) and $R \to SH \to 4\ell + E_{\mathrm{T}}^{\mathrm{miss}}$ shape (bottom). 207

B.21 Shape systematic uncertainties due to $qqZZ$ background parametrisation in the invariant mass of the four leptons. 208

B.22 Shape systematic uncertainties due to $qqZZ$ background parametrisation in the invariant mass of the four leptons. 209
B.23 The mean value for systematic uncertainties in the $m_{4\ell}$ normalisation calculated from the (390, 220), (790, 600) and (1190, 1000) mass points with $m_R - m_H \leq 200\,\text{GeV}$ for the $R \to SH \to 4\ell + E_{\text{T}}^{\text{miss}}$ signal. Top (bottom) two plots represent the High- and Low-$E_{\text{T}}^{\text{miss}}$ of the $N_{\text{jets}}^{\text{Central}} \geq 1$ ($N_{\text{jets}}^{\text{Central}} = 0$) categories, respectively. Up and Down variations are shown in descending order only for the first 50 nuisance parameters. 210
B.24 The mean value for systematic uncertainties in the $m_{4\ell}$ normalisation calculated from the (330, 220), (700, 600) and (1100, 1000) mass points with $m_A - m_H \leq 100\,\text{GeV}$ for the $A \to Z(\nu\nu)H(ZZ) \to 4\ell + X$ signal. Top two plots represent the High- and Low-$E_{\text{T}}^{\text{miss}}$ of the $N_{\text{jets}}^{\text{Central}} \geq 1$ category, respectively. The bottom plots show High-$E_{\text{T}}^{\text{miss}}$ of $N_{\text{jets}}^{\text{Central}} = 0$ and $N_{b-\text{jets}} \geq 1$ categories, respectively. Up and Down variations are shown in descending order only for the first 50 nuisance parameters. 211
B.25 The experimental systematic uncertainties on the normalisation of the $m_{4\ell}$ distribution for the other backgrounds. Top two plots represent the High- and Low-$E_{\text{T}}^{\text{miss}}$ of the $N_{\text{jets}}^{\text{Central}} \geq 1$ category, respectively. The bottom plots show High-$E_{\text{T}}^{\text{miss}}$ of $N_{\text{jets}}^{\text{Central}} = 0$ and $N_{b-\text{jets}} \geq 1$ categories, respectively. Up and Down variations are shown in descending order only for the first 50 nuisance parameters. 212
B.26 The experimental systematic uncertainties on the normalisation of the $m_{4\ell}$ distribution for the other backgrounds. Top (bottom) two plots represent the $|m_{\text{jj}} - m_Z| < 20\,\text{GeV}$ and $|m_{\text{jj}} - m_Z| > 20\,\text{GeV}$ ($N_{\text{jets}}^{\text{Central}} = 1$) categories, respectively. Up and Down variations are shown in descending order only for the first 50 nuisance parameters. 213
B.27 The shape uncertainties as a function of the invariant mass of the four leptons of the QCD scale variations for the $qqZZ$ background in different signal regions. 214
B.28 The shape uncertainties as a function of the invariant mass of the four leptons PDF variations for the $qqZZ$ background in different signal regions. 215

B.29 The shape uncertainties as a function of the invariant mass of the four leptons of the QCD scale variations for the $ggZZ$ background in different signal regions. 216
B.30 The shape uncertainties as a function of the invariant mass of the four leptons PDF variations for the $ggZZ$ background in different signal regions. 217
B.31 The likelihood profile as function of the $\sigma(gg \to R) \times \mathrm{BR}(R \to SH) \times \mathrm{BR}(H \to ZZ \to 4\ell)$ for the $R \to SH \to 4\ell + E_{\mathrm{T}}^{\mathrm{miss}}$ signal. The 2σ level represents the upper limit at 95% CL. 224
B.32 The likelihood profile as function of the $\sigma(gg \to A) \times \mathrm{BR}(A \to ZH) \times \mathrm{BR}(H \to ZZ \to 4\ell)$ for the $A \to Z(\nu\nu)H(ZZ) \to 4\ell + X$ signal. The 2σ level represents the upper limit at 95% CL. 225
B.33 The likelihood profile as function of the $qqZZ$ and $ggZZ$ normalisation (μ_{ZZ}). The normalisation scan is shown per category and inclusively. 226

List of Tables

1.1 The Higgs boson production cross-sections for $m_H = 125\,\text{GeV}$ in pp collisions at a center-of-mass energy $\sqrt{s} = 13\,\text{TeV}$ [23]. 16
1.2 Branching ratios of the Higgs decay for a Higgs boson mass $m_H = 125\,\text{GeV}$ [23]. 17
1.3 A list of experimental results utilized in constraining the relevant parameters of the 2HDM+S model [31]. 20
1.4 A list of possible decay modes of the 2HDM scalars and S based on the explicit mass selections provided in the text of Reference [1]. 24
1.5 A list of potential search channels arising from the addition of the new scalars. The list is incomplete, but contains clean search channels which could make for striking signatures at the LHC [1] . . . 24
1.6 Summary of SM+BSM fit results for the measurements considered in Reference [2]. 26

6.1 Summary of MC generators used to model signal and background processes, accuracy in QCD and the parton distribution function set. 129
6.2 Summary of the object identification and event selection requirements. The leading and sub-leading lepton pairs are denoted by m_{Z_1} and m_{Z_2}. 134
6.3 Summary of the requirements of the signal regions selection for the $R \to SH \to 4\ell + E_{\text{T}}^{\text{miss}}$ and $A \to ZH \to 4\ell + X$ signals for $m_{4\ell} > 200\,\text{GeV}$. 136

6.4 The expected yields for the $(m_R, m_H) = (390, 220)$ GeV signal mass point, and the total background calculated from the state-of-the-art MC simulation with an integrated luminosity of 139 fb^{-1}. The uncertainties included on the table are statistical uncertainty only. The expected events at the preselection are after the selection discussed in Section 6.3. $E_{\mathrm{T}}^{\mathrm{miss}}$ significance is represented by metSig on the table. The $R \to SH \to 4\ell + E_{\mathrm{T}}^{\mathrm{miss}}$ signal cross section is assumed to be 1 fb. 138

6.5 The expected yields for the $(m_A, m_H) = (330, 220)$ GeV signal mass point, and the significance calculated from the state-of-the-art MC simulation with an integrated luminosity of 139 fb^{-1}. The uncertainties included on the table are statistical uncertainty only. The expected events at the preselection are after the selection discussed in Section 6.3. The $A \to Z(\to X)H(\to 4\ell)$ and $A \to Z(\to X)H(\to 4\ell)$ cross-sections are assumed to be 1 fb and 1.87 fb, respectively. 143

6.6 Summary of the $A \to Z(\nu\nu)H(ZZ) \to 4\ell + X$ and $R \to SH \to 4\ell + E_{\mathrm{T}}^{\mathrm{miss}}$ categories, significance calculated using Equation 6.4. The combined significance is the sum in quadrature taking from all the categories except the low-$E_{\mathrm{T}}^{\mathrm{miss}}$ of the zero central jets region. 143

6.7 The signal acceptance times efficiencies for the $R \to SH \to 4\ell + E_{\mathrm{T}}^{\mathrm{miss}}$ signal taken from fully simulated MC samples. The S mass is fixed to 160 GeV, and the H and R masses are varied with $m_R = m_S + m_H + m_{\mathrm{Gap}}$. The m_{Gap} is set to be 10, 20, 30, 40, 50, 100, 200, 500, and 1000 GeV, to generate different signals. The table shows the acceptance times efficiencies for signals with H masses of 220 and 250 GeV. 148

6.8 The signal acceptance times efficiencies for the $A \to Z(\to X)H(\to 4\ell)$ signal taken from the fully simulated MC samples. The Z boson mass is fixed to 90 GeV, and the H and A masses are varied with $m_A = m_Z + m_H + m_{\mathrm{Gap}}$. The m_{Gap} is set to be 10, 20, 30, 40, 50, 100, 200, 500, and 1000 GeV, to generate different signals. The table shows the acceptance times efficiencies for signals with H masses of 220 and 250 GeV. 149

6.9 Summary of χ^2/ndof values for Equation 6.5 fitted to different background templates. The χ^2/ndof values are shown for Figure 6.14 and Figures shown in Appendices B.17, B.18 and B.19. 154

6.10 The extracted parameters after fitting $qqZZ$ MC using Equation 6.5. The m_0 parameter values are fixed during the fit to improve the fit stability. 154
6.11 Observed and expected post-fit event yields for $m_{4\ell} > 200$ GeV with their uncertainties. The expected yields and their uncertainties are obtained from a simultaneous fit to data under the background-only hypothesis on all seven signal regions discussed in Section 6.7.1. The μ^{ZZ}_{norm} is the normalisation factor for $q\bar{q} \to ZZ$ and $gg \to ZZ$ backgrounds which is considered during the fit. The others background include $q\bar{q} \to ZZ$ (EW), $t\bar{t}V$, $t\bar{t}$, Z+jets and WZ processes. 162

B.1 Yields and significance for $R \to SH \to 4\ell + E_{\text{T}}^{\text{miss}}$ signal taken from fully simulated MC samples. The S mass is fixed to 160 GeV , and the H and R masses are varied with $m_R = m_S + m_H + m_{\text{Gap}}$. The m_{Gap} is set to be 10, 20, 30, 40, 50, 100, 200, 500, and 1000 GeVs to generate different signals. The table shows event yields and significances for signals with H masses of 220 and 250 GeVs for different categories. The significance is calculated using Z_{Sig_1} and Z_{Sig_2} defined in Equation 6.4. The $R \to SH \to 4\ell + E_{\text{T}}^{\text{miss}}$ signal cross section is assumed to be 1 fb. 179
B.2 Yields and significance for $A \to Z(\to X)H(\to 4\ell)$ signal taken from fully simulated MC samples. The Z boson mass is fixed to 90 GeV, and the H and A masses are varied with $m_A = m_Z + m_H + m_{\text{Gap}}$. The m_{Gap} is set to be 10, 20, 30, 40, 50, 100, 200, 500, and 1000 GeVs to generate different signals. The table shows event yields and significances for signals with H masses of 220 and 250 GeVs for different categories. The significance is calculated using Z_{Sig_1} and Z_{Sig_2} defined in Equation 6.4. The $A \to Z(\to X)H(\to 4\ell)$ signal cross section is assumed to be 1 fb. 180
B.3 The signal acceptance times efficiencies for the $R \to SH \to 4\ell + E_{\text{T}}^{\text{miss}}$ signal taken from fully simulated MC samples. The S mass is fixed to 160 GeV, and the H and R masses are varied with $m_R = m_S + m_H + m_{\text{Gap}}$. The m_{Gap} is set to be 10, 20, 30, 40, 50, 100, 200, 500, and 1000 GeVs to generate different signals. The table shows the acceptance times efficiencies for signals with H masses of 600, 800, and 1000 GeVs. 181

B.4 The signal acceptance times efficiencies for the $A \to Z(\to 2\ell)H(\to 2\ell + X)$ signal taken from the fully simulated MC samples. The Z boson mass is fixed to 90 GeV, and the H and A masses are varied with $m_A = m_Z + m_H + m_{\text{Gap}}$. The m_{Gap} is set to be 10, 20, 30, 40, 50, 100, 200, 500, and 1000 GeV to generate different signals. The table shows the acceptance times efficiencies for signals with H masses of 220 and 250 GeV. 182
B.5 The expected and observed events in a control region of $80 < m_{4\ell} < 170$ GeV. The data used corresponds to an integrated luminosity of 139 fb^{-1}. 184
B.6 The expected and observed events for the signal regions in a control region of $80 < m_{4\ell} < 170$ GeV. The data used corresponds to an integrated luminosity of 139 fb^{-1}. 184
B.7 The expected yields for $t\bar{t}Z$, $t\bar{t}Z$, $Z + jets$, WZ and $t\bar{t}$ backgrounds from the MC simulation with an integrated luminosity of 139 fb^{-1}. The uncertainties included on the table are statistical uncertainty only. The expected events at the preselection are after the selection discussed in Section 6.3. 186
B.8 Summary of χ^2/ndof values from fitting $\mathcal{CB}+\mathcal{G}$ PDF of equation B.2 to m_H (m_A) between 220 − 250 GeV (390 − 1500) GeV of the $R \to SH \to 4\ell + E_{\text{T}}^{\text{miss}}$ model. 191
B.9 Summary of χ^2/ndof values from fitting $\mathcal{CB}+\mathcal{G}$ PDF of equation B.2 to m_H (m_A) between 220 − 400 GeV (320 − 1490) GeV of the $A \to Z(\to X)H(\to 4\ell)$ model. 192
B.10 The extracted parameters after fitting $ggZZ$ MC using Equation 6.5. The m_0 parameter values are fixed during the fit to improve the fit stability. 202
B.11 The extracted parameters after fitting VVV MC using Equation 6.5. The m_0 parameter values are fixed during the fit to improve the fit stability. 202
B.12 The extracted parameters after fitting others MC using Equation 6.5. The m_0 parameter values are fixed during the fit to improve the fit stability. 202
B.13 Summary of all systematic uncertainties considered as nuisance parameters in this analysis. The variables with brackets at the end, for example [1-7], represents different independent number variables. 203

B.14 Summary of the systematic uncertainties estimated from different sources in percentage on the $R \to SH \to 4\ell + E_{\mathrm{T}}^{\mathrm{miss}}$ signal. 219
B.15 Summary of the systematic uncertainties estimated from different sources in percentage on the $A \to Z(\nu\nu)H(ZZ) \to 4\ell + X$ signal. 220
B.16 Summary of the systematic uncertainties for the $m_{4\ell}$ normalisation estimated from different sources in percentage on the $qqZZ$ background. 220
B.17 Summary of the systematic uncertainties on the $m_{4\ell}$ shape due to background parametrisation in percentage for the $qqZZ$, $ggZZ$, VVV and others backgrounds. The numbers are organised to represent the effect on low and higher $m_{4\ell}$ regions such as $m_{4\ell}[200 - 700]$ GeV and $m_{4\ell}[700 - 1200]$ GeV, respectively. 221
B.18 Summary of the systematic uncertainties on the $m_{4\ell}$ shape estimated from different sources in percentage for the $qqZZ$ background. 221
B.19 Summary of the systematic uncertainties on the $m_{4\ell}$ shape estimated from different sources in percentage for the $ggZZ$ background. 221
B.20 Summary of the systematic uncertainties for the $m_{4\ell}$ normalisation estimated from different sources in percentage on the $ggZZ$ background. 222
B.21 Summary of the systematic uncertainties for the $m_{4\ell}$ normalisation estimated from different sources in percentage on the VVV background. 222
B.22 Summary of the systematic uncertainties for the $m_{4\ell}$ normalisation estimated from different sources in percentage on the others backgrounds. 223

Nomenclature

Abbreviations and Acronyms

2D	Two-Dimensional
2HDM	Two Higgs Doublet Model
ACR	ATLAS Control Room
ADC	Analog to Digital Converter
AFS	Andrew File System
ALICE	A Large Ion Collider Experiment
ALTI	ATLAS Local Trigger Interface
AM	Access Manager
API	Application Programming Interface
ATLAS	A Toroidal LHC ApparatuS
B175	Building 175 laboratory in Meyrin site, CERN
BC	Bunch-Crossing
BCId	Bunch-Crossing Identifier
BE	Back-End
BR	Branching Ratio
BSM	Beyond the Standard Model
CAEN	Construzioni Apparecchiature Elletroniche Nucleari S.p.A

CB	Crystal Ball
CCC	CERN Control Centre
CC	Cherenkov Counter
CERN	European Organization for Nuclear Research
CIS	Charge Injection Scan
CL$_s$	Confidence Limits
CMS	Compact Muon Solenoid
CMT	Configuration Management Tool
COOL	ATLAS-wide conditions database, also: CLIPS Object Oriented Language
CRC	Cyclic Redundancy Check
CR	Control Region
CTP	Central Trigger Processor (L1 trigger)
DAL	Data Access Library
DAQ	Data AcQuisition system
DB	DataBase
DCS	Detector Control System
DMU	Data Management Unit
DQM	Data Quality Monitoring
DSCB	Double-Sided Crystal Ball
DSP	Digital Signal Processor
DVS	Diagnostic and Verification System
DWC	Delay Wire Chambers
EBA	Extended Barrel A-side

EBC Extended Barrel C-side

EB Extended Barrel

ECal EM Calorimeter

ECP Egamma Combined Performance group

EF Event Filter

EIL4 End-cap Inner Large 4

EM ElectroMagnetic

ERS Error Reporting Service

EW ElectroWeak

FASER Forward Search Experiment

FCal Forward Calorimeter

FENICS Front End board for the New Infrastructure with Calibration and Signal Shaping

FE Front-End

FIFO First-In First-Out memory or strategy

FPGA Field-Programmable Gate Array

FSM Finite State Machine

FSR Final-State-Radiation

G-LINK Gigabit LINK

GeV Giga electron Volt

GRL Good Run List

GSF Gaussian-Sum Filter

GUI Graphical User Interface

HCal Hadronic Calorimeter

HDBS ATLAS Higgs and DiBoson Searches

HEC Hadronic End-cap Calorimeter

HL-LHC High-Luminosity LHC

HLT High Level Trigger

HOEW High-Order Electro-Weak

HOLA High speed Optical Link for ATLAS

HVPS High Voltage Power Supply

HV High Voltage

I/O Input/Output

IBL Insertable B-Layer

ICPP Institute for Collider Particle Physics

ID Inner Detector

IGUI Integrated Graphical User Interface

IPC Inter-Process Communication

IPMI Intelligent Platform Management Interface

IP Internet Protocol

IS Information Service

JVT Jet-Vertex-Tagger

L1A L1 Accept

L1Calo L1 Calorimeter Trigger

L1CT L1 Central Trigger

L1Muon L1 Muon Trigger

L1 First level trigger

L2 Second level trigger

LAr Liquid Argon

LASCAR LASer CAlibration Rod

LBA Long Barrel A-side

LBC Long Barrel C-side

LB Long Barrel

LCG LHC Computing Grid

LEP Large Electron-Positron

LHCb Large Hadron Collider beauty

LHCf Large Hadron Collider forward

LHC Large Hadron Collider

LINAC2 Linear accelerator 2

LO Leading Order

LS1 Long Shutdown 1

LS2 Long Shutdown 2

LS3 Long Shutdown 3

LTPi Local Trigger Processor interface

LTP Local Trigger Processor

LVDS Low Voltage Differential Signal

LVPS Low Voltage Power Supply

LV Low Voltage

MAPP MoEDAL Apparatus for Penetrating Particles

MB Minimum Bias

MC	Monte Carlo
MDT	Monitored Drift Tubes
MD	Mini Drawer
MeV	Mega electron Volt
MF	Matched Filter
MH	Muon Hodoscope
MoEDAL	Monopole and Exotics Detector At the LHC
MPI	Multi-Parton Interactions
MUCTPI	L1_MUon to Central Trigger Processor Interface
NIM	Nuclear Instrumentation Module
NLO	Next-to-Leading Order
NP	Nuisance Parameter
NSW	New Small Wheel
NWA	Narrow Width Approximation
OKS	Object Kernel Support
OPAL	Omni-Purpose Apparatus for LEP
OS	Opposite-Sign
PDF	Parton Distribution Function
PFlow	Particle Flow
PMG	Process ManaGer
PMT	PhotoMultiplier Tube
POI	Parameter Of Interest
PU	Processor Unit

PV	Primary Vertex
QCD	Quantum ChromoDynamics
QED	Quantum ElectroDynamics
QFT	Quantum Field Theory
RCD	ROD Crate DAQ
RC	Run Control
RMS	Root Mean Square
ROB	Read Out Buffer
ROD	Read Out Driver
RoI	Region of Interest
ROL	Read Out Link
ROS	Read Out System
S-LINK	Simple LINK
S-L	Sector-Logic
SBC	Single Board Computer
SCT	SemiConductor Tracker
SD	Super Drawer
SFOS	Same Flavour and Opposite Sign
SFP	Small Form-factor Pluggable
SHAFT	SHared A Few Trigger
SLC	Scientific Linux CERN
SM	Standard Model
SNR	Signal-to-Noise Ratio

SS Same-Sign

SV Secondary Vertex

TBM Trigger and Busy Module

TCP Transmission Communication Protocol

TDAQ Trigger and Data AcQuisition

TDR Technical Design Report

TeV Tera electron Volt

TGC Thin Gap Chamber

Tile/TileCal Tile Calorimeter

TileCal Tile Calorimeter

TilePPr Tile PreProcessor

TMDB Tile Muon Digitizer Board

TM Transition Module

TOTEM TOTal Elastic and diffractive cross section Measurement

TRT Transition Radiation Tracker

TST Track-based Soft Term

TTC Timing, Trigger, and Control

TTCDec TTC Decoder

TTCex Trigger, Timing, and Control laser transmitter

TTCoc Timing, Trigger, and Control optical coupler

TTCpr TTC receiver in PMC Form Factor

TTCRx Trigger, Timing, and Control Receiver ASIC

TTCvi Timing, Trigger, and Control VME interface module

TTL	Transistor-Transistor Logic
TType	Trigger Type
USA15	Underground counting room
VME	Versa Module Eurocard
VP1	Virtual Point 1
WLS	WaveLength Shifting
WP	Working Point
XML	Extensible Markup Language
XOFF	Message or signal indicating that data transmission has to be halted

Symbols

$< \mu >$	Average interactions per bunch spacing
ℓ	Lepton
η	Pseudorapidity
$\mathcal{G}$	Gaussian
$\mathcal{L}$	Lagrangian
μ	Muon
ν	Neutrino
σ	Significance or cross section
$\sqrt{s}$	Centre-of-mass energy
b	Bottom quark
c	Charm quark
d	Down quark
e	Electron

$E_{\mathrm{T}}^{\mathrm{miss}}$	Missing transverse energy
fb^{-1}	Inverse femtobarns
g	Gluon
H	Heavy Scalar particle
h	Standard Model higgs Boson
pp	proton-proton
q	Quark
S	Inert scalar
s	Strange quark
t	Top quark
u	Up quark
$W^{\pm}$	W boson
Z	Z boson

Chapter 1

Introduction and theoretical background

"If you want to find the secrets of the universe, think in terms of energy, frequency, and vibrations." — Nikola Tesla

1.1 Introduction

Particle physics is a fascinating field that seeks to understand the fundamental building blocks of the universe and the interactions between them. At the heart of this field is the quest to uncover the nature of matter and the fundamental forces that govern its behaviour. Over the past century, particle physicists have made remarkable progress in advancing our understanding of the subatomic world, from the discovery of the electron to the recent discovery of the Higgs boson at the Large Hadron Collider (LHC). Technological advancements at CERN,[1] (the European Organization for Nuclear Research) have played a crucial role in enabling groundbreaking discoveries in particle physics. From the development of the LHC itself to advanced particle detectors and distributed computing systems, CERN's technological innovation continues to push the boundaries of particle physics research.

One of the primary focuses of this thesis is the upgrade of the Trigger and

[1] French: "Conseil Européen pour la Recherche Nucléaire" translates to "The European Council for Nuclear Research", later renamed "the European Organization for Nuclear Research".

Data Acquisition (TDAQ) system for the ATLAS Tile Calorimeter (TileCal) subdetector during the Long Shutdown 2 (LS2) period (2019 - 2022) at CERN. The upgrade is motivated by obsolete components of the TTC system and the need for additional functionalities. The thesis details the development and implementation of the DAQ software as well as the integration of the ATLAS Local Trigger Interface (ALTI) modules in the TileCal.

Additionally, the thesis explores a study conducted in the BSM sector. The study is highly motivated by the multi-lepton anomalies observed at the LHC and one possible interpretation being the existence of a new scalar [1, 2]. Extensions of the two Higgs doublet model (2HDM) are explored. The 2HDM+S model incorporates a heavy resonance H and another scalar S. In order to consider a more general case of different missing energy magnitudes, the model is extended by adding a heavy scalar R, resulting in the 2HDM+S+R model, where R decays to H and S. The search uses data collected with the ATLAS detector between year 2015 and 2018.

This thesis is organized as follows: Chapter 1 provides an overview of the SM of particle physics and the Higgs Boson. It briefly discusses the fundamental aspects of the SM, the Higgs Boson and physics BSM. Chapter 2 introduces CERN, the LHC accelerator, and the ATLAS experiment. It shortly discusses the ATLAS subsystems, with focus on the Tile Calorimeter. Chapter 3 introduces the online software necessary for the implementation of the ATLAS Local Trigger Interface (ALTI) software in the Tile Online software. The Tile online software covers the ROD Crate DAQ, Stopless recovery and DCS-to-DAQ connection. The chapter further discusses the TDAQ software release and its versioning. The organisation of the TDAQ software and build systems are also discussed. Lastly the TileCal test bench is discussed. The author has hugely contributed to the software development of the Tile online software and management of the TDAQ infrastructure.

Chapter 4 introduces the ALTI module and discusses the implementation of the DAQ software and the integration of the ALTI module in the TileCal, where the author contributed to its software development and integration. The ALTI is a new module developed for the ATLAS experiment at CERN and it is a part of the Timing, Trigger and Control (TTC) system. The Chapter details the installation of the ALTI modules and tests conducted, to validate the TileCal TTC system. It also describes the upgrade of the TTC system for the TileCal Phase-II test beam campaigns. Calibration systems and the Diagnostics and Verification System, are discussed. The results from Run 3 pilot beam, in preparation for Run 3 data-

taking period and test beams are discussed. The author contributed hugely and continues to contribute in improving the TDAQ system during the data-taking period. Chapter 5 describes the process of identifying events from the proton-proton (pp) collisions and object reconstruction with the ATLAS detector, laying the foundation for Chapter 6. The author contributed to the BSM physics studies discussed in Chapter 6, where the study focuses on the search for the presence of a new heavy resonance produced via gluon-gluon fusion and decaying to the four-lepton (4ℓ) final state, in association with missing transverse energy. Finally, concluding remarks are given in Chapter 7.

1.2 The Standard Model of elementary particles

The SM of elementary particles [3–5] is a Quantum Field Theory (QFT) that describes the basic structure of matter and its interactions through fundamental forces. The theory describes three of the four known fundamental forces (the electromagnetic, weak, and strong interactions, excluding the gravitational force which is described by Einstein's general relativity) in the universe. The electromagnetic interaction governs the interactions among charged particles, whereas the weak interaction plays a key role in the formation of atomic nuclei and radioactive decay processes. The strong interaction binds quarks together, creating protons and neutrons, which in turn form nuclei. In the realm of particle physics, gravity is not a significant factor due to its relatively weak nature, and as a result, it is not included in the SM. The SM has been successful in explaining a wide variety of experimental results and is sometimes regarded as a *theory of almost everything*.

1.2.1 Elementary particles and their interaction

In the SM, there are seventeen identified particles, arranged in the diagram depicted in Figure 1.1. The elementary particles are organized in several classes: *fermions*, *gauge bosons*, and the *Higgs boson*.

Fermions

Fermions are spin-$\frac{1}{2}$ particles that obey Fermi-Dirac statistics. Their interactions are mediated by the exchange of spin-1 particles known as bosons, and they acquire

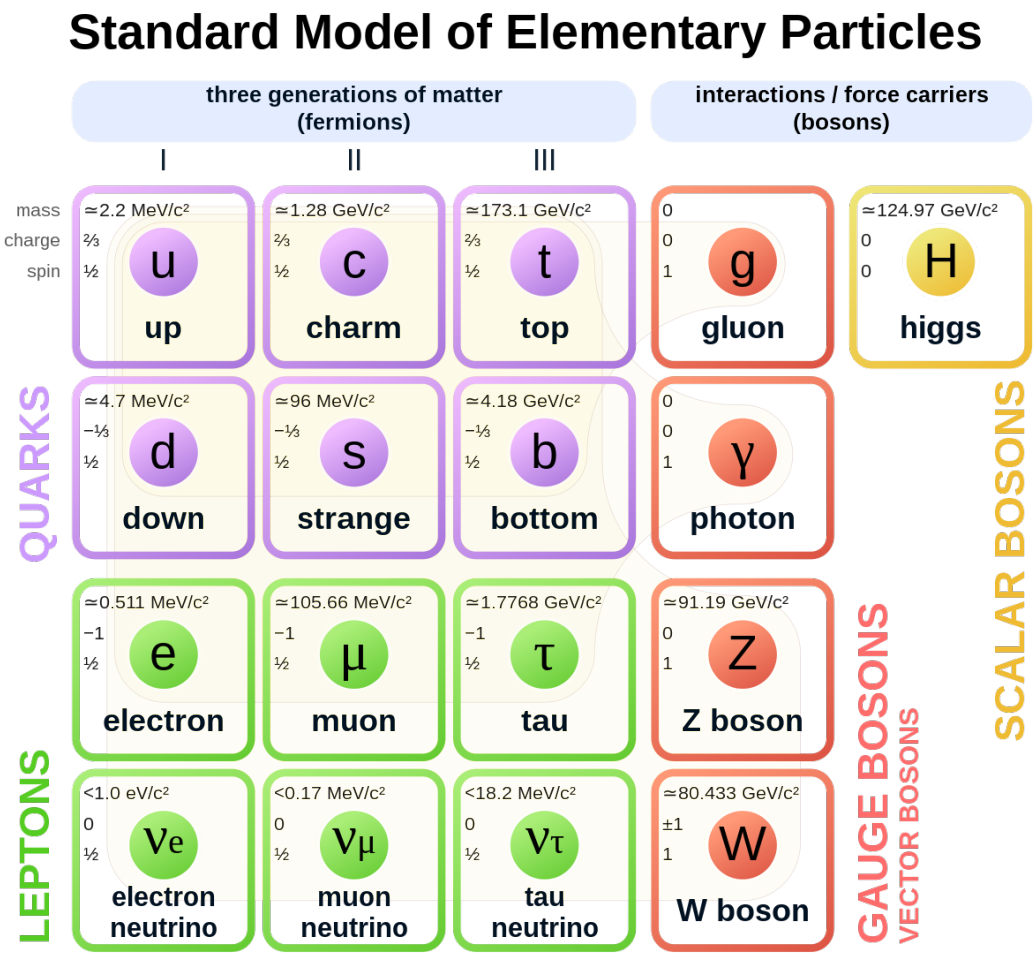


Figure 1.1: A summary of the SM elementary particles (twelve fermions and five fundamental bosons) and their properties.

mass from the Higgs field. Fermions are classified into two groups, *leptons* and *quarks*, based on their interactions. Additionally, fermions are organized into three generations of increasing mass, and each fermion has a corresponding anti-particle.

Leptons are further divided into two groups: charged leptons and neutral leptons (also called neutrinos). Charged leptons (e^-, μ^-, τ^-) interact via weak and electromagnetic forces. Neutrinos (ν_e, ν_μ, ν_τ) only interact through weak forces, as they do not carry an electric charge.

Quarks come in six flavors: up (u), down (d), charm (c), strange (s), top (t), and bottom (b). The up, charm, and top quarks have a fractional charge of $+\frac{2}{3}$, while the down, strange, and bottom quarks have a charge of $-\frac{1}{3}$. Since quarks

possess color charge, electric charge, and weak isospin, they interact with other fermions via strong, electromagnetic, and weak forces, respectively. Color charge exists in three flavors: red (r), green (g), and blue (b). Only colorless particles have been observed in nature, and free quarks have never been detected. The absence of free quarks is explained by *color confinement*, which states that colored particles are always confined to uncolored particles called *hadrons* and cannot propagate as free particles. Hadrons composed of three quarks are classified as spin-$\frac{1}{2}$ *baryons*, while hadrons consisting of a quark-antiquark pair are classified as spin-1 *mesons*. There are also Delta baryons made up of four quarks and classified as spin-$\frac{3}{2}$ *baryons*. They have an electric charge of $+\frac{3}{2}$ or -$\frac{3}{2}$. Delta baryons are unstable and rapidly decay into other particles. The strong interactions between quarks are described by Quantum Chromodynamics (QCD) theory.

Gauge bosons

The gauge bosons are spin-1 particles that follow the Bose-Einstein statistics. The twelve spin-1 bosons, are force carriers that mediate the strong, weak, and electromagnetic interactions. The photon (γ) is massless and mediates the electromagnetic force between electrically charged particles. Its interaction is described by the Quantum Electrodynamics (QED) theory. The gauge bosons W^+, W^-, and Z mediate the weak interactions between particles of various flavours (both quarks and leptons). They are massive, as seen in Figure 1.1. The weak interactions involving the $W^\pm$ only operate on left-handed particles and right-handed antiparticles. Because the $W^\pm$ has an electric charge, it couples to the electromagnetic interaction. The Z boson, on the other hand, is electrically neutral and interacts with both left-handed particles and antiparticles. These three gauge bosons, together with photons, are classified together as mediating the electroweak interaction collectively. The eight gluons are the mediators of the strong interactions between colour charged particles, or quarks. Gluons are massless and their interactions are described by QCD.

Higgs boson

The Higgs boson is an elementary particle produced by the quantum excitation of the Higgs field. It is a massive spin-0 scalar particle that plays a distinct role in the SM, providing an explanation of how elementary particles like fermions and W/Z bosons, acquire mass.

1.2.2 Gauge symmetries

The SM is a renormalizable QFT based on gauge symmetries [6]. The gauge principle summarizes the electroweak sector [3–5], and the strong sector [7,8] with the quark hypothesis. The particles and their interactions are explained in these theories by irreducible representations of particular symmetry groups.The SM is a gauge field theory in which the Lagrangian is invariant under the local gauge symmetry group $SU(3)_C \times SU(2)_L \times U(1)_Y$. The $SU(3)_C$ is a symmetry group for the strong sector, and QCD is based on its gauge symmetry. QCD describes the strong interaction between the coloured quarks with gluons being the generators of the $SU(3)_C$ group. The suffix C denotes the conserved charge of the strong interaction known as colour and 3 being the number of the possible colour states. The $SU(2)_L \times U(1)_Y$ subgroup is a symmetry group of the electroweak sector, describing both QED and weak interactions, as the electroweak interaction. The suffix L indicates that vector bosons only couple to the left-handed component of fermions, while the suffix Y refers to the weak hypercharge. The corresponding gauge bosons are the three W_μ^i bosons of weak isospin from $SU(2)_L$ (W^+, W^0 , and W^-), and the B^0 boson of weak hypercharge from $U(1)_Y$ respectively.

1.2.3 Quantum electrodynamics

Quantum Electrodynamics (QED) is a quantum field theory that describes the interaction between charged particles and photons. It is a relativistic extension of the electromagnetic force and incorporates special relativity and quantum mechanics principles. QED is based on the gauge symmetry group $U(1)$, which ensures local gauge invariance. The QED Lagrangian, representing the electron, photon fields, and their interactions, is given by:

$$\mathcal{L}_{QED} = \bar{\psi}(i\gamma^\mu D_\mu \psi - m)\psi - \frac{1}{4}F^{\mu\nu}F_{\mu\nu}, \tag{1.1}$$

where ψ denotes the fermionic field (electron), m is the electron mass, γ^μ are the Dirac matrices, D_μ is the covariant derivative, and $F^{\mu\nu}$ is the electromagnetic field strength tensor. The covariant derivative is defined as:

$$D_\mu = \partial_\mu - ieA_\mu, \tag{1.2}$$

where e is the electric charge and A_μ is the photon (vector boson) field. The electromagnetic field strength tensor can be expressed as:

$$F^{\mu\nu} = \partial^\mu A^\nu - \partial^\nu A^\mu. \tag{1.3}$$

The interaction between the fermionic field and the photon field is characterized by the electromagnetic current J^μ:

$$J^\mu = e\bar{\psi}\gamma^\mu\psi. \tag{1.4}$$

QED unifies the electromagnetic and weak interactions in the electroweak theory.

1.2.4 Quantum chromodynamics

Quantum Chromodynamics (QCD) is a quantum field theory that describes the strong nuclear force, responsible for the interactions between quarks and gluons. QCD is based on the gauge symmetry group $SU(3)_C$, which ensures local gauge invariance. The QCD Lagrangian, representing quark fields, gluon fields, and their interactions, is given by:

$$\mathcal{L}_{QCD} = \sum_{f=1}^{N_f} \bar{\psi_f}(i\gamma^\mu D_\mu^{(f)} - m_f)\psi_f - \frac{1}{4}G_{\mu\nu}^a G_a^{\mu\nu}, \tag{1.5}$$

where ψ_f denotes the quark fields with N_f flavors, m_f is the quark mass, γ^μ are the Dirac matrices, $D_\mu^{(f)}$ is the covariant derivative, $G_{\mu\nu}^a$ is the gluon field strength tensor, and a is the color index ranging from 1 to 8. The covariant derivative is defined as:

$$D_\mu^{(f)} = \partial_\mu - ig_s T^a A_\mu^a, \tag{1.6}$$

where g_s is the strong coupling constant, T^a are the generators of the $SU(3)_C$ group, and A_μ^a is the gluon (vector boson) field. The gluon field strength tensor can be expressed as:

$$G_{\mu\nu}^a = \partial_\mu A_\nu^a - \partial_\nu A_\mu^a + g_s f^{abc} A_\mu^b A_\nu^c, \tag{1.7}$$

where f^{abc} are the structure constants of the $SU(3)_C$ group.

QCD is a non-Abelian gauge theory, which means that gluons carry color charge and can interact with each other, unlike photons in QED. This property leads to the phenomenon of confinement, which prevents the observation of free

quarks and gluons in isolation, and asymptotic freedom, which implies that the strong interaction becomes weaker at shorter distances or higher energies.

1.2.5 Electroweak Theory

The Electroweak theory is a unified framework that describes the electromagnetic and weak interactions in the context of quantum field theory. It is a key component of the Standard Model of particle physics. The theory is based on the gauge symmetry group $SU(2)_L \times U(1)_Y$, where $SU(2)_L$ is associated with weak isospin and $U(1)_Y$ with weak hypercharge.

The electroweak Lagrangian can be written as:

$$\mathcal{L}_{EW} = \mathcal{L}_{gauge} + \mathcal{L}_{fermion} + \mathcal{L}_{Higgs}, \tag{1.8}$$

where $\mathcal{L}_{gauge}$, $\mathcal{L}_{fermion}$, and $\mathcal{L}_{Higgs}$ represent the gauge, fermion, and Higgs field terms, respectively. The gauge fields include three W^i_μ fields associated with the $SU(2)_L$ group and one $B\mu$ field related to the $U(1)_Y$ group. The gauge field Lagrangian can be expressed as:

$$\mathcal{L}_{gauge} = -\frac{1}{4} W^i \mu\nu W^{\mu\nu i} - \frac{1}{4} B_{\mu\nu} B^{\mu\nu}, \tag{1.9}$$

where $W^i_{\mu\nu}$ and $B_{\mu\nu}$ are the field strength tensors of the W^i_μ and B_μ fields, respectively. Fermions in the electroweak theory are represented by left-handed doublets and right-handed singlets. The covariant derivative for fermions is given by:

$$D_\mu = \partial_\mu - igW^i_\mu \frac{\sigma^i}{2} - ig' B_\mu \frac{Y}{2}, \tag{1.10}$$

where g and g' are the coupling constants for the $SU(2)_L$ and $U(1)_Y$ groups, respectively, σ^i are the Pauli matrices, and Y is the weak hypercharge. The Higgs mechanism, essential for electroweak symmetry breaking and mass generation, is introduced through the Higgs field. The Higgs Lagrangian can be written as:

$$\mathcal{L}_{Higgs} = (D_\mu \Phi)^\dagger (D^\mu \Phi) - V(\Phi), \tag{1.11}$$

where Φ is the Higgs doublet field, D_μ is the covariant derivative, and $V(\Phi)$ is the Higgs potential. The electroweak theory successfully predicts the existence of the weak gauge bosons $W^\pm$ and Z^0, as well as the Higgs boson, which have all

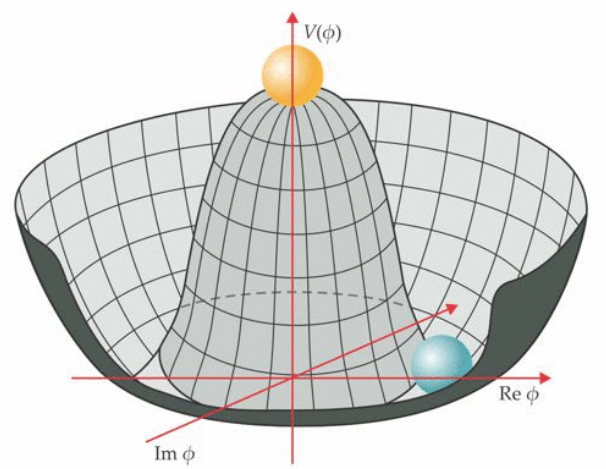


Figure 1.2: The Higgs potential $V(\Phi)$ for $\mu^2 < 0$ and $\lambda > 0$, where the energy density is a function of the $Re(\Phi)$ and $Im(\Phi)$ values.

been experimentally observed [9, 10].

1.2.6 Spontaneous symmetry breaking and the Higgs mechanism

Spontaneous symmetry breaking (SSB) is a process in which a system transitions from a symmetric state to a less symmetric state at a lower energy. The Higgs mechanism is an example of SSB in the context of the electroweak theory, which leads to the generation of masses for gauge bosons and fermions. The Higgs mechanism involves introducing a complex scalar field, the Higgs field Φ, with a self-interaction potential $V(\Phi)$. The Higgs potential is typically chosen to have a *Mexican hat* shape shown in Figure 1.2, which preserves gauge symmetry but breaks it spontaneously:

$$V(\Phi) = \mu^2 \Phi^\dagger \Phi + \lambda (\Phi^\dagger \Phi)^2, \tag{1.12}$$

where $\mu^2 < 0$ and $\lambda > 0$ ensure a non-zero vacuum expectation value (VEV) for the Higgs field. The Higgs field Φ is a doublet, containing two complex scalar fields:

$$\Phi = \begin{pmatrix} \phi^+ \\ \phi^0 \end{pmatrix}. \tag{1.13}$$

The ground state of the Higgs potential is degenerate, and one possible choice

for the vacuum expectation value is:

$$\langle \Phi \rangle = \frac{1}{\sqrt{2}} \begin{pmatrix} 0 \\ v \end{pmatrix}, \tag{1.14}$$

where $v = \sqrt{-\frac{\mu^2}{\lambda}}$.

When the Higgs field acquires a non-zero VEV, electroweak symmetry is spontaneously broken, and the gauge bosons $W^{\pm}$ and Z^0 acquire masses through their interaction with the Higgs field. The Higgs mechanism also leads to the appearance of a physical scalar particle, the Higgs boson. The Higgs mechanism is also responsible for generating fermion masses through Yukawa interactions, which couple fermions to the Higgs field:

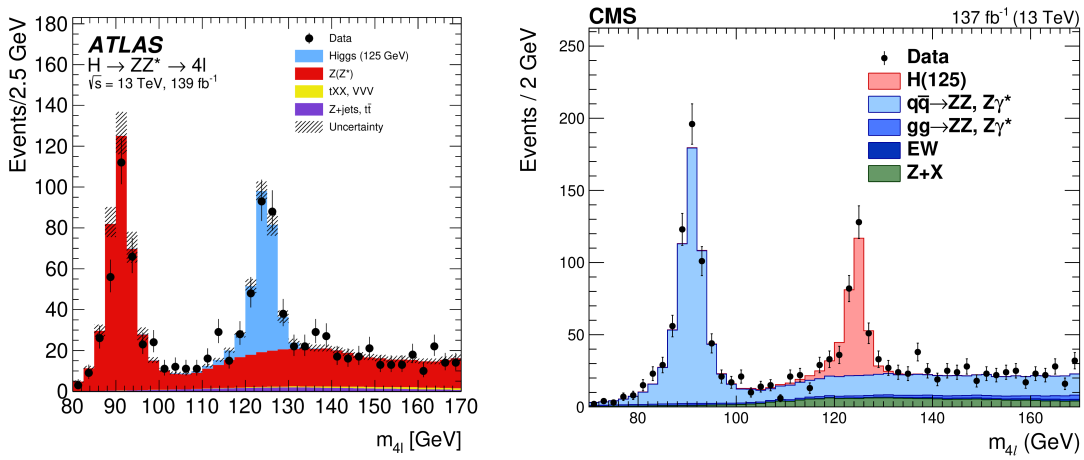
$$\mathcal{L}_{Yukawa} = -y_f \bar{\psi}_L \Phi \psi_R + \text{h.c.}, \tag{1.15}$$

where y_f is the Yukawa coupling constant, ψ_L and ψ_R are the left-handed and right-handed fermion fields, and h.c. denotes the Hermitian conjugate. After electroweak symmetry breaking, fermions acquire masses proportional to their Yukawa couplings and the Higgs VEV:

$$m_f = y_f \frac{v}{\sqrt{2}}. \tag{1.16}$$

1.2.7 The Higgs boson mass measurements

The Higgs boson's mass, a free parameter of the theory, has been extensively investigated. Initial efforts at the LEP set a lower limit of 114.4 GeV at a 95% confidence level [11]. The Tevatron accelerator excluded a mass range of 145-177 GeV at the same confidence level [12]. In 2012, the LHC's ATLAS and CMS Collaborations discovered the Higgs boson. The most recent results produced by the ATLAS and CMS collaborations in 2020 and 2021, respectively, are shown in Figure 1.3 at a center-of-mass energy of $\sqrt{s} = 13$ TeV. The latest results on the combination of Higgs boson mass measurements from the ATLAS and CMS collaborations were released in 2015 for the $H \to \gamma\gamma$ and $H \to ZZ \to 4\ell$ decay channels. The combined measurements from both collaborations determined the Higgs boson mass to be $125.09 \pm 0.21(\text{stat.}) \pm 0.11(\text{syst.})$ GeV and they are summarized in Figure 1.4.



(a) (b)

Figure 1.3: The figure shows the $m_{4\ell}$ distribution for the selected Higgs boson candidates at $\sqrt{s} = 13\,\text{TeV}$ by the ATLAS and CMS collaborations. For the ATLAS collaboration, the observed and expected $m_{4\ell}$ distributions for an integrated luminosity of $139\,\text{fb}^{-1}$ are presented in (a), where the data points with error bars are compared to background processes in red, yellow, and violet. The signal expectation for a Standard Model (SM) Higgs boson with a mass of $m_H = 125\,\text{GeV}$ is also shown in blue [13]. The CMS collaboration presents its results for the $m_{4\ell}$ distribution in the low-mass region for an integrated luminosity of $137\,\text{fb}^{-1}$ at $\sqrt{s}$ =13 TeV in (b), where the data points with error bars are compared to background processes in blue and green. The anticipated signal for a SM Higgs boson with a mass of $m_H = 125\,\text{GeV}$ is depicted in magenta [14].

1.3 The SM Higgs boson at the LHC

The Large Hadron Collider, which is discussed further in Chapter 2, provides pp collisions at very high energies. One of the primary objectives of the LHC is to explore the existence of the SM Higgs boson. To achieve this goal, comprehending the Higgs boson's production mechanisms and decay channels is crucial.

1.3.1 Proton-proton collisions

Protons are made up of three valence quarks (two up-quarks and one down-quark), sea quarks, and gluons. During pp collisions, the constituent quarks and gluons interact, leading to scattering. Scattering processes in hadron colliders can be classified as *hard* or *soft* based on the momentum transfer between the interacting partons.

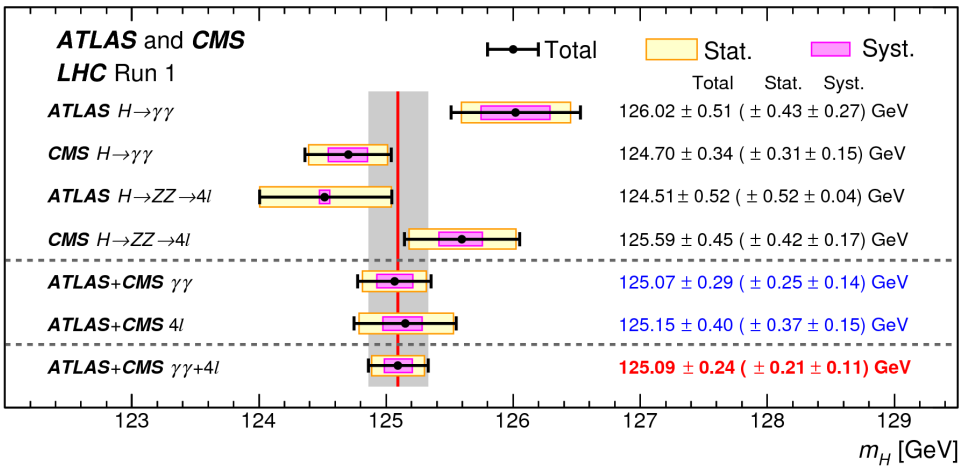


Figure 1.4: Summary of Higgs boson mass measurements from ATLAS and CMS independent analyses, as well as the combined analysis shown here. The uncertainties are given as systematic (magenta bands), statistical (yellow bands), and the total (black error bars). The (red) vertical line and corresponding (gray) band represent the combined measurement's central value and total uncertainty, respectively [15].

The momentum of each proton can be defined as p. Each component of the proton carries a portion of this momentum, denoted as x_i. The scattering interactions between hadrons can be factorized based on the factorization scale, μ^2, into hard scattering processes with a high momentum transfer Q^2, explained by perturbative QCD, and soft interactions, which are accounted for by non-perturbative QCD. When two partons, a and b, from two protons collide, the cross section, σ, for the process $pp \rightarrow c + X$, where c is a massive particle, is dependent on the scattering cross section of the two partons, $\sigma_{a+b\rightarrow c}$, and their Parton Density Functions[2] (PDFs), $f_{a/A}(x_a, \mu^2)$ and $f_{b/B}(x_b, \mu^2)$:

$$\sigma_{pp\rightarrow c+X} = \sum_{a,b} \int dx_a dx_b f_{a/A}(x_a, \mu^2) f_{b/B}(x_b, \mu^2) \sigma_{a+b\rightarrow c}(x_a x_b, mu^2), \qquad (1.17)$$

where the summation encompasses all partonic processes that result in the generation of particle c. Figure 1.5 illustrates the collision of two hadrons. A summary of the features of the hadronic collisions is given below:

[2]functions that represent the probability of finding a parton with a fraction x of the initial proton's momentum at a specific factorization scale μ^2.

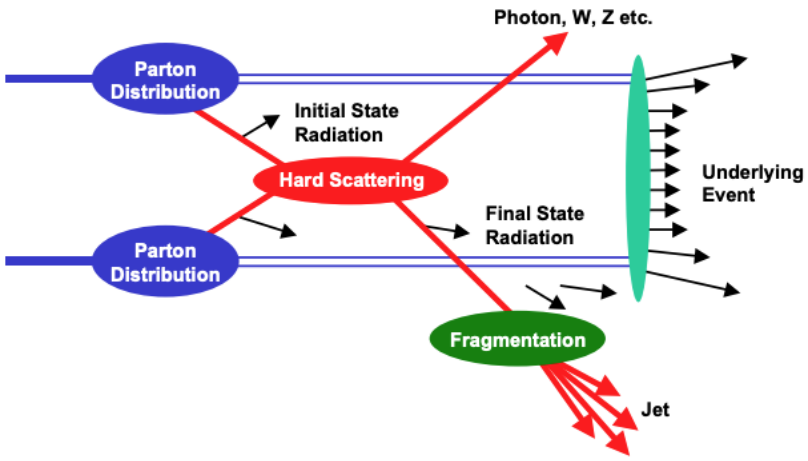


Figure 1.5: An illustration of a hadron-hadron collision [16].

- **Parton distributions**: protons are not point-like particles, but rather are made up of broad-band quarks and gluons
- **Fragmentation or hadronization**: a process of generating final state particles (jets) from a parton produced in hard scattering
- **Initial/Final state radiation**: incoming or leaving colour-charged partons can emit more QCD radiation, known as initial state radiation (ISR) or final state radiation (FSR), in the form of gluons, which can lead to additional jets
- **Underlying event**: particles produced from proton remnants

1.3.2 Production modes

The SM Higgs boson predominantly couples to heavy particles, such as top and bottom quarks, or to the Z and W bosons. At the LHC, there are four primary SM Higgs boson production modes:

i) **gluon-gluon Fusion** (ggF): This is the most prevalent production mode (the $pp \to gg \to H$ process accounts for nearly 90% of the total Higgs cross-section) in which the Higgs boson indirectly couples to gluons through a triangular loop of quarks, primarily top or bottom quarks. The cross section of this process is mainly governed by strong interactions, with leading order (LO) contributions [17], next-to-leading order (NLO) QCD radiative

corrections [18], and NLO electroweak (EW) radiative corrections [19] being applied.

ii) **Vector Boson Fusion** (VBF)[3]: This production mode ($q\bar{q} \to q\bar{q}H$ process) has the second largest cross-section and involves the Higgs boson being produced by the fusion of two weak vector bosons (W or Z) emitted from quarks in the initial state. The scattered quarks result in two hard jets in the forward and backward regions of the detector, with the Higgs boson decaying in the central region. No additional hadron activity is expected between the two jets, creating a distinct detector signature that helps suppress background from jets. The cross section of this process is calculated with full NLO QCD and EW corrections [20].

iii) **associated production with a Vector Boson** (VH): Also referred to as *Higgs-strahlung*, this production mode ($q\bar{q} \to W/ZH$ process) features the Higgs boson being produced alongside a W or a Z boson. The vector boson in the final state is experimentally utilized to better identify events and reduce background event contributions. The cross sections of this process are accurately calculated at NLO and next-to-next-to-leading order (NNLO) [21] in QCD, with NLO EW radiative corrections applied.

iv) **associated production with a pair of heavy quarks** ($t\bar{t}H$, $b\bar{b}H$): Also known as *Higgs bremsstrahlung of heavy quarks*, this production mode ($q\bar{q} \to q\bar{q}H$ and $gg \to q\bar{q}H$ processes) involves the Higgs boson being produced in association with top quark pairs. Although these production modes contribute the least to Higgs production due to their low cross-section, they provide an opportunity to study the direct coupling of the Higgs boson to fermions. The cross sections are calculated at NLO QCD [22].

In pp collisions, the four primary Higgs boson production modes are illustrated by the Feynman diagrams in Figure 1.6. Additionally, Figure 1.7 displays the cross-sections of the Higgs boson for $m_H = 125\,\text{GeV}$ as a function of the center-of-mass energy $\sqrt{s}$, as well as a function of the Higgs mass at $\sqrt{s} = 14\,\text{TeV}$. Table 1.1 summarizes the Higgs boson production cross-sections for $m_H = 125\,\text{GeV}$, for different production modes in pp collisions at a center-of-mass energy $\sqrt{s} = 13\,\text{TeV}$.

[3]Here, V can be either a W or a Z boson.

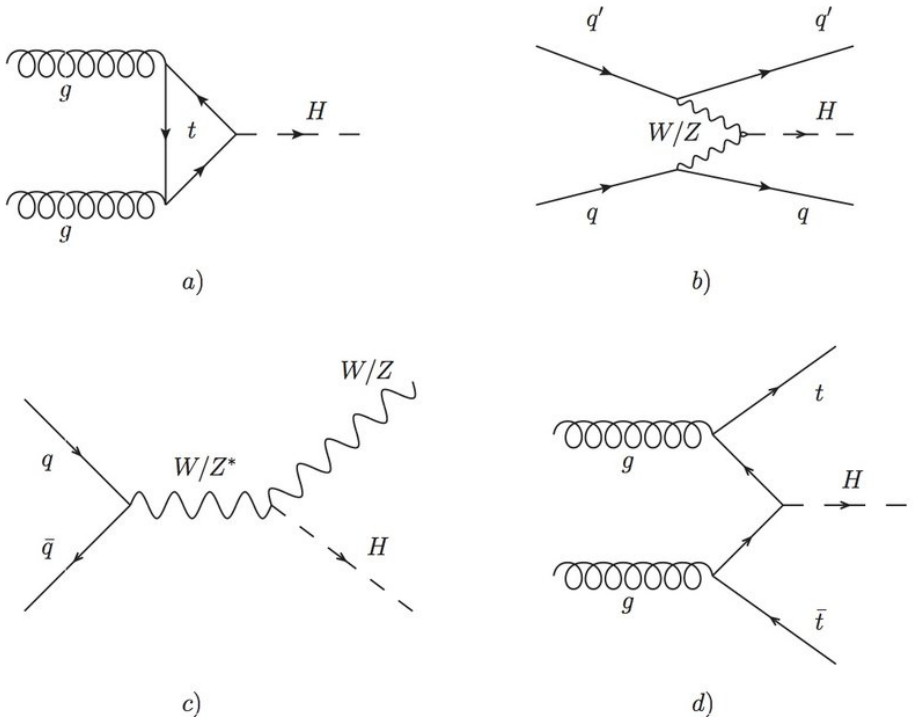
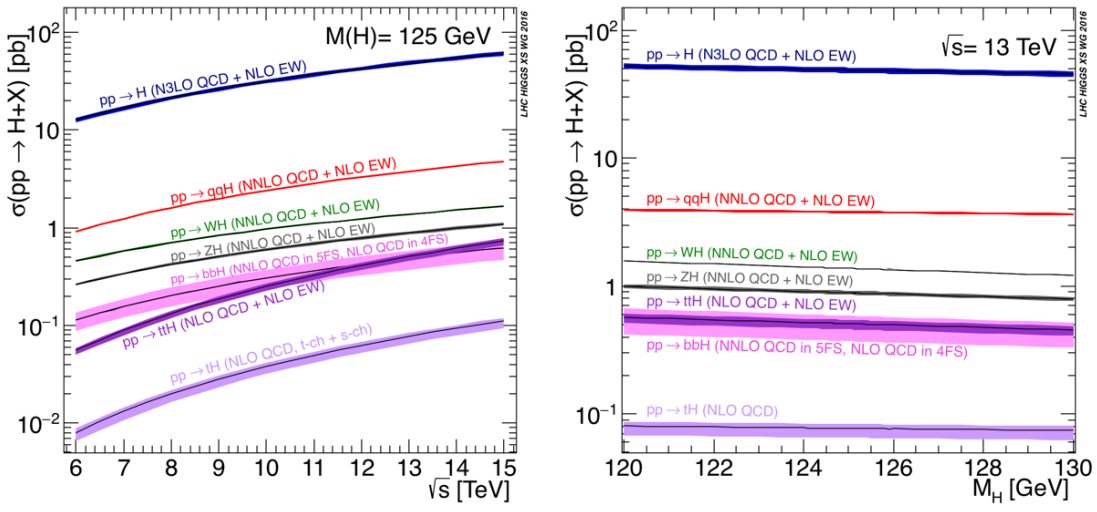


Figure 1.6: Feynman diagrams for the Higgs boson production modes at the LHC: (a) gluon-gluon fusion, (b) vector boson fusion, (c) associated production with a vector boson and (d) associated production with a pair of heavy quarks.



(a) (b)

Figure 1.7: Cross-sections of the SM Higgs boson with $m_H = 125\,\text{GeV}$ as a function of the center-of-mass energy $\sqrt{s}$ in (a) and in (b) the cross sections as a function of the Higgs mass at $\sqrt{s} = 13\,\text{TeV}$ [24].

Table 1.1: The Higgs boson production cross-sections for $m_H = 125\,\text{GeV}$ in pp collisions at a center-of-mass energy $\sqrt{s} = 13\,\text{TeV}$ [23].

Production Mode	σ **[pb]**
$ggF(pp \to H)$	48.6
$VBF(pp \to qqH)$	3.78
$WH(pp \to WH)$	1.37
$ZH(pp \to ZH)$	0.88
$t\bar{t}H(pp \to t\bar{t}H)$	0.50
$b\bar{b}H(pp \to b\bar{b}H)$	0.48
Total	55.61

1.3.3 Decay channels

The Higgs boson has an extremely short lifetime, decaying into either fermions or bosons. Its presence in the detector can only be determined by measuring its decay products. The decay probability is proportional to the mass of the products, indicating that heavier particles decay more rapidly. Figure 1.8 presents the Feynman diagrams for the Higgs boson decay channels. The branching ratio (BR) for any specific channel is expressed as the ratio of the partial width to the total width, where the total width is the sum of all possible partial widths:

$$BR(H \to XX) = \frac{\Gamma(H \to XX)}{\sum_i \Gamma(H \to X_i X_i)} \tag{1.18}$$

Figure 1.9 displays the predicted BRs for the various decay channels of the Higgs boson as a function of its mass [23]. Table 1.2 summarizes the BRs for the Higgs boson mass $m_H = 125\,\text{GeV}$. The bottom pairs have the dominant BR (approximately 58%) mainly due to the kinematic constraint that prevents decay into a pair of top quarks (as the top quark mass is higher than the Higgs boson mass). The second largest BR is for the W boson pair (approximately 22%) with one of the bosons off-shell. The W boson can then decay into either quarks or a charged lepton and a ν. The $H \to gg$ pair has the third largest BR (approximately 8%) and is indistinguishable from the SM background, so it is not studied at the LHC. Next is the τ lepton pairs (approximately 6%), which have a high background due to the $Z \to \tau^+\tau^-$ decay process but allow for testing the coupling with leptons. The charm pair decay has a low BR (approximately 3%) and is heavily contaminated by the QCD process. The $H \to ZZ$ decay (approximately 2.6%) offers a cleaner experimental signature due to the lepton decay of the Z

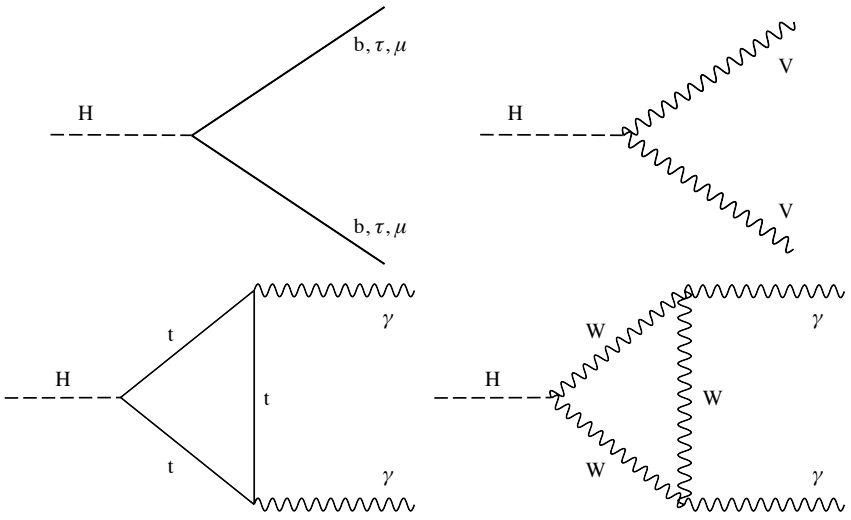


Figure 1.8: LO Feynman diagrams of the Higgs boson decay channels for the $H \to b\bar{b}$, $H \to \tau\tau$, and $H \to \mu\mu$ (upper left); $H \to ZZ$ and $H \to WW$ (upper right); and $H \to \gamma\gamma$ (lower) channels.

boson. Despite the extremely low production rate of the $H \to ZZ^* \to 4\ell$ decay, this channel has minimal background contributions. The $H \to \gamma\gamma$ decay is a loop-induced decay channel with a very low decay rate (approximately 0.2%) and is another clean process. The $H \to Z\gamma$ decay is another rare loop-induced decay mode with a BR of approximately 0.15%. The μ lepton pair has a very low BR (approximately 0.03%), but this decay channel allows for the measurement of the Higgs couplings to the second generation of fermions at the LHC.

Table 1.2: Branching ratios of the Higgs decay for a Higgs boson mass $m_H = 125\,\text{GeV}$ [23].

Decay Channel	**Branching Ratio**
$H \to b\bar{b}$	58.2 %
$H \to WW^*$	21.4 %
$H \to gg$	8.19 %
$H \to \tau^+\tau^-$	6.27 %
$H \to c\bar{c}$	2.89 %
$H \to ZZ^*$	2.62 %
$H \to \gamma\gamma$	0.23 %
$H \to Z\gamma$	0.15 %
$H \to \mu^+\mu^-$	0.03 %

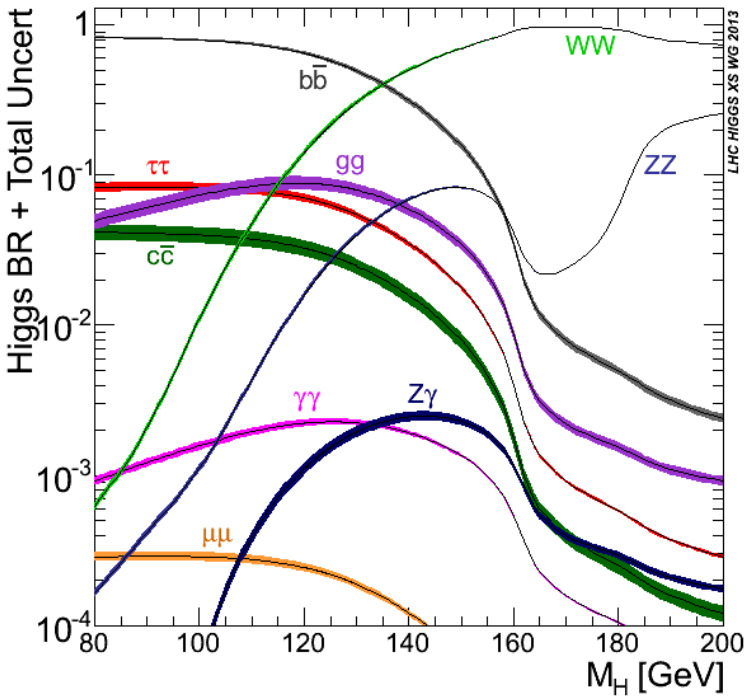


Figure 1.9: The Higgs boson decay branching ratios and their theoretical uncertainties (bands) as a function of the Higgs boson mass [24].

1.4 Physics beyond the Standard Model

The SM is presently a well-established theory that effectively explains phenomena at the electroweak scale. It provides a comprehensive interpretation of the experimental results. However it has some shortcomings and does not answer certain questions. Some of the unexplained phenomena and theoretical problems are:

- **Gravity**: it is not fundamentally unified with other interactions in the SM. Einstein's theory of General Relativity is the most successful theory of gravity to date. General relativity is not a quantum theory and this presents challenges in incorporating it in the SM. Possible solutions include BSM theories, Kaluza-Klein [25] and supergravity [26].

- **Dark matter and dark energy**: based on cosmological observations by the Planck collaboration [27] and the SM of cosmology, the SM accounts for the 4.9% of the mass-energy present in the universe, 26.8% is dark matter (DM) and 68.3% is dark energy. The SM does not offer explanation of any fundamental particles that are good dark matter candidates.

- **Neutrino masses**: The SM predicts that neutrinos have no mass, but observations from various experiments, have confirmed neutrino oscillations, which indicate that neutrinos do possess mass [28, 29].

- **CP violation**: The observed matter-antimatter asymmetry in the universe, which is attributed to CP violation, is not adequately explained [30]. Theoretically it can be argued that the SM should contain a term that breaks CP symmetry in the strong interaction sector (QCD), however there is no experimentally known violation of the CP symmetry in strong interactions.

There are several experimental results that deviate from the SM-based predictions and these could be a statistical fluke or experimental error, or a sign of new physics. The unexplained phenomena suggest that the SM is a low-energy approximation of a more fundamental theory that may unify all four interactions. To this end, several beyond-the-standard-model (BSM) theories aim to extend the SM. The LHC program includes a search for new physics predicted by these BSM theories. One of the models that seeks to describe physics BSM is the "*2HDM+S*" developed by the Wits Institute for Collider Particle Physics (ICPP) and collaborators. The 2HDM+S model and its recommended inputs have been informally dubbed the *Madala hypothesis*.

1.4.1 Multilepton anomalies and the 2HDM+S model

The 2HDM+S model [1, 31, 32] was formulated on the basis of several anomalies observed by ATLAS and CMS experiments in Run 1 data. It was formulated as a simplified scalar extension to the SM. The model proposes the existence of a heavy scalar boson and an intermediate scalar that can decay into both SM particles and dark matter. In the previous sections, the SM Higgs boson has been denoted by H and will now be denoted by h in the 2HDM+S model context. The new heavy scalar boson will be denoted by H. This new notation will be used for the remainder of the manuscript. The Run I data indicated an excess in the Higgs boson $p_{\mathrm{T},h}$ spectrum, which contradicted the SM prediction, leading to speculation about BSM physics. Table 1.3 shows a list of the experimental results made by ATLAS and CMS, which were considered in the construction of the 2HDM+S model. The distortion of the Higgs boson $\mathrm{p}_{\mathrm{T},h}$ spectrum might be interpreted as a hint of Higgs production in association with missing energy, implying new physics. In order to describe the Higgs p_{T} spectrum, a heavy scalar

Table 1.3: A list of experimental results utilized in constraining the relevant parameters of the 2HDM+S model [31].

Result		**Publication**
Differential Higgs boson p_{T} spectra	ATLAS	Fiducial cross section measurements on $h \to \gamma\gamma$ [33] and $h \to ZZ^* \to 4\ell$ [34]
	CMS	Fiducial cross section measurements on $h \to \gamma\gamma$ [35] and $h \to ZZ^* \to 4\ell$ [36]
Di-Higgs boson resonance searches	ATLAS	Limits on $H \to hh \to bb\tau\tau, \gamma\gamma WW^*$, $\gamma\gamma b\bar{b}$ and $b\bar{b}b\bar{b}$ [37]
	CMS	Limits on $H \to hh \to \gamma\gamma b\bar{b}$ [38], $b\bar{b}\tau\tau$ [39] and multi-lepton [40]
Top associated Higgs boson production	ATLAS	Limits on $h \to \gamma\gamma$ [41] Measurements on multi-lepton decay channels [42] and $h \to b\bar{b}$ [43]
	CMS	Measurements on $h \to \gamma\gamma$, $h \to b\bar{b}$ and multi-lepton decay channels [44]
$H \to VV$ decays	ATLAS	Limits on $H \to WW$ [45] and ZZ [46]
	CMS	Limits on $H \to WW$ and ZZ [47]

H decaying to at least one h is introduced, $H \to hh$ and $h\chi\chi$, where χ is a DM candidate. Figure 1.10 shows Feynman diagrams of the production and decay modes of H.

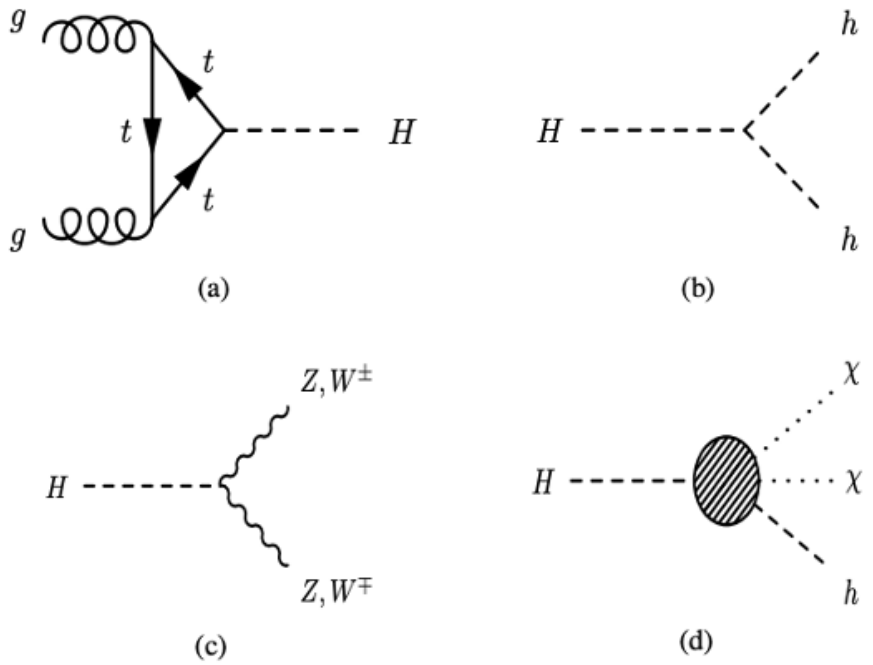


Figure 1.10: The Feynman diagrams depicting the production (a) and decay (b,c,d) of the heavy scalar boson H.

In order to explain the excesses in data, the interactions of the 2HDM+S model are described by the Lagrangian:

$$\mathcal{L} = \mathcal{L}_{\mathrm{SM}} + \mathcal{L}_{\mathrm{BSM}}, \tag{1.19}$$

where the SM interactions are described by $\mathcal{L}_{\mathrm{SM}}$. The new interactions are treated as arising from effective couplings and are described by $\mathcal{L}_{\mathrm{BSM}}$:

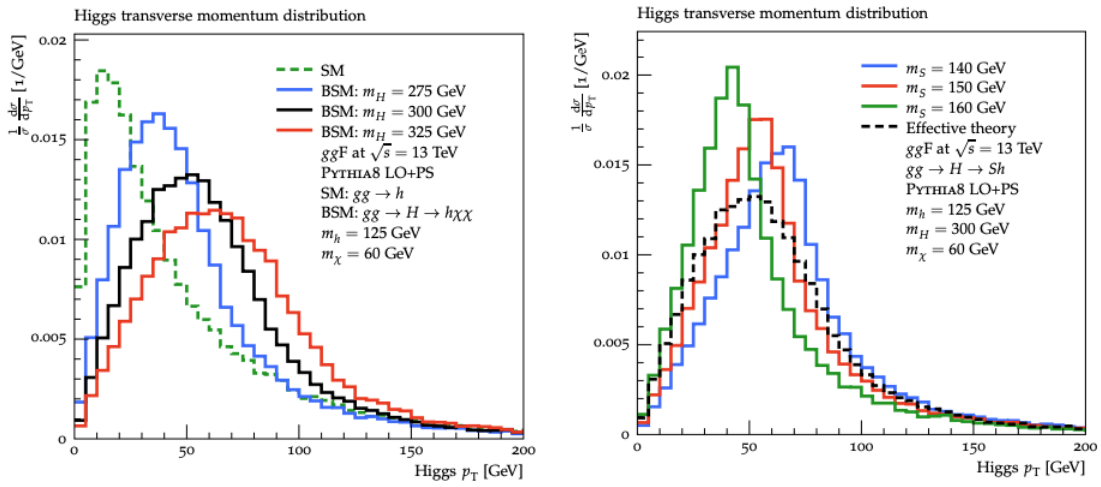
$$\mathcal{L}_{\mathrm{BSM}} = \mathcal{L}_{\mathrm{H}} + \mathcal{L}_{\mathrm{Y}} + \mathcal{L}_{\mathrm{T}} + \mathcal{L}_{\mathrm{Q}}, \tag{1.20}$$

where the terms $\mathcal{L}_{\mathrm{H}}$, $\mathcal{L}_{\mathrm{Y}}$, $\mathcal{L}_{\mathrm{T}}$ and $\mathcal{L}_{\mathrm{Q}}$ are the production of H, Yukawa, tri-linear and quartic interactions, respectively. These terms are defined as:

$$\mathcal{L}_H = -\frac{1}{4}\beta_g \kappa^{\mathrm{SM}}_{h_{gg}} G_{\mu v} G^{\mu v} H + \beta_V \kappa^{\mathrm{SM}}_{hVV} V_\mu V^\mu H, \tag{1.21}$$

$$\mathcal{L}_{\mathrm{Y}} = -\frac{1}{\sqrt{2}}\left[y_{ttH}\bar{t}tH + y_{bbH}\bar{b}bH\right], \tag{1.22}$$

$$\mathcal{L}_{\mathrm{T}} = -\frac{1}{2}v[\lambda_{Hhh}Hhh + \lambda_{h\chi\chi}h\chi\chi + \lambda_{H\chi\chi}H\chi\chi], \tag{1.23}$$



(a) (b)

Figure 1.11: The impact of the effective decay process $H \to h\chi\chi$ on the Higgs p_T spectrum. Under the BSM hypothesis of $gg \to H \to h\chi\chi$ (solid lines), the spectrum is distorted with respect to the SM prediction (dashed line) (a). A comparative view of the Higgs p_T spectrum as described by the S-mediated interaction (solid lines) and the effective $H \to h\chi\chi$ interaction (dashed line) (b) [1].

$$\mathcal{L}_Q = -\frac{1}{2}\lambda_{Hh\chi\chi} Hh\chi\chi - \frac{1}{4}\lambda_{HHhh} HHhh - \frac{1}{4}\lambda_{hh\chi\chi} hh\chi\chi - \frac{1}{4}\lambda_{HH\chi\chi} HH\chi\chi, \quad (1.24)$$

where H and χ are the heavy scalar and the DM candidate, respectively, and $v = 246\,\text{GeV}$ is the vacuum expectation value responsible for the $W^\pm$ and Z boson masses. The first term in Equation 1.21 represents the effective coupling of gluons to H, where the SM-like coupling $\kappa_{hgg}^{SM} = \frac{\alpha_s}{3\pi v}$. A variable dimensionless parameter β_g[4] controls the rate at which H is produced via ggF. The product $\beta_g \kappa_{h_{gg}}^{SM}$ is considered as the effective coupling strength of gluons to H. The second term in Equation 1.21 represents the coupling of H to the weak vector bosons $W^\pm$ and Z, with the SM-like coupling $\kappa_{hVV}^{SM} = \frac{m_V^2}{v}$. β_v controls the BR of $H \to VV$. Equation 1.22 describes the Yukawa couplings between H and the heaviest quarks, which are SM-like Yukawa couplings multiplied by the factor β_g. This term allows for $H \to bb$ decay but is regarded as insignificant owing to its low BR. Equations 1.23 and 1.24 encompass the possible trilinear and quartic couplings

[4] $\beta_g = y_{ttH}/y_{tth}$, where y_{tth} is the SM top Yukawa coupling. The bottom Yukawa coupling y_{bbH} is neglected since the effect of bottom quarks in ggF loops is insignificant.

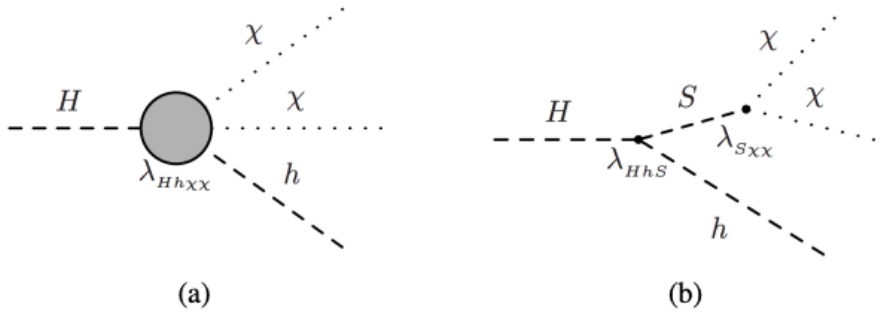


Figure 1.12: Feynman diagrams of the production of the Higgs boson in association with DM: (a) the decay of a heavy scalar H through the effective quartic $\lambda_{Hh\chi\chi}$ vertex and (b) due to the additional scalar S under a replacement of $\lambda_{Hh\chi\chi}$ with λ_{HhS} and $\lambda_{S\chi\chi}$ [1].

between h, H and the DM candidate, considered to be scalar for simplicity. The trilinear coupling in Equation 1.23 allows for $H \to hh$ decays because of the excesses reported in the resonant di-Higgs production results. In Equation 1.24 the quartic couplings ($\lambda_{Hh\chi\chi}$) allow for Higgs boson decays in association with the missing transverse energy ($E_{\mathrm{T}}^{\mathrm{miss}}$).

The decay $H \to h\chi\chi$ is addressed in Equation 1.24 by an effective quartic interaction. A distortion in the intermediate range of the Higgs p_{T} spectrum is anticipated due to h recoiling against a pair of invisible χ particles. The effect on the Higgs p_{T} spectrum can be seen in Figure 1.11 (a). When the scalar S [1, 48] is introduced to mediate the effective interaction, the kinematics of the effective theory become similar to the full theory. S is assumed to have a mass $m_h \leq m_S \leq m_H - m_h$, allowing for new processes associated to the H decays. The Higgs p_{T} spectrum arising from the S-mediated interaction is shown in Figure 1.11(b), where three mass points have been chosen to demonstrate the effect of m_S on the spectrum. In Figure 1.12, S is assumed to mediate the $H \to h\chi\chi$ interaction by decaying into a pair of DM particles. The $S \to \chi\chi$ process allows for new prospective searches such as $H \to SS$ and $H \to Sh$ which produce events that include photons, jets, leptons and $E_{\mathrm{T}}^{\mathrm{miss}}$. The introduction of the two scalars S and χ to the 2HDM model results in generation of five additional scalars and several new decay possibilities, which are summarized in Table 1.4. In this table, A is a CP-odd scalar and contributes to the decay mode of $A \to ZH$, where $H \to Sh$, requires $m_A > m_Z + m_H$. This decay mode also implies processes with multi-lepton final states, which are produced in both same-sign (SS) and opposite-sign

Table 1.4: A list of possible decay modes of the 2HDM scalars and S based on the explicit mass selections provided in the text of Reference [1].

S. No.	Scalar	Decay Modes
D.1	h	$b\bar{b}, \tau^+\tau^-, \mu^+\mu^-, s\bar{s}, c\bar{c}, gg, \gamma\gamma, Z\gamma, W^+W^-, ZZ$
D.2	H	D.1, hh, SS, Sh
D.3	A	D.1, $t\bar{t}, Zh, ZH, ZS, W^\pm H^\mp$
D.4	$H^\pm$	$W^\pm h, W^\pm H, W^\pm S$
D.5	S	D.1, $\chi\chi$

Table 1.5: A list of potential search channels arising from the addition of the new scalars. The list is incomplete, but contains clean search channels which could make for striking signatures at the LHC [1]

Scalar	Production Mode	Search Channels
H	$gg \to H, Hjj$ (ggF and VBF)	Direct SM decays as in Table 1.4
		$\to SS/Sh \to 4W \to 4\ell + E_{\mathrm{T}}^{\mathrm{miss}}$
		$\to hh \to \gamma\gamma b\bar{b}, b\bar{b}\tau\tau, 4b, \gamma\gamma$ etc.
		$\to Sh$ where $S \to \chi\chi \Longrightarrow \gamma\gamma$,$b\bar{b}, 4\ell + E_{\mathrm{T}}^{\mathrm{miss}}$
	$pp \to Z(W^\pm)H(H \to SS/Sh)$	$\to 6(5)\ell + E_{\mathrm{T}}^{\mathrm{miss}}$
		$\to 4(3)\ell + 2j + E_{\mathrm{T}}^{\mathrm{miss}}$
		$\to 2(1)\ell + 4j + E_{\mathrm{T}}^{\mathrm{miss}}$
	$pp \to t\bar{t}H, (t+\bar{t})H(H \to SS/Sh)$	$\to 2W + 2Z + E_{\mathrm{T}}^{\mathrm{miss}}$ and b-jets
		$\to 6W \to 3$ SS leptons + jets + $E_{\mathrm{T}}^{\mathrm{miss}}$
$H^\pm$	$pp \to tH^\pm(H^\pm \to W^\pm H)$	$\to 6W \to 3$ SS leptons + jets + $E_{\mathrm{T}}^{\mathrm{miss}}$
	$pp \to tbH^\pm(H^\pm \to W^\pm H)$	Same as above with extra b-jet
	$pp \to H^\pm H^\mp(H^\pm \to HW^\pm)$	$\to 6W \to 3$ SS leptons + jets + $E_{\mathrm{T}}^{\mathrm{miss}}$
	$pp \to H^\pm H^\pm(H^\pm \to HW^\pm)$	$\to 6W \to 3$ SS leptons + jets + $E_{\mathrm{T}}^{\mathrm{miss}}$
A	$gg \to (ggF)$	$t\bar{t}$
		$\gamma\gamma$
	$gg \to A \to ZH(H \to SS/Sh)$	Same as $pp \to ZH$ above, but with resonance structure over final state objects
	$gg \to A \to W^\pm H^\mp(H^\mp \to W^\mp H)$	$6W$ signature with resonance structure over final state objects
S	$gg \to S(ggF)$	Resonantly through decays as in Table 1.4 ($\gamma\gamma, b\bar{b}, \tau\tau, ZZ \to 4\ell$)
	or $H \to SS/Sh$ (associated production)	Non-resonantly through multilepton + $E_{\mathrm{T}}^{\mathrm{miss}}$ decays

(OS) configurations, in association with jets. Table 1.5 shows a list of potential search channels arising from the addition of the new scalars.

A study conducted in Reference [49] showed that a simplified model predicting H with a mass of 270 GeV that decays to h in association with a scalar singlet S of $m_S = 150$ GeV can accommodate several anomalous multi-lepton results in pp collisions at the LHC. Thereafter, a wider set of LHC results pertaining to the

production of multiple leptons was studied in an attempt to find how compatible these discrepancies in data are [2]. The results use a profile likelihood ratio to constrain the single fit parameter β_g^2 under the SM+BSM hypothesis. A simultaneous fit is performed and a combination of the independent data sets is constructed under the SM+BSM hypothesis. The combined profile likelihood is constructed by multiplying the profile likelihood ratios for each individual measurement. Then, the best-fit value of β_g^2 and significance (Z) are calculated similarly to the individual results. This constrains the parameter β_g^2 to the value 2.92 ± 0.35 which corresponds to a significance of $Z = 8.04\,\sigma$ in favour of the SM+BSM hypothesis over the SM-only hypothesis. This significance is the result of the combination of ATLAS and CMS data. The significance of each fit is calculated as,

$$Z = \sqrt{-2 \log \lambda(\beta_g^2)}. \tag{1.25}$$

Table 1.6 shows a summary of all the individual fit results as well as the combination. Figure 1.13 also shows each of the individual profile likelihood ratios and the combination. The combination of the observed results show strong anomalies between the data and SM Monte Carlo (MC) predictions. Systematic uncertainties from the prediction of SM processes evaluated with currently available tools seem unable to describe the multi-lepton anomalies.

In this thesis, the search for heavy resonances in the four lepton final state in association with $E_{\mathrm{T}}^{\mathrm{miss}}$ exploits two models. The first model is an extension of the 2HDM+S model to 2HDM+S+R, where R is an additional scalar boson. The model can be written as $R \to SH \to 4\ell + E_{\mathrm{T}}^{\mathrm{miss}}$, where R decays to two lighter scalar bosons (S and H). The S decays to a pair of DM particles, neutrinos ($E_{\mathrm{T}}^{\mathrm{miss}}$) and H decays to 4ℓ, through ZZ bosons. The S mass is fixed to 160 GeV and the scan is performed through R and H masses to control the $E_{\mathrm{T}}^{\mathrm{miss}}$. The S mass is suggested to have the best fit value around 150 GeV, as shown in Reference [49]. When the S mass is below 200 GeV, the missing energy is less sensitive to m_S. The second model is $A \to Z(\nu\nu)H(ZZ) \to 4\ell + X$, a traditional 2HDM model, where $m_A > m_H$. A is considered to be a CP-odd scalar which decays to a CP-even scalar H and the Z boson. The Z boson decays inclusively to X, which includes neutrinos, jets and leptons. H decays to the 4ℓ final state. A detailed study is documented in Chapter 6.

Table 1.6: Summary of SM+BSM fit results for the measurements considered in Reference [2].

Selection	**Best-fit β_g^2**	**Significance (σ)**
ATLAS Run 1 SS leptons + b-jets	6.51 ± 2.99	2.37
ATLAS Run 1 DFOS di-lepton + b-jets	4.09 ± 1.37	2.99
ATLAS Run 2 SS leptons + b-jets	2.22 ± 1.19	2.01
CMS Run 2 SS leptons + b-jets	1.41 ± 0.80	1.75
CMS Run 2 DFOS di-lepton	2.79 ± 0.52	5.45
ATLAS Run 2 DFOS di-lepton + b-jets	5.42 ± 1.28	4.06
CMS Run 2 tri-lepton + $E_{\mathrm{T}}^{\mathrm{miss}}$	9.70 ± 3.88	2.36
ATLAS Run 2 tri-lepton + $E_{\mathrm{T}}^{\mathrm{miss}}$	9.05 ± 3.35	2.52
Combination	2.92 ± 0.35	8.04

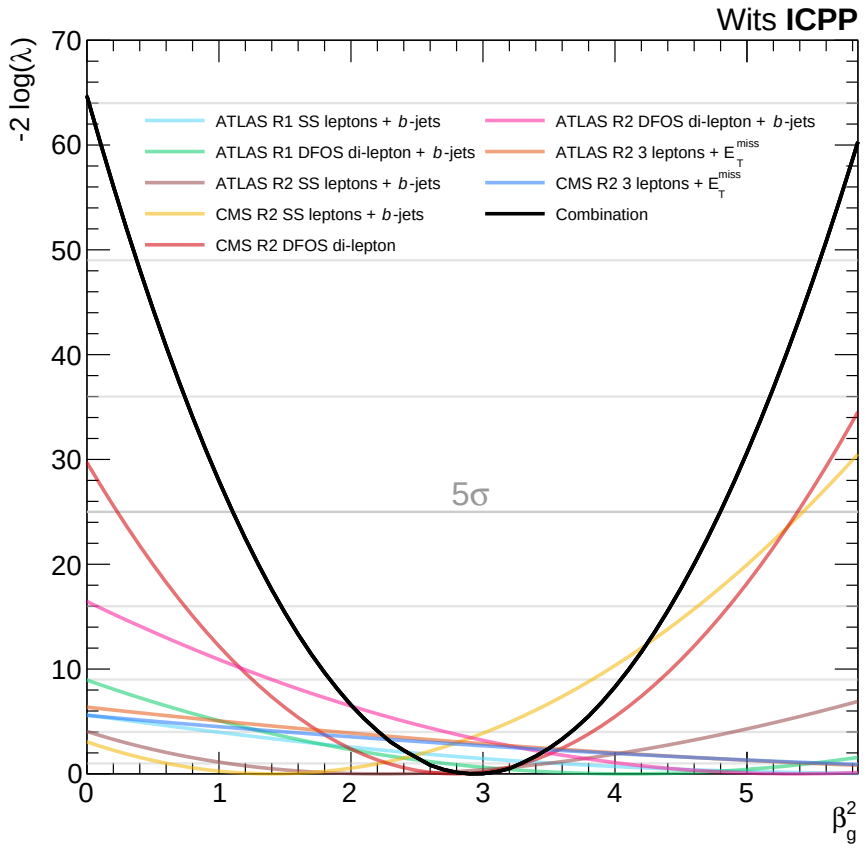


Figure 1.13: The negative 2 times the logarithm of the profile likelihood ratios for each of the individual fit results considered in this article, overlaid with that of their combination. The significance of a result is calculated as the square root of the point which intersects the y-axis (that is, the SM-only hypothesis where ($\beta_g = 0$)) [50].

Chapter 2

CERN, LHC and the ATLAS experiment

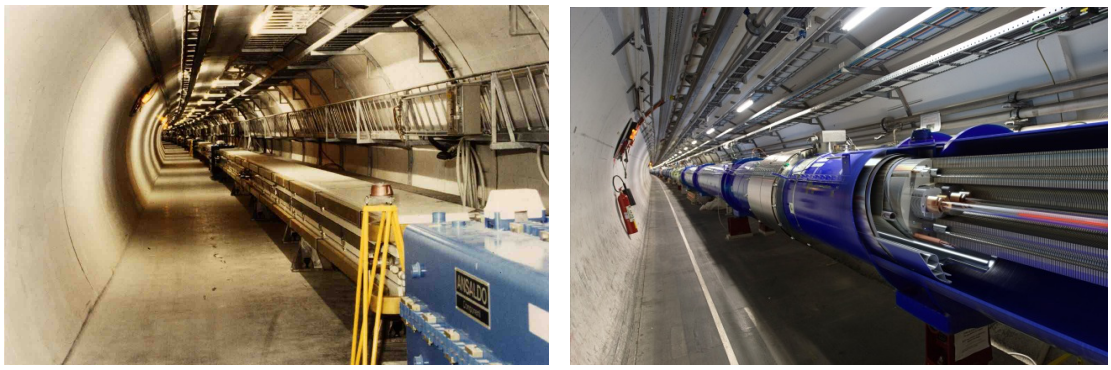
Chapter 2 introduces CERN, the LHC and the ATLAS experiment. It briefly describes the ATLAS subsystems and focuses more on the TileCal, laying the foundation for the Phase-I upgrades discussed in Chapter 4.

2.1 CERN

CERN operates the world's largest particle physics laboratory. It was founded in 1954 with a mandate to establish a fundamental physics research organisation in Europe. CERN is administered by 23 member states and many non-European states. CERN employs over 2500 personnel. Its facilities are used by over 600 institutes and universities worldwide, with over 12 000 visiting research scientists. The member and non-member states are responsible for the finance, construction, and operation of the experiments. CERN played a crucial role in the formulation of the SM of particle physics. The organization continues to be a hub for groundbreaking research in particle physics.

2.2 The Large Hadron Collider

The Large Hadron Collider (LHC) is the world's most powerful and biggest particle collider. CERN constructed the complex experimental facility between 1998 and 2008. The LHC is located in a 27 km long circular tunnel that runs 100 meters deep under the France-Switzerland border near Geneva. The 27 km tunnel



(a) LEP (b) LHC

Figure 2.1: The LEP [51] was situated in a tunnel underground between year 1989 and 2000, and the tunnel now houses the LHC [52].

was originally used by the Large Electron-Positron (LEP) collider shown in Figure 2.1(a). In 2000, the LEP was decommissioned to make way for the construction of the LHC, which began operation in 2008. One of LEP's most significant achievements was the precise measurement of the Z and the W bosons. These measurements helped confirm the electroweak theory, which describes the unification of the electromagnetic and weak nuclear forces. The LHC was constructed with the goal of investigating and possibly answering some of physics' most fundamental questions, focusing on elementary particles physics. The LHC ring is designed to accelerate and collide two beams of protons or heavy ions traveling in opposite directions. The particles are guided by powerful superconducting magnets, which are cooled to a temperature colder than outer space (-271.3 degrees Celsius) using liquid helium. These magnets help maintain the particles' trajectories around the ring, as well as focus the particle beams to increase the probability of collisions. Several acceleration systems are employed to increase the energy of particles as they travel around the accelerator. They are arranged in series as illustrated in Figure 2.2. The linear particle accelerator LINAC 4 accelerates negative hydrogen ions to an energy of 160 MeV, which are then stripped of their electrons to form protons. These protons are further accelerated by the Proton Synchrotron Booster and the Proton Synchrotron, before being injected into the LHC. Protons are injected into the LHC ring in bunches and accelerated to their peak energy, which is currently 6.8 TeV per beam ($\sqrt{s} = 13.6$ TeV) for the Run 3 data-taking period.

The LHC ring contains four main experimental stations where the particle

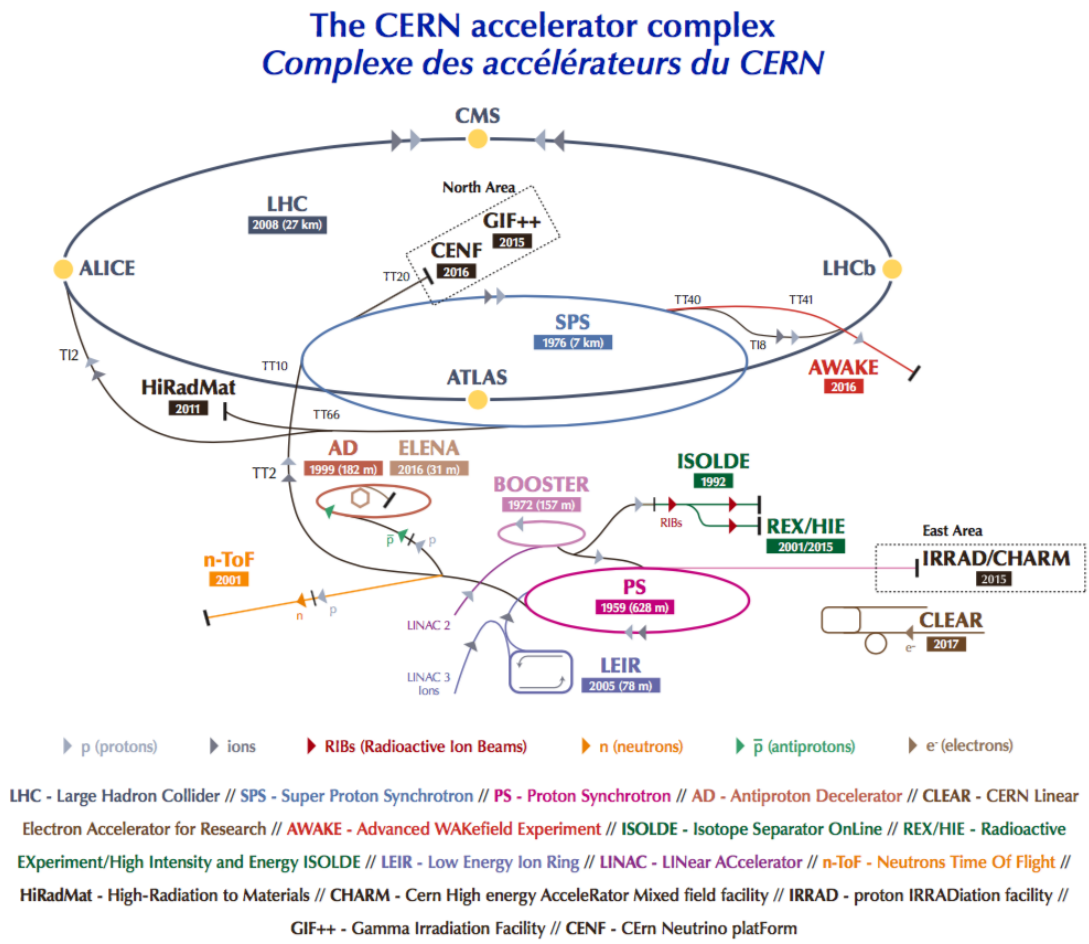


Figure 2.2: An illustration of the CERN's accelerator complex [53].

beams collide: The four main stations (shown in Figure 2.2) represent the four particle detectors: ATLAS, CMS, ALICE, and LHCb. After a successful commissioning of the LHC in 2010, the LHC delivered a $\sqrt{s} = 8$ TeV pp collisions with 50 ns between bunch crossings during Run 1 at a peak luminosity of 8×10^{33} cm^{-2}s^{-1}, ending in 2013. After the LS1 period, Run 2 commenced in 2015 to 2018, with the LHC delivering $\sqrt{s} = 13$ TeV pp collisions at 25 ns bunch crossings at a peak luminosity of 1.7×10^{34} cm^{-2}s^{-1}. After the LS2 period (2019-2021), Run 3 commenced in 2022 and the LHC is currently delivering $\sqrt{s} = 13.6$ TeV pp collisions. The LHC also rarely collides beams of lead nuclei (Pb) and Xenon (Xe) nuclei. The LHC will undergo a series of upgrades during the Long Shutdown 3 (2026–2028) leading to the High-Luminosity LHC (HL-LHC). The HL-LHC will have the capability to deliver an instantaneous peak luminosity of up to 7×10^{34}

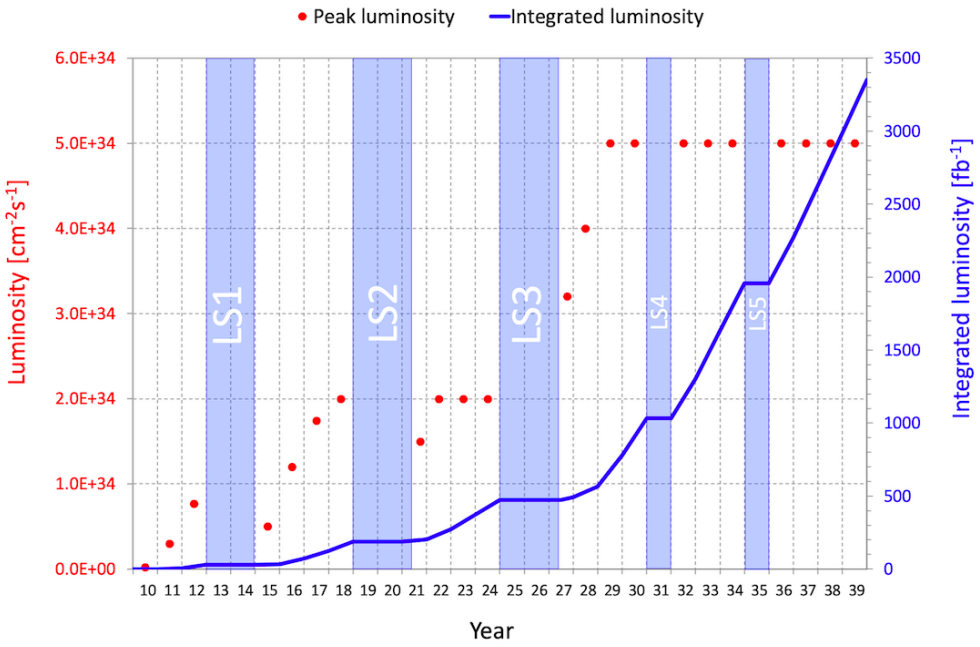


Figure 2.3: The LHC will go through several long shutdown periods before constant nominal luminosity [54].

$cm^{-2}s^{-1}$, corresponding to an average of 200 simultaneous pp interactions per bunch crossing. The goal of the HL-HLC is to achieve an integrated luminosity of 3000 fb^{-1} after year 2028. The upgrades will boost the accelerator's potential for new particle physics discoveries and improve the marginal measurements statistically. Figure 2.3 summarizes the peak luminosity and the integrated luminosity over the years (2010-2039).

2.2.1 Particle production rate

The LHC particle production rate (R) is calculated using several factors, including the centre of mass energy ($\sqrt{s}$), which determines the cross-section,[1] (σ) and the instantaneous luminosity (L_{inst}). The production rate is given by:

$$R = \sigma(\sqrt{s})L_{inst}, \tag{2.1}$$

where L_{inst}, is determined from equation 2.2 by assessing beam parameters while performing van der Meer (vdM) scans.

[1] Cross-section is the probability of interaction

$$L_{inst} = \frac{1}{4\pi} \frac{N^2 f}{\sigma_x \sigma_y t}, \tag{2.2}$$

where the number of protons per bunch is represented by N, while f denotes the proportion of bunch positions containing protons. The Gaussian beam profiles' transverse dimensions are given by σ_x and σ_y, and the time interval between bunches is represented by t. During the LHC's Run 2, data production increased fivefold compared to Run 1. By 2018, the target of $150\,\mathrm{fb}^{-1}$ was achieved, with both ATLAS and CMS receiving this data.

2.2.2 LHC experiments

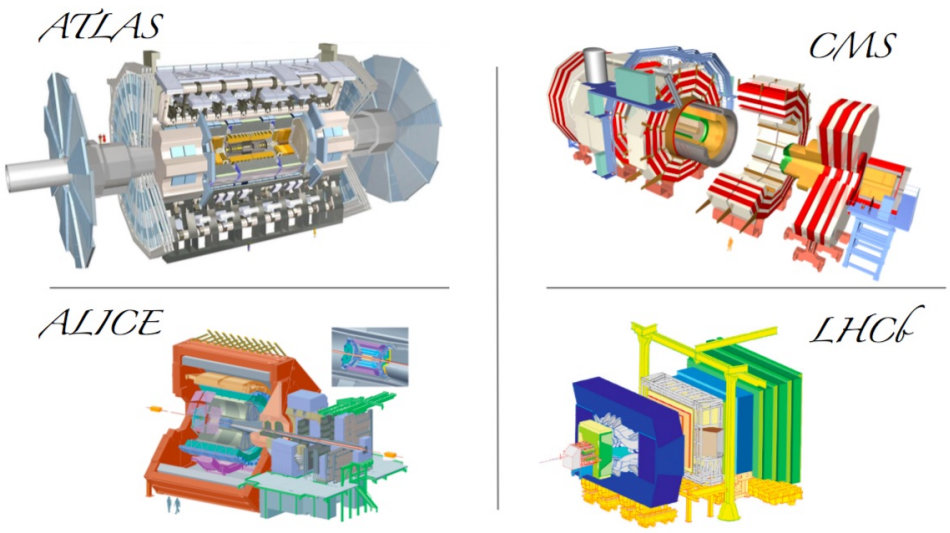


Figure 2.4: The four main experiments at the LHC.

At the LHC, nine experiments use detectors to analyse numerous particles produced by collisions in the accelerator. The LHC has four main experiments (depicted in Figure 2.4), all designed for specific purposes. These four main detectors are:

ATLAS (*A Toroidal LHC ApparatuS*)
ATLAS [55] is a general-purpose detector designed to investigate a wide range of physics phenomena, such as the Higgs boson, dark matter, and supersymmetry.

CMS (*Compact Muon Solenoid*)

CMS [56] is another general-purpose detector, with similar goals as ATLAS but using a different magnet design and detector technology.

ALICE (*A Large Ion Collider Experiment*)
The ALICE [57] detector is designed to study the properties of quark-gluon plasma, a state of matter that is believed to have existed a few microseconds after the Big Bang.

LHCb (*Large Hadron Collider beauty*)
The LHCb [58] is an experiment focused on understanding the differences between matter and antimatter by studying particles containing bottom (or beauty) quarks.

The LHC has five other small scale experiments. The TOTEM (Total Elastic and Diffractive Cross Section Measurement) located near CMS is one of the smaller experiments designed to precisely measure the size of protons, as well as study the elastic and diffractive scattering processes in pp collisions. The LHCf (LHC forward) is dedicated to studying the forward production of particles in high-energy pp and heavy-ion collisions. It measures the energy and quantity of neutral pions created in collisions. The experiment has two detectors which sit along the LHC beamline, at 140 m either side of the ATLAS collision point. MoEDAL-MAPP,[2] [59] uses detectors deployed near LHCb to search for a hypothetical particle called the magnetic monopole. FASER (Forward Search Experiment) [60] and SND@LHC (Scattering and Neutrino Detector at the LHC) [61], the two newest LHC experiments, are situated close to the ATLAS collision point in order to search for light new particles and to study neutrinos.

2.3 The ATLAS experiment

The ATLAS [55,62] collaboration comprises roughly 3000 physicists from over 181 institutions. As a general-purpose detector with a specific design for precision SM

[2]In preparation for data taking during Run 3 of the LHC, the MoEDAL (Monopole and Exotics Detector at the LHC) detector has been upgraded to MoEDAL-MAPP. The additional detector, MAPP (MoEDAL Apparatus for Penetrating Particles), was approved in 2021 to extend MoEDAL's physics reach by providing sensitivity to milli-charged particles and long-lived exotic particles.

measurements and beyond-SM studies, the ATLAS detector, shown in Figure 2.5, is the largest among the four primary experiments at the LHC.

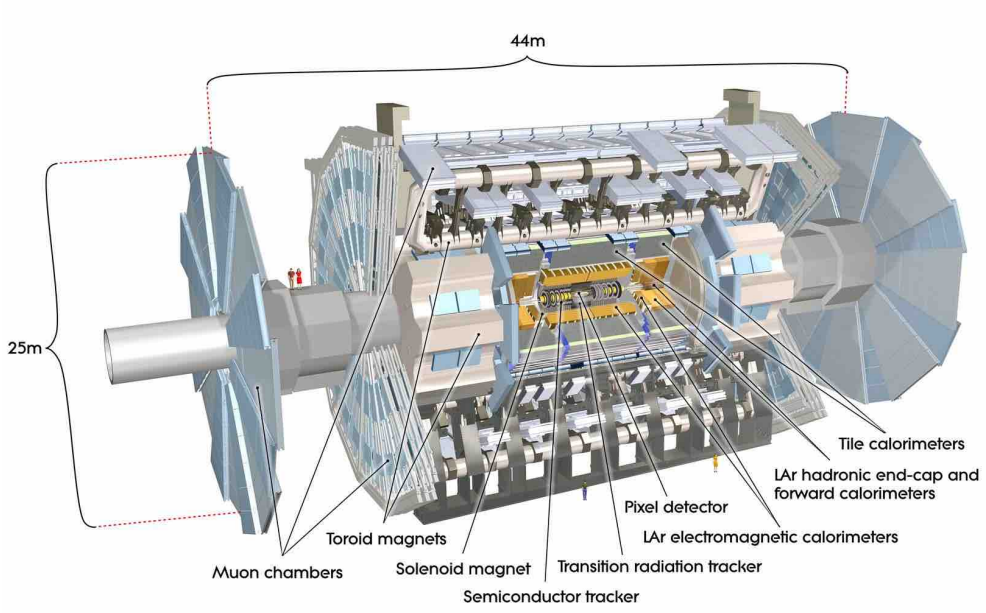


Figure 2.5: Overview of the ATLAS experiment. Energetic particles collide at the experiment's center. Tracking detectors (dark grey), calorimeters (grey and orange), and the muon system (blue) record the resulting particles. The magnets generate magnetic fields essential for measuring charged particle momenta. Image sourced from [63].

As depicted in Figure 2.6, particles produced from collisions radiate from the detector's center in all directions. The detector's multi-layered design is crucial for identifying all particles generated during collisions. The ATLAS detector is composed of four primary components: the Inner Detector, Calorimeters, Magnet System, and Muon Spectrometers. Various subdetectors make up the main components, each designed to detect different particles. The diverse tracks left by particles in each subdetector enable particle identification and measurements of energy and momentum. The subsequent subsections provide a brief overview of these subdetectors. The ATLAS detector features a symmetric forward-backward and cylindrical geometry. Measuring approximately 45 m long and 25 m in diameter, it weighs around 7000 tons. The ATLAS detector is described using a right-handed Cartesian coordinate system. The interaction point is at the detector's center, with the x-axis pointing toward the LHC ring's center, the y-axis pointing upward, and the z-axis, also known as the beam axis. The polar angle

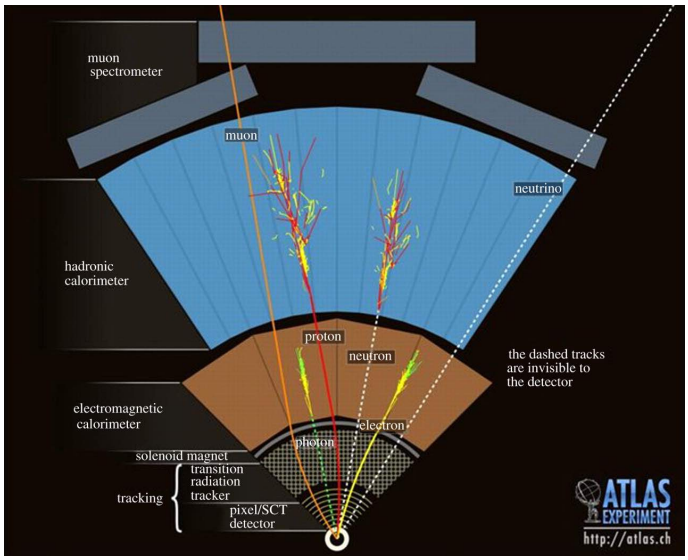


Figure 2.6: A cross-sectional representation of the ATLAS detector, illustrating how each subdetector contributes to particle identification and tracking.

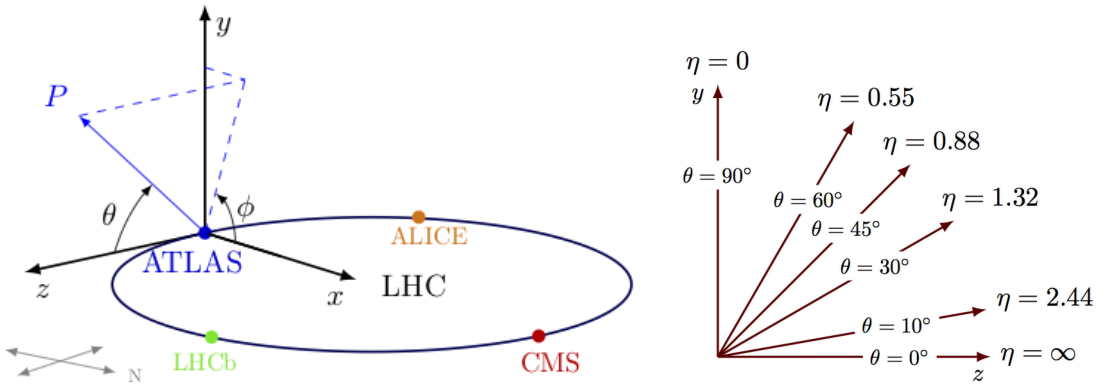
(θ) is the positive angle of elevation from the beam's axis. The xy-plane, or transverse plane, employs cylindrical coordinates with radial distance r and azimuthal angle ($\phi \in [-\pi, \pi]$) around the beam axis. Figure 2.7(a) illustrates the detector's orientation relative to these coordinates. Particle physics defines a particle's rapidity as:

$$y = \frac{1}{2} \ln \left(\frac{E + p_z}{E - p_z} \right), \tag{2.3}$$

where p_z represents the momentum component along the beam axis's magnitude. Conversely, the magnitude of the momentum projected onto the xy-plane, which is perpendicular to the beam axis, is known as the transverse momentum (p_{T}) of a particle. In the relativistic limit, the rapidity approaches a spatial coordinate that measures the angle of the particle with respect to the beam axis, which is called pseudorapidity (η), as shown in Equation 2.4.

$$\eta = -\ln \tan \left(\frac{\theta}{2} \right). \tag{2.4}$$

The detector used in the experiment covers an angle of 2.5 for the trackers and 4.9 for calorimeters measured in terms of η. For massless particles, η remains unchanged under boosts along the z-axis. In the case of relatively light, high-energy particles, pseudorapidity is a good approximation of true rapidity. The detector



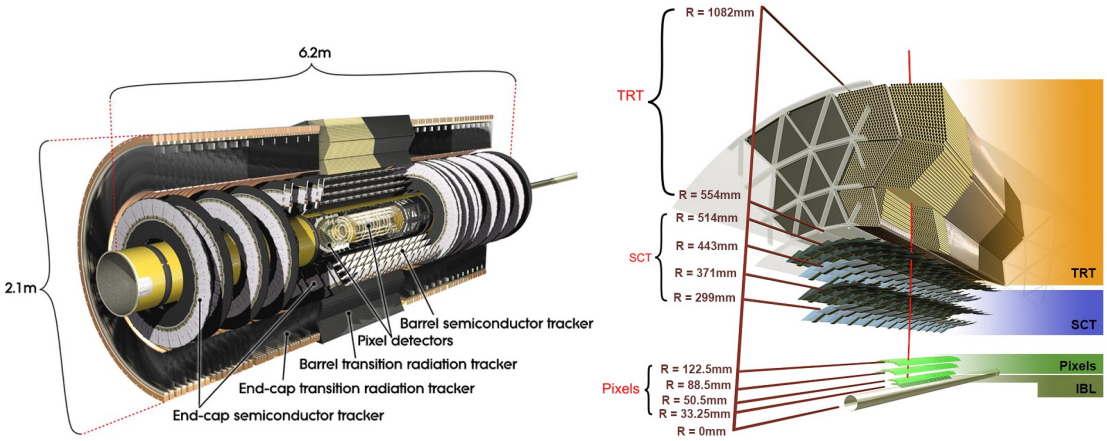
(a) (b)

Figure 2.7: The ATLAS uses a right handed coordinate system (a). Central regions approach $\eta_{det} = 0$, while $|\eta_{det}| \gg 0$ for forward regions (b).

η_{det} indicates the angular position of several detector regions, as illustrated in Figure 2.7(b). The central regions correspond to η_{det} values close to zero, while the forward regions correspond to high $|\eta_{det}|$ values. The right-handed ATLAS coordinate system is shown in Figure 2.7(a).

2.3.1 Inner Detector

The ATLAS Inner Detector (ID) is a sub-detector system located closest to the beam pipe in the ATLAS experiment at CERN's Large Hadron Collider (LHC). It is responsible for tracking the path of charged particles produced in proton-proton collisions. The ID is composed of three sub-detectors: the pixel detector, the semiconductor tracker (SCT), and the transition radiation tracker (TRT). The ID's layout is shown in Figures 2.8(a) and 2.8(b). The pixel detector is the innermost sub-detector and consists of approximately 80 million pixels, each measuring 50 μm$\times$ 400 μm in size. It provides the highest resolution and precision tracking in the ATLAS detector, allowing for the detection of particles that are produced close to the beam pipe. Figure 2.8(b) shows the pixel layers (green) and a fourth layer, the Insertable B-Layer (IBL). The SCT is the next layer of the inner detector and consists of approximately 6.3 million silicon strips, each measuring 6.4 mm $\times$ 80 μm in size. The SCT is responsible for measuring the trajectory of charged particles as they move outward from the beam pipe. The TRT is the outermost sub-detector of the inner detector and consists of approximately 351 000 straw tubes filled with a mixture of gases. The TRT is designed to detect the



(a) (b)

Figure 2.8: The ATLAS ID is depicted in (a). A blow-up diagram of the ID sub-detectors is illustrated in (b) with layers of the IBL, pixels, SCT, and TRT. A charged particle track is indicated by the red line.

transition radiation emitted when charged particles pass through the boundary between two materials with different dielectric constants. The TRT provides particle tracking information at intermediate radii between the pixel and SCT detectors. The combined information from the three sub-detectors allows for the measurement of charged particle tracks with high accuracy and precision, enabling the reconstruction of the decay products of short-lived particles such as the Higgs boson. The inner detector is also used to identify particles by their energy loss, ionization and the patterns of their tracks. Chapter 5 discusses event identification from pp collisions and object reconstruction using the ATLAS detector.

2.3.2 Calorimeters

The Calorimeter is responsible for measuring the energy of particles and jets. It plays a crucial role in detecting neutral particles that traverse undetected by the ID. Figure 2.9 illustrates the ATLAS ID surrounded by the calorimeters.

Liquid Argon EM Calorimeter

Liquid Argon EM Calorimeter (LAr ECal) surrounds the ID. It is an electromagnetic (EM) calorimeter that only measures the energy of electromagnetically

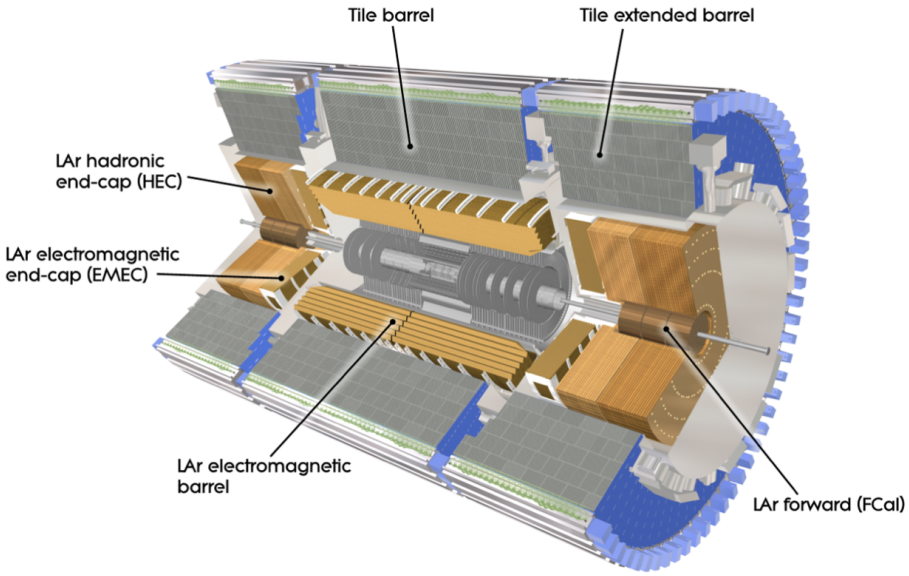


Figure 2.9: The calorimeters of the ATLAS detector [64] consist of an inner liquid argon EM calorimeter (depicted in orange), which is surrounded by the TileCal. Several forward calorimeters surround the beam pipe, covering an angular range of -5 $< \eta <$ 5.

interacting particles like photons, electrons, and positrons.[3] Photons are converted to electron/positron pairs during their interaction with the material in the EM calorimeter, and they emit photons as they traverse the LAr ECal. Photons produce the e^+e^- pairs, which in turn produce particle showers in the LAr ECal [65]. The LAr ECal can be divided into three segments, namely, a barrel segment with an η range of -1.475 to 1.475, and two endcap segments covering the range of $1.375 < |\eta| < 2.5$ and $2.5 < |\eta| < 3.2$. A module, as depicted in Figure 2.10, is composed of three layers or layers in depth (front, middle and back as viewed from the interaction point).

Tile Calorimeter

The TileCal is the central hadronic calorimeter ($|\eta| < 1.7$) of the ATLAS experiment and surrounds the LAr ECal. It contributes to the measurement of hadrons, jets, taus, and the missing transverse energy [55]. TileCal comprises alternating layers of steel plates and plastic scintillating tiles designed for detecting hadronic showers. Excited by charged shower particles, the plastic scintillating tiles emit

[3]Other electromagnetically interacting particles exist yet not detected by the EM calorimeter.

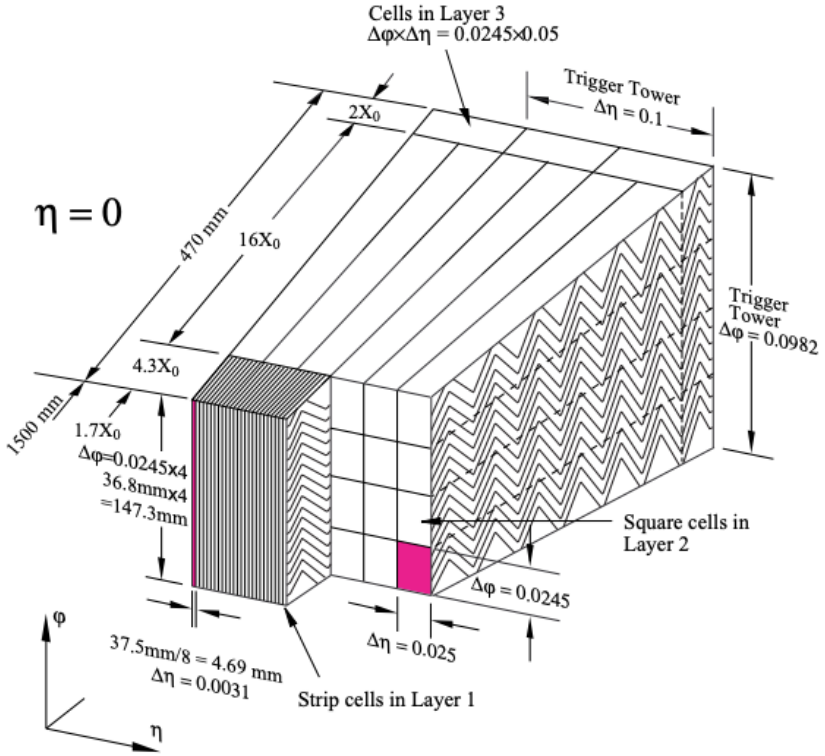
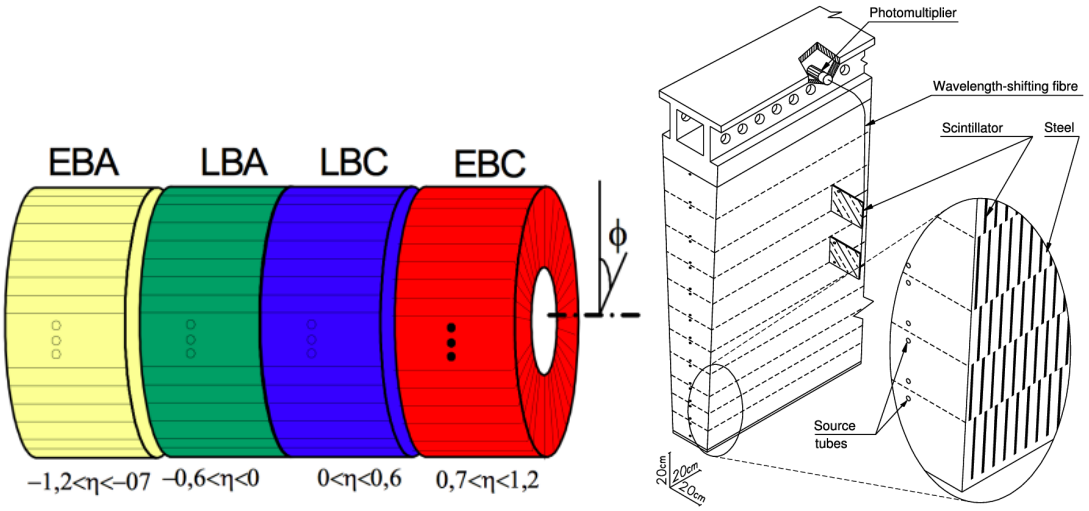


Figure 2.10: The ATLAS EM calorimeter consists of liquid argon cells separated by lead inserted between them. These liquid argon cells are responsible for measuring the deposited charge from electromagnetic showers. [66].

light. Neutral pions decay into photon pairs, subsequently generating electromagnetic showers, which can be detected. Wavelength-shifting (WLS) fibers guide the light from plastic scintillators to photomultiplier tubes (PMTs). The quantity of light captured by the PMTs serves as a measure of the energy of incoming hadrons or jets. The TileCal is divided into four cylindrical readout partitions along the beam axis as depicted in Figure 2.11(a). It consists of one central long barrel (LB) with two partitions (one on A-side and the other on C-side) known as LBA and LBC. The other two short extended barrels (EB) form two partitions, EBA and EBC. Each barrel is segmented azimuthally into 64 wedge-shaped TileCal modules (shown in Figure 2.11(b)), staggered in the ϕ direction, with a granularity of $\triangle\phi \times \triangle\eta = 0.1 \times 0.1$. The cell layout for LB and EB modules is shown in Figure 2.12 for $z > 0$. The TileCal Front-End (FE) and Back-End (BE) electronics are discussed in Section 2.4.



(a) (b)

Figure 2.11: TileCal detector is divided into three barrels and four partitions (a). Schematic diagram of the TileCal wedge module (b) [67].

2.3.3 Muon Spectrometer

The muon spectrometer is tasked with measuring muon momenta. As the largest and most distant sub-detector from the interaction point in the ATLAS experiment, it is shown in Figure 2.5 (grey and light-blue). The muon system covers a pseudorapidity range of $|\eta| < 2.7$, offering higher acceptance than the ID. It is capable of detecting muons because calorimeters absorb all other particles, excluding muons and neutrinos. Given that muons are significantly heavier than electrons, they deposit minimal energy as they travel through the calorimeters. The muon spectrometer functions as a tracking detector, measuring track curvatures and momenta within a magnetic field that varies from 0.5 to 4 T. This magnetic field is produced by eight large coils in the barrel region, with the field range determined by the distance to the coils. The endcaps also feature sixteen small toroid coils with the same magnetic field range as the muon spectrometer. Comprising three layers of tracking detectors in both the barrel and forward regions, the muon system employs a combination of fast detectors with low position resolution and slow detectors with high position resolution. This is crucial for ensuring accurate timing and position precision, ultimately leading to more accurate momentum measurements.

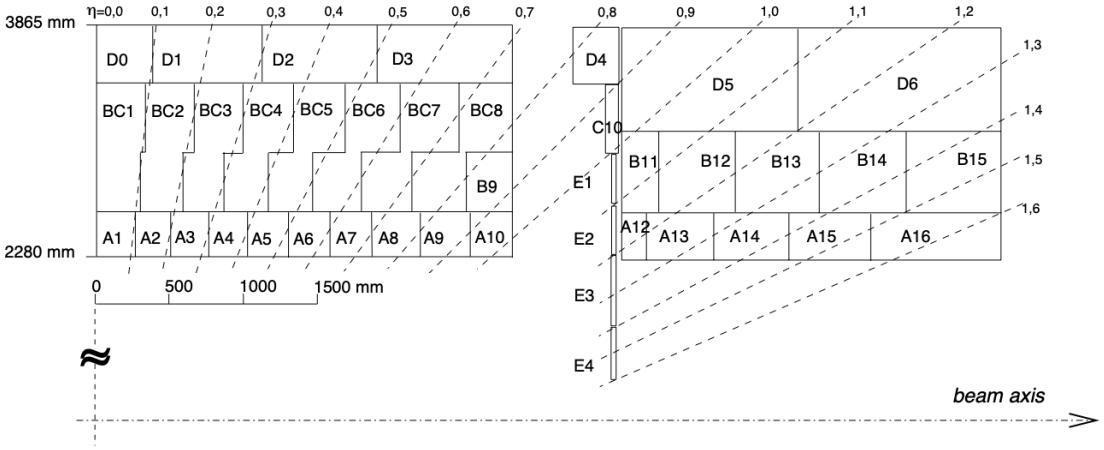


Figure 2.12: Segmentation in depth and $|\eta|$ of the Tile Calorimeter modules in the central and extended barrels. The central barrel has a coverage up to $|\eta| < 1.0$. The extended barrel covers the region $0.8 < |\eta| < 1.7$ [55].

2.3.4 The Trigger and Data Acquisition System

The ATLAS detector is engineered to investigate up to a billion pp collisions every second while handling an integrated data volume exceeding 60 Tbps. Only a tiny fraction of these events will exhibit intriguing properties, potentially resulting in groundbreaking discoveries and measurements. The ATLAS experiment utilizes a dedicated, multi-tiered computing system called the Trigger and Data AcQuisition (TDAQ) system (depicted in Figure 2.13) to decrease the data throughput to more manageable levels. The system selects events with distinctive properties that might be interesting for physics analyses. The trigger system is structured in a 2-level architecture, the Level-1 (L1) and the High Level Trigger (HLT). The L1 and the HLT are essential for reducing the event rate from 40 MHz (25 ns) to about 1 kHz, for which the events are further processed and stored in a permanent repository.

The L1 trigger system is built from custom hardware to reduce the rate of accepted events from an input rate of 40 MHz to 100 kHz, while operating at a maximum latency budget of 2.5 μs [69, 70]. The event selection within the calorimeter relies on both electromagnetic and hadronic calorimeter information, which is combined into a single subsystem called the L1 Calorimeter Trigger (L1Calo). Utilizing configurable algorithms, the L1Calo trigger system triggers on electrons, photons, jets, $E_{\mathrm{T}}^{\mathrm{miss}}$, and hadronically decaying τ-leptons. The L1 Muon Trigger (L1Muon) system searches for hits with specific patterns that are consistent

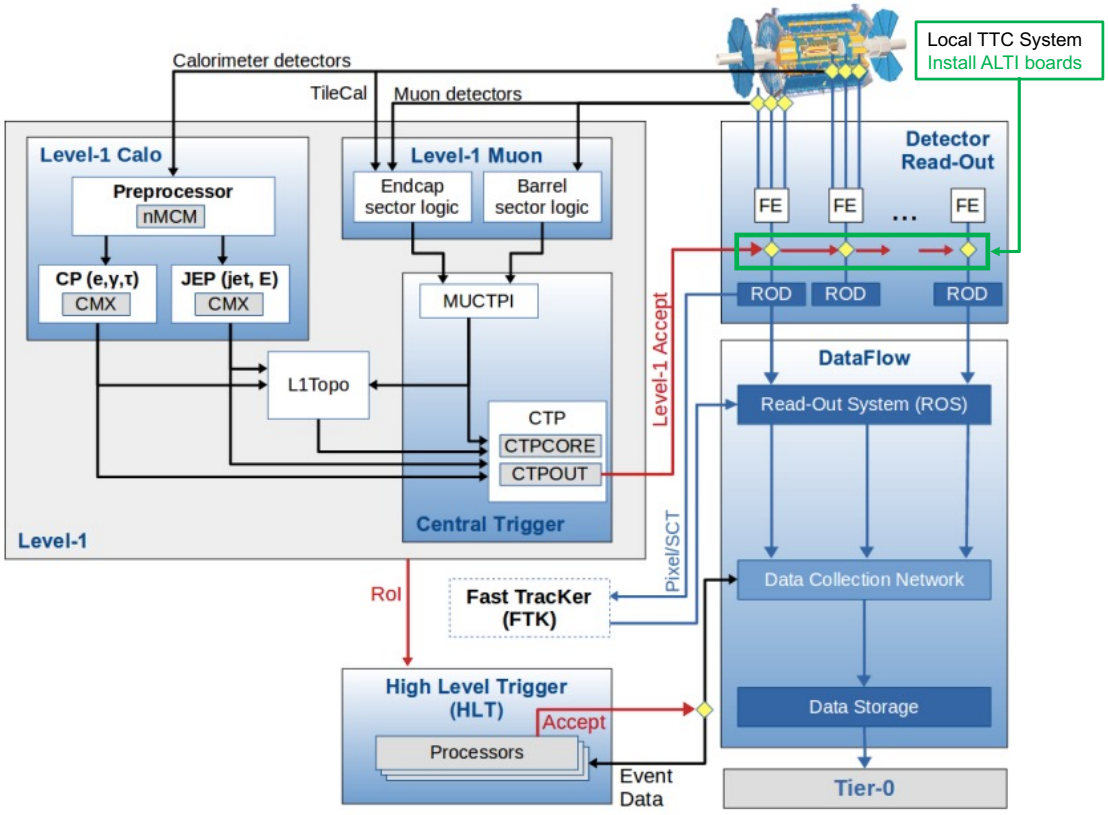


Figure 2.13: This is a general overview of the TDAQ system [68].

with high p_{T} muons originating from the collision point. The L1 Central Trigger Processor (CTP) [71] merges L1Calo and L1Muon data before making the final Level-1-Accept (L1A) decision. Each sub-system retains event data for a predetermined duration, ensuring the event data is read out as soon as the L1A arrives.

Composed of custom software, network switches, and commercial computers, the High-Level Trigger (HLT) [72, 73] further reduces the recorded event rate from 100 kHz to 1 kHz [69]. The Read Out Driver (ROD) receives event data from pipeline memories, performs data compression and zero suppression, and transfers data to the Read Out System (ROS) through the Readout Links (ROLs) using the S-LINK protocol [74]. Upon receiving data, the ROS sends Region of Interest (RoI) fragments to the HLT and stores the event data in a customized memory buffer [75, 76] for the full HLT latency period. The HLT then applies additional selection criteria based on the L1 RoI data and full-granularity data, executing software algorithms essential for early rejection. Once an event is accepted by

the HLT, the event builder reads out event fragments from all ROSes and combines them into complete events. These events are then sent to the Event Filter (EF) farm, where offline-type algorithms utilizing full calibration and alignment information are applied. Events approved by the EF in the HLT are permanently stored at a CERN computer center [77].

2.4 The Tile Calorimeter electronics

The TileCal read-out electronics consist of Front-End (FE) and Back-End (BE) electronics. The FE electronics are mounted on the detector, while the BE electronics are housed in the ATLAS Underground Counting Room USA15, a low radiation environment.

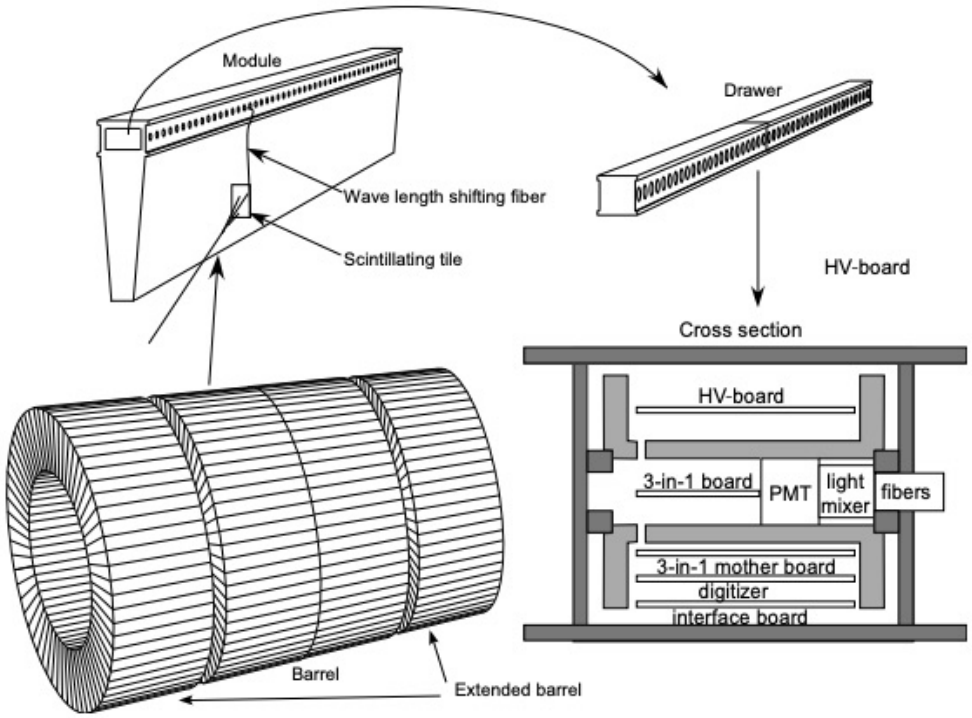


Figure 2.14: The TileCal barrels comprise 256 modules, containing drawers with FE electronics. The cross-section displays the electronics within the drawer. Scintillating tiles are connected to PMTs via WLS fibres for light transmission [78].

2.4.1 Front-End Electronics

The FE electronics are situated inside drawers at the outer edges of TileCal modules, as shown in Figure 2.14. They are powered by low voltage power supply (LVPS) and high voltage power supply (HVPS). The FE electronic components

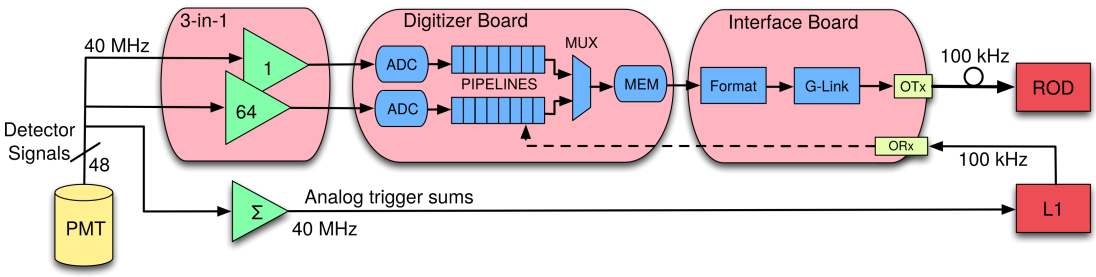
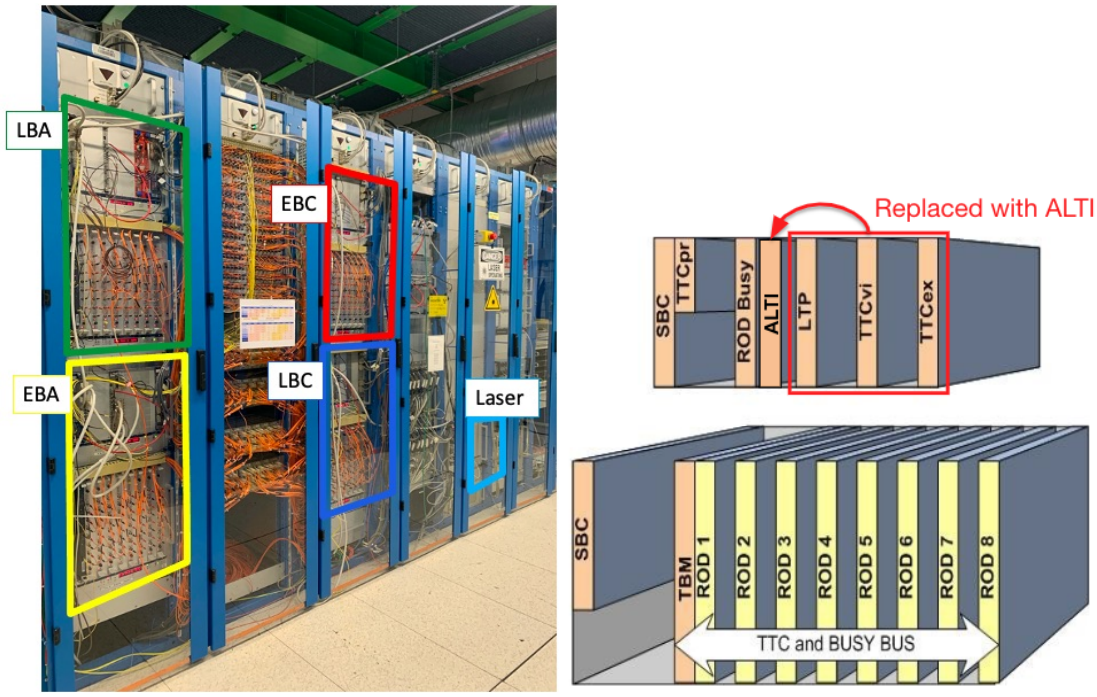


Figure 2.15: The TileCal BE electronics signal chain.

essential for TileCal include mother-boards, PMTs, digitizer boards, and interface boards [79]. The flow of signals through these components is shown in Figure 2.15. As a particle traverses scintillating tiles, it produces light, which is then transmitted to the PMT by WLS fibers. The PMT block converts the light into analog signals, which are digitized using two separate ADCs with a gain ratio of 1:64. The PMT block is constructed with a mu-metal shield for magnetic shielding and a steel cylinder for mechanical stability. It consists of a light mixer, a PMT, a voltage divider, and a 3-in-1 card [80]. Each drawer module can house up to 48 PMT blocks. The mother-board is the base component holding all drawer electronics together. It distributes power and TTC commands to the 3-in-1 boards and can accommodate four digitizer boards and a single interface board. Two mother-boards are present in each super-drawer. Once the L1 trigger system sends a L1A signal, the interface card receives digitized data from the digitizer board. A single interface card is present in each super-drawer, and it encodes and transmits data through dedicated fiber-optic links to the BE electronics while receiving TTC commands. The readout section for the interface board is duplicated with two dedicated output optical fibers for redundancy and to decrease single event upset errors. Additionally, the interface board computes the Check Sum (CRC) for input and output data streams, which is utilized by the BE electronics to eliminate processing data affected by single event upset errors and to perform online data quality checks [81]. The trigger summation board, located on the mother-board, combines low gain analog signals from a maximum of six 3-in-1 cards to generate



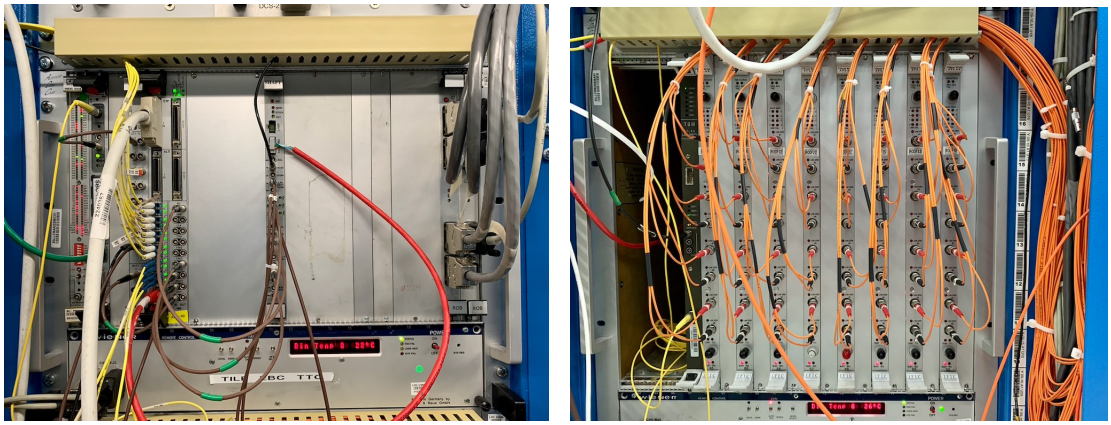
(a) (b)

Figure 2.16: In Point 1, the TileCal BE read-out electronics are partitioned into four crates labelled EBA, LBA, LBC and EBC, which correspond to the colours of the TileCal detector barrels shown in Figure 2.11(a). The TTC and ROD VME modules in the crates are represented diagrammatically in panel (b).

the analog trigger-tower sums that are necessary for the L1 trigger system.

2.4.2 Back-End Electronics

The BE electronics are organized into four TTC partitions (EBA, LBA, LBC, and EBC), as seen in Figure 2.16(a). Each partition consists of 64×2 TTC links for writing and 64×2 ROD links for reading from the detector. The TTC links are connected to TTC modules situated in a 6U VME crate, while the ROD links are connected to ROD modules located in a 9U VME crate. The TTC and ROD crates are shown in Figure 2.16(b). An SBC is included in each crate for controlling the VME crate, and the fan-tray is responsible for the DCS and monitoring of the crate. The DCS also performs read-out via CANbus [82]. The TTC crate houses the SBC, ATLAS Local Trigger Interface (ALTI) module, TTC receiver in PMC Form Factor (TTCpr) module, ROD Busy module, and SHared A Few Trigger (SHAFT) module, as shown in Figure 2.17(a). The ALTI module integrates the



(a) (b)

Figure 2.17: One of the P1 TTC crate housing different modules (a). The ROD crate housing eight ROD modules, TBM and a SBC (b).

functionalities of the LTP, LTPi, TTCvi, and TTCex, with additional features. It replaces a set of TTC modules used during Run 1 and Run 2 data-taking periods. The upgrade of the TTC system with the ALTI module during the LS2 period is discussed in Chapter 4. The ALTI module is currently in use for the Run 3 data-taking period (2022-2025).

The SBC controls the TTC crate and interfaces with other modules in the crate through the VMEbus [82]. The legacy TTC modules, used during Run 1 and Run 2 data-taking periods, are integrated into the ALTI module for the Run 3 data-taking period (2022-2025) with additional features. The TTCpr module provides Tile TTC information to the TDAQ framework for calibration runs [83]. The RODBusy module monitors the busy signal, while the SHAFT module controls calibration trigger requests. The laser ROD module provides information from the Laser calibration system and transmits TTC signals to the Laser system. The ROD crate houses the RODs controlled and monitored by the SBC through the VMEbus. TileCal has 4 ROD crates in P1, corresponding to 4 partitions, with a total of 32 RODs. The ROD module comprises four Processing Units (PUs) which are responsible for calculating the energy and time information for each readout channel [84]. The TMDB, a component of the Tile-Muon trigger system, is utilized for identifying intriguing muon events by employing the TileCal's outermost radial layers (D5 and D6 cells) in the EB [85]. The ROS, a server-class PC, accommodates up to 12 ROBs and acquires event data from the RODs via the ROLs.

Detector Control System

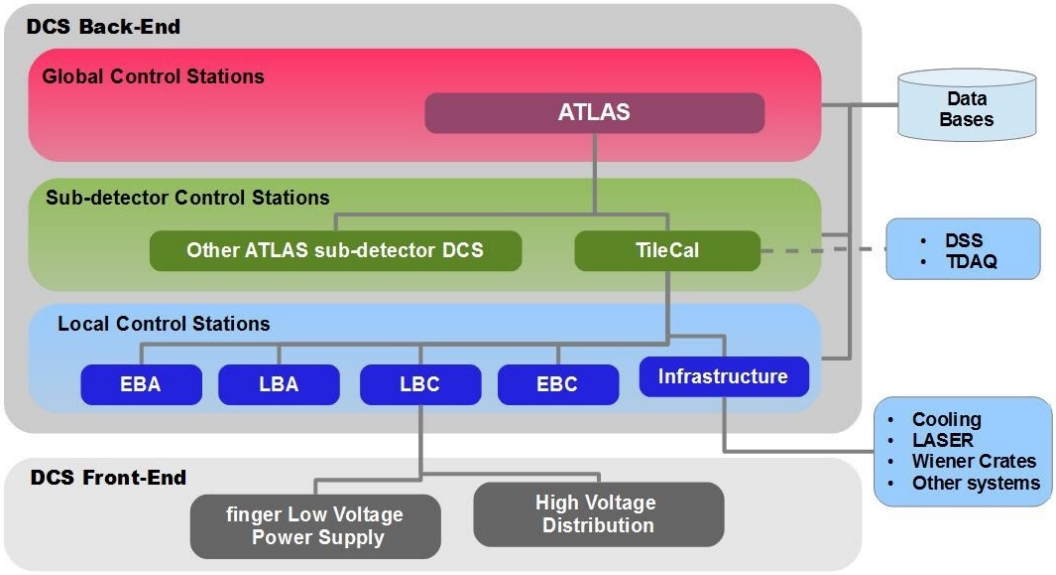


Figure 2.18: Diagrammatic representation of TileCal DCS hierarchal system used in Run 2 [82].

The DCS architecture [82] is set up as a distributed BE system operating on computer nodes and a variety of FE systems. This system offers capabilities for controlling and supervising operations, analyzing and processing data, storing information, and displaying results, as well as handling alarms, messages, and commands. The TileCal DCS follows the ATLAS DCS structure and is organized into three operational layers as shown in Figure 2.18. The main DCS systems for the TileCal are responsible for monitoring and controlling the LVPS, HVPS, and the cooling of the electronics. The HVPS provides high voltage to the PMTs, while the LVPS provides low voltage to the on-detector readout electronics. The cooling system ensures that the temperature of all electronics is maintained within the required range.

Calibration Systems

The construction of TileCal has been augmented to achieve excellent energy resolution through the implementation of precise and accurate calibration systems. At each level of the TileCal signal reconstruction, there is a dedicated calibration system to monitor the behavior of the different detector components. Figure 2.19

shows the different calibration systems along with the paths followed by the signals from different sources. The reconstructed energy of each TileCal channel, E [GeV], is derived from the raw response, A [ADC], as follows:

$$E\ [\text{GeV}] = A\ [\text{ADC}] \cdot C_{\text{pC}\to\text{GeV}} \cdot C_{\text{Cs}} \cdot C_{\text{Las}} \cdot C_{\text{ADC}\to\text{pC}}, \tag{2.5}$$

where the C factors are calibration constants. Variations in PMT HV, stress induced on the PMTs by high light flux, or aging of scintillators due to radiation damage can all cause the calibration constants to change over time. Calibration systems are utilized in monitoring the stability of the calibration constants and provide corrections for each channel. The electromagnetic scale calibration constant $C_{\text{pC}\to\text{GeV}}$, [4] is the only fixed calibration constant. The other calibration constants are provided by the Cesium, laser, CIS, and the Minimum Bias Systems.

Cesium The Cesium calibration system employs three radioactive sources that are circulated around TileCal using a hydraulic system to scan all TileCal cells. The scintillators are illuminated by 662 keV photons emitted from ^{137}Cs $\gamma-$sources, which in turn emit photons to the WLS, enabling the optical response stability and uniformity of the cells to be tested.

Laser system The Laser calibration system sends laser pulses to the PMTs, allowing for calibration with respect to each PMT's response. This allows for the calculation of corrections to the optical gain of the PMT and a test for the stability of each PMT over time. Laser pulses are also sent during empty bunch crossings of the LHC and the events are used in monitoring the evolution in time of the time calibration. For calibration purposes, data is collected in dedicated runs in the LHC inter-fill periods.

Charge Injection Scan A Charge Injection System is used for monitoring the electronics and extracting the conversions factor from ADC counts to pC, $C_{\text{ADC}\to\text{pC}}$. The calibration system involves simulating physics signals by injecting known charge values into the readout electronics and evaluating the electronic response. Charge injection employs dedicated capacitors (5 pF and 100 pF) and a 4096 DAC controlled by the ADC. The relationship between the peak amplitude

[4] Converts the calorimeter signals measured as electric charge in pC to the energy deposited by measured electrons which produced the signals.

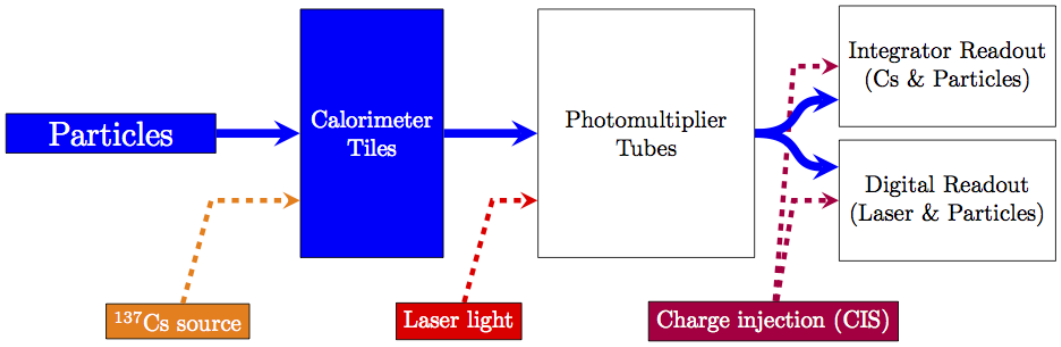


Figure 2.19: A diagram illustrating the sequence of signal readout in the calibration systems of TileCal [86].

in the electronics' response (measured in ADC counts) and the injected charge value (in pC) yields the calibration of each ADC in terms of ADC counts/pC. This enables the detection and identification of errors in the readout chains, as well as the calibration of each PMT's individual ADC output.

Minimum Bias System Soft parton interactions, known as Minimum Bias (MB) events, dominate the *pp* collisions. The MB readout system integrates response to Minimum Bias events over a time span of approximately 10 ms. During *pp* collisions, data from the integrator is continuously recorded. The TileCal's response to signals produced by MB interactions provides an estimation of instantaneous luminosity [87]. The MB system monitors the stability of the entire optical chain and provides an independent cross-check of the Cesium calibration [88].

Chapter 3

TileCal Online Software

In this chapter, the necessary online software for implementing the ALTI software in the Tile online software is presented. The Tile online software includes the ROD Crate DAQ and TileCal run types. The chapter also covers the TDAQ software release, versioning, and the organization of the TDAQ software and build systems. Additionally, the Diagnostics and Verification System is discussed. The author built the test bench station using the resources discussed in this Chapter, the contribution to the Tile online software is highlighted in different sections, leading to the main contributions of the author in Chapter 4.

3.1 Online software

The TDAQ system's online software encompasses the software responsible for configuring, controlling, and monitoring the TDAQ, excluding the processing and transportation of physics data. The online software integrates different subsystems without any detector-specific elements, as it is intended for use with the required configurations of the DAQ and the detector's instrumentation. It operates in conjunction with other sub-systems. The online software is composed of multiple components, which provide essential services for operating a partition. These components are:

- **Configuration databases**: The implementation of the database system utilized for the specification of the DAQ system configuration.
- **Process Manager (PMG)**: A service accountable for the running of ap-

plications on the nodes.

- **Resource Manager**: A service responsible for the bookkeeping of allocated resources. It controls the usage of the available hardware and software resources described in the configuration database.
- **Access Manager**: A service responsible for access to nodes and resources for an authorized user, based on their expertise and experiment status.
- **Inter Process Communication**: The primary communication service that utilizes TCP/IP message passing.
- **Information Services (IS)**: A service designed to facilitate information sharing between software applications within a distributed environment.
- **Run control (RC)**: The Finite State Machine (FSM) service that is responsible for the application control structure.
- **Monitoring infrastructure**: The online monitoring system for ATLAS, organized as a distributed framework.
- **Integrated Graphical User Interface (IGUI)**: The TDAQ IGUI provides a graphical interface that allows operators to monitor the status of the TDAQ system, view real-time data from the detector, and control various aspects of the data acquisition process.
- **Expert System**: A service that monitors and oversees the recovery actions in case of failures or errors.

To meet the requirements of distribution, robustness, flexibility, scalability and modularity, the online software has been designed as a customizable framework. The TDAQ is defined as a collection of applications running on hosts, modelled around a common FSM that specifies clearly defined states and transitions. The RC service maintains the overall TDAQ status by implementing a hierarchical tree with a Root Controller at the top. The Configuration Database service includes detector-specific information and run parameters, gathered as configuration for specific run types. Sub-detector experts use this service to configure their applications using standard tools. The implementation of this service is based on the Object Kernel System (OKS), which uses well-structured XML files to provide persistent in-memory object management. The configurations database can be

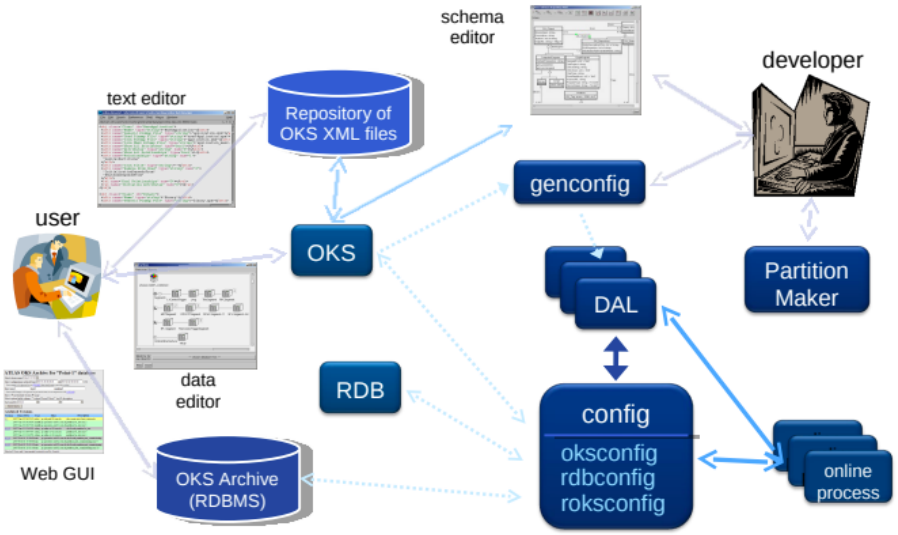


Figure 3.1: A depiction of the Configuration Databases: architecture, management and access [70].

accessed through the config package API based on two layers: the first config layer provides an abstract interface, and the second Data Access Libraries layer maps the database schema on C++, Java and Python classes [89].

3.1.1 Partition

The TDAQ configuration is initially defined in the partition. In ATLAS, a partition is a software element that defines the set of software and hardware to be executed at a given time for data taking. TileCal uses the Tile partition for taking calibration runs, and the ATLAS partition groups all sub-systems together. The TDAQ software can operate only one partition at a time, and partitions cannot be nested. Therefore, sub-systems include their partitions as segments to the ATLAS partition. Figure 3.2 shows the IGUI of the TileCal test bench partition (Tile175) with the RC in the RUNNING state. The TDAQ system has several specific functionalities, including the TTC partition, Segments, Resources, and the TDAQ partition. The author has contributed to building the Tile175 partition and maintaining it throughout the TileCal upgrade to ALTI project.

- **TTC partition**: A TTC partition is the smallest element that can be operated with the TDAQ independently. It corresponds to a single TTCvi/ALTI module. ATLAS TTC partitions are fully described in [90], and the TileCal TTC partitions are described in the previous chapter.

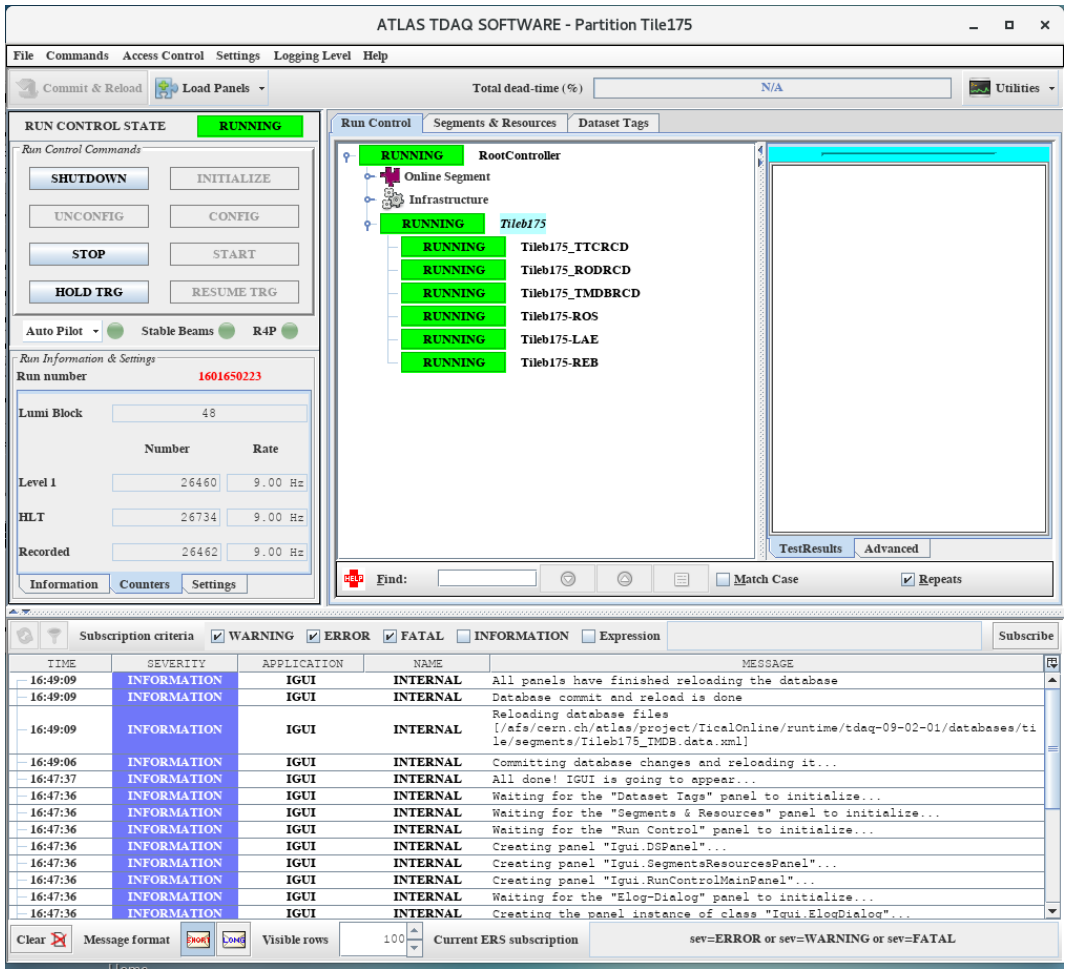


Figure 3.2: The IGUI of the Tile175 partition.

- **Segment and Resource**: A segment refers to a group of TDAQ system elements that can be configured and controlled separately from the rest of the TDAQ system. Segments can be added or removed from an active TDAQ partition without interrupting the run. The four TTC partitions of the TileCal are each represented as a TDAQ segment. A resource is a component of the TDAQ system that can be enabled or disabled individually, without stopping the data-taking process.

- **TDAQ partition**: A TDAQ partition is a subset of the TDAQ system responsible for data-taking. A TDAQ partition corresponds to one or more TTC partitions, and the full TDAQ functionality is available to the subset of the detector covered by the partition.

3.2 Tile online software

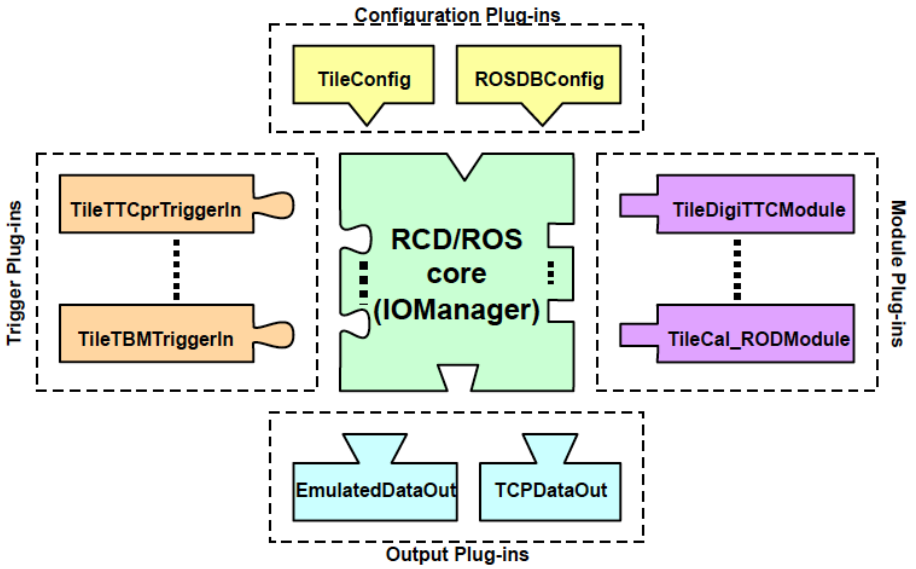


Figure 3.3: The RCD schematic diagram. The RCD handles the TileCal BE hardware operation, with one RCD application running in each TTC and ROD crate [91].

The TileCal Online software is a specialized TDAQ software that is designed to operate the TileCal detector. It builds on the ATLAS TDAQ software and includes various components such as software for the BE electronics, calibration systems infrastructure, software and hardware monitoring, and diagnostic and verification systems tests (DVS). The ROD Crate DAQ (RCD) for BE electronics is a critical part of the TileCal online software, and is supported by the ATLAS Data Flow policy. This allows programmers to focus on hardware handling, while the core software is centrally managed.

The RCD framework extends the ROS software to integrate custom hardware into the TDAQ software. It uses a multi-threaded read-out application core that loads specific plug-ins at runtime to adapt to the detector's specific requirements. The RCD is an RC application that responds to FSM transition commands initiated by TDAQ users through the GUI. Different plug-ins serve various purposes, such as the Configuration plug-in that retrieves information from the configuration database and passes it to the RCD core application. The TileCal specific read-out application with its plug-ins is shown in Figure 3.3, and details about the TileCal specific plug-ins can be found in [91]. These plug-ins include the

Configuration plug-in, Trigger plug-in, Module plug-in, and Output plug-in.

3.2.1 TileCal run types

The TileCal makes use of six different run types, five of which are calibration runs and the other being a physics run. The detector configuration is different for the calibration and physics runs. The calibration run types require the storage charge value sent to the FE electronics along with the data readout from the RODs. This requires the inclusion of additional elements in the readout which slows down the acquisition rate. Therefore, the calibration configuration is not feasible for physics runs. All run types are taken using the seven samples window at a readout window of $25\,\text{ns} \times 7 = 175\,\text{ns}$. The runs are either bi-gain: both ADC gains are readout for each channel, or mono-gain: only one ADC gain is read-out per channel. The gain is chosen automatically by the DMU on the basis of the two following criteria:

- **High Gain overflow**: if the number of ADC counts in HG is 1023 for at least 1 of the samples, then the gain is switched to LG.
- **High Gain underflow**: if the number of ADC counts in HG is 0, then the gain is switched to LG.

Calibration Runs

- **Pedestal**: This is a bi-gain calibration run to monitor electronics noise without a signal. This is used to verify the noise level of the detector and the data integrity.
- **CIS**: This is a bi-gain calibration run that yields the ADC count/pC conversion for each channel. A DAC ramp is performed for each of the two capacitors (5 pF and 100 pF). For each DAC step the timing is varied. This run scans the entire range of the TileCal electronics to verify the correct linearity of the ADC, the control of the DAC settings and to find stuck bits and data integrity problems.
- **Mono CIS**: This is a mono-gain calibration run in which a constant charge is injected to monitor electronics stability. The purpose of this run is to verify the correct response of the ADC, find gain switching, Mother-board timing, and data integrity problems.

- **CIS ramp**: CIS is fired with a configurable pattern and data is read-out in physics mode for Optimal Filtering reconstruction validation.
- **Laser**: This is another mono-gain calibration run in which a Laser light is injected into the laser fibers to make sure there are no dead PMTs/fibers and to calculate PMT gain and timing. The purpose of this run is to verify the correct response of the PMT, find gain switching, digitizers timing, and data integrity problems.

Physics Run

This a mono-gain run with ATLAS setup and TileCal included as a segment running in the combined partition. The L1A is provided by the CTP through the LTPi and the LTP/ALTI.

3.3 TDAQ software release and versioning

The TileCal Online software is structured into packages within the TileCal Online software release, following the ATLAS TDAQ software policies and release, which means that it is updated simultaneously with ATLAS TDAQ updates and policies. The packages are built using CMake and stored in a GitLab repository (https://gitlab.cern.ch/atlas-tile-online). The release build directory contains a packages.txt file listing the included packages. When a new release is available, all packages are checked out into an Andrew File System (AFS) or CernVM-File System (CVMFS) account and compiled in one go. Git's annotated lightweight version tags, which require a message, are assigned to all packages ready for a new release build. Once pushed to the GitLab remote repository, these tags are never removed. These tags adhere to the standard of three groups of letters and numbers indicating the major, minor, and patch version, such as v3r1p2. The latest tag for each package is used to build the release. The TileCal Online release versioning (tile-X.Y.Z.U) is based on the TDAQ versioning (tdaq-X-Y-Z), with an additional enumeration indicating the number of times the release has been rebuilt due to updates.

After successful compilation, the binaries are copied to the P1 detector installation area. No write permissions are granted to the release files once installed. If a particular patch is required for the release, the patch is compiled and copied

to a patches directory in P1. During his studies, the author has created and installed multiple TileCal releases for the B175 test bench, P1 area, and test beam area, and has also maintained and installed TDAQ drivers in all locally managed nodes. GitLab is used by the ATLAS experiment for software version and revision control. Git is a modern distributed version control system (VCS) widely adopted in the open-source community that allows for a more decentralized approach to software version control. Git is fully supported by CERN as the recommended VCS tool for all software projects. Git VCS is used for the Tile Online software and the OKS database, which has been migrated to GitLab in preparation for Run 3. The author is responsible for migrating the TileCal OKS database to GitLab for each new release. The following section describes the organization and build systems of the TDAQ software.

3.4 TDAQ software organization and build systems

The TDAQ software is composed of three projects, namely tdaq-common, dqm-common, and tdaq, which offer access to external software packages from CERN's SFT group shared with offline and other experiments. The tdaq-common project is a basic project used by both TDAQ and offline software and includes packages such as the raw event format and storage as well as the ERS. dqm-common is used for data quality monitoring (DQM) for both TDAQ and offline DQM. The tdaq project includes all the other packages utilized by sub-detectors and the HLT, and the TileCal Online software is built against this TDAQ project. Figure 3.4 provides a diagrammatic representation of the TDAQ software organization, while Figure 3.5 shows the TileCal Online software release packages and their dependencies. The packages modified to include the new ALTI software by the author, are highlighted in green. The TDAQ software uses CMake to build, test, and package software, and the software is built and distributed as packages, which are the smallest manageable unit of software. The TileCal online software is primarily developed using C++, accounting for 97% of all services and libraries, while Java is used for the IGUI that handles TDAQ sessions, and Python is the preferred scripting language, which is used when speed is the least important factor.

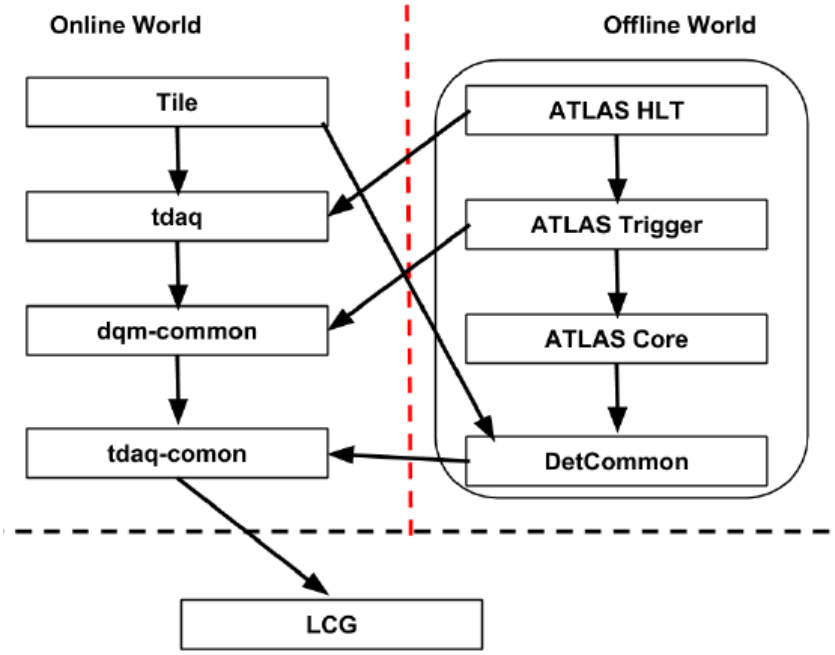


Figure 3.4: A visual overview of the TDAQ software organization, where the TileCal and other sub-detector software projects are constructed using the tdaq project. The tdaq project, in turn, is developed based on the dqm-common and tdaq-common projects.

3.5 Diagnostics and Verification System

DVS is a part of the ATLAS TDAQ online software packages used for configuring and executing tests for TDAQ components, detecting and diagnosing faults, and advising recovery actions to the TDAQ operator/user [92]. DVS is a framework that enables TDAQ developers and experts to integrate tests and information into it so that it can subsequently be used by a non-experienced shift operator to evaluate the TDAQ's functionality and identify issues. It enables the definition of several tests for a single TDAQ component. Tests can be run sequentially or concurrently on several hosts/computers. High precision DVS tests are available for TileCal under the TileDVS package. These tests the digital and integrator readouts of the super-drawers. Other set of tests are also available as tools for special purposes. The digital tests are;

- **CIS (Low and High gains)**: Checks the existence of a pulse inside some bands for low and high gains.

- **Pedestal**: Computes the low and high frequency noise for the data and compare it to the nominal values.
- **DMU Memory**: A bitwise pattern is written into the memory of the DMU. Pattern data is read-out and checked for mistakes.
- **Stress**: A 100 kHz random trigger and a full busy logic is used to veto the acquisition. Data is processed inside the DSP. The number of CRC errors found in the data is reported.
- **Digitizer addresses**: This is a list of tests used to get the correct addresses of the components on the digitizer boards.

The TileCal DVS tests use two binaries which are executed on different nodes and interact with each other via the IS server. Prior to running the DVS tests, the IS server is firstly booted by starting the TileCal DAQ partition and the DVS tests can be run in two ways: from the command line or from the DVS GUI provided by the TDAQ system. The GUI method provides a much quicker and easy way of running DVS tests for drawer certification after repairs. The tests also produce detailed test output log files and plots in an accessible predefined location. Figure 3.6 shows a result of a high gain CIS test. A Gaussian function is fit through the samples for pulse recognition. The plots are also color coded, green means everything is fine, and red means that something is wrong with that particular channel i.e channel 3. The log files for this test show that there was an incorrect pulse amplitude, width and phase for this channel in 100 events. Figure 3.7 shows results of a bi-gain pedestal test. The plots show that there are no noise or pedestal problems for EBC52 module.

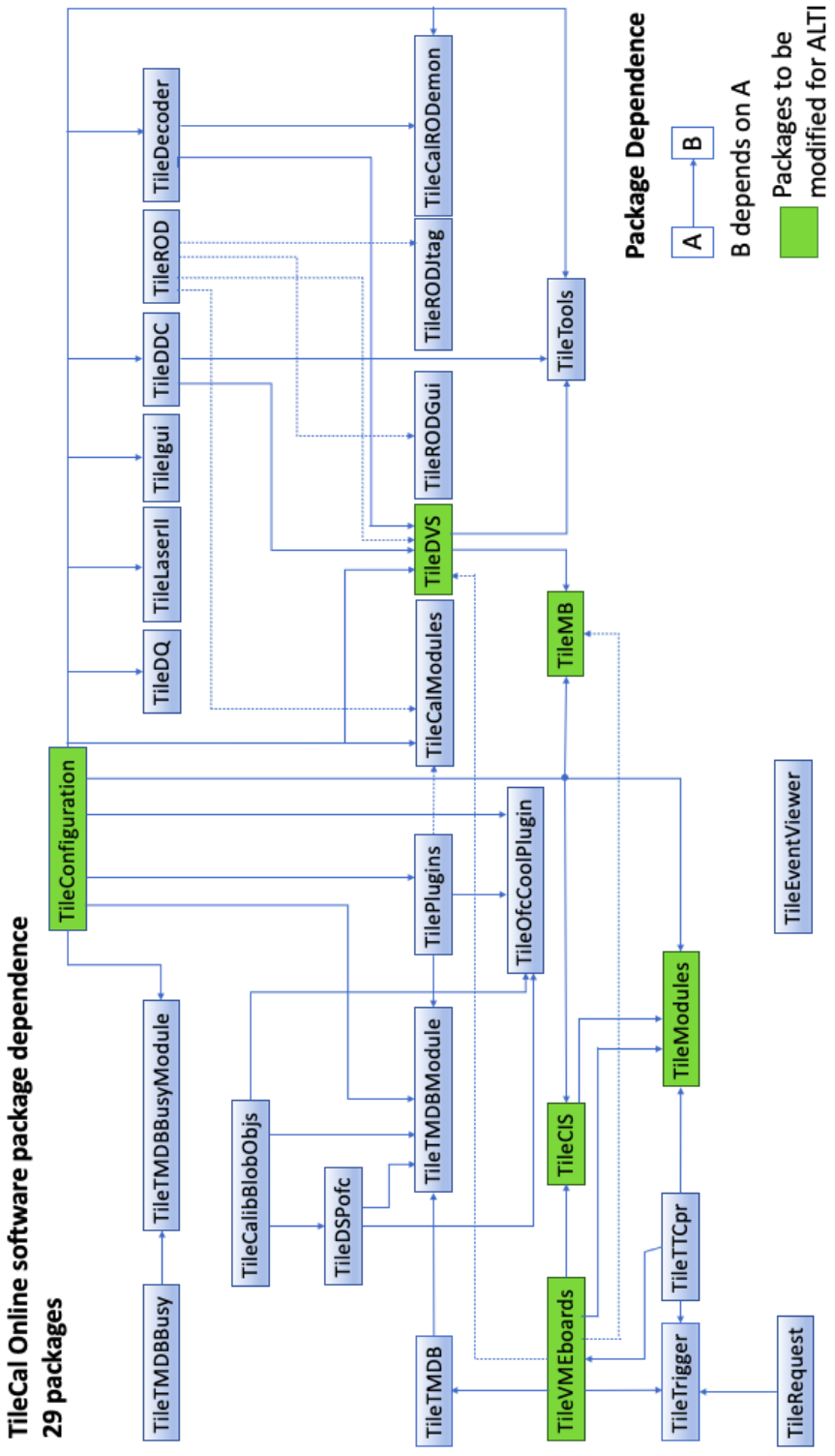


Figure 3.5: A diagrammatic representation is shown for the Tile Online software release packages, which consist of twenty-nine packages, with the majority dependent on the TileConfiguration package.

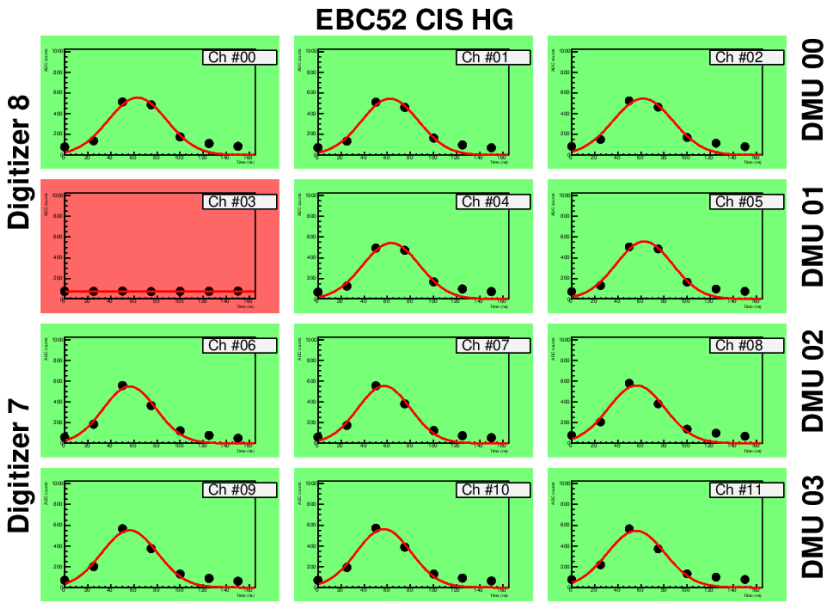


Figure 3.6: CIS HG DVS test result from IGUI. The test result shows that there are problems in the amplitude of channel 3. Log files show that the pulse amplitude, width and phase were incorrect in 100 events, and thus the channel is color coded red for bad.

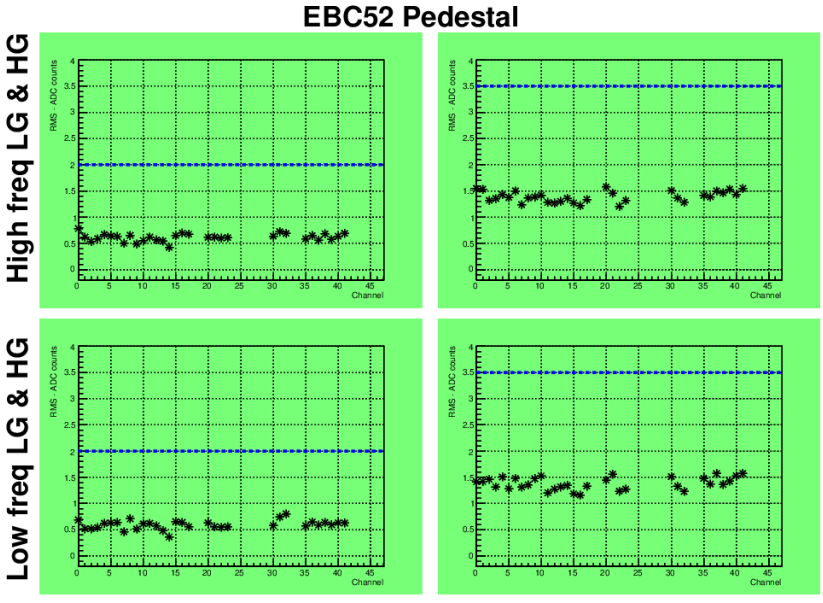


Figure 3.7: Plots showing results from DVS pedestal test for both high and low gain. Results show that noise levels are within acceptable levels for this module (EBC52).

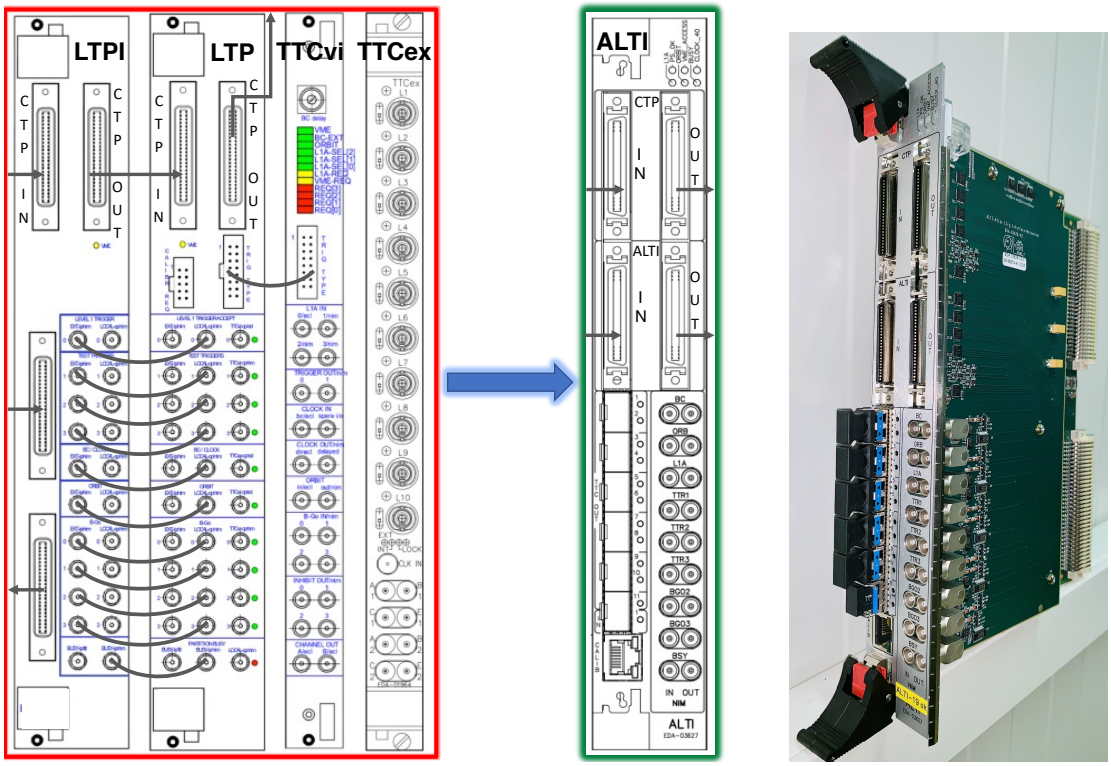
Chapter 4

Implementation of the DAQ software and integration of the ALTI Module in the TileCal

This Chapter introduces the ALTI module and discusses the implementation of the DAQ software and the integration of the ALTI module in the TileCal, where the author contributed to its software development and integration. The Chapter details the installation of the ALTI modules and validation of the TileCal TTC system. It also describes the upgrade of the TTC system for the TileCal Phase-II test-beam campaigns. Calibration and DVS results are discussed. Run 3 pilot beam results, the first Run 3 stable beam collisions (July 2022) and test-beam results (November 2022) are discussed.

4.1 Introduction

The ALTI module [93] is a new electronic board developed for the ATLAS experiment at CERN as part of the TTC system [94]. The module integrates the functionalities of four legacy modules previously used in the experiment during the Run 1 and Run 2 data-taking periods: LTP, LTPI, TTCvi and TTCex. The four legacy modules and the ALTI board are shown in Figure 4.1. Several ALTI modules were installed and tested during the LS2 of the LHC in 2019-2021, in preparation for the Run 3 data-taking period. The main function of the ALTI module is to provide an interface between the L1 CTP and the sub-detector's local TTC system. It consists of state-of-the-art components and the logic is



(a) (b)

Figure 4.1: The four legacy TTC modules (LTPi, LTP, TTCvi and TTCex) will be replaced by the ALTI module (a). ALTI module (b).

implemented in a single FPGA, which allows more flexibility and additional functionalities. During the operation of the detector, the ALTI module receives the TTC signals from the CTP via parallel twisted pair of low voltage differential signaling cables and distributes them to the sub-detector electronics via the optical TTC distribution network. The complete LHC turn consists of 3564 bunch crossings (BCs). The signals received from the CTP are the bunch clock, the orbit signal, L1A with 8-bit trigger type, and the event counter reset. The bunch clock is the main timing signal generated by the LHC and has a frequency of 40 MHz. The orbit signal is the second timing signal that indicates the start of a new LHC turn and allows the identification of the BCs.

4.2 ALTI hardware

The ALTI module design is based on commercial off-the-shelf components and most of its functionality is implemented in a Xilinx Artix-7 XCA200T FPGA.

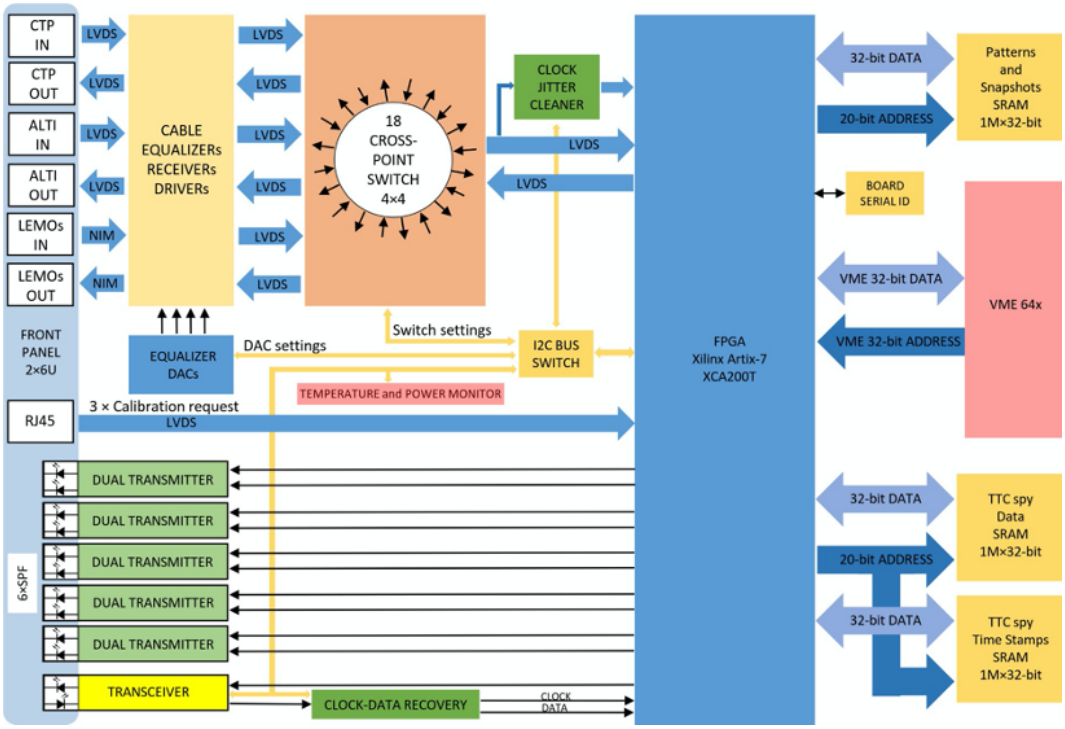


Figure 4.2: ALTI functional block diagram.

The block diagram of the module is shown in the Figure 4.2. The ALTI module is a 6U VME64x module which takes up 2 slots in the crate. The module is fitted with P1 and P2 VME64x 5×32 pin connectors of type DIN 41612-expanded. The ALTI module is implemented on two printed circuit boards, the motherboard and a mezzanine board that plugs onto the motherboard [95]. The ALTI motherboard houses all logic, implemented in discrete integrated circuits, the FPGA, two LVDS-LINK input interfaces, 6 SFP modules, the RJ45 calibration inputs connector, the VMEbus interface and the power supplies modules. This PCB has 12 layers and uses the VME 6U form factor. The mezzanine board carries the LVDS output interfaces for the CTP and ALTI LVDS outputs as well as all the coaxial input and output interfaces. The PCB has 6 layers and is smaller than the motherboard. The connection between two boards is done via a high-speed QSH/QTH series connector from Samtec [96] carrying 180 signals, 3 power supplies and ground.

The 7A200T FPGA device from the Xilinx Artix-7 family has been chosen to implement the programmable functionality of the ALTI. Due to the large number of the input and output signals required, the FFG1156 BGA package is used for providing 500 user I/O pins.

In normal operation, the ALTI module is clocked by the LHC bunch clock

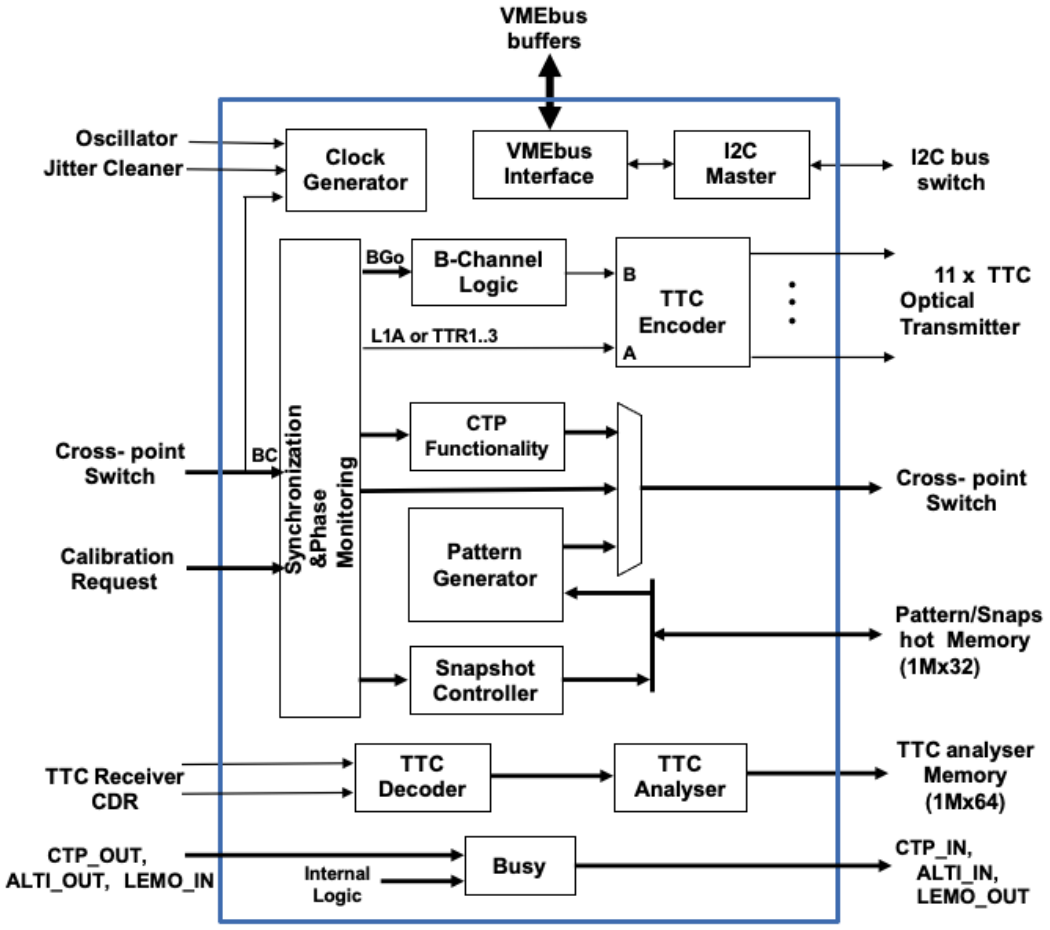


Figure 4.3: ALTI firmware block diagram.

(BC) signal which it receives from the CTP. When running a partition in local mode or when using the ALTI_IN/OUT chain connections for running several partitions combined, the clock can be sourced from other inputs. A high-speed cross-point switch chip configured through an I2C interface handles the selection of the possible BC signal sources. The BC can be sourced from:

- CTP_IN LVDS input
- ALTI_IN LVDS input
- BC front-panel LEMO input
- On-board 40.08 MHz oscillator

The ALTI also features a 4-channel jitter attenuating clock multiplier circuit, which can be used to feed a cleaned clock signal to the FPGA. The device is

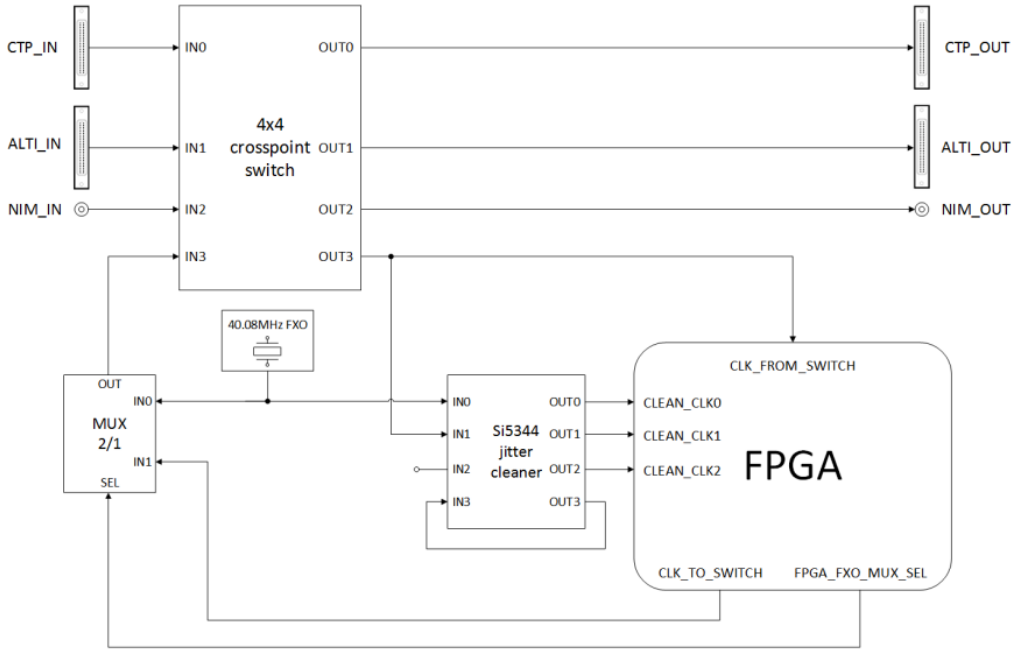


Figure 4.4: ALTI clock source paths and distribution.

configured though its I2C interface. It features a zero-delay mode which ensures a fixed input-to-output clock phase relation, which is essential in this application. It also provides a holdover mode which can be automatically activated when the selected input clock becomes invalid. This minimizes the disturbance of the output clock phase and frequency when the input clock suddenly fails. The block diagram of the ALTI clock distribution is shown in Figure 4.4.

A set of eighteen 4×4 LVDS cross-point switch chips [97] handle the routing of the signals between the front-panel inputs and outputs and the FPGA. Each of the 4 outputs of the cross-point connects to a 4:1 multiplexer which allows any input to be routed to any output. The device uses differential LVDS signalling throughout, which enables high speeds and low signal skew. The typical propagation delay of the cross-point switch is 500 ps, with the peak-to-peak jitter below 8 ps. The device is configured through an I2C interface connected to the FPGA. The routing can be configured for every signal independently. The signal routing through the cross-point switches for the Orbit, L1A, BC, trigger type and test trigger signals, can also be seen in Figure 4.4, however the trigger type signal do not have a LEMO connection on the front-panel. The B-Go signal path is also slightly different because of the limited number of LEMO inputs and outputs that can be fitted on the front-panel.

The ALTI module consists of two inputs for LVDS-LINK cables. Since these cables can be long in certain setups, up to 35 m in the experiment, a cable equalizer is required to compensate for the high-frequency transmission losses in the twisted-pair cables. A set of six triple differential receivers with adjustable line equalization devices (Analog devices AD8123 [98]) are used for each of the two LVDS-LINK input cables. Fast LVDS comparators (Analog devices ADCMP604 [99]) are used to translate single-ended equalizer outputs back to LVDS signal level. The AD8123 has three analog control pins for adjusting cable frequency response of the equalizer, as well as an output offset voltage adjustment. The analog control inputs for each LVDS-LINK cable are driven independently by an I2C programmable quad 8-bit DAC device (Analog devices AD5305 [100]), which enable tuning the equalization setting to the cable length through VME. The ALTI motherboard carries 6 single-mode fibre optical standard Small Form Factor Pluggable (SFP) modules. Five of them are dual transmitters (W-Optics SAA-1AF1-111 [101]) and one is a transceiver (Finisar FTLF1323P1xTL [102]). The main optical characteristics are summarized below:

W-Optics SAA-1AF1-111 SFP dual transmitter

- **Single-mode FP laser, wavelength**: 1310 nm typical
- **Optical output power**: -9 dBm (min.) / 0 dBm (max.)
- **Link length**: 10 km
- **Data rate**: 156.25 MB/s
- **LC optical connector**

Finisar FTLF1323P1xTL SFP transceiver

- **Single-mode FP laser, wavelength**: 1310 nm typical
- **Transmitter optical output power**: -5 dBm (min.)/0 dBm (max.)
- **Link length**: 40 km
- **Data rate**: 155 MB/s
- **Duplex LC optical connector**

- **Receiver optical sensitivity**: -34 dBm (min.)/-10 dBm (max.)
- **Digital diagnostic monitoring with I2C interface**

The ALTI module uses six 1M×16-bit asynchronous SRAM chips (Cypress CY7C10612G30-10ZS [103]). The memories are organized in three banks of 1M×32-bit for the access through VME. The first bank is used as pattern generator and snapshot memory, while the other two banks are used for the TTC data stream analyser. The ALTI module has a number of devices which are configured or read through an I2C bus interface, namely the 18 cross-point switches, the jitter cleaner, the CDR chip, the SFP transceiver and a temperature and a voltage monitoring chip. The I2C network is partitioned into four segments using a quad bidirectional translating I2C switch device (Texas Instruments TCA9546A) and the primary I2C SCL/SDA signal pair is connected to the FPGA. The ALTI module uses the +3.3 V, +5 V, +12 V and -12 V supply voltages from the VME64x backplane, the current requirement is about 2.0 A, 7.0 A, 0.5 A and 0.6 A respectively. Four DC/DC converter modules (Maxim MAXM17515 [104]) with a maximum output current of 5 A each are used to generate the supply voltages required to power the FPGA. The power-good output and enable inputs of the DC/DC converters are daisy-chained in a way to ensure the proper power-on sequence required by Artix-7 FPGA device. An isolated DC-DC converter (THN15-221 [105], maximum output current 3 A) generates the -5 V supply necessary for the NIM inputs and output drivers from ±12 V supply of the VMEbus backplane. In total, the ALTI module uses nine different power supply voltages. The module module has hardware monitoring capabilities, allowing all power supply voltages as well as some device and board temperatures to be monitored. The measurements are performed using the FPGA on-chip XADC block as well as two external sensor chips which are connected through I2C (LTC2991 [106] and MAX1617A [107]) to the FPGA.

The firmware contains most of the basic features of the legacy TTC modules. New additional features, are the ability to change the phase of the TTC outputs and the MiniCTP functionality. The firmware has been written in Verilog and VHDL, as top level block diagram of the firmware is shown in Figure 4.3. IP blocks and library components from Xilinx and OpenCores (for the I2C master) have been used. A scheme to automatically update the firmware version number and add a timestamp is available, making it possible to read the version number and the compilation time from a register through VMEbus. In-system firmware

upgrades are supported using the Xilinx QuickBoot method [108]. This enables a reliable field update using in-system programming through the VMEbus interface.

An on-chip Mixed-Mode Clock Manager (MMCM) is used to generate all the required FPGA-internal clocks. The MMCM control and status signals are accessible through VME. Most of the internal FPGA logic, including the VME interface, is operated using the selected BC clock source. This is potentially problematic in case of loss of the input clock, e.g. when a cable is disconnected. However a small subset of the logic is clocked by the on-board crystal oscillator clock, e.g. the I2C controller used to configure the cross-point switches and the jitter cleaner, which allows recovering from this situation. A coarse input phase monitoring circuit has been implemented for all external inputs of the FPGA. Each input is sampled by four 90° phase-shifted clocks derived from the BC signal and input signal edge are detected by comparing adjacent phase samples. Both input signal edges positions are continuously stored in VMEbus accessible registers, and based on this the information one of four sampling clocks selection can be done automatically or imposed via a VME register settings. Each input synchronization circuit can be configured independently.

The TTC system uses a unidirectional optical fibre based distribution system, where two information channels, A and B, are Time Division Multiplexed (TDM) and Bi-Phase Mark (BPM) encoded using the LHC BC clock as the carrier frequency and transmitted at a rate of 160 MHz of optical fibres. The A-channel carries exclusively the L1A trigger signal, while the B-channel carries packaged commands with address and data information. The encoder logic multiplexes and encodes the L1A input and the internally generated commands onto the A and B communication channels. The A- and B-channel data is sampled alternatively every half period of the BC clock and then encoded using a BPM scheme. The BPM encoded signal is then transmitted to the sub-detector electronics using the on-board SFP fibre optic transceivers. The data packets sent on the B-channel can either be of short (8 bits) or of long format (30 bits). Error correction coding is implemented by adding a Hamming code of 5 or 7 bits respectively. The B-channel data format is illustrated in Figure 4.5. In order to optimize the timing and reduce the output signal skew, the last stage of registers of the TTC BPM encoder circuit were placed into the FPGA I/O cells.

The ALTI allows synchronous and asynchronous short- and long-format B-channel command/data cycles to be generated in a number of different ways explained in the following sections. The generation of B-channel cycles follows a

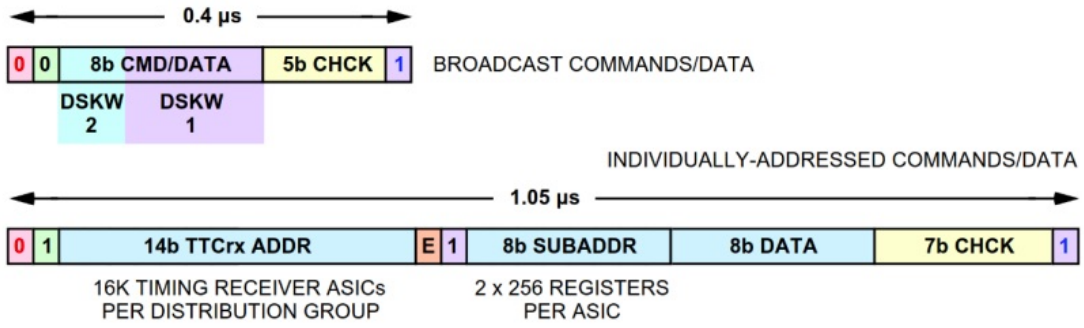


Figure 4.5: TTC B-channel data format.

fixed priority scheme as shown below:

- Synchronous cycles B-Go0 to B-Go3
- Asynchronous B-Go0 to B-Go3
- Trigger type cycle
- Asynchronous cycle triggered by a VME access

Four VME-addressable FIFOs are provided which may be pre-loaded with commands and data to be transmitted by B-channel cycles. For each of the four channels, the actual transmission of the pre-loaded information is initiated by a signal called B-Go which can be generated either by a VME write to a key address or by an external signal received through the front panel. It is also possible to start the cycle transmission as soon as the FIFO is not empty. The FIFO can be filled using VMEbus block transfers to optimize the performance. A register is used to monitor the status of the FIFO's. Sequences of B-channel cycles can be generated by loading the FIFOs with several commands. In addition, a re-transmission mode allows to load the FIFO once and to always transmit the same B-channel cycle(s) by resetting the read pointer of the FIFO as soon as it becomes empty. This can be used for instance to transmit repetitive commands such as the Bunch Counter Reset. A control register allows the selection of synchronous or asynchronous mode of either VME or front panel initiated B-Go cycles for each of the four channels. If synchronous mode is selected, the B-channel cycle is generated at the end of the corresponding internally generated inhibit signal. The cycle can be programmed to be either single or repetitive. In single mode, only one cycle is generated if a B-Go has occurred before Inhibit. In repetitive

mode, the cycle is generated at the end of each Inhibit signal (i.e. once per LHC orbit) and does not require a B-Go to occur. This repetitive mode, for example, sends the bunch counter reset command. If asynchronous mode is selected, the B-channel cycle is only generated once when the B-Go signal becomes active.

After each L1A is transmitted, the contents of the 24-bit event/orbit counter in the ALTI is broadcast together with an 8-bit trigger type parameter, which is usually received from the CTP through the front panel. This broadcast is made asynchronously and takes about 4.4 μs if the B-channel is free. The following sub-addresses of the long B-channel cycle are used:

- **0**: Trigger type
- **1**: Event/Orbit counter bits 23..16
- **2**: Event/Orbit counter bits 15..8
- **3**: Event/Orbit counter bits 7..0

Internally, the event/orbit counter and the trigger type are stored in a FIFO to avoid any data loss due to the random time of arrival of L1A. The status of these FIFOs are available in a register. The TTC address used for this type of transfer can also be configured through a VME register. The trigger type cycle can also be completely disabled. Short- and long-format asynchronous cycles Asynchronous cycles may be initiated by writing the required data to a control register. Both short-format and long-format cycles are supported. Normally short-format cycles are used for broadcast commands or data while long-format cycles are used for individually addressed commands or data. However, a broadcast of 16 bits of data can be made with long-format cycles if the TTCrx address 0 is chosen. The timing of the asynchronous cycles is not aligned with the LHC orbit.

A programmable pattern generator is implemented in the FPGA in order to produce arbitrary sequences of bit patterns at the FPGA outputs, which can then be individually routed to any destination through the external cross-point switches. This is useful especially when the ALTI is used as a master of a TTC partition. The output of the pattern generator is 21-bit wide, i.e. all of the signals on the LVDS-LINK signals can be driven. The pattern is stored in an external 1M×32-bit memory bank. Each memory location contains a 21-bit wide pattern and an 11-bit wide multiplicity count. The multiplicity specifies how many clock cycles the pattern will be repeated. This scheme is an improvement with respect

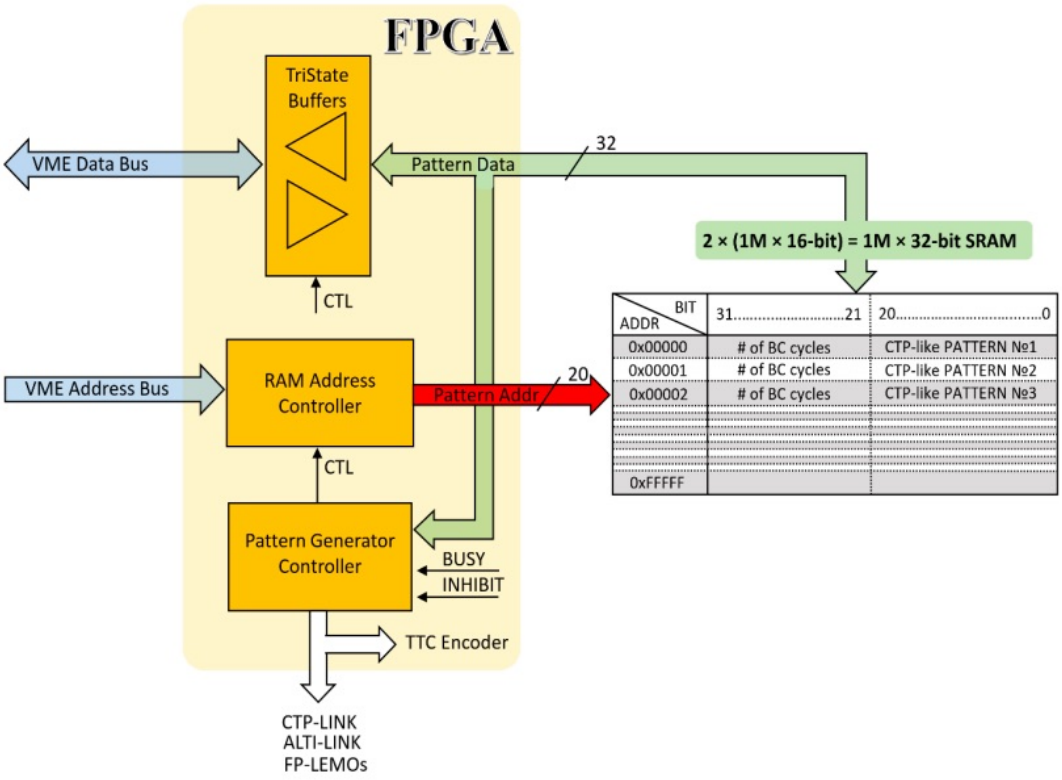


Figure 4.6: Pattern generator block diagram.

to the pattern generator of the LTP and enables very long pattern sequences to be generated. The pattern generator and implementation and the memory organization are illustrated in Figure 4.6. If the ALTI is set to use the snapshot function, this memory is populated in a similar manner with the specified CTP-link input data. The ADN2814 from Analog Devices [109] is used for the clock-data recovery (CDR) which extracts and provides the 160 MHz carrier clock and A/B channels bit-stream to the FPGA for further decryption. Once a command is identified, decoded and reconstructed, the transmission control fields are dropped, while the L1A status, the 8-bit or 32-bit command word, and matching time stamp counter values are stored in the external SRAM memory. The TTC stream analyser is used to decode and store the information receives from an optical TTC data stream. The L1A signal (A-channel) and B-channel commands received are stored together with a timestamp in an external 1M×64-bit SRAM memory. Two 1M×32-bit memory banks mapped into the VME address space of the module are used for this purpose. The first memory bank contains the B-channel broadcast and individually-addressed commands, while the second bank stores the L1A

command, the TTC link status, as well as a 28-bit time stamp which is incremented with the BC. During the data taking operation, both memory banks are written in parallel (1M×64-bit), while, during the VME read/write cycle, each bank (1M×32-bit) is accessed individually by performing Single or Block Data Transfer in random access mode. A simple I2C master controller is implemented in the firmware that can be used to communicate with I2C devices located on the ALTI mother board. The I2C controller registers are programmable via a VME access.

4.3 ALTI software

The TDAQ system provides the software infrastructure for L1 trigger, DAQ and HLT systems. Software packages for L1 trigger and TTC modules are part of ATLAS TDAQ. These packages include the low-level software for control, configuration and monitoring of the modules. High-level run control application software, built on top of the low-level APIs is also included in the ATLAS TDAQ. VME-addressable TTC legacy modules (LTPI, LTP and TTCvi) and the other modules, have a similar low-level software organization. The ALTI module has its low-level software organized in a similar way. The ALTI package depends on several software packages specific to the TDAQ RCD and the L1 Central Trigger (L1CT).

4.3.1 Low-level and high-level software

The low-level software provides programmable support for control, configuration and monitoring of the ALTI module in terms of its registers, memories, and FIFO buffers. The software was developed for the SBC of the ATLAS readout driver crate. The SBC uses a library and a driver to communicate with the ALTI module using VMEbus. As with other modules of the L1CT, a code generator is used to translate the register map description of the ALTI module, provided in an XML file, into all necessary functions and data types accessing all hardware and firmware features. From these, an API was developed in the form of a C++ class, *AltiModule*, which provides all user functions required for control, configuration and monitoring the ALTI. A menu program based on the API provides interactive access of the hardware. A class for the configuration of the ALTI module, *AltiConfiguration*, which can read or write from or to a file containing key and

value pairs, provides complete configuration of the ALTI module. Several test programs are provided for testing and diagnostics of all features of the hardware and the firmware of the ALTI module:

i) *testAltiVME* for reading and writing registers and memories;

ii) *testAltiInitial* for configuring the ALTI module;

iii) *testAltiCapture* for reading the snapshot memory and for comparison with expected patterns;

iv) *testAltiTtc* for reading the TTC decoder memory and for comparison with expected patterns.

The high-level software provides the run control application necessary to integrate the ALTI module into the ATLAS run control system and to allow its operation within the running experiment. The RC application is based on the ATLAS RC scheme and implements the state machine model of the ATLAS RC. It makes use of the low-level software for communication with the actual ALTI hardware.

4.3.2 OKS configuration

This section discusses a description of the OKS schema file used to configure the ALTI DAQ controller. A segment running the ALTI controller has a RCD object in Resources, which contains an AltiBoard. The AltiBoard class inherits from the ReadoutModule, ResourceSet and BusyChannel classes. The Busy tree has to be configured according to its description, where the busy cabling is described in OKS through BusyChannel objects being contained in RCD-plugins (RODBusyModule, RCDLTPModule, etc). With this description, certain RCD-plugins like the RODBusyModule or the RCDLTPModule can now configure their busy mask automatically by checking for each BusyChannel whether the corresponding busy source is enabled or disabled. In particular, the following scheme is used for BusyChannel Id with the ALTI:

- **Id = 0**: busy coming from CTP_OUT
- **Id = 1**: busy coming from ALTI_OUT
- **Id = 2**: busy coming from NIM_IN.

The sub-transition "ALTI_configure_subTransition" is included in the configuration segment. The AltiBoard class has the following attributes:

- **slot**: the first of the 2 slots used by the ALTI in the VME crate
- **IS_server**: name of the IS server where are published the monitoring data. Use Monitoring by default.
- **CTP_cable_length**: length in meters of the cable connected on the CTP link-in port. This is used to configure the equalizer.
- **Alti_cable_length**: length in meters of the cable connected on the ALTI link-in port. This is used to configure the equalizer.
- **CTP_EQZ_enabled**: keep the CTP_IN equalizer ON even after SHUTDOWN (to keep receiving the clock and Orbit signals)
- **ALTI_EQZ_enabled**: keep the ALTI_IN equalizer ON even after SHUTDOWN (to keep receiving the clock and Orbit signals.
- **busy_level**: Busy signal level from the LEMO connector on the FrontPanel: NIM or TTL.
- **do_monitoring**: enable or disable monitoring, enabled by default.
- **cnt_ttyp_lut**: configuration file of the 8 counter available for the monitoring of the trigger types. The default file configures the counters to monitor individually each bit of Physics trigger types, and the calibration request.

Additionally, it has six relationships: TTC_L1A_source, mode, Bchannel_config, transmitters, calibration_requests and AltiTTCdecoder. The TTC_L1A_source contains the signal sources of the L1A in the TTC stream from: L1A, TTR1, TTR2, TTR3. When several signals are included, the L1A in the TTC stream will be an OR of these signals.

ALTI mode configuration

One "mode" should be selected among the five available modes. All modes inherits from the AltiModeConfigBase class. The five modes are:

- **AltiModeCtpSlave**: this is the standard configuration to run with the CTP in a combined run, or in a daisy chain with the inputs coming from the CTP_IN cable. This mode has 1 relationship timing described below.

- **AltiModeAltiSlave**: this is the standard configuration to run as a slave of another ALTI with the inputs coming from the ALTI_IN cable. This mode has 1 relationship timing described below.
- **AltiModeLemoSlave**: this is the standard configuration to run as a slave of another ALTI with the inputs coming from the LEMO cables. This mode has 1 relationship timing described below.
- **AltiModeMaster**: this is the standard configuration to run as a trigger master in a standalone partition. This mode has five attributes:
  - **input_clock**: select the internal clock or an external clock
  - **input_orbit**: input ORBIT selection: PG, CTP_IN, NIM_IN. Note: an internal ORBIT signal is generated if input_orbit = PG and if the ORBIT signal is masked in the Pattern Generator (or if the Pattern Generator is disabled, for instance when the partition is shutdown)
  - **input_l1a**: select the L1A from the pattern generator or an external NIM input
  - **input_ttr1/2/3**: select the test triggers 1/2/3 from the pattern generator or an external NIM input
 and 3 relationships described below. Note that the corresponding ALTI RCD and AltiBoard are used as Controller and TriggerModule, respectively, of the partition's MasterTrigger.
  - **AltiModeAltiExpert**: the configuration is done with a configuration file provided as input. This mode is useful to recover a previous configuration saved in a file

AltiTiming relationship

A relationship named timing is needed for all configuration modes to configure the timing of the input/output signals. It has the following attributes:

- **input_clock_phase_sync**: input signals clock phase synchronisation: 0, 90, 180, 270 degrees, or disabled. The synchronisation has to be configured separately for signals coming from the FPGA or the CTP_IN, ALTI_IN and LEMO_IN cables. The timing should be defined once using the menu program as described below in section

- **input_shaping**: the shaping is used to set the length of input signals to 1 BC for NIM inputs that are not directly clocked by the BC or have a timewalk
- **clock_phase**: PLL output clock phase by step of +/- 15 ps
- **JitterCleaner_filename***:
  - **if empty**: JitterCleaner is not re-configured and current configuration is kept. This is to avoid short loss of clock during CONFIGURE
  - **if "DEFAULT"**: JitterCleaner is configured with the default configuration. A short loss of clock during CONFIGURE is expected
  - **if "file_name"**: the JitterCleaner is configured with this configuration file. A short loss of clock during CONFIGURE is expected

AltiMasterTriggerConfig relationship

A relationship named master_trigger_config is needed in AltiModeMaster for the configuration of the trigger master. It has the following attributes:

- **ECR_periodic**: generate periodic ECR. If set to false, the following ECR attributes are not used and the ECR can be generated from B-Go-1 in pattern generator.
- **ECR_period**: period of the ECR signal in microseconds (minimum 1 orbit).
- **ECR_length**: length of ECR/B-Go-1 signal in units of BCs.
- **ECR_pre_deadtime**: internal deadtime before each ECR in microseconds.
- **ECR_post_deadtime**: internal deadtime after each ECR in microseconds.
- **LB_period**: period between two lumiblocks in seconds.
- **LB_minimum_distance**: minimum distance between two lumiblocks in seconds.
- **TTC2LAN_activate**: activate TTC2LAN when the ALTI is the trigger master of the partition
- **TTC2LAN_poll_frequency**: approximate polling frequency for L1ID polls: 10 Hz, 100 Hz or 1 kHz.

AltiPatternGeneratorConfig relationship

A relationship named pattern_generator_config can be added in AltiModeMaster for the configuration of the pattern generator. It has the following attributes:

- **repeat**: set to true to continuously repeat the pattern generation
- **start_address**: first line of memory to consider for the pattern generation
- **stop_address**: last line of the memory to consider for the pattern generation
- **pattern_filename**: input file for the pattern generator
- **start_pattern_transition**: FSM trsansition during which the pattern generator starts: Configure, Connect or PrepareForRun
- **keep_running**: keep the pattern generator running after SHUTDOWN

In addition, any signal (ORB, L1A, TTR1, TTR2, TTR3, TTYP, B-Go0, B-Go1, B-Go2, B-Go3, BUSY) from the pattern generator can be masked using the relationship signals_masked. If the ORBIT signal source is the FPGA (.i.e PG in Master Mode), and if the ORBIT signal is masked in the Pattern Generator or if the Pattern Generator is disabled, an internal ORBIT signal of 40 BCIDs is generated every 3564 BCIDs.

B-channel configuration

The TTC B-channel is used to transmit formatted commands and data cycles to the electronics. These can be either short-format (16 bits), or long-format (42 bits) for individually addressed commands as shown on Figure 4.5. Error correction coding is implemented by adding a Hamming code of 5 or 7 bits respectively. Short-format broadcast commands can be sent at controllable times relative to the LHC orbit, such as the BCR. The relationship Bchannel_config of the AltiBoard should contain 1 object of the class AltiBChannelConfig. This class has the following attributes:

- **trigger_type_enabled**: trigger type cycle enabled or disabled
- **trigger_type_frame_type**: trigger type frame type: Short or Long
- **trigger_type_address_space**: trigger type address space: Internal or External

- **trigger_type_delay**: trigger type delay in BC (should be 2 BC when running with the CTP)
- **trigger_type_address**: trigger type address (14-bit)
- **trigger_type_subaddress**: trigger type subaddress (6-bit)
- **B-Go2_output**: B-Go2 NIM output: B-Go0 or B-Go2
- **B-Go3_output**: B-Go3 NIM output: B-Go1 or B-Go3

In addition, 3 types of asynchronous cycles can be configured to be sent at different states of the FSM:

- **cycles_for_configure**: ordered list of asynchronous cycles (long or short) to be executed during configure
- **cycles_for_connect**: ordered list of asynchronous cycles (long or short) to be executed during connect
- **cycles_for_prepareForRun**: ordered list of asynchronous cycles (long or short) to be executed during prepareForRun

These cycles can contain several cycles or a container of cycle from the class AltiCycleContainer. The cycles can be either short (class AltiCycleShort) or long (AltiCycleLong). The B-Go channels can be configured via the relationship BGo_channels from the class AltiBGoChannelBase. Two B-Go channels are pre-defined: AltiBGoBCR with B-Go-0 and AltiBGoECR with B-Go-1. The attribute delay of AltiBGoBCR is used to adjust the coarse timing. The Generic B-Go channels, topically defined with the channels 2 and 3 can be configured with the class AltiBGoChannel which has the following attributes and relationship:

- **number**: B-Go channel number
- **source**: B-Go signal input: NIM, CTP, ALTI, PG
- **mode**: generation of the B-channel cycle:
- **synchronous_single_bgo_signal**: only one cycle is generated if a B-Go signal has occurred before Inhibit
- **synchronous_repetitive**: the cycle is generated once per orbit at the end of Inhibit, and doesn't require a B-Go signal to occur
- **asynchronous_bgo_signal**: the cycle is generated each time a B-Go signal occurs

- **asynchonous_vme_on_trigger**: the cycle is generated by VME write to a key address
- **asynchronous_vme_when_not_empty**: the cycle is generated as soon as the FIFO is not empty
- **retransmit**: retransmit data or stop after B-Go FIFO becomes empty
- **inhibit_delay**: delay of B-Go Inhibit signal in BCs
- **inhibit_width**: width of B-Go Inhibit signal in BCs
- **busy_gate**: Gate B-Go command when busy
- **cycles**: relationship containing the list of cycles (long or short) for the B-Go FIFO

Transmitters configuration

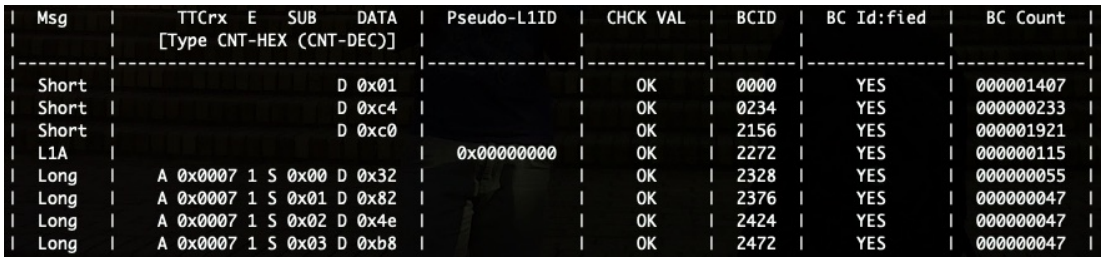
By default, all transmitters are disabled. Transmitters can be enabled individually by adding AltiTransmitter objects via the relationship transmitters. This class has the following attributes:

- **name**: name of the transmitter
- **slot**: slot of the transmitter
- **delay**: delay, in steps of 3.12 ns, applied to the transmitter
- **enabled**: transmitter enabled or disabled
- **keep_enabled**: keep the transmitter enabled after SHUTDOWN (to always send the clock)

Calibration requests configuration

Up to three calibration requests can be configured in the OKS via the calibration_requests relationship. The class CalibrationRequest has the following attributes:

- **bit**: bit number: 0, 1 or 2
- **input**: calibration request input used in local path: RJ45, FRONT_PANEL, CTP, ALTI, PG, VME
- **source**: calibration request source is directly from CTP_OUT, ALTI_OUT, or from the local path



Msg	TTCrx E SUB DATA [Type CNT-HEX (CNT-DEC)]	Pseudo-L1ID	CHCK VAL	BCID	BC Id:fied	BC Count
Short	D 0x01		OK	0000	YES	000001407
Short	D 0xc4		OK	0234	YES	000000233
Short	D 0xc0		OK	2156	YES	000001921
L1A		0x00000000	OK	2272	YES	000000115
Long	A 0x0007 1 S 0x00 D 0x32		OK	2328	YES	000000055
Long	A 0x0007 1 S 0x01 D 0x82		OK	2376	YES	000000047
Long	A 0x0007 1 S 0x02 D 0x4e		OK	2424	YES	000000047
Long	A 0x0007 1 S 0x03 D 0xb8		OK	2472	YES	000000047

Figure 4.7: TTC decoder

Configuration of the TTC stream analyser

The ALTI board features a TTC stream analyser which can record and decode the TTC data received from an optical link. To use it, an optical fibre should be installed between any optical transmitter and the receiver connector (last optical connect at the bottom). The TTC analyser can be enabled in the AltiController by adding a relationship AltiTTCdecoder to the AltiBoard object. It is enabled in the Configure_transition, therefore all TCC commands sent during the Configure, Connect and PrepareForRun are recorded. In addition, the TTC monitoring can be automatically stopped upon IS callback, according to the OKS configuration. The AltiTTCdecoder class contains the following parameters:

- **enabled**: enable the TTC decoder at the start of the run (during the Configure_transition)
- **IS_stop_enabled**: stop the TTC decoder when the given IS variable has the expected value
- **IS_partition**: name of the partition where lives the IS attribute used to stop the decoder
- **IS_name**: server.name of the IS publication used to stop the decoder
- **IS_index**: index of the IS attribute in the IS class used to stop the decoder (as defined in IS_name)
- **IS_value**: value of the IS attribute which stops the decoder

The TTC stream can be read from the HW using the menuAltiModule program on the SBC. Choose 10 [“DEC” menu] TTC decoder. You should always disable the decoder in order to read the memory. The TTC decoder will display the short and long commands (such as the BCR with data = 0x1), the L1A and trigger type cycle if it is enable. Their BCID is also shown, it needs to receive the first BCR



(a) (b)

Figure 4.8: B175 test bench (a). On top is the ROD crate with one ROD module, a TBM and a SBC. At the bottom is the TTC crate (b).

to start counting the BCIDs, as indicated in the "BC Id:fied" field. If a different data word is used for the BCR, it should be set to 3 in the BCR scheme. The output is shown in Figure 4.7.

4.4 The TileCal test bench setup

The TileCal test bench (seen in Figure 4.8) was setup by the author and the technical supervisor at the CERN Meyrin site. The expertise gained from the test bench would later be utilized in integrating the ALTI modules and software in the ATLAS detector and upgrading the Local TTC system for Phase-II test beam campaigns. The test bench consists of one TTC partition. The ROD crate has one ROD module that receives data from one drawer in B175. The ROD trasmits the data to the ROS through the ROLs. The TCC crate includes one SBC, RodBusyModule, ALTI, SHAFT, CAEN Dual timer and a legacy set (LTP, TTCvi and TTCex). The ALTI is setup in master mode and the legacy set in slave mode. The slave setup is used for laser runs and is connected to the LASCAR (LASer Calibration Rod) setup in the laser lab.

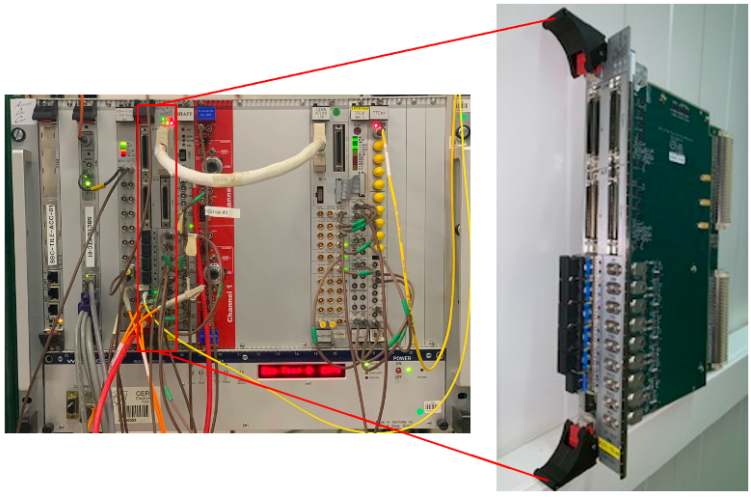


Figure 4.9: The ALTI module inserted in the TTC crate of a test-bench at CERN.

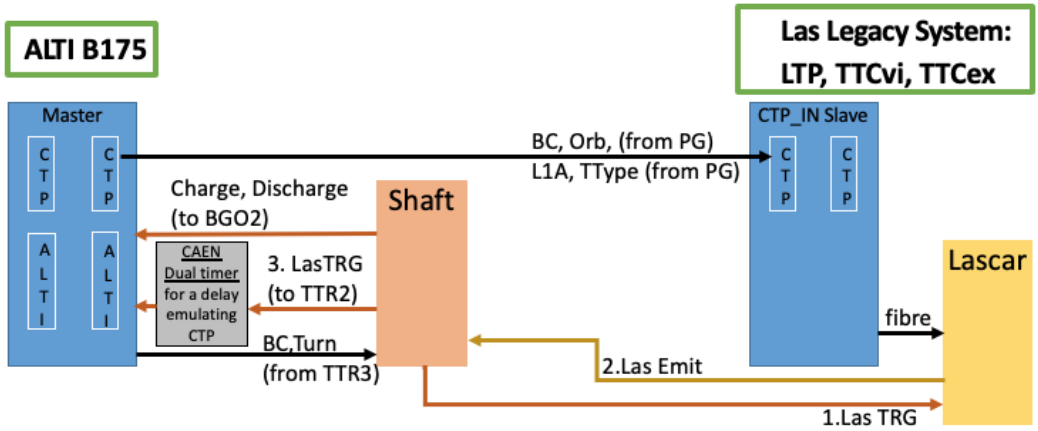


Figure 4.10: The schematic diagram of the ALTI configuration for B175 standalone runs.

The ALTI module is installed in slot 6 of the TTC crate as shown in Figure 4.9 and the latest firmware is loaded, as seen in Figure 4.11. The proper configuration and the loaded firmware is verified with the *testAltiInitial* command. The ALTI schema file is loaded in the OKS database and new ALTI objects are created within the ALTI classes (see Figure 4.12). The setup scripts are updated to source the latest L1CT patches. Changes are made to objects of different classes in the OKS database. In RODBusyModule@TileB175_RODBusy, the ID is updated from 1 to 2. In RCD@TileB175_TTCRCD, the LTP object is replaced with the ALTI object TileB175_ALTI2@AltiBoard2. A switch is made from the TTCvi to ALTI for the TTC attribute in TileB175_DigiTTCModule@TileDigiTTCModule.

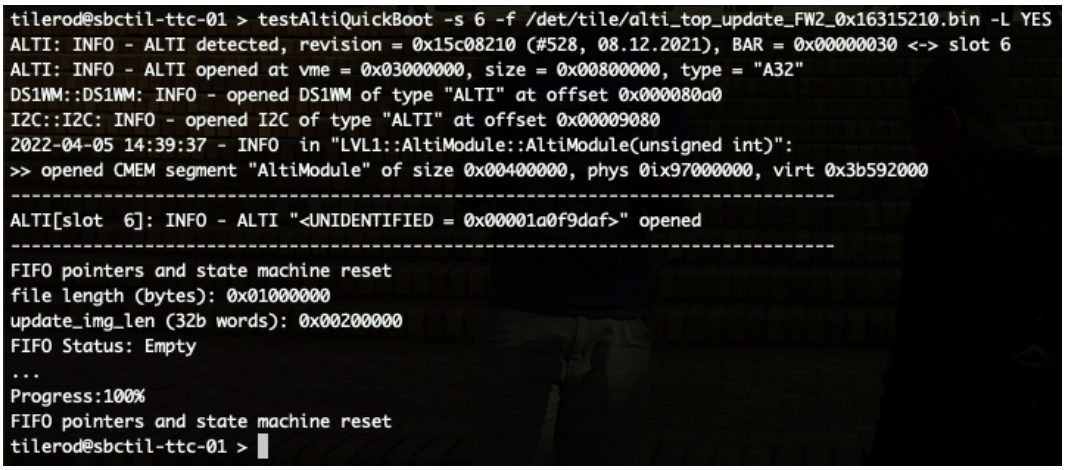


Figure 4.11: A screenshot of the execution of the *testAltiQuickBoot* command to load the firmware. The ALTI module is detected in slot 6 and the latest firmware is loaded.

Within the same object of the same class, the position attribute is also updated to 6, which is the slot number of the ALTI module in the TTC VME crate. The MasterTrigger object is updated from LTP class to use the AltiBoard2 class. The subtransitions are updated to add the ALTI_CONFIGURATION object. Signal delays and pipelines are adjusted accordingly, in order to place the pulse shape of the samples within the readout window. Figure 4.10 shows the configuration of the ALTI board for the standalone runs at the test bench area. A TileCal specific pattern generator implemented for the ALTI module in the test bench area (see Figure 4.13), generates test trigger signals every 3564 BCs as follows:

- Orbit signal asserted for 40 BC (1 micro-second)
- No activity for 2282 BCs
- A single L1A, with trigger type 0x32
- Trigger-type 0x32 asserted for 54 BCs (corresponding to the default simple deadtime)
- No activity for 850 BCs
- Trigger-type 0x34 asserted for 337 BCs

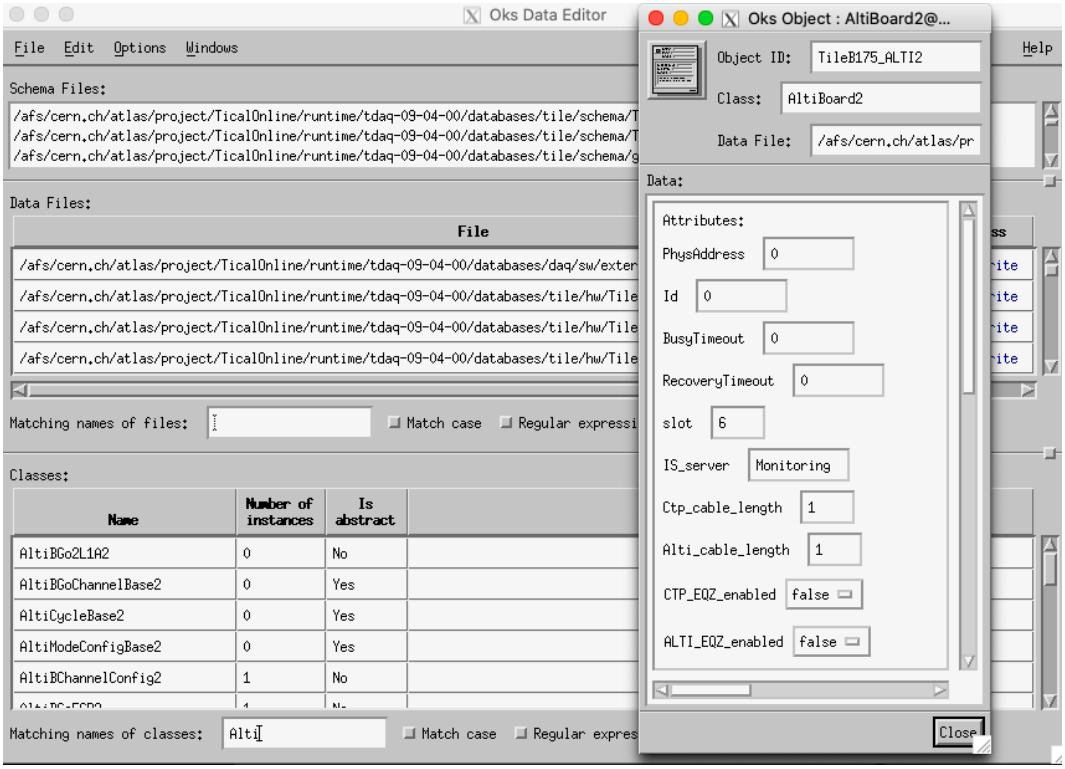


Figure 4.12: OKS Data Editor showing the ALTI classes and the TileB175_ALTI2 object.

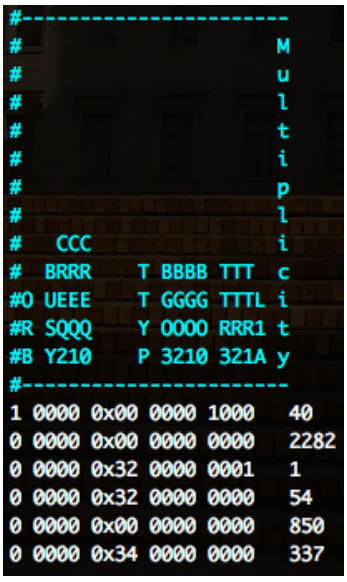


Figure 4.13: Pattern generator for the B175 test bench.

A brief description of the low-level software used for the ALTI operation in

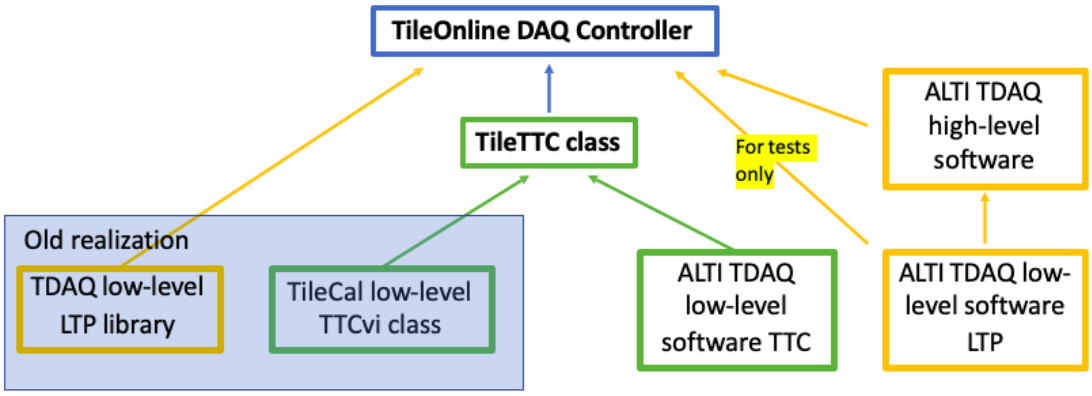


Figure 4.14: TileTTC class provides an interface between the TTCvi and the ALTI class.

TileCal is given in 4.4.1 and Section 4.5 describes the integration of ALTI modules in P1.

4.4.1 TileCal low-level software

The TileCal low-level software has been modified in order to integrate the ALTI functionalities. As discussed in Chapter 3, the TileCal online software consists of 29 packages in total. Six software packages (see Figure 3.5) have been modified and the TileTTC class has been developed, to provide access to the TTCvi and the ALTI low-level software as seen in Figure 4.14. The OKS database has been modified to include new variables for the TileTTC class. C++ is the main programming language with GitLab used as the source code repository. The software was tested and validated using the B175 test bench.

4.4.2 Eventviewer

The eventviewer has been used to view the data from the ROD and mostly checking if the samples appear within the read-out window during pipeline adjustments. Additional command line tools have been used to quickly scan through the samples. In Figure 4.15, the eventviewer shows 7 samples which form a pulse shape in the read-out window. The pulse formed by these samples is shifted around by adjusting the pipelines until it is centered in the read-out window. The pipeline adjustments are done for CIS, laser and physics run types.

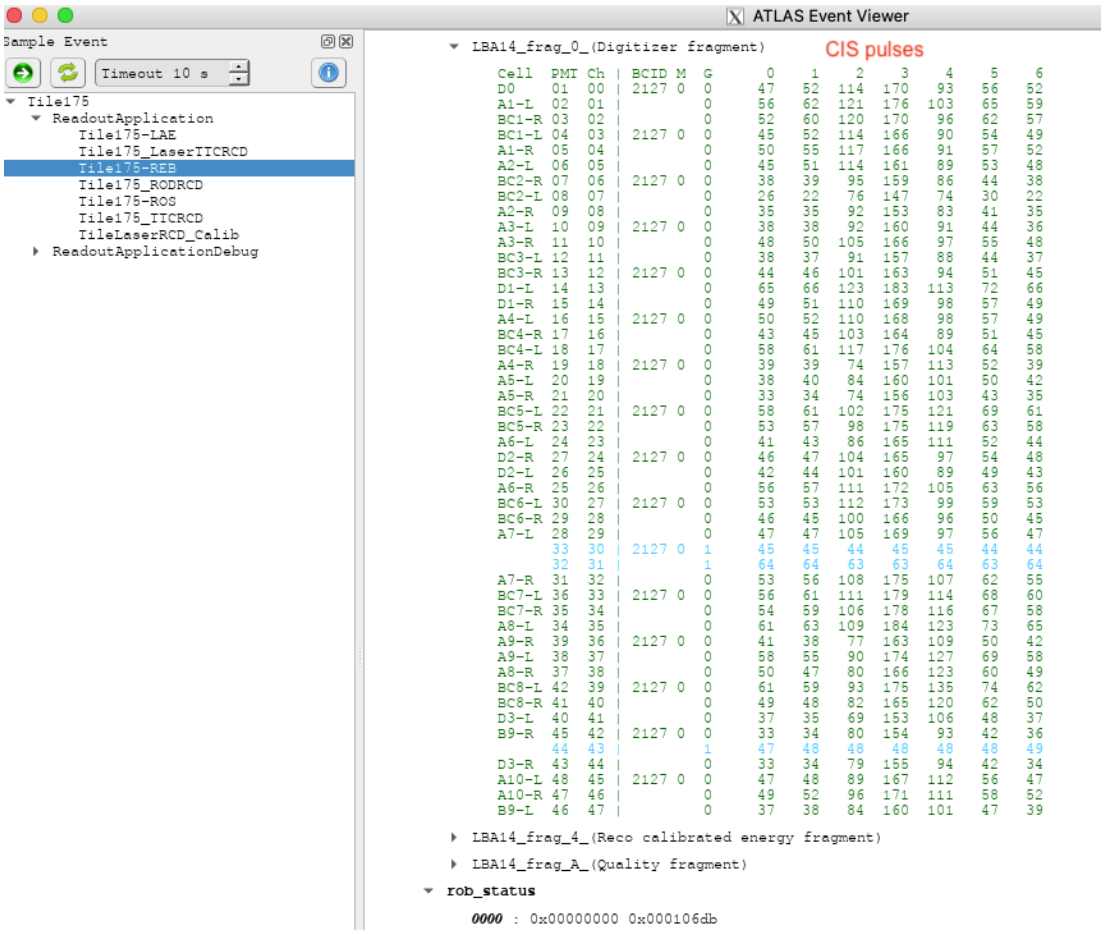


Figure 4.15: The Tile175 eventviewer showing CIS run results. Results show 7 samples that form a Gaussian distribution. In the absence of a pulse, only the pedestal is shown.

4.5 Integration of the ALTI module in the TileCal system

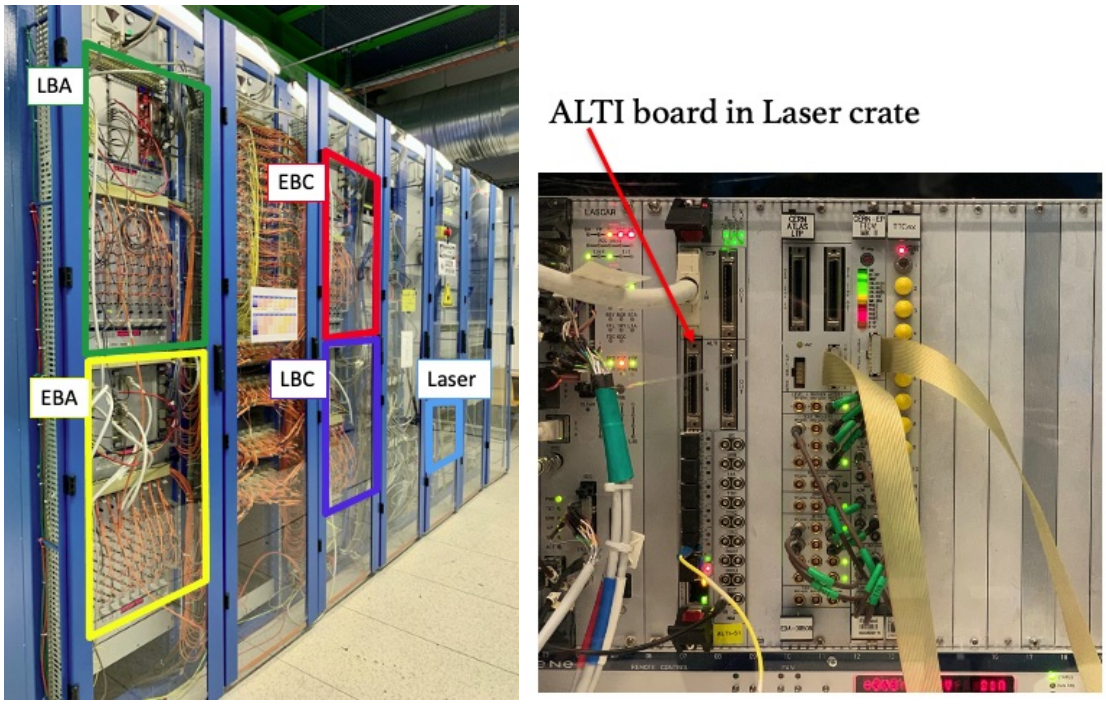
This section details the installation of the ALTI modules and tests conducted to validate the TileCal TTC system. Calibration systems and DVS are discussed. Lastly the results from Run 3 pilot beam, in preparation for Run 3 data-taking period, are discussed.



Figure 4.16: ALTI modules with new optical fibres, ready to be installed in the TTC crates of the BE electronics.

4.5.1 Installation of ALTI modules

Five ALTI modules shown in Figure 4.16 were prepared for the installation in the BE electronics counting room in ATLAS USA15 cavern shown in Figure 4.17 and Appendix A.1. Additional material include forty 0.5 m Lucent Connector (LC) to Straight Tip (ST) patch fibres with forty ST-ST connectors, five TTC loop fibres for the TTC decoder and four calibration request cables. All the LTP, TTCvi and the TTCex modules in EBA, LBA, LBC and EBC TTC crates and the laser crate were removed and replaced with the five ALTI modules. The ALTI modules are configured to use two different configurations for physics and calibration runs. Figure 4.19 shows the configuration of the ALTI modules for the standalone runs and Figure 4.20 shows the configuration of the ALTI modules for physics runs. During physics runs, all the ALTI modules are configured to be in slave mode and receive the CTP input. During the calibration runs, the LBA ALTI module is configured as the master and it generates the signals through the pattern generator (shown in Figure 4.18) and propagates them to the other TTC crates. EBA ALTI module is configured as the slave to the LBA ALTI module. All the other ALTI modules in LBC, EBC and the laser crate are configured as slaves to receive the CTP input. The P1 OKS database has been extensively modified to include new configuration objects.



(a) (b)

Figure 4.17: The TileCal TTC crates are located above the read-out driver crates in the BE electronics (a). ALTI modules were installed in the TTC crates of LBA, LBC, EBA, EBC and the Laser crate (b).

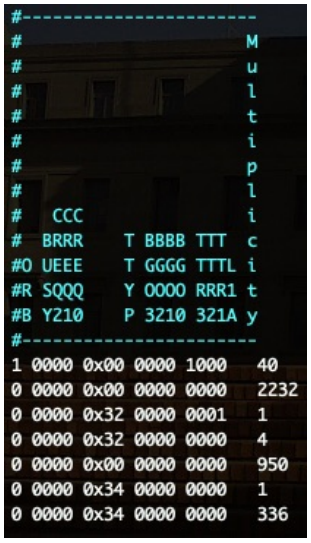


Figure 4.18: Pattern generator

Figure 4.18 shows a pattern generator. A single pattern generator is used for

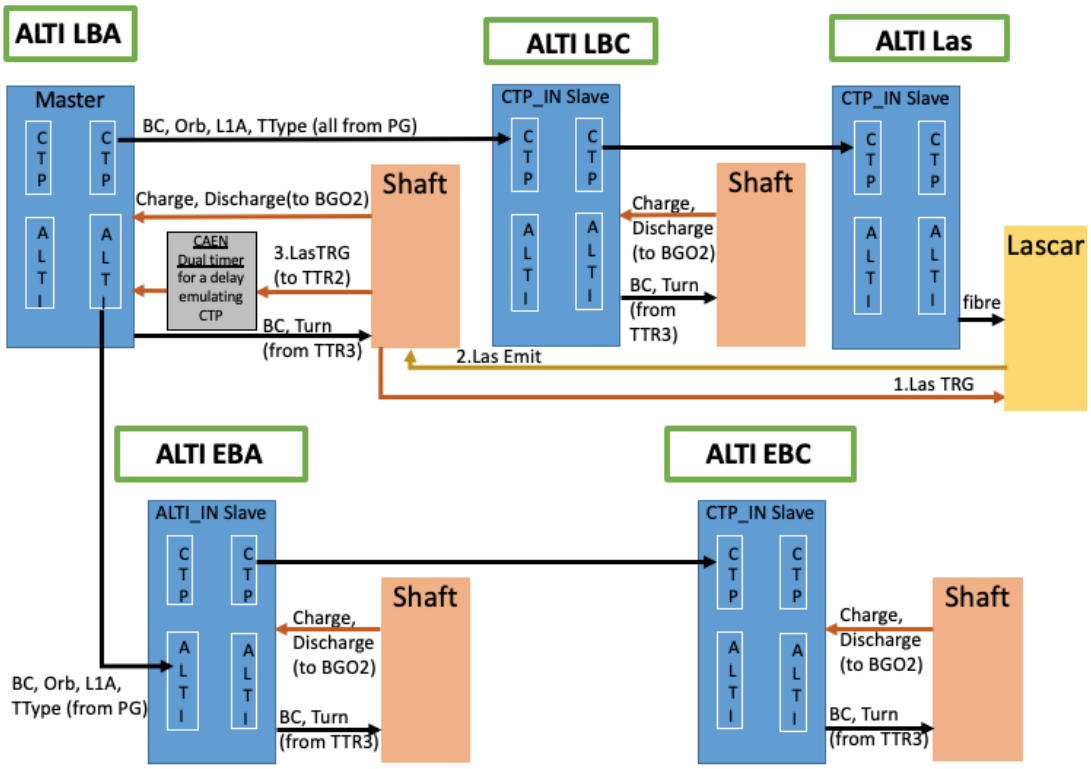


Figure 4.19: The schematic diagram of the ALTI configuration for P1 standalone runs.

all run types. It defines 1 full turn (3564 BC long) intended to be used in a repeating pattern as follows:

- Orbit signal asserted for 40 BCs (1 micro-second)
- No activity for 2232 BCs
- A single L1A, with trigger type 0x32
- Trigger-type 0x32 asserted for 4 BCs (corresponding to the default simple deadtime)
- No activity for 950 BCs
- Trigger-type 0x34 asserted for 1 BC
- Trigger-type 0x34 asserted for 336 BCs

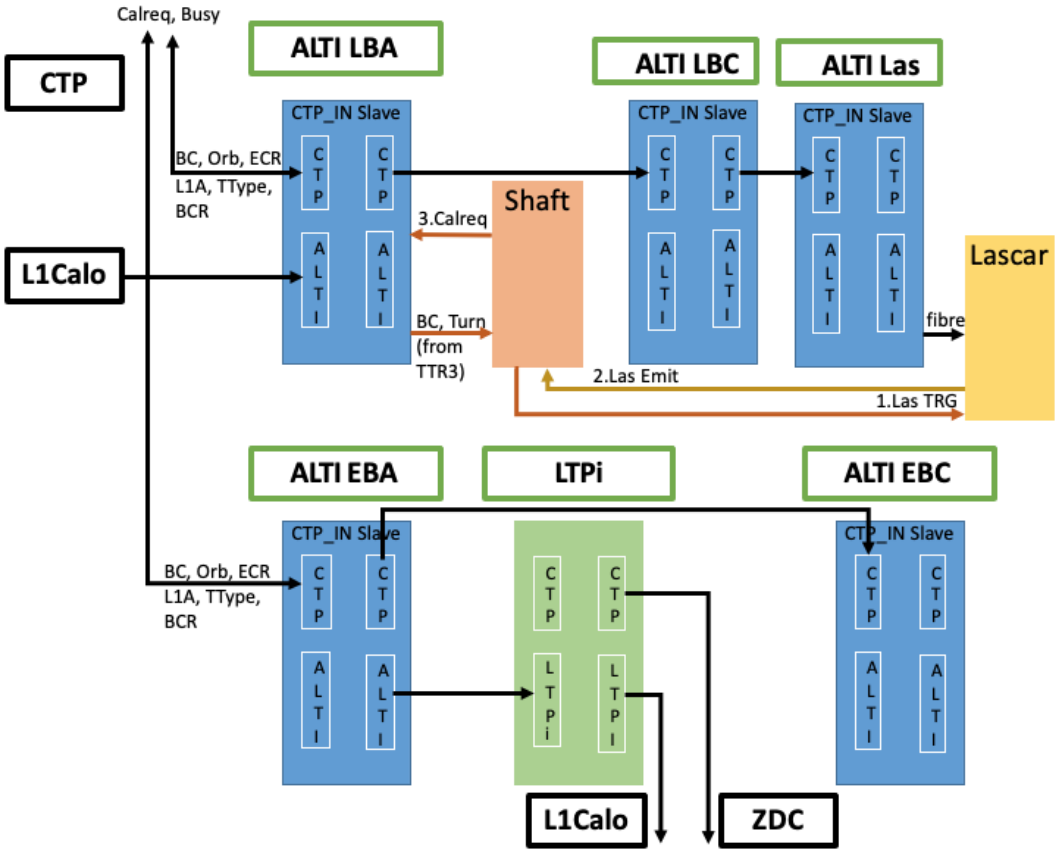


Figure 4.20: The schematic diagram of the ALTI configuration for P1 physics runs.

4.5.2 Calibrations and DVS results

The implementation of the new TileCal ALTI software involved the upgrade of the calibration systems and the DVS packages. These systems have been extensively validated in relation to the legacy TTC system.

Calibrations

The calibration runs are taken during the LHC inter-fill periods. These calibration systems require a special handling of their calibration signal requests, which has been adapted for the ALTI system. The following plots are results from the calibration runs after the installation of the ALTI modules. A few selected plots are discussed.

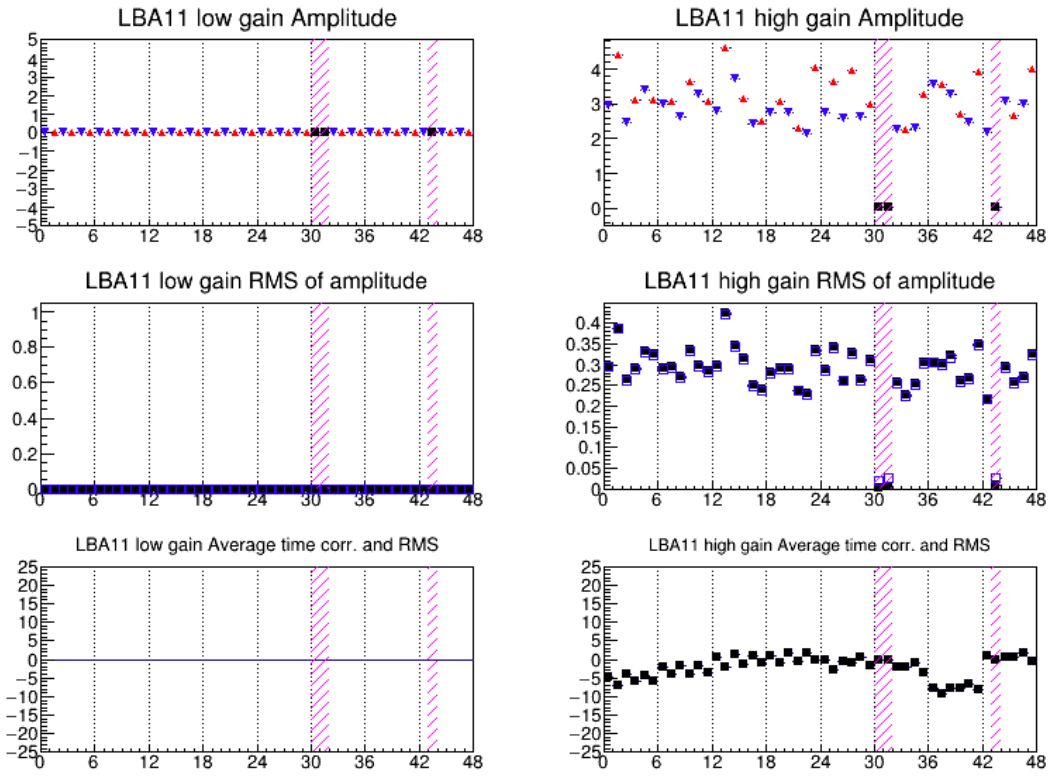


Figure 4.21: Laser calibration test results in TileCal.

The Laser calibrations Figure 4.21 shows the results of a drawer with good laser response in all channels (see the HG amplitude plot). The run verifies the correct response of the PMTs. There are no gain switching problems and the Digitizers have acceptable timing within the threshold and no data integrity problems are detected.

The Charge Injection Scan calibrations Figure 4.22 shows the Amplitude/Q ratio plots in for the CIS run. The plots show the result of the fit of the amplitude calculated by the Amplitude Fit method divided by the charge injected by the 3in1 card. Corresponding CIS constants are applied, therefore the result for a good channel should be close to 1.

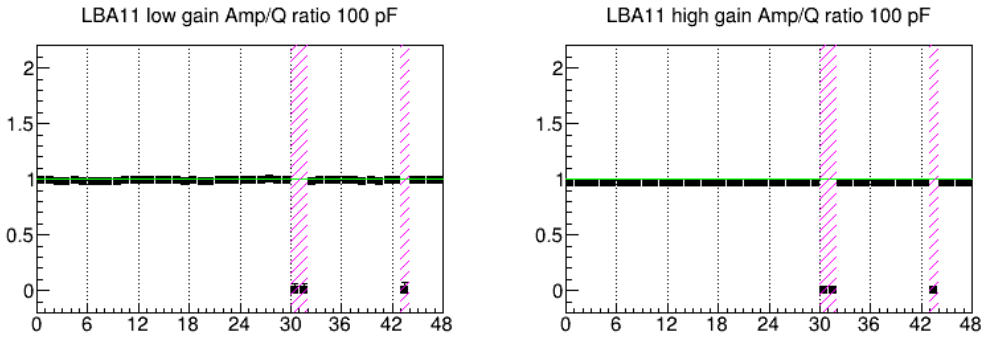


Figure 4.22: CIS calibration results showing the Amp/Q plots.

Figure 4.23 shows the time against CIS phase plots. The plots show the result of the fit of the time obtained by the Fit method against the known CIS phase. The plots displayed are for each gain and a 100 pF capacitor. The first set of plots shows the time slope (for a good channel it should be close to 1). The second set shows the time offset (all channels should have roughly the same offset, typically close to -25 ns). Channels with no CIS response typically have a slope equal to zero.

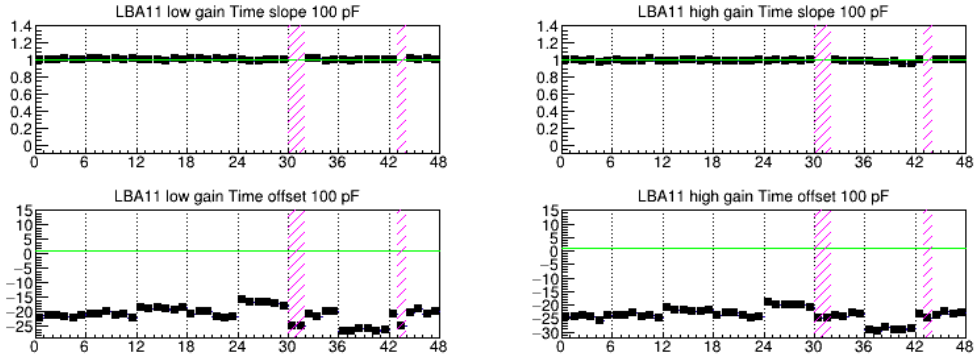


Figure 4.23: CIS calibration results showing the time plots.

Correlations in Pedestal run Figure 4.24 shows the digital noise. The pedestal plots show the average value, in ADC counts, of the first time-sample for each channel. The red lines indicate the allowed limits. Plots in the first row show the low-frequency noise, which is the RMS of the pedestal distribution and it monitors how the pedestal changes with the low-frequency sampling. Plots in the second row show the high-frequency noise, represented by the mean value of the distribution of the RMS of the samples of each event and, hence, it monitors how the pedestal changes with the high-frequency sampling (40 MHz).

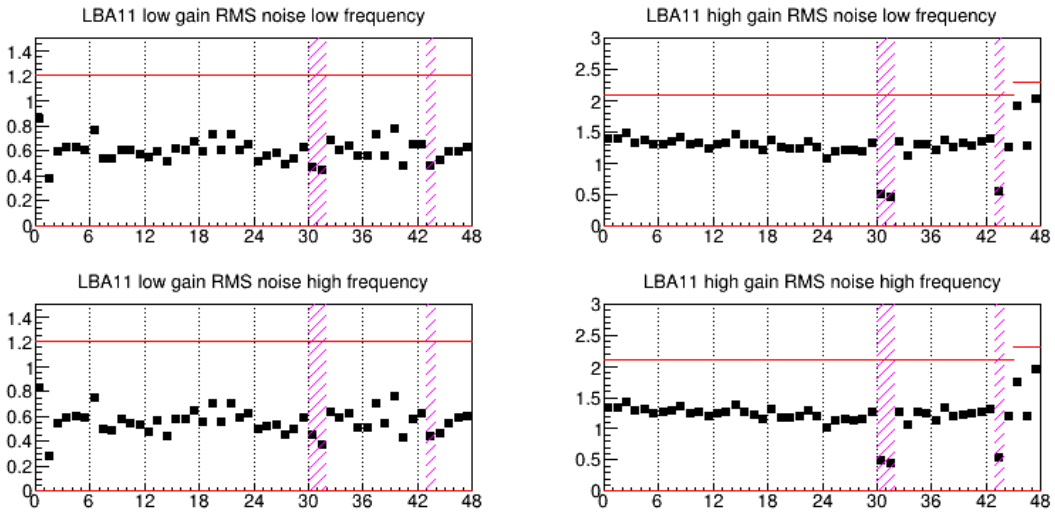


Figure 4.24: Pedestal calibration test results in TileCal.

The 2D plots in Figure 4.25 show the correlation of the amplitudes among the 48 channels of the same motherboard. Higher correlations appear due to a source of coherent noise in the module.

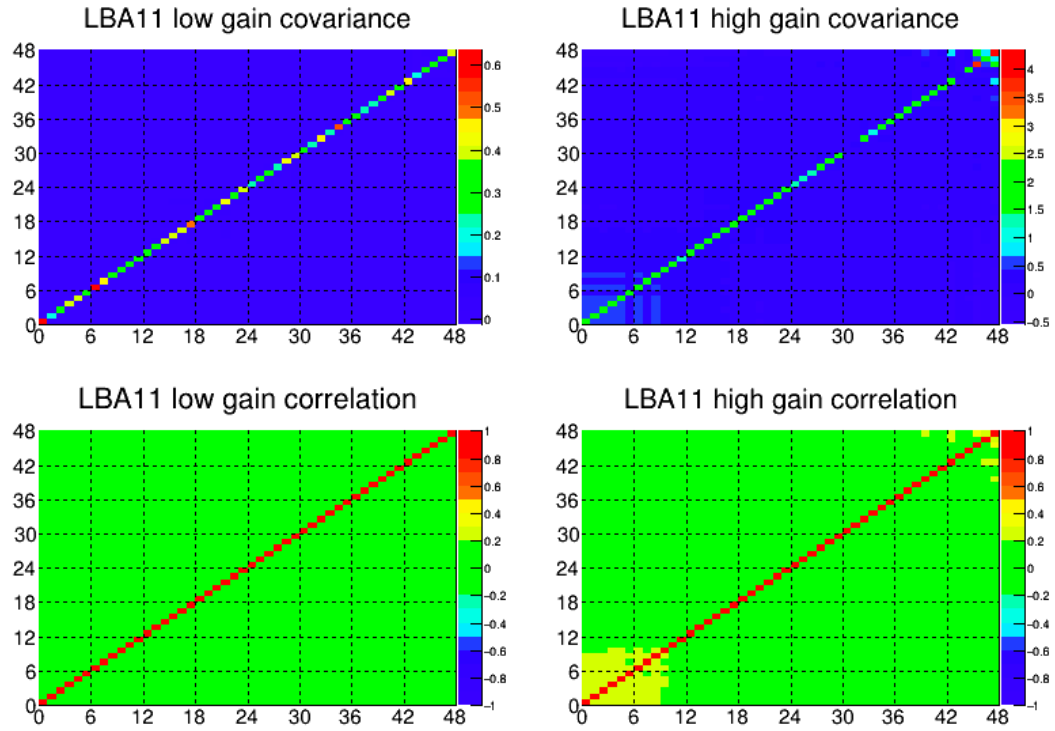
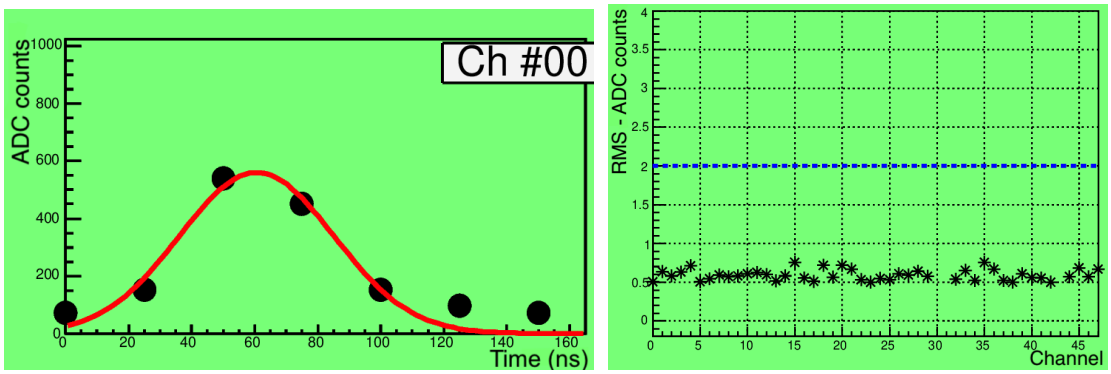


Figure 4.25: Pedestal calibration test results in TileCal.

DVS results



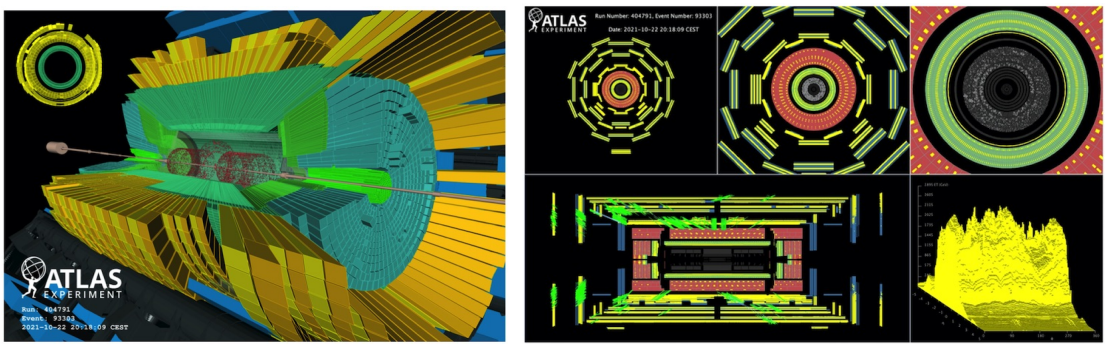
(a) (b)

Figure 4.26: The CIS DVS test taken for one read-out module in good working condition, shows a good reconstructed pulse of the ADC counts against time, for seven samples per channel (a). The pedestal DVS test shows the RMS ADC counts against the channel number and the electronics noise level is below the threshold for all read-out channels (b).

The DVS software package has been modified for the TileCal ALTI system. Figure 4.26 shows part of the DVS test results taken with the ALTI system. The results are for the CIS and pedestal runs. CIS shows the existence of the pulse reconstructed with the seven samples in Figure 4.26(a). Figure 4.26(b) shows the output of the pedestal DVS test, where the noise for a given channel is the standard deviation of the signal in pedestal events. For a given channel, the signal in a pedestal event is sampled seven times and the standard deviation of the samples is averaged over all events and termed "high frequency noise". Likewise, for a given channel, the value of the first of the seven samples is recorded for all pedestal events and the standard deviation of this distribution is called the "low frequency noise".

4.5.3 Pilot Run results with the ALTI system

To test the TileCal ALTI system during the Run 3 pilot beam, the TileCal subsystem was included in the ATLAS combined run. The pilot beam took place between 18-31 October 2021, with 3 to 4 days of collisions including stable beams. The ATLAS detector successfully recorded 25–30 beam splashes from each beam on the 22nd of October 2021. A view of a few event displays from the run is

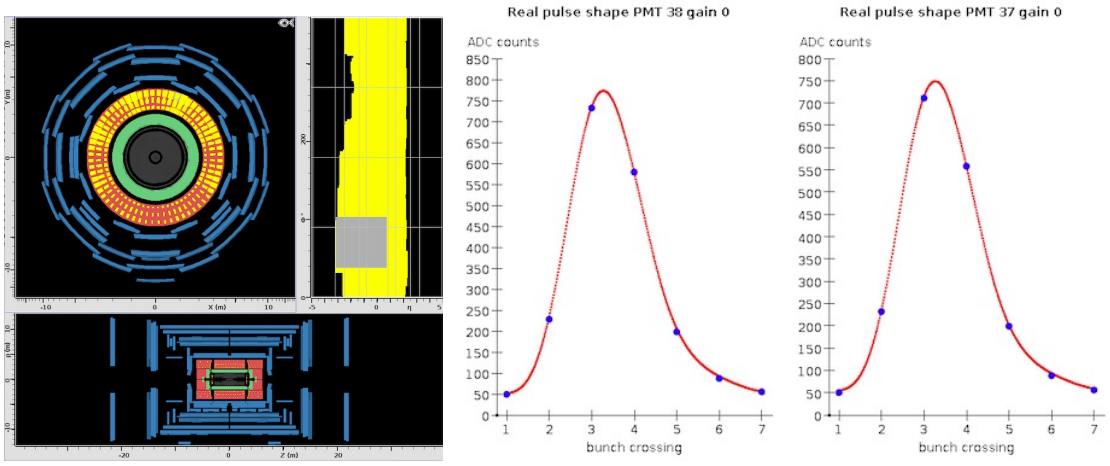


(a) (b)

Figure 4.27: a view of a few event displays from the pilot run is shown on VP1 (a) and the ATLANTIS display (b).

shown in Figure 4.27. Figure 4.27(a) shows the Virtual Point 1 (VP1),[1] event display [110, 111]. VP1 shows all ATLAS data in a 3D environment, letting users interact with the display, select data collections, apply cuts on quantities, set cut-out views of detector parts and visualize all sort of data about the event and the physics objects. Figure 4.27(b) shows an Atlantis,[2] event display image with different views and projections of the events combined and the simplified geometry overlay. Atlantis [111] is a Java stand-alone application aimed at visualizing physics objects (like jets, particles and energy deposits) for physics analysis. As input data, it uses a custom intermediate XML format, generated from the ATLAS data. It shows a simplified geometry of the ATLAS detector, in two dimensions. The event display image of a splash event (Run 418554, Event 187483) shown in Figure 4.28(a) was recorded in ATLAS on 22 April 2022. Figure 4.28(b) shows the pulse shape of seven samples for EBC13 D6 Tile cell, displaying the bunch crossing against the ADC counts for two PMTs.

[1] An interactive 3D event display for the ATLAS experiment at CERN
[2] Atlantis is an event display tailored for the visual investigation of complete ATLAS events



(a) (b)

Figure 4.28: a view of the Atlantis display (a) and pulse shape for EBC13 D6 Tile cell PMTs (b).

4.5.4 Run 3 data-taking results

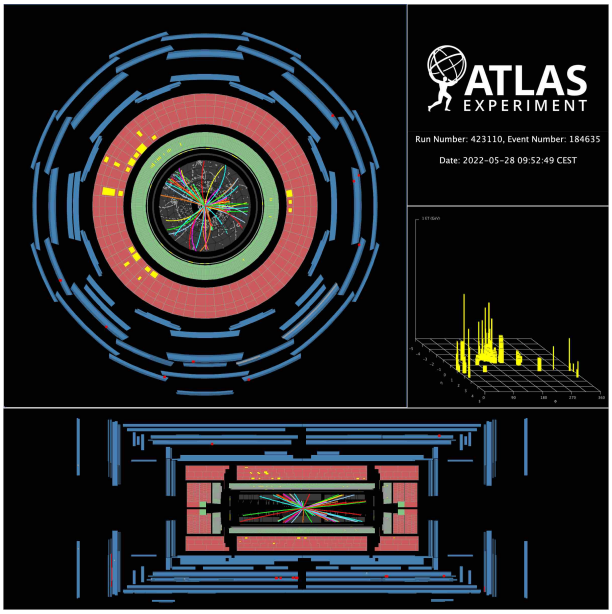


Figure 4.29: Event display of a collision event displayed by Atlantis.

The event display of a collision event (Run 423110, Event 184635) shown in figure 4.29 was recorded in ATLAS on 28 May 2022, when stable beams of protons at the injection energy of 450 GeV per beam were delivered to ATLAS by the LHC.

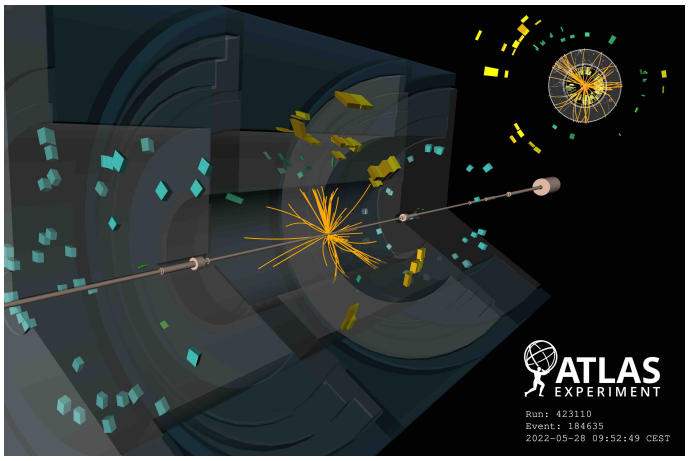


Figure 4.30: Event display of a collision event displayed by VP1.

The figure on the left shows an axial view of the ATLAS detector. The figure on the right shows the energy deposits in the cells of the ATLAS calorimeter. The figure at the bottom shows a side view of the ATLAS detector. Starting from the center of the ATLAS detector, the hits and reconstructed tracks of the charged particles in the Inner Detector are shown as dots and colored lines, respectively. The energy deposits in the electromagnetic (the green layer) and hadronic (the red layer) calorimeters are shown as yellow boxes. The hits in the Muon Spectrometer (the outer blue layer) are shown as red and gray blocks.

Event display image of a collision event (Run 423110, Event 184635) shown in figure 4.30 was recorded in ATLAS on 28 May 2022, when stable beams of protons at the injection energy of 450 GeV per beam were delivered to ATLAS by the LHC. The view on the left shows a cut-out view of the ATLAS detector: from the interaction point, the orange lines represent reconstructed tracks, the green and yellow boxes show energy deposits in the electromagnetic (EMB and EMEC) and hadronic (Tile) calorimeters, respectively, and the teal blocks show energy deposits in the hadronic endcap calorimeter (HEC). The top right inset shows a projection of the reconstructed tracks on the transverse plane of the detector. The orange lines represent reconstructed tracks, the pink dots in the center show the measurements from the Pixel detector, the yellow boxes visualize the measurements from the SCT, and the white dots in the gray annulus represent measurements in the TRT. The energy deposits in the cells of the electromagnetic (EMB and EMEC) and hadronic (Tile) calorimeters are shown in the green and yellow boxes respectively.

4.6 TTC system upgrade for the TileCal Phase-II test beam campaigns

Several test beam campaigns have been conducted at the CERN SPS North area in the Prévessin site, to evaluate the TileCal Phase-II upgrade electronics for the HL-LHC project. There are usually two test beam periods during the year and each test beam period takes two weeks, with access to the beam line. Data is collected, with Tile modules being exposed to varying energy beams and positioning to the beam line. This section describes the TileCal Phase-II upgrades, the test beam setup, the upgrade of the TTC system with the ALTI board and results from the 2022 test beam campaign using the ALTI system.

The upgrade of the LHC to the HL-LHC will provide a great opportunity to search for physics BSM, observe new details of electroweak symmetry breaking, and precisely measure the properties of the recently discovered Higgs boson. The HL-LHC will have the capability to deliver up to seven times the LHC nominal instantaneous luminosity in 2029. An increase in luminosity will result in around 200 pp collisions every bunch crossing, as well as a large increase in particle flux. The ATLAS Phase-II upgrade will adapt the sub-detectors to the requirements of the HL-LHC. As part of the upgrades, the on- and off-detector electronics of TileCal will be replaced during the Long Shutdown 3 period (2026-2028). The new readout system is required to be able to handle an increased data rate. It also needs to be more radiation tolerant for the on-detector electronics, and to be compatible with a completely digital ATLAS TDAQ system for the HL-LHC. The new readout strategy will make it possible for the on-detector electronics to digitize detector data and send it to the off-detector electronics at a bunch crossing frequency of 40 MHz.

Off-detector electronics in counting rooms will compute the reconstructed first-level trigger objects and store digitized samples in pipelines, pending a trigger acceptance signal. The LHC clock will also be sent via the off-detector electronics to the on-detector electronics incorporated within the digital data stream. The TileCal Phase-II upgrade project has conducted substantial research and development, including the construction of a Demonstrator module to assess the performance of the new clock and readout architecture envisioned for the HL-LHC project. The Demonstrator module was developed and put into the ATLAS experiment with the most recent version of the on-detector electronics. The Tile PreProces-

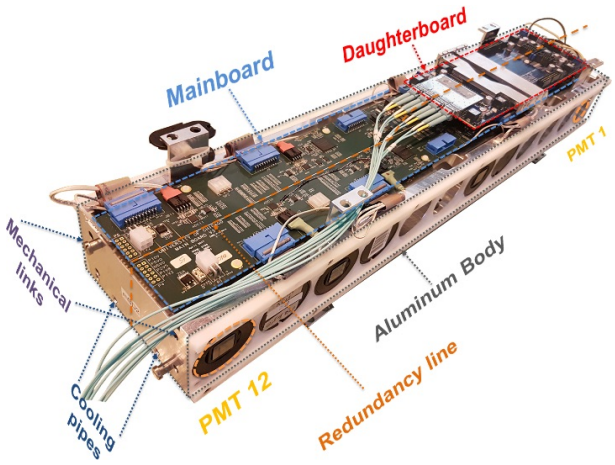


Figure 4.31: TileCal hybrid Demonstrator Minidrawer.

sor (TilePPr) Demonstrator [112] is used to run and read out the Demonstrator module, allowing backward compatibility with the current ATLAS TDAQ and TTC system. The TTC system of the test beam facility has been upgraded for the TileCal Phase-II test beam campaigns. A new TTC interface module, the ALTI is being deployed during the LS2 period (2019-2022) of the LHC, as part of Phase-I upgrades.

4.6.1 TileCal Phase-II upgrade electronics

The Demonstrator's on-detector read-out electronics are made up of a Superdrawer (SD) that divides a legacy TileCal Drawer into four Minidrawers (MD, Figure 4.31), each of which can service up to 12 PMT channels. The SD will continually digitize up to 48 TileCal PMT gains and provide the digitized sampled data to the off-detector systems at 40 MHz (Figure 4.32) [113]. Figure 4.31 shows the TileCal hybrid Demonstrator Minidrawer. Before being digitized by a Mainboard, each PMT analogue signal is conditioned, shaped, and fed into amplifiers with low- and high-gain of ratio 1:32 by a 3-in-1 card. The 3-in-1 card is an early version of the Front End board for the New Infrastructure with Calibration and Signal Shaping (FENICS) card, designed to be backwards compatible with legacy TileCal trigger system.

A Daughterboard receives and transmits LHC-synchronized timing, control signals, and configuration commands to the front-end while simultaneously delivering continuous read-out from the MainBoard channels to the off-detector systems. Compatibility with the legacy trigger system of TileCal is achieved by

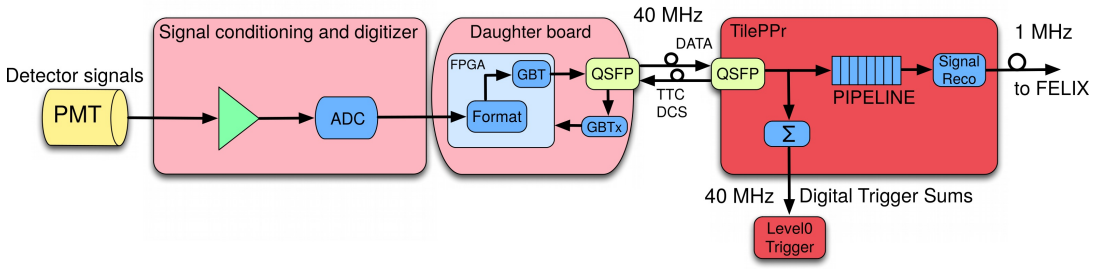


Figure 4.32: Sketch of the TileCal Phase-II upgrade readout electronics. The left side of the sketch (magenta) are the on-detector electronics and the right side (red) are the off-detector electronics.

an Adder-based-board that groups the PMT analogue in cell pseudo-projective towers and sends analogue sums to the legacy L1Calo trigger system. The High Voltage (HV) distribution system provides the individual PMTs with regulated high voltage. Contrary to the current system, which performs on-detector regulation, the upgraded HV system performs regulation remotely in the counting rooms. This eliminates the need for radiation hardness and provides good access to the system. Each HV regulation board has 48 outputs for individual PMTs in each module. Low Voltage (LV) Distribution, Control, and Monitoring System is an upgraded three stage system. It differs from the current 2-stage LV distribution system, in which the LV box provides different voltage levels to the front-end electronics. In the upgraded system, all LVPS bricks supply 10 V to the front-end electronics, which are converted by point-of-load regulators to various voltages required by the electronics. A TilePPr on the Off-Detector electronics continually collects and stores the PMT data of the whole SD in pipelines until the reception of a trigger decision event, at which point the related data is sent to the legacy ROD (Read Out Driver). The TilePPr acts as an interface between the legacy system and the new electronics, sending LHC synchronous clocks and configuration commands to each MD, receiving commands and trigger signals from the TTC, interacting with the DCS, and sending triggered data to the legacy ROD.

4.6.2 Test beam setup

The test beam setup consists of three TileCal modules placed on a scanning table that can rotate the modules at any angle and position with regard to the incident beam. Currently, the legacy readout electronics described in Chapter 2



Figure 4.33: Beam elements and the scanning table in the test beam setup.

are installed in two modules (LBA65 and LBC0), the Phase-II upgrade electronics are installed in LBA0, LBC65 and EBC65. This module configuration can change depending on the test beam program. For interface with the back-end electronics, these modules comprise of PMT blocks with 3-in-1 cards, Digitizer boards, and Interface boards. During test beams, legacy modules are critical in allowing a comparison between the legacy and new readout electronics. The Demonstrator module incorporates two options: the PMT blocks in the outside MDs are powered by the HV remote system, while the PMTs in the central MDs are powered by the HV internal system. Each upgraded module receives low voltage power from a fLVPS connected to the module's extreme and controlled by the legacy DCS software through CANBus. The back-end electronics are a combination of the legacy and the new readout electronics. The legacy back-end ROD crate consist of a SBC, a ROD and a TBM. The upgraded modules transmit data to two TilePPr boards integrated within the legacy TDAQ software through the TTC and ROD interfaces. The legacy TTC system comprising of a LTP, a TTCvi and a TTCex has been replaced with the ALTI board. The TTC system uses the TDAQ software to configure the legacy and upgraded electronics.

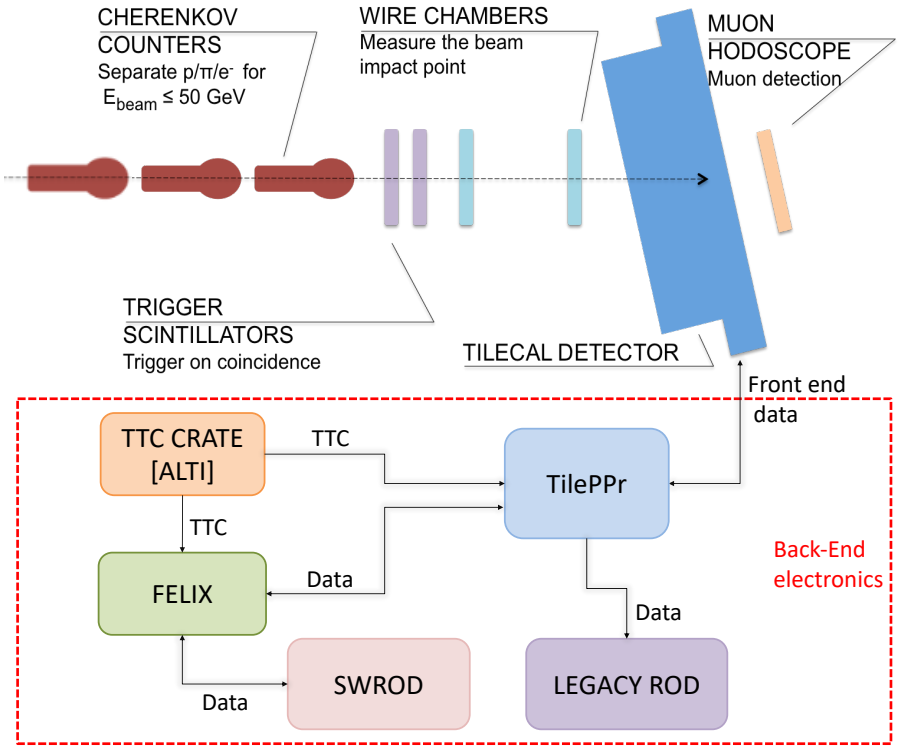


Figure 4.34: Schematic diagram of the FE and BE electronics in the test beam setup.

Beam elements

In the beam line, a number of detectors were put to monitor the beam's quality, position, and particle composition [114]. A schematic of the beam components put in the test beam line is shown in Figure 4.34. The beam position is measured with a precision of 0.2 mm using two beam chambers. The beam chambers utilized at the testbeam are CERN-developed Delay Wire Chambers (DWC) [115]. The DWC is made up of two sandwich parts, each of which is made up of two cathode planes encircling a central anode wire-plane. The sandwich components are orthogonally arranged to provide a two-dimensional position measurement. Because the beam is not made up of a single type of particle, a Muon Hodoscope (MH) and three Cherenkov Counters (CCs) were installed to aid in data interpretation and particle identification. The MH, also known as the Muon wall, is a mobile detector comprised of 12 scintillators installed behind the Tile modules. It is largely utilized in offline analysis to suppress the pions' low energy tail in high energy hadrons runs.

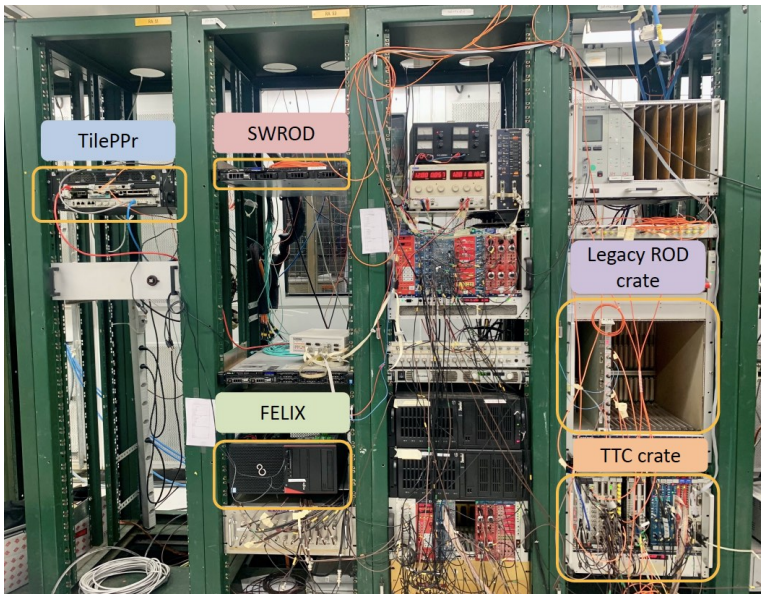


Figure 4.35: Beam elements and the scanning table in the test beam setup.

The CCs are installed in the beam line to enhance particle identification by distinguishing between pions and electrons at energies less than 50 GeV. Two CCs were deployed in the beam line during the first two test beam sessions in September 2015 and June 2016. One CC was designed to record interactions with kaons, pions, and electrons but not protons, whilst the other was designed to report only interactions with pions and electrons. During the September 2016 test beam, a third CC was inserted and configured for electron identification. As part of the beam trigger system, two scintillators S1 and S2 (Figure 4.34) were put in the beam line. Coaxial cables are used to connect the scintillator signals to the beam trigger mechanism in the control room. Because the lengths of the scintillator cables vary, signals are time-equalized using delay boxes before reaching the trigger mechanism.

In a NIM crate, the beam trigger logic is developed using timer counters, discriminators, and Fan-in/Fan-out modules. When a beam particle creates a signal on both scintillators, the beam trigger provides a Master trigger signal. The Master signal is then sent to a second NIM crate, which starts the TDC measurement of the beam chamber signals and reads out the ADCs used for scintillator signal digitization. In addition to generating the Master trigger, the trigger logic sends the L1A signal to the ALTI in the TTC crate, unless the busy signal indicates that the readout path is unavailable. The ALTI then sends the

L1A signal to the TilePPr, RODs, and FE electronics.

4.6.3 Integration of the ALTI module

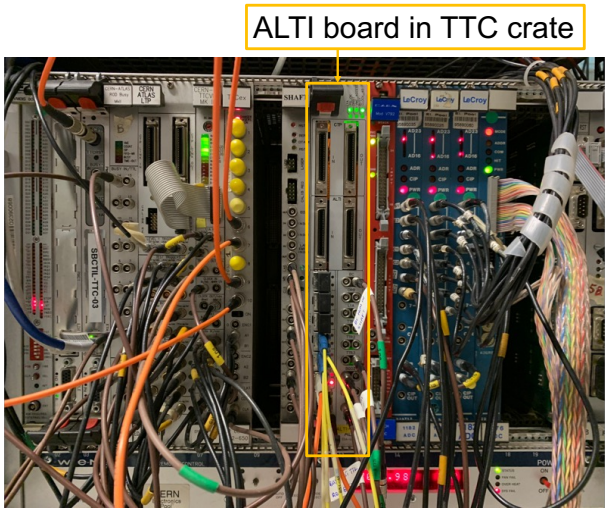


Figure 4.36: ALTI installed in the TTC crate at test beam area.

The ALTI board was inserted in slot 11 of the TTC crate as shown in Figure 4.36 and the latest firmware is loaded. Similarly to the Tile175 test bench, the ALTI schema file was loaded in the OKS database and ALTI objects were created within the ALTI classes. The setup scripts were updated to source L1CT patches and the database was linked to the Tile175 installed DAQ software. Changes were made to objects of different classes in the OKS database. Signal delays and pipelines were adjusted accordingly, in order to place the pulse shape of the samples within the readout window.

Figure 4.37 shows the new cable connection scheme for all different run types. Separate cable connection schemes for each run type can be found in Appendix A.2. The connection scheme allows for the use of three pattern generators for different run types, which will be discussed in the next section. During a CIS run, the ALTI sends the TURN and BC signals to the SHAFT module and receives the charge and discharge signals from the SHAFT module. The ALTI also sends the TTR1 and BC signals to the Trigger system and receives the L1A signal for CIS runs. During a laser run, the ALTI sends the TURN and BC signals to the SHAFT module and also sends the BC signal to the Trigger system. The Trigger system receives the BC signal from the ALTI as well as the laser trigger signal from the

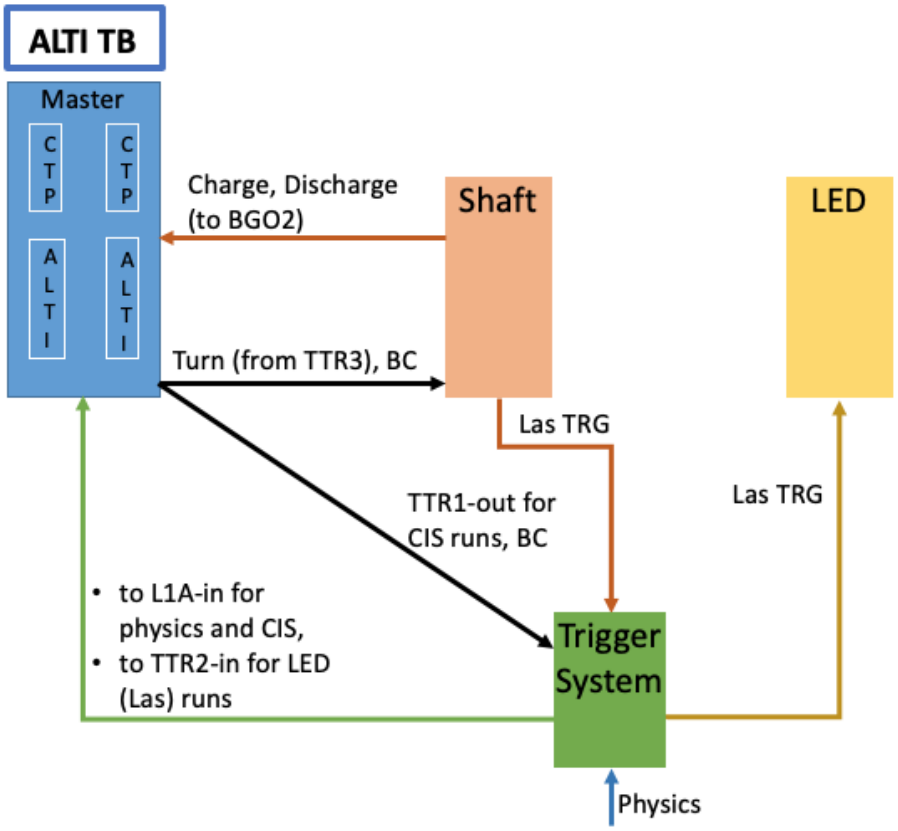
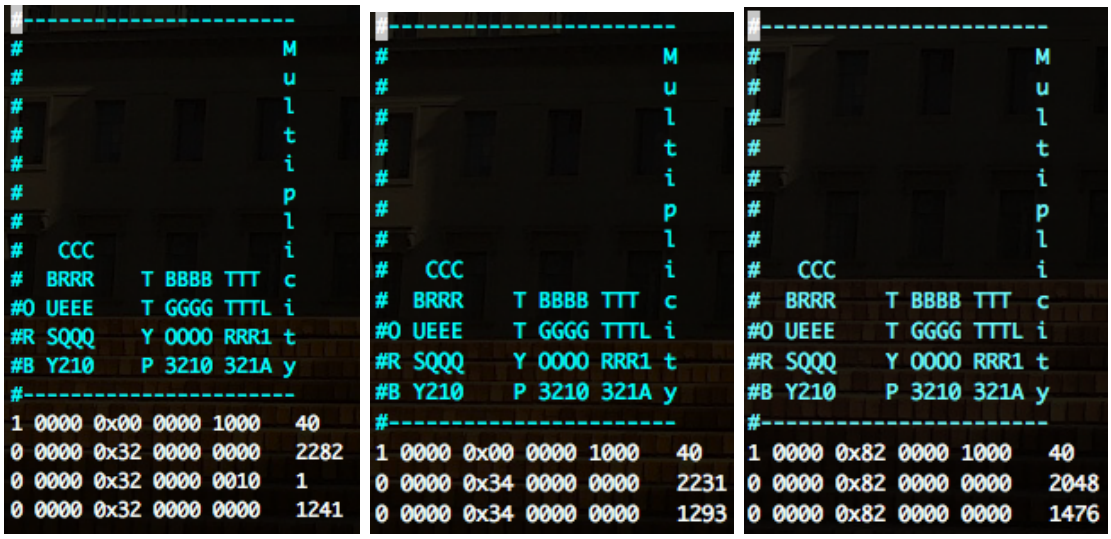


Figure 4.37: The schematic of the ALTI configuration at test beam area for all run types.

SHAFT module. The Trigger system then sends the laser trigger signal to the LEDs attached to the Tile modules. In return the ALTI receives the LED signal for laser runs. During a physics run, the ALTI sends the BC signal to the trigger system. The trigger system receives the physics signal from the beam line setup and sends the signal to the ALTI for physics runs.

Pattern generators

Contrary to the B175 test bench and P1 detector configurations, the test beam setup uses three different pattern generator files for all run types (pedestal, CIS, laser, and physics). CIS and pedestals use the same pattern generator. Laser and physics runs have independent pattern generators. Figure 4.38 shows the pattern generators used for different run types.



(a) (b) (c)

Figure 4.38: Three pattern generator files used at the test beam setup. File for pedestal and CIS runs (a). File for laser runs (b). File for physics runs (c).

Eventviewer

The test beam upgrades make use of a higher number of samples. The number of samples have been increased from 9 to 15. In Figure 4.39, the eventviewer shows 15 samples which form a Gaussian-Like distribution in the read-out window. The pulse formed by these samples is also scanned by adjusting the pipelines until it is centered in the read-out window. The pipeline adjustments are also done for CIS, laser and physics run types.

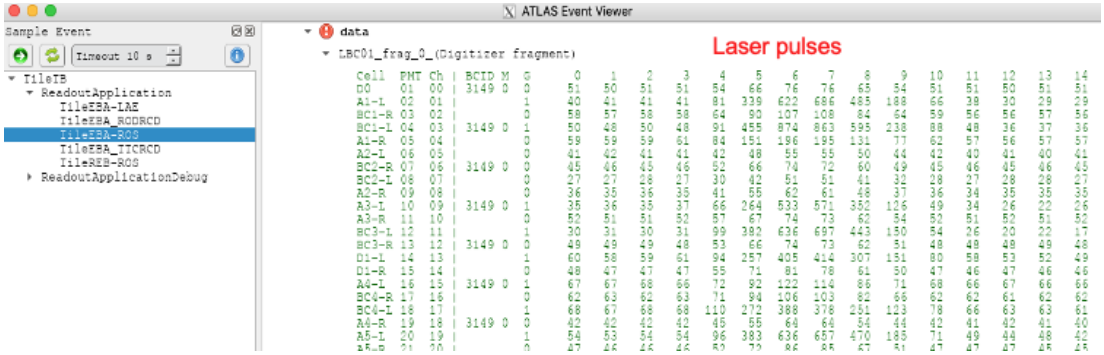


Figure 4.39: The test beam eventviewer for a laser run. Results show 15 samples that form a Gaussian distribution. In the absence of a pulse, only the pedestal is shown.

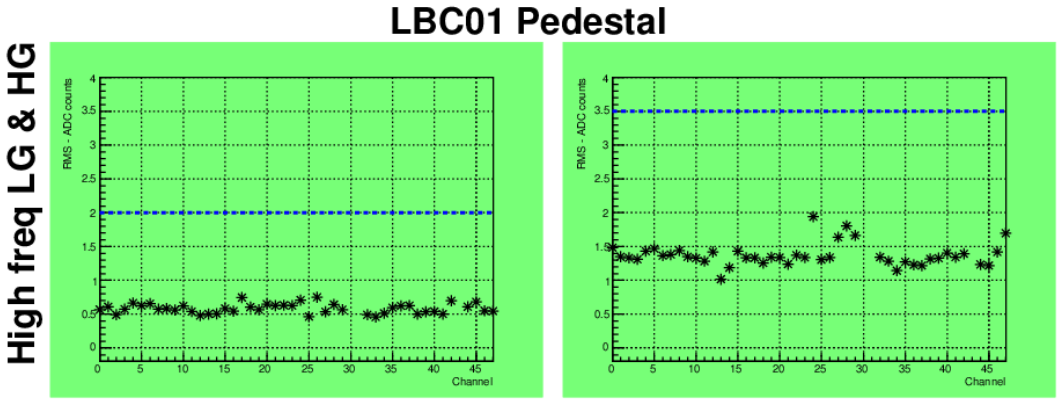


Figure 4.40: Results from DVS pedestal test for high frequency noise in both high and low gain. Results show that noise levels are within acceptable levels for the LBC01 module.

4.6.4 Performance and test beam results

Calibration system tests are critical for validating the functioning of the readout electronics prior to data collection and obtaining calibration data to establish the electromagnetic energy scale and system stability. Prior to the physics runs, daily pedestal and CIS runs are performed during the test beam periods. DVS tests are also perfomed from time to time.

DVS tests

Figure 4.40 shows plots from the DVS pedestal test for both high and low gain. The plots show the RMS ADC counts versus the channel number, and the electronics noise level is below the set RMS ADC threshold (dotted in blue colour) for all read-out channels. Figure 4.41 shows the CIS DVS test performed on one operational read-out module. It indicates a good reconstructed pulse of ADC counts versus time for seven samples in five channels shown in green colour. The test results also indicate that there is an issue with the amplitude of several channels. Log files show that the pulse amplitude, width, and phase are incorrect in 100 events for channel 6, hence the channel is flagged red for bad.

Test beam results

The results discussed in this section, were obtained during the November 2022 test beam campaign. It was the first time the ALTI module was used for data-taking at the test beam area. Some of the results show comparisons of the previous

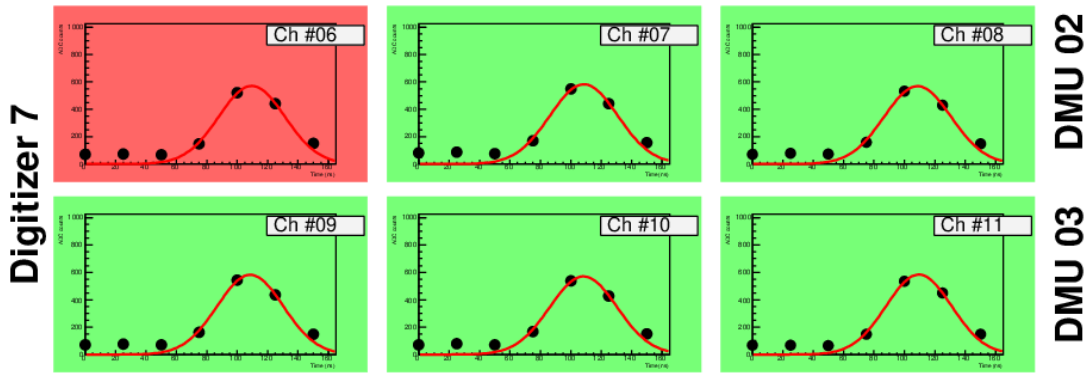
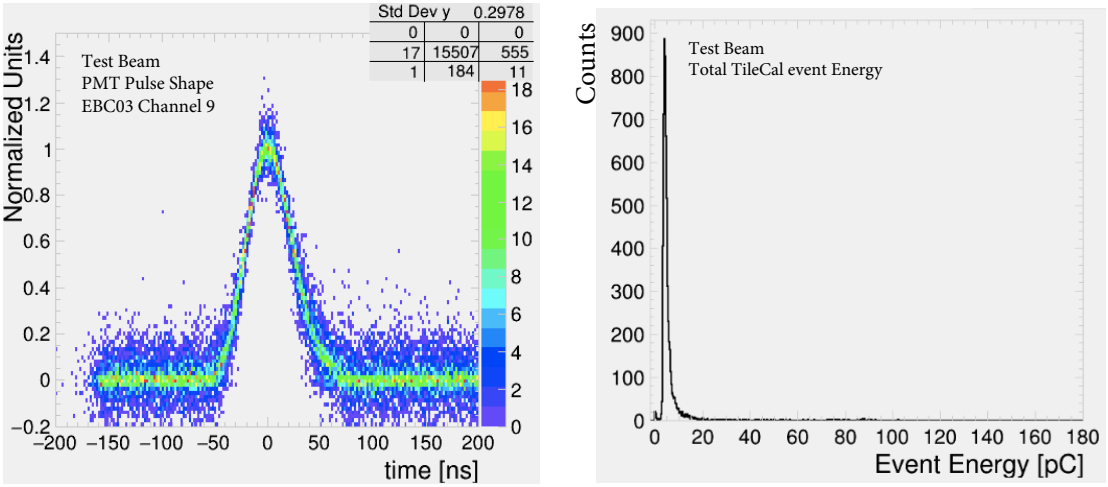


Figure 4.41: LBC01 CIS HG DVS test result from IGUI. The test results indicate that there is a deviation in the amplitude, width or phase of channel 6, hence the channel is flagged red for bad, to trigger further investigation.

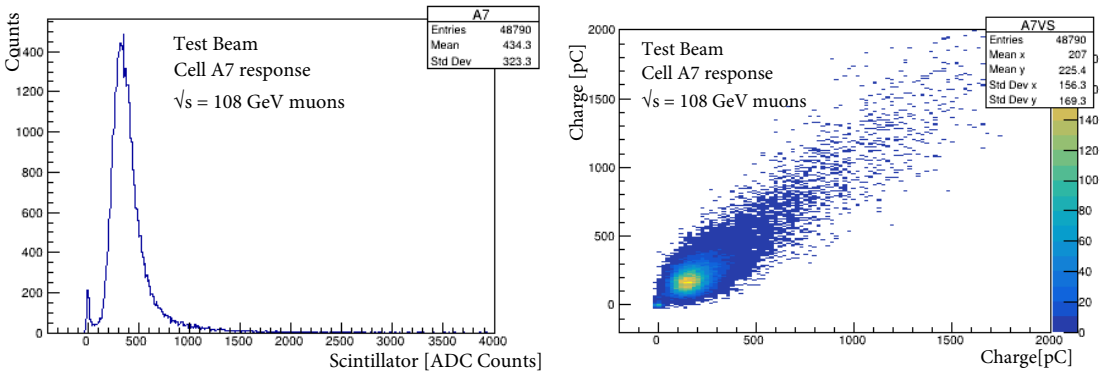
test beam results (legacy TTC modules) with the current results (ALTI TTC system). Figure 4.42 shows some of the test beam results during physics data-



(a) (b)

Figure 4.42: Test of the pulse shape in the PMT. The test also checks if the histogram is not empty (a). The total TileCal event energy measured in pCs (b).

taking. Figure 4.42(a) shows a good pulse shape in the PMT and Figure 4.42(b) shows the total TileCal event energy measured in pCs. The results confirm a good calibration of the system. Figure 4.43(a) shows one of the ten A cells in Tile row 3 for LBC02. The cells are exposed to 108 GeV beam of muons. In this figure, the A7 cell response distribution is shown for almost 50 000 events. Figure 4.43(b) shows a good distribution of the A7 cell's PMT energy response



(a) (b)

Figure 4.43: Layer A7 cell response in LBC02 module, exposed to 108 GeV muon beam (a). Layer A7 cell's PMT energy response correlation plot (b).

correlation. Data-taking at the test beam area has been a success, validating a successful integration of the ALTI module in the test beam TTC system.

Chapter 5

Object reconstruction and identification with ATLAS

This chapter describes the process of identifying events from the pp collisions and object reconstruction with the ATLAS detector. Precise reconstruction of the physics objects in the ATLAS detector is important for physics analysis. The search for the presence of a new heavy resonance produced via gluon-gluon fusion and decaying to the 4ℓ final state, in association with missing transverse energy, requires the precise reconstruction and identification of electrons, muons, jets and missing transverse energy.

5.1 Tracks

Track reconstruction at the LHC is a challenging task which requires extremely high performance and efficient usage of resources. To meet the needs of the LHC environment, sophisticated algorithms (termed *event reconstruction*) have been developed. The algorithms are used for the reconstruction of objects from raw detector data and providing tools for measuring various kinematic properties of such objects efficiently. ATLAS reconstructs a track [116, 117] from clusters and space points defined using information from the ID sub-detectors. The tracking detectors measure charged particles as they emerge from the interaction point. The charged particles deposit energy and leave signals as they traverse through the detector. The space points are referred to as *hits*, and the hits are categorised into trajectories, referred to as tracks. A reconstructed track is used to determine a particle's origin, direction, and momentum.

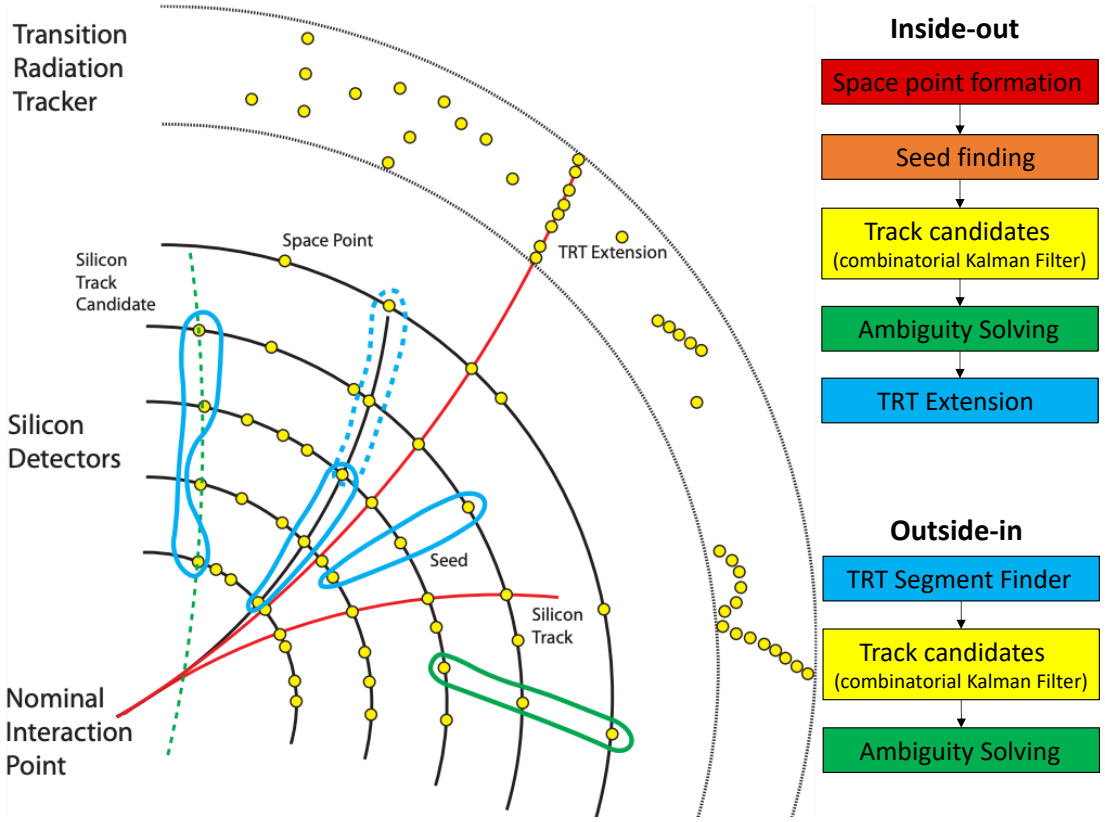


Figure 5.1: Track reconstruction showing the *inside-out* and the *outside-in* approaches.

The *inside-out* and the *outside-in* approaches are used for track reconstruction and Figure 5.1 illustrates these two approaches:

i) *inside-out*, is the main tracking algorithm and it searches for and reconstructs a track starting from the pixel layers and add hits from other detectors moving away from the interaction point. It is designed to efficiently reconstruct primary charged particles, directly produced in a *pp* collision with a mean lifetime greater than 3×10^{-11} s.

ii) *outside-in*, the tracking algorithm searches for and reconstructs a track in the opposite direction, starting from TRT segments and extending inwards by adding silicon hits.

The *inside-out* approach features a series of steps in reconstructing a track:

- **Space-point formation**: clusters are created in the Pixel layers and SCT

layers while drift circles are created in the TRT layers. Clusters and drift circles are then transformed into 3D space-points.

- **Track finding seeded by space-points**: sets of three space-points form a seed, either only in Pixel or only in SCT or a Mixed seed. Seeds which pass the initial transverse momentum (p_{T}) and impact parameter resolution cuts are also required to match a fourth space-point that is compatible with the particle's trajectory estimated from the seed. A pattern recognition algorithm, the combinatorial Kalman filter [118] is then used to complete track candidates within the silicon detector.

- **Ambiguity solving**: after finding the track candidates, ambiguities between any tracks sharing the same hits are resolved. Track candidates are ranked based on track score, favouring tracks with a higher score. Track candidates are rejected if they fail to meet any of the following basic quality criteria:

  - $p_{\mathrm{T}} > 400$ MeV,
  - $|\eta| < 2.5$,
  - 12 pixel and SCT clusters are expected (minimum of 7),
  - On the same layer, there can only be one shared pixel cluster or two shared SCT clusters,
  - The combined pixel and SCT detectors must have no more than two holes (absence of a hit at an expected position),
  - The pixel detector must have no more than one hole,
  - $|d_0^{\mathrm{BL}}| < 2.0$ mm,
  - $|z_0^{\mathrm{BL}} \sin\theta| < 3.0$ mm,

  where d_0^{BL} is the computed transverse impact parameter with respect to the observed beam-line position. z_0^{BL} is the longitudinal difference along the beam line between the point where d_0^{BL} is measured and the primary vertex, and θ is the polar angle of the track. A neural network clustering algorithm has been implemented for the Pixel clusters assigned to multiple track candidates in order to separate multiple particles within a merged cluster in dense environments [119].

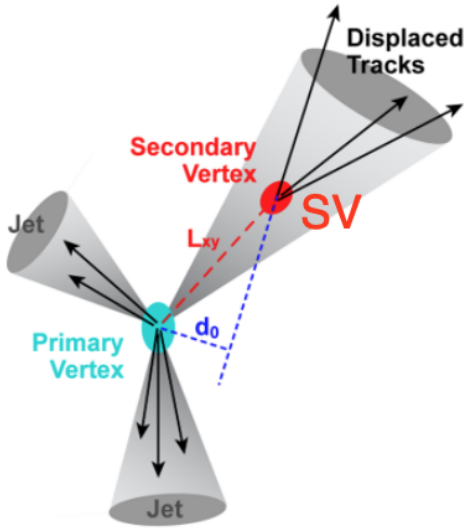


Figure 5.2: Illustration of reconstructed vertices showing the primary vertex and the secondary vertex.

- **TRT extension**: Track candidates are extended to the TRT layers to locate the remaining hits and a track refit is performed to improve momentum resolution.

The efficiency of track reconstruction is dependent on pile-up conditions [117]. The detector occupancy increases in a high pile-up scenario, affecting the number of tracks without corresponding primary and secondary particles, termed "*fake tracks*".

5.2 Vertices

After the reconstruction of the track candidates, it is necessary to reconstruct the Primary Vertices (PVs) and Secondary Vertices (SVs). Figure 5.2 shows a PV and a resulting SV. A PV is a *pp* interaction point where most of the reconstructed tracks are produced. Two algorithms [120] are used to identify the vertices: a vertex finding algorithm that correlates the tracks with vertex candidates, and a vertex fitting algorithm that reconstructs the vertex parameters.

- **vertex finding**: The vertex finding algorithm identifies the reconstructed tracks that are compatible with the emergence of tracks from the interaction region and selects a vertex seed to identify the precise correlation of tracks with vertices.

- **vertex fitting**:

  The vertex position is determined using a χ^2 based fitting technique: any track that deviates by more than 7 σ from the fit is used to establish a new seed, and the operation is repeated until there are no tracks remaining. Vertex reconstruction requires at least two tracks with $p_{\mathrm{T}} > 400$ MeV associated with them in order to improve the resolution of the vertex spatial position.

The efficiency of vertex reconstruction is dependent on the pile-up scenario: as pileup increases, so does the number of fake tracks, and the accuracy in reconstructing the vertex position decreases. An event may have more than one vertex; in this case, the primary vertex is defined as the one with the highest sum of p_{T} of the associated tracks. The remaining PVs are treated as a result of pile-up interactions. Additionally, all vertices that are incompatible with the beam collision region are considered as secondary PVs.

5.3 Leptons

The ATLAS detector has the ability to identify and reconstruct electrons, muons and taus. This section only discusses the identification and reconstruction of electrons and muons with the exception of taus, as they are not used in the study. References [121, 122] contain information on the performance of tau identification and reconstruction.

5.3.1 Electrons

When an electron interacts with a material, it may lose a considerable amount of energy due to bremsstrahlung. The radiated photon that may be converted into an electron-positron pair, which may then interact with the detector material. Positrons, electrons and photons are often emitted with high collimation and reconstructed as part of the same electromagnetic cluster. These interactions may happen within the inner-detector volume or even in the beam pipe, resulting in several tracks in the inner detector, or they can take place downstream of the inner detector, only affecting the shower in the calorimeter. Consequently, several tracks may be produced and matched to the same electromagnetic cluster, all from the same primary electron. Figure 5.3 illustrates an electron (in red) traversing the

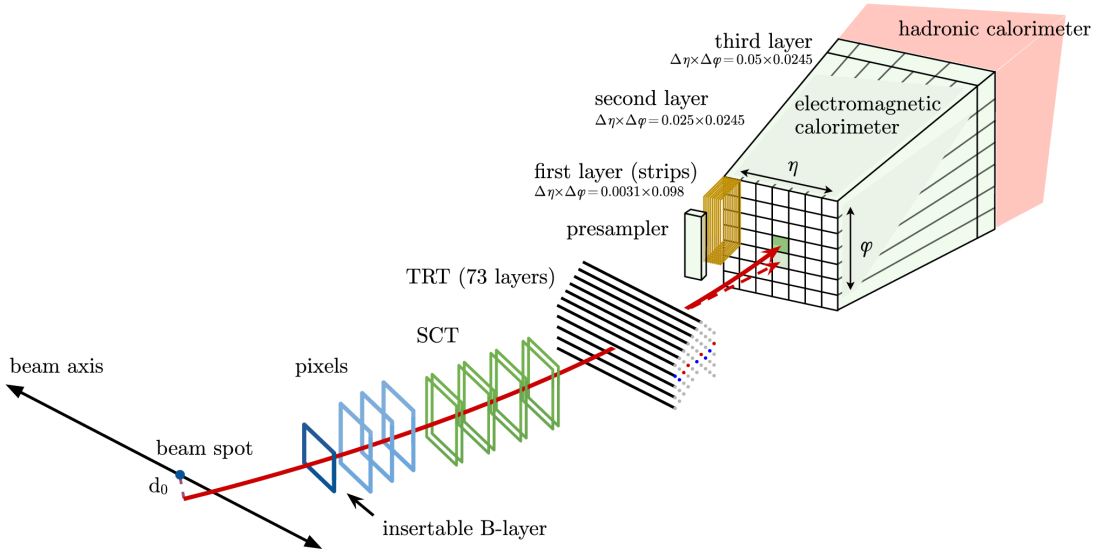


Figure 5.3: Illustration of an electron (in red) traversing through the detector [123]. It first traverses the tracking system (Pixel, SCT and TRT) and enters the EM calorimeter.

tracking system (Pixel, SCT and TRT) to the EM, showing components involved in the reconstruction and identification of an electron.

The reconstruction of electron candidates within the kinematic region encompassed by the high-granularity EM calorimeter and the inner detector is based on three fundamental components characterizing electron signatures. These are: localised clusters of energy deposits found within the electromagnetic calorimeter, charged-particle tracks identified in the inner detector, and close $\eta \times \phi$ spatial matching of the tracks to the clusters to form the final electron candidates. As a result, electron reconstruction in the precision region of the ATLAS detector ($|\eta| < 2.47$) proceeds in the specific sequence, which includes seed-cluster reconstruction, track reconstruction and electron-candidate reconstruction.

Track reconstruction

As discussed in Section 5.1, charged-particle reconstruction in pixel and SCT detectors starts with hits, where clusters produce 3D space-points, leading to the formation of track seeds. Pattern recognition, ambiguity resolution, and TRT extension are the next steps in reconstructing the track (described in Section 5.1). The pattern-recognition algorithm models particle energy loss using the pion the-

ory. If a track seed with $p_{\mathrm{T}} > 1$ GeV cannot be extended to a full track of at least seven silicon hits per candidate track and the EM cluster meets shower width and depth requirements, a second attempt is made with modified pattern recognition that allows up to 30% energy loss for bremsstrahlung at each track-detector intersection. ATLAS Global χ^2 Track Fitter [124] fits track candidates with $p_{\mathrm{T}} > 400$ MeV, according to the pattern recognition hypothesis. Track candidates sharing hits are resolved at the same stage. In order to avoid inefficiencies for electron tracks with significant bremsstrahlung, the following criteria is used; if the fit fails under the pion hypothesis and its polar and azimuthal separation to the EM cluster is below a value, a second fit is attempted under an electron hypothesis (an extra degree of freedom, in the form of an additional Gaussian term, is added to the χ^2 to compensate for the additional bremsstrahlung losses from electrons; such an energy-loss term is neglected in the pion fit).

The clusters of raw measurements are then fitted using an improved Gaussian-sum filter (GSF) [125] to account for charged particle energy loss. This method is used for tracks with four silicon hits and loosely matched EM clusters. The cluster-barycentre position and the track position extrapolated from the perigee to the second layer of the calorimeter must meet $|\eta_{cluster} - \eta_{track}| < 0.05$ and one of two azimuthal separation requirements: $-0.20 < \Delta\phi < 0.05\,\mathrm{rad}$ or $-0.10 < \Delta\phi_{res} < 0.05$ rad, where q is the particle's electric charge and $\Delta\phi$ and $\Delta\phi_{res}$ are computed as $-q \times (\eta_{cluster} - \eta_{track})$ with the track's momentum rescaled to the cluster's energy for $\Delta\phi_{res}$. Asymmetric matching reduces energy loss due to bremsstrahlung, which occurs when negative (positive) electric charge tracks bend in the positive (negative) direction. The GSF approach [126] is based on the generalization of the Kalman filter and accounts for bremsstrahlung's non-linear effects. GSF models experimental noise as a sum of Gaussian functions. The GSF comprises of several parallel Kalman filters, which approximates each track parameter as a weighted sum of Gaussian functions. Up to twelve Gaussian functions are utilized to characterize track parameters. In the last step, the energy loss mode is used. Radiative energy losses reduce momentum, increasing the electron's magnetic field trajectory curvature. With the GSF method, all bending-plane track parameters are expected to improve.

Reconstruction of the electron-candidate

Electron reconstruction involves matching the GSF-track candidate to the calorimeter seed cluster and determining the final cluster size. This matching technique is identical to the loose matching outlined above before the GSF step, but with tighter requirements; track-matching in is tightened to $-0.10 < \Delta\phi < 0.05\,\text{rad}$, retaining the original alternative requirement $-0.10 < \Delta\phi_{res} < 0.05\,\text{rad}$. If several tracks match the criteria, the primary electron track is selected using an algorithm that considers the distance in and between the extrapolated tracks and the cluster barycentres measured in the second layer of the calorimeter, the number of hits in the silicon detectors, and the number of hits in the innermost silicon layer; a candidate with an associated track with at least four hits in the silicon layers and in the innermost silicon layer is chosen. Objects are classified as photon candidates if the main candidate track matches a secondary vertex and has no pixel hits (likely a conversion). Using the candidate electron's E/p and p_{T}, the existence of a pixel hit, and the secondary-vertex information, it is determined clearly whether the object is an electron candidate or whether it should be ambiguously classified as either a photon or an electron candidate. This classification system helps maintain photon-reconstruction efficiency.

Finally, reconstructed clusters are built around the seed clusters by expanding the cluster size in η or ϕ on either side of the original seed cluster. In the transition region of $1.37 < |\eta| < 1.52$, both extended-window elements are used. Cluster energy must match initial electron energy. This detailed calibration is achieved using multivariate approaches [127] based on data and simulated samples after identifying electron candidates, not during reconstruction, which uses approximate EM-scale energy clusters. The final electron candidate's energy is estimated using the extended-window cluster's calibrated energy, while ϕ and η directions are derived from the track parameters of the track best matched to the original seed cluster.

Electrons are identified using the `ElectronPhotonSelectorTools`, provided by the Egamma Combined Performance group. A likelihood discriminant is formed from the combination of the information from the EM calorimeter and the ID. The tool provides several working points (WP) for the likelihood identification of electrons corresponding to different efficiency and fake rejection probability. These different identification selections *Loose*, *Medium* and *Tight* are defined in ref. [123], with typical efficiencies for electrons of $E_{\text{T}} \approx 40$ GeV of 92%, 85%

and 75% respectively. This analysis makes use of the *loose* WP, with an efficiency in the range of 90% for transverse momentum $p_{\mathrm{T}} = 20$ GeV and 96% for $p_{\mathrm{T}} > 60$ GeV. It is also required to isolate electrons using both calorimeter-based and track-based isolation variables. More information is available in ref. [123].

5.3.2 Muons

The reconstruction of muons is first performed independently in the ID and MS. The combined information from the ID and MS is used for the formation of the muon tracks that are used in physics analyses. The reconstruction of muons in the ID is similar to other charged particles as described in Section 5.1. Section 5.3.2 discusses the reconstruction of muons in the MS and Section 5.3.2 discusses the combined reconstruction of muons.

Reconstruction in the MS

In the MS, muon reconstruction begins with a search for hit patterns inside each muon chamber to build segments. A Hough transform [128] is used to look for hits aligned on a trajectory in the detector's bending plane in each MDT chamber and neighboring trigger chamber. The hits are used to reconstruct the MDT segments by performing a straight line fit and the coordinate orthogonal to the bending plane is measured by the RPC or TGC hits. In the η and ϕ planes of the CSC detector, the segments are constructed using a combinatorial search algorithm with a loose constraint on track compatibility with the luminous region. Muon track candidates are then constructed by combining hits from segments in multiple layers. The algorithm executes a segment-seeded combinatorial search, starting with seeds in the segments created in the middle layers of the detector, where there are more trigger hits available. The search is then expanded to include outer and inner layer segments as seeds. The segments are chosen based on hit multiplicity and fit quality, and their relative coordinates are used to match them. At least two matching segments are needed to construct a track, except in the barrel–endcap transition zone, where a single high-quality segment containing η and ϕ information may be used. Initially, the same segment may be utilized to construct many track candidates and an overlap removal algorithm is used to determine the optimal assignment to a single track or allow the segment to be shared between two tracks. To achieve high efficiency for surrounding muons, all tracks with segments in three separate layers of the spectrometer are retained

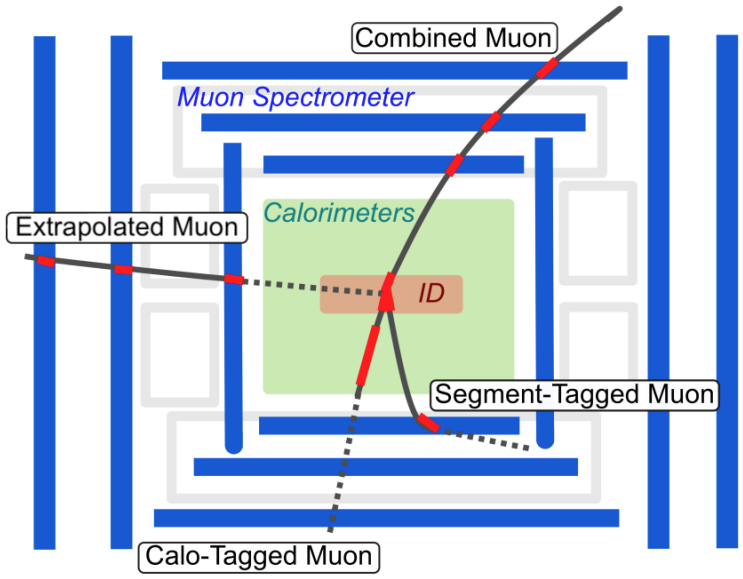


Figure 5.4: Combined muon reconstruction requires the combination of tracks from the ID and MS. The ATLAS software provides four complementary types of reconstructed muons: Combined, Segment-tagged, Calorimeter-tagged and Extrapolated muons.

if they are similar in two out of three layers but do not share any hits in the outermost layer. Using a global χ^2 fit, the hits linked with each candidate track are fitted. A track candidate is selected if the χ^2 of the fit meets the selection criteria. The track fit is repeated, and hits contributing significantly to χ^2 are rejected. In addition, a procedure for hit recovery is carried out in an effort to recover additional hits associated with the candidate trajectory. If additional hits are identified, the track candidate is refit.

Combined reconstruction

The combined muon reconstruction is performed using information provided by the ID, MS, and calorimeters. Several reconstruction algorithms are employed, defining four muon types:

- **Combined (CB) muon**: the reconstruction of the track is performed independently in the ID and MS, and a combined track is constructed using hits from both the ID and MS subdetectors. During the global fit method, MS hits are added or deleted from the track in order to enhance the quality of the fit. A significant number of muons are reconstructed using outside-in

pattern recognition, in which the muons are first reconstructed in the MS and then extended inward and matched to an ID track. A complementary method applies an inside-out combined reconstruction in which ID tracks are extended outward and matched with MS tracks.

- **Segment-tagged (ST) muons**: a track in the ID is identified as a muon if it is connected with at least one local track segment in the MDT or CSC chambers after extrapolation to the MS. ST muons are used when muons traverse just one layer of MS chambers, either due to their low p_{T} or because they occur in regions with lower MS acceptability.

- **Calorimeter-tagged (CT) muons**: if a track in the ID matches an energy deposit in the calorimeter that is consistent with a minimum-ionizing particle, it is classified as a muon. This type has the lowest purity of all muon types, but it regains acceptance in the region where the muon spectrometer is only partly instrumented to accommodate cabling and services to the calorimeters and inner detector. The CT muon identification criteria are optimized for this region ($|\eta| < 0.1$) and a momentum range of $15 < p_{\mathrm{T}} < 100$ GeV.

- **Extrapolated (ME) muons**: the muon trajectory is reconstructed using just the MS track and a loose requirement for compatibility with the IP origin. At the interaction point, the parameters of the muon track are determined, taking into consideration the expected energy loss of the muon in the calorimeters. In general, the muon must traverse at least two layers of the MS chambers for a track measurement, but in the forward region, three levels are required. ME muons are primarily used to extend the muon reconstruction acceptance into the region $2.5 < |\eta| < 2.7$, which is not covered by the ID.

Before generating a collection of muons for use in physics analysis, overlaps between different types of muons are resolved. When two types of muons share the same ID track, priority is given to CB muons, followed by ST muons, and then CT muons. The overlap with ME muons in the muon system is resolved by evaluating the track hit content and identifying the track with the higher fit quality and higher number of hits.

Muon identification is achieved by applying quality requirements that suppress background, mostly from pion and kaon decays, while identifying prompt muons

with high efficiency and providing a robust momentum measurement. Specific requirements for the number of hits in the ID and MS are used to provide a reliable momentum measurement. The quality cuts for the ID require at least one Pixel hit, at least five SCT hits, no more than three Pixel or SCT holes, and at least 10% of the TRT hits originally assigned to the track are included in the final fit where $0.1 < |\eta| < 1.9$, in the region of full TRT acceptance. Four muon identification selections (*Medium*, *Loose*, *Tight*, and *High-*p_{T}) are defined to address the specific needs of different physics analyses [129]. *Loose*, *Medium*, and *Tight* are inclusive categories, meaning muons identified with tighter requirements are also included in the looser categories. A *Loose* muon identification WP, which uses all muon types, with an efficiency of 98.5%, is used in this analysis.

5.4 Jets

Jets are reconstructed from clusters of topologically connected calorimeter cells (topo-clusters), described in Ref. [130]. The topo-clusters are calibrated at the EM energy scale. The reconstruction is performed using the anti-k_t algorithm, with a radius parameter $R = 0.4$ [131]. The particle flow (PFlow) objects are used as inputs to the `FastJet` package [132]. In PFlow, the removal of clusters is based on the expected energy being deposited by tracks during jet reconstruction. Prior to jet-finding, the topo-cluster η and ϕ are recomputed with respect to the PV position, rather than the detector origin. After a built up of jets, the jets are first calibrated to the EM scale with an effect of pile-up removal. Additional techniques are used to derive the calibration constants necessary for the correction of data, in order to improve data and MC agreement.

To further reduce the effect of pile-up jets, an additional requirement that uses the track and vertex information inside a jet, jet-vertex-tagger (JVT), is used to select jets with $20 < p_{\mathrm{T}} < 60$ GeV and $|\eta| < 2.4$. The JVT uses a discriminant based on the projection of the missing transverse momentum from pile-up jets in the central region onto the forward jet. Selected events are required to have at least one vertex with two associated tracks with $p_{\mathrm{T}} > 500\,\mathrm{MeV}$, and the primary vertex is chosen to be the vertex reconstructed with the largest $\sum p_{\mathrm{T}}^2$. Only central jets within $|\eta| < 2.5$ and $p_{\mathrm{T}} > 30\,\mathrm{GeV}$ are used in the study.

5.5 Missing transverse momentum

The Missing Transverse Momentum ($E_{\mathrm{T}}^{\mathrm{miss}}$), is the imbalance of visible momenta in the plane transverse to the beam axis. It may be indicative of weakly interacting, stable particles in the final state, such as neutrinos, hence its importance in certain physics analysis at the LHC, including Higgs boson measurements and BSM studies. $E_{\mathrm{T}}^{\mathrm{miss}}$ is calculated as the negative sum of the momenta of all identified hard objects (electrons (e), muons (μ), photons (γ), hadronically decaying taus (τ_{had}) and jets) and the "soft term", that accounts for unclassified soft tracks and calorimeter clusters:

$$E_{\mathrm{T}}^{\mathrm{miss}} = -\left(\sum_{i\in e} p_{\mathrm{T}}^{i} + \sum_{i\in\mu} p_{\mathrm{T}}^{i} + \sum_{i\in\gamma} p_{\mathrm{T}}^{i} + \sum_{i\in\tau_{\mathrm{had}}} p_{\mathrm{T}}^{i} + \sum_{i\in\mathrm{jets}} p_{\mathrm{T}}^{i} + \sum_{i\in\mathrm{soft\ term}} p_{\mathrm{T}}^{i}\right). \quad (5.1)$$

This study uses the track-based soft term $E_{\mathrm{T}}^{\mathrm{miss}}$, also called TST $E_{\mathrm{T}}^{\mathrm{miss}}$ [133]. The combined information from the ID and the calorimeter is used in reducing the effect of pile-up, which degrades the $E_{\mathrm{T}}^{\mathrm{miss}}$ performance, as observed in Run-I. In TST $E_{\mathrm{T}}^{\mathrm{miss}}$ the soft term is calculated using momentum of the tracks associated with the primary vertex, whereas the hard objects have their momentum being computed at the calorimeter level, to include the momentum measurements for neutral particles. Reconstruction of $E_{\mathrm{T}}^{\mathrm{miss}}$ takes place at the analysis level provided by the Jet-$E_{\mathrm{T}}^{\mathrm{miss}}$ performance group [134], with the consideration of all calibrated objects in the event. PFlow $E_{\mathrm{T}}^{\mathrm{miss}}$ is built from PFlow jets and the algorithm filters the calorimeter clusters with associated tracks. The advantage of this, is the tracker has a higher level p_{T} resolution at low p_{T} and hence improves pile-up rejection. Enabled jet-muon overlap handling in $E_{\mathrm{T}}^{\mathrm{miss}}$, corrects for fake jets due to pile-up close to muons which pass the JVT requirement and jets that have been double counted from muon energy losses.

5.6 Overlap removal

After object reconstruction, an overlap-removal procedure is applied to all selected objects, to remove ambiguities resulting from objects being reconstructed by several algorithms. As the same detector information can be used to reconstruct lepton and jet candidates, a procedure is applied to resolve the overlap

ambiguities. The muon is selected when an electron and a muon share the same ID track. Unless the muon is calorimeter-tagged and is missing an MS track, the electron is selected. Reconstructed jets which overlap with electrons (muons) in a cone of size $\Delta R = \sqrt{(\Delta\eta)^2 + (\Delta\phi)^2} = 0.2\,(0.1)$ are removed.

Chapter 6

The search for heavy resonances in the 4ℓ final state in association with $E_{\mathrm{T}}^{\mathrm{miss}}$

This chapter discusses the search for the presence of a new heavy resonance produced via gluon-gluon fusion and decaying to the 4ℓ final state, in association with missing transverse energy. The search uses pp collisions at $\sqrt{s} = 13\,\mathrm{GeV}$ with the ATLAS detector.

6.1 Introduction

The SM including the discovery of the Higgs boson and its properties, has been described in Chapter 1 as a well-developed model that adequately describes phenomena at the electroweak scale. It provides a comprehensive interpretation of the experimental results. Some of the unexplained phenomena and theoretical problems have been briefly discussed. It is still contested whether the Higgs boson is a particle in its own right or just a part of the Higgs sector postulated by the 2HDM [135, 136]. The 2HDM suggests an additional Higgs doublet, which leads to five Higgs bosons, namely CP-even, like the SM Higgs h and a heavier Higgs H, together with a CP-odd acting as A and a charged Higgs scalar $H^{\pm}$. The additional Higgs sector generates a rich phenomenology with different parameters to explore. Many searches at the LHC explore these characteristics in different channels to find heavy Higgs bosons. In [137], for example, $m_A > m_H$ was considered where A decays into a Z boson and H. Hence, H subsequently decays to $b\bar{b}$ and

Z to two leptons. The CMS experiment also assumes a similar framework, but in this case, $m_H > m_A$ [138]. Both analyses used early Run 2 data. Another search within the 2HDM using the full ATLAS Run 2 dataset, focusing on the 4ℓ final states is described in [139], however the search never investigated the possibility of the missing transverse energy in the final states. The 4ℓ decay channel has played an important role in the discovery of the Higgs boson and the measurement of its properties. Searches in this channel depend on a very clean signature in which the final state has a high signal-to-background ratio. Additionally, the accurate reconstruction of the final state allows the kinematics of the Higgs boson to be fully determined. The 4ℓ final state in association with $E_{\mathrm{T}}^{\mathrm{miss}}$, in the contest of this study, has never been examined within the ATLAS experiment. Therefore, in this analysis, the production of heavy resonances via gluon-fusion associated with $E_{\mathrm{T}}^{\mathrm{miss}}$ is investigated. The search focuses on the high mass region of the heavy bosons where the $m_{4\ell} > 200\,\mathrm{GeV}$.

This study uses pp collision data at a $\sqrt{s} = 13\,\mathrm{TeV}$, and integrated luminosity of 139 fb^{-1} collected by the ATLAS detector on 2015 - 2018 period at the LHC. The data is interpreted in terms of two models. The first model produces the 4ℓ from the resonance H in association with $E_{\mathrm{T}}^{\mathrm{miss}}$, a decay product of the scalar boson S. The model originates from $R \to SH \to 4\ell + E_{\mathrm{T}}^{\mathrm{miss}}$ [140, 141], and $A \to Z(\nu\nu)H(ZZ) \to 4\ell + X$ [140, 142]. The original model only includes a heavy resonance H and another scalar S. In order to consider a more general case of different missing energy magnitudes, the model is extended by adding a heavy scalar R, where R decays to H and S. This is produced using a 2HDM+S+R model. The Feynman diagram in Figure 6.1(a) shows the first model where R is a scalar boson, which decays to two lighter scalar bosons S and H. The S decays to dark matter particles (referred to as $E_{\mathrm{T}}^{\mathrm{miss}}$), and H decays to four leptons. The S mass is fixed at 160 GeV, and the R and H masses are scanned to control the $E_{\mathrm{T}}^{\mathrm{miss}}$. The S mass is suggested to have the best fit value around 150 GeV, as shown in Ref [143]. However, the choice of the S mass does not significantly affect the kinematics of the $R \to SH \to 4\ell + E_{\mathrm{T}}^{\mathrm{miss}}$ signal if it is less than 200 GeV. The second model is the traditional 2HDM model where m_A is greater than m_H and A decays to Z and H, the H decays to two Z bosons and further decays to four leptons. The associated Z boson decays inclusively including the neutrinos, where the missing energy comes from. The Feynman diagram in Figure 6.1(b) shows the topology of this model.

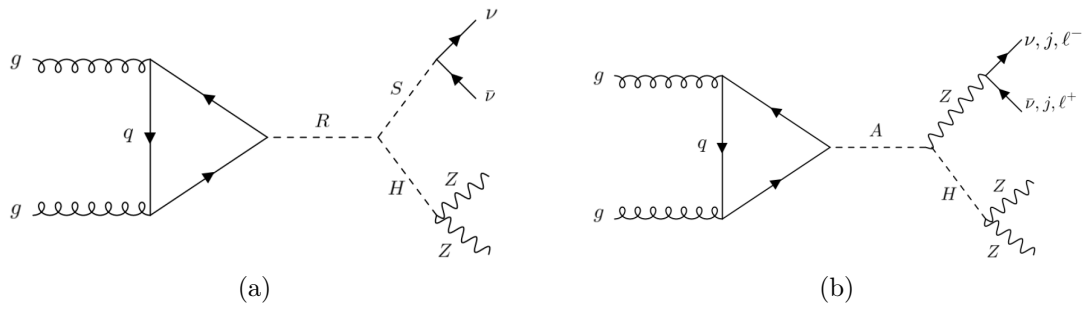


Figure 6.1: Feynman diagrams represent the production of heavy bosons via gloun-fusion (a) $R \to SH \to 4\ell + E_{\mathrm{T}}^{\mathrm{miss}}$ and (b) $A \to Z(\nu\nu)H(ZZ) \to 4\ell + X$ models.

6.2 Data and Monte Carlo simulation

The search uses 2015–2018 pp collision data at a centre of mass of $\sqrt{s} = 13\,\mathrm{TeV}$ corresponding to an integrated luminosity of 139 fb^{-1}. The 2015 (2016) dataset corresponds to an integrated luminosity of 3.86 (35.6) fb^{-1} with an average pile-up of 13.4 (25.1). The recorded integrated luminosity for 2017 dataset is 46.9 fb^{-1} with an average pile-up up to 37.8. The 2018 dataset reported integrated luminosity is 62.2 fb^{-1} and average pile-up is 36.1. The total pile-up for the dataset combined is 33.7. Figure 6.2 summaries the pile-up for 2015 to 2018 dataset. An event must pass the data quality requirements to ensure the quality of the collected data [144–146]. Therefore, in this analysis, the standard "All Good" Good Run List (GRL) configurations[1] are used for the dataset generation. After applying the event cleaning criteria, the total integrated luminosity of the Run 2 dataset reached 139 fb^{-1}.

The background and signal samples are simulated using the Monte Carlo (MC) generators according to ATLAS detector configurations. They are generated in three campaigns mc16a, mc16d and mc16e in such a way to emulate 2015 - 2016,

[1]For the 2015 dataset:
`GoodRunsLists/data15_13GeV/20170619/data15_13GeV.periodAllYear_DetStatus-v89-pro-21-02_Unknown_PHYS_StandardGRL_All_Good_25ns.xml`.
For the 2016 dataset:
`GoodRunsLists/data16_13GeV/20180129/data16_13GeV.periodAllYear_DetStatus-v89-pro21-01_DQDefects-00-02-04_PHYS_StandardGRL_All_Good_25ns.xml`.
For the 2017 dataset:
`GoodRunsLists/data17_13GeV/20180619/data17_13GeV.periodAllYear_DetStatus-v99-pro22-01_Unknown_PHYS_StandardGRL_All_Good_25ns_Triggerno17e33prim.xml`.
For the 2018 dataset:
`GoodRunsLists/data18_13GeV/20190219/data18_13GeV.periodAllYear_DetStatus-v102-pro22-04_Unknown_PHYS_StandardGRL_All_Good_25ns_Triggerno17e33prim.xml`.

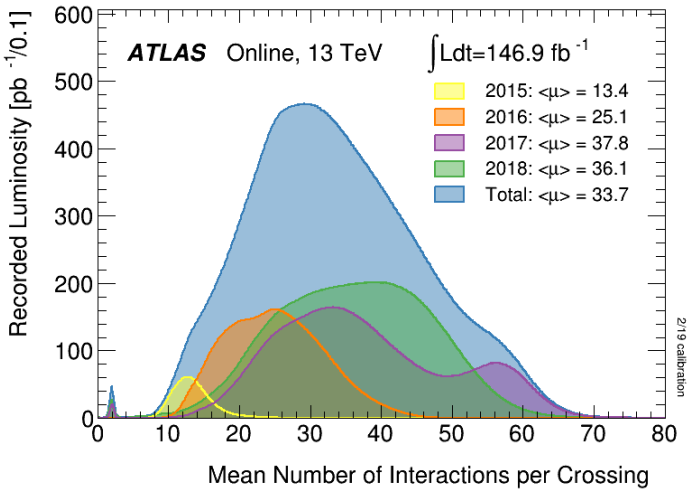


Figure 6.2: The luminosity-weighted distribution of the mean number of interactions per crossing for pp collision data collected by the ATLAS experiment in the period between 2015 - 2018 at the LHC.

2017 and 2018 datasets, respectively. The combination of all MC campaigns is normalized to the total integrated luminosity of the data (139 fb^{-1}). MC samples are used in the signal optimisation, signal and background parametrisation, estimation of the systematic uncertainties and statistics.

The background process from quark-antiquark annihilation, $qqZZ$, is generated using Sherpa 2.2.2 [147–149] with NNPDF30NNLO PDF set [150]. The generation is done with the NLO in the matrix element calculation for zero- and one-jet final states, and leading LO for two- and three-jet final states. The Sherpa parton shower [151] for merging is achieved by using the MePs@NLO recommendation [152]. The EW correction at NLO, as a function of the ZZ invariant mass, m_{ZZ}, is applied [153, 154]. Similarly, the $ggZZ$ process is generated using Sherpa 2.2.2 and OpenLoops generators [147, 155–157]. Matrix elements for zero- and one-jet at LO are calculated and merged with the Sherpa parton Shower [151] and the PDF set NNPDF30NNLO is used in the generation. The VVV backgrounds, including processes such as ZZZ, ZZW and $WWWZ$ with at least four prompt charged leptons, are simulated using Sherpa 2.2.2 and the NNPDF30NNLO PDF set is used during the simulation. The $qqZZ$ (EW) process, consisting of four leptons and two jets, is generated using Sherpa 2.2.2 and the NNPDF30NNLO PDF set. Events containing four prompt charged leptons ermeging from ttV backgrounds, where V is either Z or $W^{\pm}$ bosons, are mod-

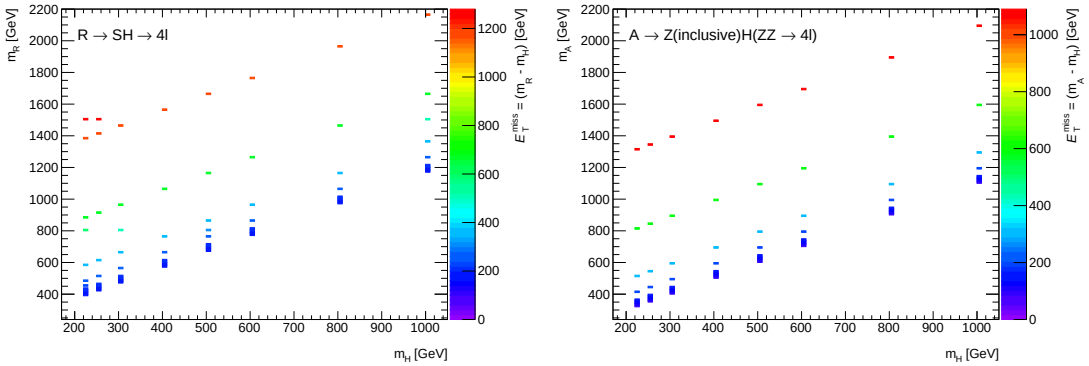
elled using MadGraph5_aMC@NLO [158] interfaced with Pythia8 [159] for hadronisation. The $t\bar{t}$ events were generated using Powheg-Box v2 [160] and the NNPDF30NNLO PDF set. Pythia8 is used as an interface for showering and hadronisation with A14 NNPDF23LO tune, and EvtGen is used to simulate B-hadron decays. Powheg-Box v2 and Pythia8 are used for the generation and hadronisation of the WZ process, respectively. The Z+jets events are modelled using Sherpa 2.2.1 generator. Matrix elements for zero- and two-jet at NLO, and three- and four-jet at LO are calculated with Comix [149] and OpenLoops. For the merging, the Sherpa parton shower MePs@NLO recommendation is used.

The signal samples are also generated, where the gluon-fusion production mechanism is generated for the two BSM models considered in this study, the $R \to SH \to 4\ell + E_{\mathrm{T}}^{\mathrm{miss}}$ and $A \to Z(\nu\nu)H(ZZ) \to 4\ell + X$ models. In both cases, the heavy resonant H is assumed to decay to a pair of Z bosons. Signal samples are produced for the Narrow Width Approximation (NWA). The $R \to SH \to 4\ell + E_{\mathrm{T}}^{\mathrm{miss}}$ process is modelled using Pythia8 with A14 tune and the NNPDF23LO PDF set. The mass of S is fixed to 160 GeV, and the mass of H spans 220, 250, 300, 400, 500, 600, 800, and 1000 GeV. Using the mass gap, m_{Gap}, of 10, 20, 30, 40, 50, 100, 200, 500, and 1000 GeV, the mass of R is evaluated by $m_R \geq m_H + m_S(160\,\mathrm{GeV}) + m_{\mathrm{Gap}}$. All generated signal mass points are shown in Figure 6.3(a), where the energy gap, $m_R - m_H = m_S + m_{\mathrm{Gap}}$, is shown on the z-axis. Appendix B.1 shows the kinematic distributions for $R \to SH \to 4\ell + E_{\mathrm{T}}^{\mathrm{miss}}$ signal with different S mass. These distributions indicate that the kinematics of $R \to SH \to 4\ell + E_{\mathrm{T}}^{\mathrm{miss}}$ signal are not affected when the S mass is below 200 GeV. MadGraph5_aMC@NLO is used to simulate the $A \to Z(\to X)H(\to 4\ell)$ and $A \to Z(\to 2\ell)H(\to 2\ell + X)$ signals with A14 tune and the NNPDF23LO PDF set. The showering and hadronisation is done using Pythia8. The same mass gap of the $R \to SH \to 4\ell + E_{\mathrm{T}}^{\mathrm{miss}}$ model is used to calculate the mass of A as $m_A \geq m_H + m_Z(90\ \mathrm{GeV}) + m_{\mathrm{Gap}}$. The degenerate scenario where $m_A = m_H$ is not considered in this study. The produced signal mass points are shown in Figure 6.3(b). Table 6.1 summarises the generators and PDF sets used in both signal and background simulation.

The gluon-fusion production cross-section (σ) of the $R \to SH \to 4\ell + E_{\mathrm{T}}^{\mathrm{miss}}$ signal is arbitrary set to 1 fb (this is the observable that is going to be probed by the likelihood fit of data/background+signal). Two signals are generated for the $A \to Z(\nu\nu)H(ZZ) \to 4\ell + X$ signal and then merged to form the combined signal. Firstly the $A \to Z(\to X)H(\to 4\ell)$ is generated where the $H \to ZZ \to 4\ell$

Table 6.1: Summary of MC generators used to model signal and background processes, accuracy in QCD and the parton distribution function set.

Process	Generator	QCD accuracy	Tune and PDF set
$R \to SH \to 4\ell + E_{\mathrm{T}}^{\mathrm{miss}}$	Pythia8 [159]	LO	A14 NNPDF23LO
$A \to Z(\to X)H(\to 4\ell)$	MadGraph5+Pythia8 [158, 159]	LO	A14 NNPDF23LO
$A \to Z(\to 2\ell)H(\to 2\ell + X)$	MadGraph5+Pythia8 [158, 159]	LO	A14 NNPDF23LO
$qqZZ$	Sherpa+MePs [147–149, 152]	NLO (0- and 1-jet), LO (2- and 3-jet)	NNPDF30NNLO [150]
$ggZZ$	Sherpa+OpenLoops [147, 155–157]	LO (0- and 1-jet)	NNPDF30NNLO [150]
$qqZZ$ (EW)	Sherpa [147–149]	LO	NNPDF30NNLO [150]
$ZZZ(4\ell 2\nu, 6\ell 0\nu)$	Sherpa [147–149]	NNLO	NNPDF30NNLO [150]
$WZZ(5\ell 1\nu)$	Sherpa [147–149]	NNLO	NNPDF30NNLO [150]
$WWZ(4\ell 2\nu)$	Sherpa [147–149]	NNLO	NNPDF30NNLO [150]
$t\bar{t}V$ ($V = W/Z$)	MadGraph5+Pythia8 [158, 159]	LO	A14 NNPDF23LO
$t\bar{t}$	Powheg-Box+Pythia8 [159, 160]	NNLO+NNLO	A14 NNPDF23LO
$WZ \to 3\ell 1\nu$	Powheg-Box+Pythia8 [159, 160]	NNLO	CT10NLO, AZNLOCTEQ6L1 [150]
Z+jets	Sherpa+Comix+OpenLoops+MePs [147–149]	NLO (0- and 2-jet), LO (3- and 4-jet)	NNPDF30NNLO [150]



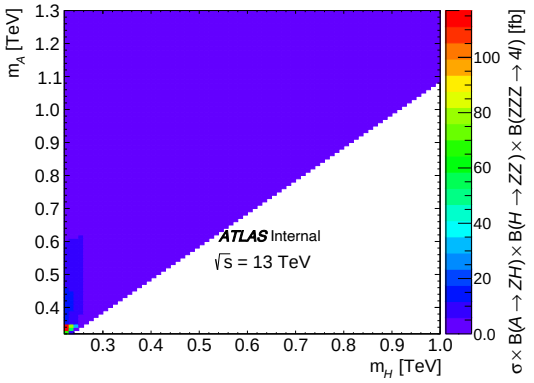
(a) (b)

Figure 6.3: 2D plots showing the energy gap of the (a) $R \to SH \to 4\ell + E_{\mathrm{T}}^{\mathrm{miss}}$ and (b) $A \to Z(\to X)H(\to 4\ell)$ and $A \to Z(\to 2\ell)H(\to 2\ell)$ models. The energy gap is represented by the z-axis as $m_R - m_H$ or $m_A - m_H$.

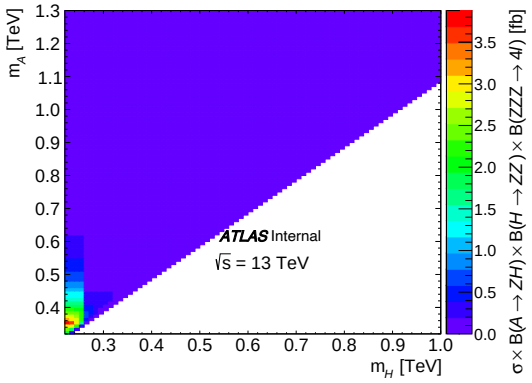
and the associated Z boson decays inclusively with the 1 fb assumed cross-section. Hence, the $A \to Z(\to 2\ell)H(\to 2\ell + X)$ is generated considering the associated Z boson decays to 2ℓ and the $H \to ZZ \to 2\ell + X$. The cross-section for this process is calculated as follows:

$$\begin{aligned} \sigma^{A\to Z(\to 2\ell)H(\to 2\ell+X)} &= 2 \cdot \left(\sigma^{A\to Z(\to X)H(\to 4\ell)} - \sigma^{A\to Z(\to 2\ell)H(\to 4\ell)}\right) \qquad (6.1) \\ &= 2 \cdot (1 - 0.067)\ \text{fb} \\ \sigma^{A\to ZH\to 4\ell+X}_{\text{total}} &= \sigma^{A\to Z(\to X)H(\to 4\ell)} + \sigma^{A\to Z(\to 2\ell)H(\to 2\ell+X)} \qquad (6.2) \\ &= 2.87\ \text{fb} \end{aligned}$$

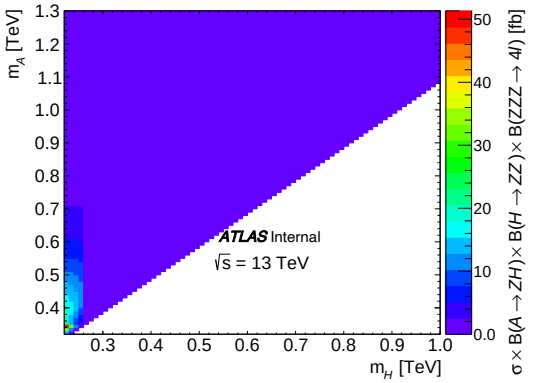
Further cross-section calculation using the 2HDM calculator [161] is performed for the $A \to Z(\nu\nu)H(ZZ) \to 4\ell + X$ signal. Figure 6.4 shows the cross-section multiplied by the BR for $A \to ZH$ times the BR for $H \to ZZ$ for different mass points, and $\tan(\beta)$ and $\cos(\beta - \alpha)$ assumption. All these terms are calculated by the 2HDM calculator, except the $ZZZ \to 4\ell$ is a constant value.



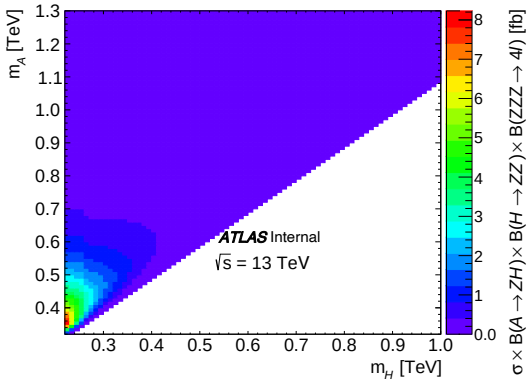
(a) Type-I with $\tan(\beta) = 0.5$ and $\cos(\beta-\alpha) = 0.1$



(b) Type-II with $\tan(\beta) = 7.0$ and $\cos(\beta - \alpha) = 0.1$



(c) Type-I with $\tan(\beta) = 1.0$ and $\cos(\beta-\alpha) = 0.4$



(d) Type-II with $\tan(\beta) = 3.0$ and $\cos(\beta - \alpha) = 0.4$

Figure 6.4: The cross-section of the $A \to Z(\nu\nu)H(ZZ) \to 4\ell + X$ calculated using the 2HDM with different $\tan(\beta)$ and $\cos(\beta - \alpha)$ assumptions.

6.3 Event selection

The events considered in this study, are classified into three different channels, based on the flavours of the selected leptons. These channels are 4μ, $4e$ and $2\mu 2e$, and are assigned on the basis of which triggers are activated in the event. They are selected with single-lepton, dilepton and trilepton triggers, including electron(s)-muon(s) triggers. Single-electron triggers apply *Medium* or *Tight* likelihood identification, whereas multi-electron triggers apply *Loose* or *Medium* identification. At least one vertex with two associated tracks having $p_{\mathrm{T}} > 500$ MeV should also be present for each event. The primary vertex is identified as the one with the highest sum of p_{T}^2 track.

The possible quadruplets in each channel of an event are created by picking two lepton pairs with the same flavour and opposite signs (SFOS). The p_{T} thresholds for the three leading leptons in the quadruplet should be: 20 GeV, 15 GeV and 10 GeV. The leading and the sub-leading lepton pairs in the quadruplet should have an invariant mass closest and second closest to the nominal mass of the Z boson. The invariant mass of the leading and sub-leading lepton pairs refer to as m_{Z_1} and m_{Z_2}, respectively. In the selected quadruplet, m_{Z_1} must be $50\,\mathrm{GeV} < m_{Z_1} < 106\,\mathrm{GeV}$ and $m_{Z_2} < 115\,\mathrm{GeV}$. The lower bound for m_{Z_2} is 12 GeV for $m_{4\ell} < 140\,\mathrm{GeV}$ and 50 GeV for $m_{4\ell} > 190\,\mathrm{GeV}$. For any value of $m_{4\ell}$ between 140 and 150 GeV, the bound will rise according to a linear slope.

In order to remove fake or non-prompt backgrounds, multiple additional cuts are placed on the leptons. Firstly, selected lepton pairs must have their leptons isolated from each other by $\Delta R > 0.1$. If any two SFOS leptons are detected with $m_{\ell\ell}$ below 5 GeV for 4μ and $4e$ quadruplets, the quadruplet is excluded to suppress the contamination from J/ψ mesons. If, at this point, several quadruplets of different channels are selected, only the quadruplet of the channel with the highest expected signal rate is retained in this order: 4μ, $2e2\mu$, $4e$.

Backgrounds which involve non-resonant and the associated production of four leptons, such as the Z+jets and $t\bar{t}$ processes, are suppressed using the impact-parameter and track- and calorimeter-based isolation requirements. The transverse impact-parameter significance is defined as the impact-parameter calculated with respect to the measured beam line position in the transverse plane divided by its uncertainty, $|d_0|/\sigma d_0$. This significance is required to be less than 3 for muons and 5 for electrons. Additionally, all leptons are required to be associated with the same originating vertex. Leptons are isolated using both track-based and calorimeter-based discriminants. The track-based discriminant takes into account the scalar p_{T} sum of all tracks in the width cone $\Delta R = 0.3$ for muons and 0.2 for electrons (excluding the lepton itself). The ratio of this sum to the lepton p_{T} is expected to be less than 0.15. The pile-up contributions are suppressed by requiring the cone tracks to originate from the primary vertex. In order to retain efficiency at higher p_{T}, the size of the track-isolation cone is reduced to $10\,\mathrm{GeV}/p_{\mathrm{T}}$ for p_{T} above 33 GeV for muons and 50 GeV for electrons.

Similarly, the calorimeter-based discriminant adds up the cluster E_{T} values used to reconstruct jets inside a cone of width $\Delta R = 0.2$ around the candidate leptons barycenter. The clusters used for isolation are the same as those used for the reconstruction of jets. The E_{T} sum divided by the p_{T} of the lepton must be

less than 0.3 for the muons and 0.2 for the electrons. The calculated calorimeter energy around the muon (within the cone of size $\Delta R = 0.1$) and the cells within 0.125×0.175 rad in $\eta \times \phi$ around the electron barycenter are removed from the respective sums. The pile-up and underlying-event contributions to the calorimeter isolation are subtracted event by event [162]. For both track- and calorimeter-based isolation requirements, any contribution resulting from other quadruplet leptons is subtracted. To further reduce the Z+jets and $t\bar{t}$ background contributions, an additional requirement based on a vertex-reconstruction algorithm is required. Track- and calorimeter-based isolation requirements are imposed on the vertexing of the 4ℓ events. Since leptons must originate from a common vertex, the vertexing algorithm [163] is used to fit the ID tracks of the 4ℓ candidates under the assumption that they emanate from a common vertex. The resulting fit quality (χ^2/ndof) is found to provide a good signal discrimination from backgrounds [164]. For the 4μ channel $\chi^2/\text{ndof} < 9$, and for the other channels, a loose cut of $\chi^2/\text{ndof} < 6$ is applied, which maintains a signal efficiency greater than 99% for all channels.

In Z boson decays, the QED process of radiative photon production is well modelled by simulation. In the calorimeter, some of the final-state-radiation (FSR) photons can be detected and incorporated into the analysis of $\ell^+\ell^-\ell^+\ell^-$. As in Run 1 [162], the strategy to use FSR photons in the reconstruction of Z bosons is the same. It consists of a search for collinear (muons) and non-collinear FSR photons (muons and electrons) with only one FSR photon per event permitted. By means of a Z-mass-constrained kinematic fit, the lepton four-momenta of both dilepton pairs are recomputed after the FSR correction [165]. After the FSR correction, the lepton four-momenta of the both dilepton pairs is recomputed by the Z-mass-constrained kinematic fit. The fit uses a Breit-Wigner Z boson lineshape and a single Gaussian function per lepton to model the momentum response function with a Gaussian width set to the expected resolution of each lepton. The Z-mass constraint is applied to both Z candidates and improves the resolution of $m_{4\ell}$ by around 15%. Table 6.2 summarises the object identification and event selection described above.

Table 6.2: Summary of the object identification and event selection requirements. The leading and sub-leading lepton pairs are denoted by m_{Z_1} and m_{Z_2}.

Physics Objects	
Electrons	
Loose Likelihood quality electrons with hit in innermost layer, $E_{\mathrm{T}} > 7$ GeV and $\lvert\eta\rvert < 2.47$	
Interaction point constraint: $\lvert z_0 \cdot \sin\theta\rvert < 0.5$ mm (if ID track is available)	
Muons	
Loose identification with $p_{\mathrm{T}} > 5$ GeV and $\lvert\eta\rvert < 2.7$	
Calo-tagged muons with $p_{\mathrm{T}} > 15$ GeV and $\lvert\eta\rvert < 0.1$, segment-tagged muons with $\lvert\eta\rvert < 0.1$	
Stand-alone and silicon-associated forward restricted to the $2.5 < \lvert\eta\rvert < 2.7$ region	
Combined, stand-alone (with ID hits if available) and segment-tagged muons with $p_{\mathrm{T}} > 5$ GeV	
Interaction point constraint: $\lvert d_0\rvert < 1$ mm and $\lvert z_0 \cdot \sin\theta\rvert < 0.5$ mm (if ID track is available)	
Jets	
anti-k_T jets with *bad-loose* identification, $p_{\mathrm{T}} > 30$ GeV and $\lvert\eta\rvert < 2.5$ (Central jets only)	
Overlap removal	
Jets within $\Delta R < 0.2$ of an electron or $\Delta R < 0.1$ of a muon are removed	
Vertex	
At least one collision vertex with at least two associated track	
Primary vertex	
Vertex with the largest p_{T}^2 sum	
Event Selection	
Quadruplet Selection	- Require at least one quadruplet of leptons consisting of two pairs of same-flavour opposite-charge leptons fulfilling the following requirements: - p_{T} thresholds for three leading leptons in the quadruplet: 20, 15 and 10 GeV - Maximum one calo-tagged or stand-alone muon or silicon-associated forward per quadruplet - Leading di-lepton mass requirement: $50 < m_{Z_1} < 106$ GeV - Sub-leading di-lepton mass requirement: $m_{\mathrm{threshold}} < m_{Z_2} < 115$ GeV - $\Delta R(\ell, \ell') > 0.10$ for all leptons in the quadruplet - Remove quadruplet if alternative same-flavour opposite-charge di-lepton gives $m_{\ell\ell} < 5$ GeV - Keep all quadruplets passing the above selection
Isolation	- Contribution from the other leptons of the quadruplet is subtracted - FixedCutPFlowLoose WP for all leptons
Impact Parameter Significance	- Apply impact-parameter significance cut to all leptons of the quadruplet - For electrons: $d_0/\sigma_{d_0} < 5$ - For muons: $d_0/\sigma_{d_0} < 3$
Best Quadruplet	- If more than one quadruplet has been selected, choose the quadruplet with highest Higgs decay ME according to channel: 4μ, $2e2\mu$, $2\mu2e$ and $4e$
Vertex Selection	- Require a common vertex for the leptons: - $\chi^2/\mathrm{ndof} < 6$ for 4μ and $\chi^2/\mathrm{ndof} < 9$ for others decay channels

6.4 Analysis strategy

After the pre-selection described in Section 6.3, an additional selection depending on the signal model is applied. This section focuses on determining signal regions where the invariant mass of the four leptons is above 200 GeV. The main source of background in this kinematic region is the leptonic decay of the Z boson. In all background processes, the quark and antiquark annihilation ($q\bar{q} \to ZZ$) is the most significant, accounting for approximately 84.6% of the expected background, while gluon-initiated production ($gg \to ZZ$) accounts for approximately 11.7%. Other SM backgrounds, such as $t\bar{t}V$, Z+jets, $t\bar{t}$, WZ, and VVV, account for about 2.6% of the total background events. These numbers were estimated from the MC simulation. However, this study modelled the SM backgrounds using an analytical function, discussed in Section 6.5, after determining the signal regions.

A cut-based categorization is applied to increase the sensitivity of the $R \to SH \to 4\ell + E_{\mathrm{T}}^{\mathrm{miss}}$ and $A \to ZH \to 4\ell + X$ signal models. This involves setting thresholds on various kinematic and topological variables, such as the number of jets ($N_{\mathrm{jets}}^{\mathrm{Central}}$) and b-jets ($N_{b\text{-jets}}$), the invariant mass of the two leading jets ($m_{jj}^{\mathrm{Central}}$), the momentum of the four-lepton system ($p_{\mathrm{T}}^{4\ell}$), and the $E_{\mathrm{T}}^{\mathrm{miss}}$ significance, defined as:

$$E_{\mathrm{T}}^{\mathrm{miss}}\ \text{significance} = \frac{E_{\mathrm{T}}^{\mathrm{miss}}}{\sqrt{\sum E_{\mathrm{T}}}}. \tag{6.3}$$

The aim is to distinguish signal events from background events and maximize the expected significance of the signals. To suppress top-related backgrounds such as $t\bar{t}$ and $t\bar{t}V$, events containing b-jets are vetoed. The remaining events are divided into two groups based on the number of jets: those with no jets ($N_{\mathrm{jets}}^{\mathrm{Central}} = 0$) and those with at least one jet ($N_{\mathrm{jets}}^{\mathrm{Central}} \geq 1$). A 2D scan is applied twice to each group using the $p_{\mathrm{T}}^{4\ell}$ and $E_{\mathrm{T}}^{\mathrm{miss}}$ significance. The initial scan identifies the optimal threshold values for the variables, while the subsequent scan detects other optimal thresholds that are lower than the initial ones. This process results in specific requirements on the variables that define the signal region. The signal region requirements depend on the number of jets and b-jets in the event. For events with no jets and no b-jets, $p_{\mathrm{T}}^{4\ell}$ must be greater than 20 GeV, and the $E_{\mathrm{T}}^{\mathrm{miss}}$ significance must be greater than 2. For events with at least one jet but no b-jets, $p_{\mathrm{T}}^{4\ell}$ must be greater than 10 GeV, and the $E_{\mathrm{T}}^{\mathrm{miss}}$ significance must be greater than 3.5. For events with at least one b-jet but no other jets for the scan below the previous thresholds, the $E_{\mathrm{T}}^{\mathrm{miss}}$ significance must be greater than 2.5. Therefore,

Table 6.3: Summary of the requirements of the signal regions selection for the $R \to SH \to 4\ell + E_{\mathrm{T}}^{\mathrm{miss}}$ and $A \to ZH \to 4\ell + X$ signals for $m_{4\ell} > 200\,\mathrm{GeV}$.

Category	$R \to SH \to 4\ell + E_{\mathrm{T}}^{\mathrm{miss}}$	$A \to ZH \to 4\ell + X$
High-$E_{\mathrm{T}}^{\mathrm{miss}}$ & $N_{\mathrm{jets}}^{\mathrm{Central}} = 0$	$N_{b\text{-jets}} = 0$, $N_{\mathrm{jets}}^{\mathrm{Central}} = 0$, $p_{\mathrm{T}}^{4\ell} > 20$, $E_{\mathrm{T}}^{\mathrm{miss}}$ sig > 2.0	
High-$E_{\mathrm{T}}^{\mathrm{miss}}$ & $N_{\mathrm{jets}}^{\mathrm{Central}} \geq 1$	$N_{b\text{-jets}} = 0$, $N_{\mathrm{jets}}^{\mathrm{Central}} \geq 1$, $p_{\mathrm{T}}^{4\ell} > 10$, $E_{\mathrm{T}}^{\mathrm{miss}}$ sig > 3.5	
Low-$E_{\mathrm{T}}^{\mathrm{miss}}$ & $N_{\mathrm{jets}}^{\mathrm{Central}} \geq 1$	$N_{b\text{-jets}} = 0$, $N_{\mathrm{jets}}^{\mathrm{Central}} \geq 1$, $E_{\mathrm{T}}^{\mathrm{miss}}$ sig > 2.5	
–	–	$N_{b\text{-jets}} \geq 1$
–	–	$\lvert m_{jj}^{\mathrm{Central}} - m_Z \rvert < 20$
–	–	$\lvert m_{jj}^{\mathrm{Central}} - m_Z \rvert > 20$
–	–	$N_{\mathrm{jets}}^{\mathrm{Central}} \geq 1$

events in the signal region are required to satisfy the following requirements:

- $N_{b\text{-jets}} = 0$ and $N_{\mathrm{jets}}^{\mathrm{Central}} = 0$ with $p_{\mathrm{T}}^{4\ell} > 20\,\mathrm{GeV}$ and $E_{\mathrm{T}}^{\mathrm{miss}}$ significance > 2
- $N_{b\text{-jets}} = 0$ and $N_{\mathrm{jets}}^{\mathrm{Central}} \geq 1$ with $p_{\mathrm{T}}^{4\ell} > 10\,\mathrm{GeV}$ and $E_{\mathrm{T}}^{\mathrm{miss}}$ significance > 3.5
- $N_{b\text{-jets}} = 0$ and $N_{b\text{-jets}} \geq 1$ with $E_{\mathrm{T}}^{\mathrm{miss}}$ significance > 2.5

The aforementioned signal regions are used for both $R \to SH \to 4\ell + E_{\mathrm{T}}^{\mathrm{miss}}$ and $A \to ZH \to 4\ell + X$ models. However, since the $A \to ZH \to 4\ell + X$ signal involves more jet activities, additional four-jet categories are defined as follows:

- The $N_{b\text{-jets}} \geq 1$ category requires at least one b-jet in the event.
- The $|m_{jj}^{\mathrm{Central}} - m_Z| < 20\,\mathrm{GeV}$ category includes events inside the m_Z peak within a 20 GeV.
- The $|m_{jj}^{\mathrm{Central}} - m_Z| > 20\,\mathrm{GeV}$ category for the events outside the m_Z peak within a 20 GeV.
- The $N_{\mathrm{jets}}^{\mathrm{Central}} \geq 1$ category requires at least one jet in the event.

Table 6.3 gives a summary of the signal regions defined for both models. Three signal regions were defined for the $R \to SH \to 4\ell + E_{\mathrm{T}}^{\mathrm{miss}}$ signal and the $A \to ZH \to 4\ell + X$ signal. Additional four signal regions were defined for the $A \to ZH \to 4\ell + X$ signal.

6.4.1 Signal optimisation

This section discusses the selection used for signal optimisation. The optimisation is quantified with the following significance formula:

$$Z_{\mathrm{Sig}_1} = \frac{s}{\sqrt{k \cdot b}}, \quad \text{and} \quad Z_{\mathrm{Sig}_2} = \frac{s}{\sqrt{s + k \cdot b}}, \tag{6.4}$$

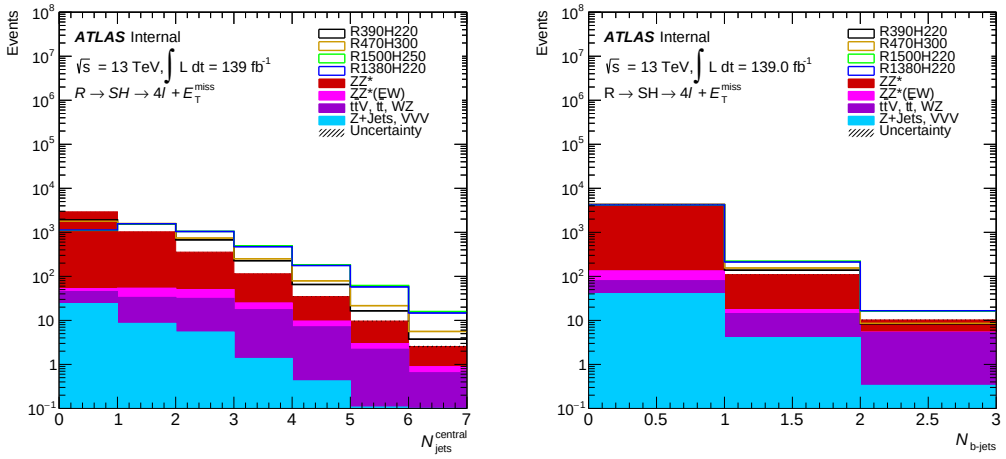
where s and b represent the signal and background events, respectively. Both the signal and the background are considered for $m_{4\ell} > 200\,\text{GeV}$. k is a fraction applied on the background to consider only the background under the signal peak. For instance, k for the $(m_R, m_H) = (390, 220)\,\text{GeV}$ signal is 19.9%; it is the ratio between events in the signal peak $\pm 10\,\text{GeV}$ and the entire $m_{4\ell}$ region greater than 200 GeV. The optimisation of each signal model is discussed in the following sections.

$R \to SH \to 4\ell + E_{\text{T}}^{\text{miss}}$ signal optimisation

For simplicity, four signal samples are selected to compare their shapes to the SM backgrounds for some kinematic distributions. Figure 6.5 shows number of jets and b-jets, and Figure 6.7 shows the 4ℓ invariant mass, 4ℓ momentum, $E_{\text{T}}^{\text{miss}}$ and $E_{\text{T}}^{\text{miss}}$ significance. Two signals with lower energy gap around 50 GeV, and the other with high energy gap above 600 GeV, are shown in Figure 6.7(c). The $E_{\text{T}}^{\text{miss}}$ significance is used on the optimisation instead of the $E_{\text{T}}^{\text{miss}}$ and object-based $E_{\text{T}}^{\text{miss}}$ significance [166], as it gives higher significance as shown in Appendix B.2. The zero central jets region contains most of the background, and it drops to $\sim 66\%$ in the one central jets region. After the preselection, b-tagged jets are vetoed to suppress $t\bar{t}$ related background. Events are then categorised into zero and at least one central jet regions. The $p_{\text{T}}^{4\ell}$ and $E_{\text{T}}^{\text{miss}}$ significance are employed to discriminate the signal from backgrounds by performing 2D scan. The $(m_R, m_H) = (390, 220)\,\text{GeV}$ signal sample is used on the optimisation because using a sample with low-$E_{\text{T}}^{\text{miss}}$ covers the ones with high-$E_{\text{T}}^{\text{miss}}$, see Figure 6.7(c). However, since the number of SM backgrounds under the high-$E_{\text{T}}^{\text{miss}}$ sample's peak is less than that of the low-$E_{\text{T}}^{\text{miss}}$ samples, this strategy underestimates the high-$E_{\text{T}}^{\text{miss}}$ sample significance, as demonstrated in Appendix B.3. Two optimal points are found at $E_{\text{T}}^{\text{miss}}$ significance $> 2.0\,\sqrt{\text{GeV}}$ and $p_{\text{T}}^{4\ell} > 20.0\,\text{GeV}$ with significance of 3.08 for the zero central jets region. This is shown in Figure 6.6(a) in which the Z_{Sig_1} formula in Equation 6.3 is used to calculate the significance. In addition, a comparison using Z_{Sig_2} is shown in Figure 6.6(c) where the same optimal points are found but with a low significance of 2.47. Another scan carried out at low-$E_{\text{T}}^{\text{miss}}$ after removing the optimal points. Figures 6.6(b) and 6.6(d) show the low-$E_{\text{T}}^{\text{miss}}$ scan results where $E_{\text{T}}^{\text{miss}}$ significance $> 1.5\,\sqrt{\text{GeV}}$ and $p_{\text{T}}^{4\ell} > 10.0\,\text{GeV}$ give the best significance of 0.78 and 0.73. The same technique is used for at least one central jet category, see Appendix B.2. The low-$E_{\text{T}}^{\text{miss}}$ scan of at least one central jets

Table 6.4: The expected yields for the $(m_R, m_H) = (390, 220)$ GeV signal mass point, and the total background calculated from the state-of-the-art MC simulation with an integrated luminosity of 139 fb^{-1}. The uncertainties included on the table are statistical uncertainty only. The expected events at the preselection are after the selection discussed in Section 6.3. $E_{\mathrm{T}}^{\mathrm{miss}}$ significance is represented by metSig on the table. The $R \to SH \to 4\ell + E_{\mathrm{T}}^{\mathrm{miss}}$ signal cross section is assumed to be 1 fb.

	$(m_R, m_H) = (390, 220)$ GeV	$qqZZ$	$ggZZ$	$qqZZ$(EW)	ttV	VVV	$Z+$jets	WZ	$t\bar{t}$	Total background
Preselection	64.54±0.26	2518.94±4.23	349.23±0.67	32.77±0.27	47.18±0.44	19.05±0.11	3.85±1.15	4.89±0.31	2.80±0.19	2978.72±7.38
b-veto	62.74±0.26	2458.26±4.21	342.44±0.67	30.97±0.26	12.24±0.23	18.54±0.11	3.73±1.15	4.75±0.31	1.85±0.14	2872.80±7.07
$N_{\mathrm{jets}}^{\mathrm{Central}} = 0$	27.91±0.17	1622.87±3.64	213.09±0.53	2.97±0.11	2.44±0.09	9.38±0.07	2.52±0.89	2.64±0.23	0.82±0.09	1856.73±5.65
$p_{\mathrm{T}}^{4\ell} > 20$ & metSig > 2.0	17.37±0.13	115.24±1.15	27.74±0.19	0.48±0.03	2.07±0.08	7.48±0.06	0.58±0.07	1.73±0.19	0.64±0.08	155.96±1.86
$p_{\mathrm{T}}^{4\ell} > 15$ & metSig > 1.5	5.11±0.07	177.34±1.26	34.58±0.21	0.49±0.03	0.19±0.03	0.79±0.02	0.33±0.05	0.45±0.10	0.06±0.02	214.23±1.72
Rest1	5.44±0.08	1330.29±3.21	150.77±0.44	2.00±0.10	0.19±0.03	1.11±0.02	1.61±0.89	0.45±0.10	0.12±0.03	1486.54±4.82
$N_{\mathrm{jets}}^{\mathrm{Central}} \geq 1$	34.83±0.19	835.39±2.11	129.36±0.41	28.00±0.24	9.80±0.21	9.16±0.08	1.21±0.73	2.12±0.21	1.04±0.11	1016.07±4.09
$p_{\mathrm{T}}^{4\ell} > 10$ & metSig > 3.5	13.26±0.12	12.93±0.25	2.68±0.06	0.38±0.02	5.31±0.15	4.78±0.06	0.05±0.02	0.75±0.12	0.58±0.08	27.47±0.77
$p_{\mathrm{T}}^{4\ell} > 0$ & metSig > 2.5	8.30±0.09	44.15±0.45	8.54±0.10	1.18±0.04	1.79±0.09	1.51±0.03	0.11±0.03	0.32±0.08	0.20±0.06	57.78±0.89
Rest2	13.28±0.12	778.31±2.05	118.15±0.39	26.45±0.23	2.71±0.11	2.87±0.04	1.05±0.73	1.04±0.14	0.25±0.04	930.82±3.74



(a) (b)

Figure 6.5: Distribution for the $R \to SH \to 4\ell + E_{\mathrm{T}}^{\mathrm{miss}}$ signal compared to the different background components of the (a) Number of central jets, (b) Number of b-tagged jets. Each signal is normalised to the total number of the background.

region gives the best cuts at $p_{\mathrm{T}}^{4\ell} > 2.5\,\mathrm{GeV}$ and $E_{\mathrm{T}}^{\mathrm{miss}}$ significance $> 2.5\sqrt{\mathrm{GeV}}$ when using the Z_{Sig_1} formula. The $p_{\mathrm{T}}^{4\ell} > 0\,\mathrm{GeV}$ cut is considered in this case since the significance is the same for these points. The cross section significance's formula, Z_{Sig_2}, gives slightly different optimal points than the Z_{Sig_1}. However, the optimal points discovered by Z_{Sig_1} formula are used. A cut-flow of the zero and at least one central jet regions with their optimal points found after the 2D scan is shown in Table 6.4. A summary of the optimal cuts, their representation and the significance of each cut is shown in Table 6.6. The combined significance for the $R \to SH \to 4\ell + E_{\mathrm{T}}^{\mathrm{miss}}$ signal optimisation is 6.85. It is obtained by the quadrature sum of all the categories except the low-$E_{\mathrm{T}}^{\mathrm{miss}}$ of the zero central jets region.

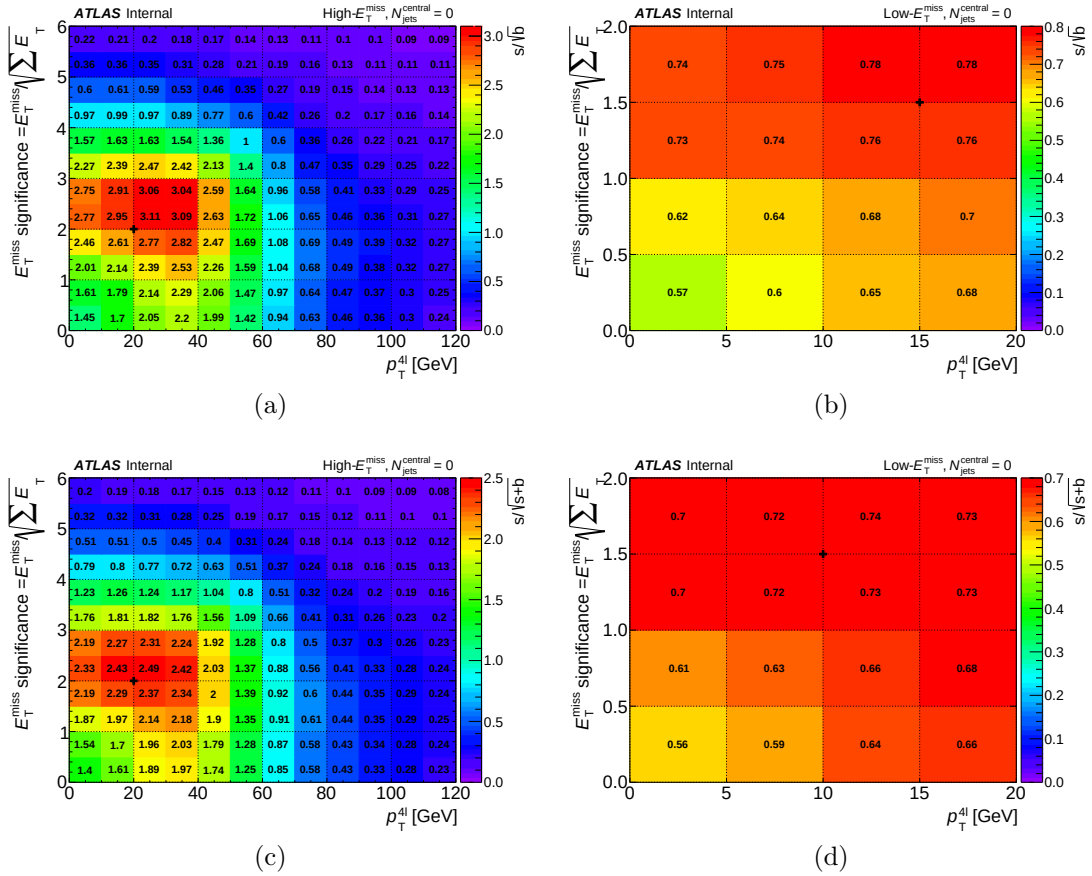


Figure 6.6: 2D scan of the $p_{\mathrm{T}}^{4\ell}$ and $E_{\mathrm{T}}^{\mathrm{miss}}$ significance for the $R \to SH \to 4\ell + E_{\mathrm{T}}^{\mathrm{miss}}$ signal in the zero central jets region. The z-axis shows the significance calculated using $s/\sqrt{b}$ (top) and $s/\sqrt{s+b}$ (bottom). The High-$E_{\mathrm{T}}^{\mathrm{miss}}$ scans are shown in (a) and (c), and Low-$E_{\mathrm{T}}^{\mathrm{miss}}$ in (b) and (d).

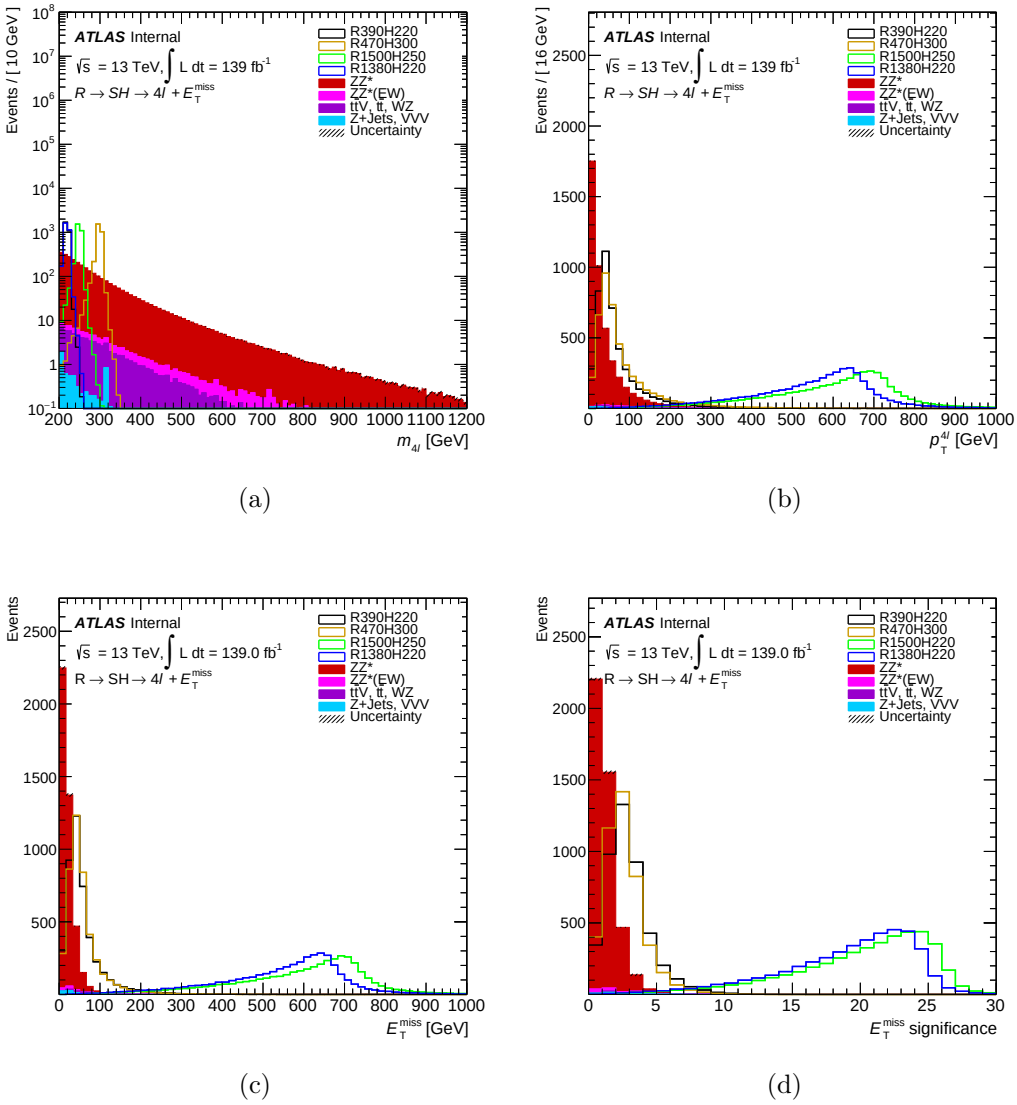
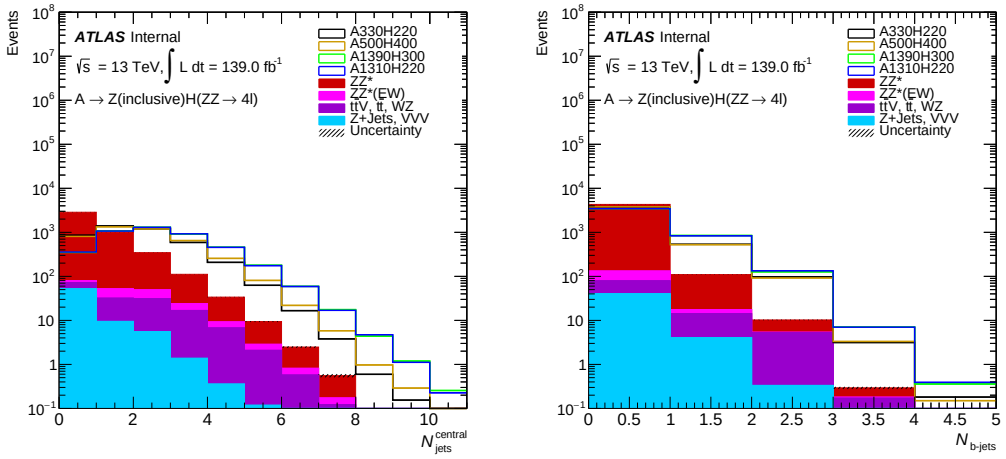


Figure 6.7: Distribution for the $R \to SH \to 4\ell + E_{\mathrm{T}}^{\mathrm{miss}}$ signal compared to the different background components of the (a) Four-lepton invariant mass, (b) Four-lepton transverse momentum, (c) Missing transverse energy and (d) $E_{\mathrm{T}}^{\mathrm{miss}}$ significance. Each signal is normalised to the total number of background to obtain a better comparison to the background.

$A \to Z(\nu\nu)H(ZZ) \to 4\ell + X$ signal optimisation

Although the $A \to Z(\nu\nu)H(ZZ) \to 4\ell + X$ signal consists of both $A \to Z(\to X)H(\to 4\ell)$ and $A \to Z(\to 2\ell)H(\to 2\ell + X)$ signals, the $A \to Z(\to X)H(\to 4\ell)$ process is used in the optimisation. Figure 6.9 shows that $A \to Z(\to X)H(\to 4\ell)$



(a) (b)

Figure 6.8: Distribution for the $A \to Z(\nu\nu)H(ZZ) \to 4\ell + X$ signal compared to the different background components of (a) Number of central jets and (b) Number of b-tagged jets. Each signal is normalised to the total number of SM backgrounds.

signal model has the same $p_{\mathrm{T}}^{4\ell}$ and $E_{\mathrm{T}}^{\mathrm{miss}}$ significance kinematics as the $R \to SH \to 4\ell + E_{\mathrm{T}}^{\mathrm{miss}}$ model. Therefore, the same four $E_{\mathrm{T}}^{\mathrm{miss}}$ categories developed for the $R \to SH \to 4\ell + E_{\mathrm{T}}^{\mathrm{miss}}$ signal hypothesis can be used. With the $(m_A, m_H) = (320, 220)$ GeV mass point, the combined significance for $E_{\mathrm{T}}^{\mathrm{miss}}$ categories is found to be 2.23. This value is less than the combined $E_{\mathrm{T}}^{\mathrm{miss}}$ significance for the $R \to SH \to 4\ell + E_{\mathrm{T}}^{\mathrm{miss}}$ signal. It can be noticed that the significance for the Low-$E_{\mathrm{T}}^{\mathrm{miss}}$ in the 0-jets category is less than the other $E_{\mathrm{T}}^{\mathrm{miss}}$ categories. Figure 6.8 shows up to ten central jets and five b-tagged jets for the $A \to Z(\to X)H(\to 4\ell)$. Thus, further jet categorisations are required in addition to the $E_{\mathrm{T}}^{\mathrm{miss}}$ categories. Since the $E_{\mathrm{T}}^{\mathrm{miss}}$ categories vetoed b-tagged jets, events with at least one b-jet can be considered a category.

This gives a significance of 1.87, which is more significant than each of the individual $E_{\mathrm{T}}^{\mathrm{miss}}$ categories. Figure 6.10 shows the kinematic distributions of the central jet for the leading and the sub-leading jet. The invariant mass of the first two jets is more useful in further classifying the events. Events inside and outside the $m_{\mathrm{jj}}^{\mathrm{central}}$ peak within 20 GeV and are selected as two separate categories. They yield a significance of 2.04 and 1.86 for the inside and outside the $m_{\mathrm{jj}}^{\mathrm{central}}$ peak categories, respectively. Then events with exactly one central jet are selected

Table 6.5: The expected yields for the $(m_A, m_H) = (330, 220)$ GeV signal mass point, and the significance calculated from the state-of-the-art MC simulation with an integrated luminosity of 139 fb^{-1}. The uncertainties included on the table are statistical uncertainty only. The expected events at the preselection are after the selection discussed in Section 6.3. The $A \to Z(\to X)H(\to 4\ell)$ and $A \to Z(\to X)H(\to 4\ell)$ cross-sections are assumed to be 1 fb and 1.87 fb, respectively.

	$A \to Z(\to 2\ell)H(\to 2\ell + X)$	$A \to Z(\to X)H(\to 4\ell)$	$q\bar{q} \to ZZ$	$gg \to ZZ$	$q\bar{q} \to ZZ$ (EW)	$t\bar{t}V$	VVV	Z+jets	WZ	$t\bar{t}$	N backgrounds
Preselection	71.24±0.40	60.92±0.12	2518.94±4.23	349.23±0.67	32.77±0.27	47.18±0.44	19.05±0.11	3.85±1.15	4.89±0.31	2.80±0.19	459.78±3.15
High-$E_{\mathrm{T}}^{\mathrm{miss}}$ & $N_{\mathrm{jets}}^{\mathrm{Central}} = 0$	7.18±0.13	6.15±0.04	115.24±1.15	27.74±0.19	0.48±0.03	2.07±0.08	7.48±0.06	0.58±0.07	1.73±0.19	0.64±0.08	40.72±0.71
Low-$E_{\mathrm{T}}^{\mathrm{miss}}$ & $N_{\mathrm{jets}}^{\mathrm{Central}} = 0$	1.82±0.06	1.82±0.02	177.34±1.04	34.58±0.18	0.49±0.03	0.19±0.03	0.79±0.02	0.33±0.03	0.45±0.08	0.06±0.02	36.89±0.38
High-$E_{\mathrm{T}}^{\mathrm{miss}}$ & $N_{\mathrm{jets}}^{\mathrm{Central}} \geq 1$	4.28±0.10	3.16±0.03	12.93±0.23	2.68±0.06	0.38±0.02	5.31±0.15	4.78±0.06	0.05±0.02	0.75±0.12	0.58±0.07	14.53±0.51
Low-$E_{\mathrm{T}}^{\mathrm{miss}}$ & $N_{\mathrm{jets}}^{\mathrm{Central}} \geq 1$	5.52±0.11	4.74±0.03	44.15±0.46	8.54±0.11	1.18±0.04	1.79±0.09	1.51±0.03	0.11±0.03	0.32±0.08	0.20±0.07	13.64±0.45
$N_{b-\mathrm{jets}} \geq 1$	11.12±0.16	8.66±0.05	60.68±0.49	6.79±0.10	1.80±0.06	34.94±0.38	0.50±0.02	0.12±0.03	0.14±0.05	0.95±0.13	45.24±0.77
$\lvert m_{jj}^{\mathrm{Central}} - m_Z \rvert < 20$	7.68±0.13	6.77±0.04	44.10±0.29	7.38±0.10	2.16±0.07	0.30±0.04	0.19±0.01	0.00±0.00	0.04±0.03	0.01±0.01	10.07±0.25
$\lvert m_{jj}^{\mathrm{Central}} - m_Z \rvert > 20$	16.06±0.19	13.19±0.06	196.51±0.60	27.79±0.19	15.09±0.16	1.35±0.09	1.09±0.02	0.80±0.73	0.31±0.08	0.08±0.02	46.50±1.29
$N_{\mathrm{jets}}^{\mathrm{Central}} = 1$	14.55±0.18	12.74±0.06	537.70±1.94	82.98±0.33	9.20±0.15	1.06±0.06	1.60±0.03	0.24±0.05	0.69±0.12	0.17±0.04	95.94±0.77
Rest	3.03±0.09	3.68±0.03	1330.29±3.29	150.77±0.46	2.00±0.10	0.19±0.03	1.11±0.02	1.61±0.89	0.45±0.11	0.12±0.03	156.25±1.65

Table 6.6: Summary of the $A \to Z(\nu\nu)H(ZZ) \to 4\ell + X$ and $R \to SH \to 4\ell + E_{\mathrm{T}}^{\mathrm{miss}}$ categories, significance calculated using Equation 6.4. The combined significance is the sum in quadrature taking from all the categories except the low-$E_{\mathrm{T}}^{\mathrm{miss}}$ of the zero central jets region.

Categories			Representation	$Z_{\mathrm{Sig_i}} = s/\sqrt{b}$	
				$A \to Z(\nu\nu)H(ZZ) \to 4\ell + X$	$R \to SH \to 4\ell + E_{\mathrm{T}}^{\mathrm{miss}}$
$E_{\mathrm{T}}^{\mathrm{miss}}$ categories	$N_{\mathrm{jets}}^{\mathrm{Central}} = 0$	$p_{\mathrm{T}}^{4\ell} > 20$ & $E_{\mathrm{T}}^{\mathrm{miss}}$ significance > 2.0	High-$E_{\mathrm{T}}^{\mathrm{miss}}$ & $N_{\mathrm{jets}}^{\mathrm{Central}} = 0$	1.10	3.11
		$p_{\mathrm{T}}^{4\ell} > 15$ & $E_{\mathrm{T}}^{\mathrm{miss}}$ significance > 1.5	Low-$E_{\mathrm{T}}^{\mathrm{miss}}$ & $N_{\mathrm{jets}}^{\mathrm{Central}} = 0$	0.28	0.78
	$N_{\mathrm{jets}}^{\mathrm{Central}} \geq 1$	$p_{\mathrm{T}}^{4\ell} > 10$ & $E_{\mathrm{T}}^{\mathrm{miss}}$ significance > 3.5	High-$E_{\mathrm{T}}^{\mathrm{miss}}$ & $N_{\mathrm{jets}}^{\mathrm{Central}} \geq 1$	1.35	5.66
		$p_{\mathrm{T}}^{4\ell} > 0$ & $E_{\mathrm{T}}^{\mathrm{miss}}$ significance > 2.5	Low-$E_{\mathrm{T}}^{\mathrm{miss}}$ & $N_{\mathrm{jets}}^{\mathrm{Central}} \geq 1$	1.39	2.44
Jet categories	$N_{b-\mathrm{jets}} \geq 1$		$N_{b-\mathrm{jets}} \geq 1$	1.88	-
	$\lvert m_{\mathrm{jj}}^{\mathrm{Central}} - m_Z \rvert < 20$		$\lvert m_{\mathrm{jj}}^{\mathrm{Central}} - m_Z \rvert < 20$	2.05	-
	$\lvert m_{\mathrm{jj}}^{\mathrm{Central}} - m_Z \rvert > 20$		$\lvert m_{\mathrm{jj}}^{\mathrm{Central}} - m_Z \rvert > 20$	1.89	-
	$N_{\mathrm{jets}}^{\mathrm{Central}} = 1$		$N_{\mathrm{jets}}^{\mathrm{Central}} = 1$	1.13	-
Combined significance				4.19	6.90

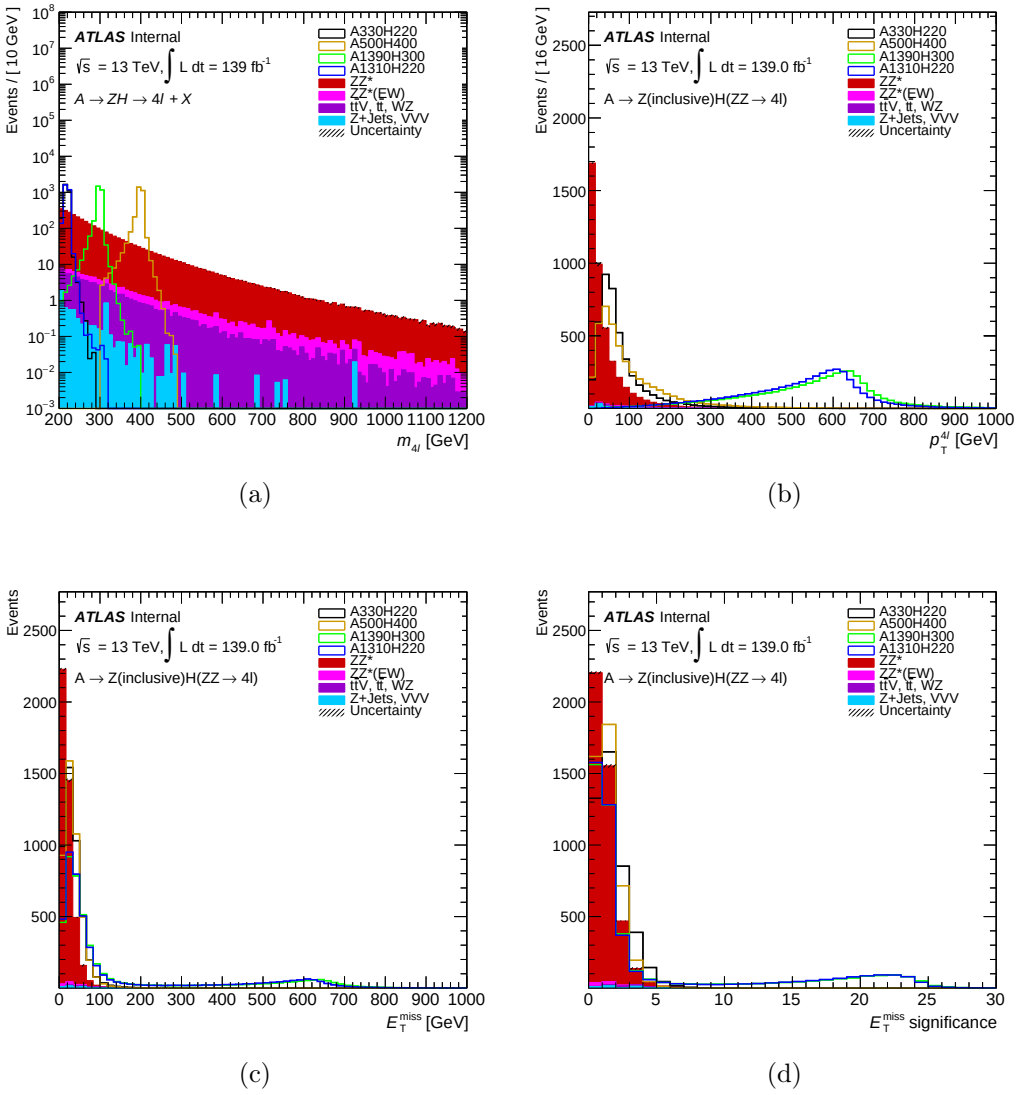
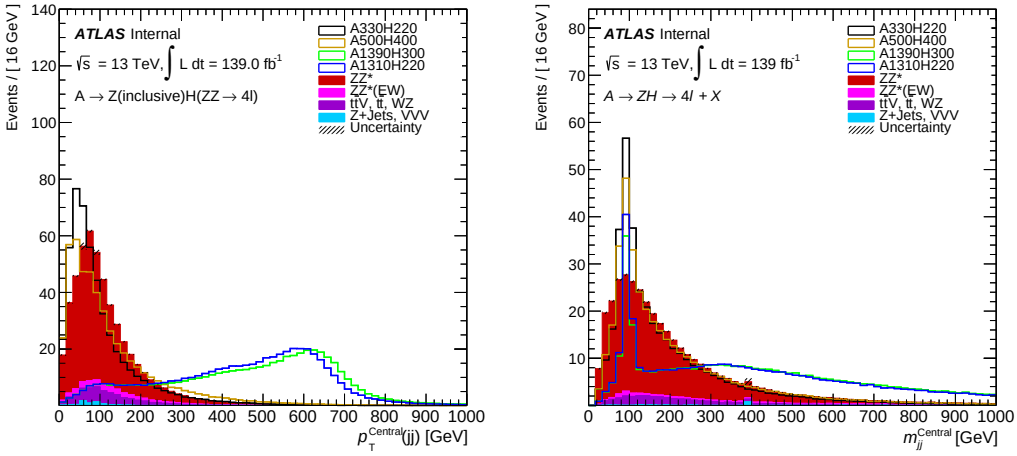
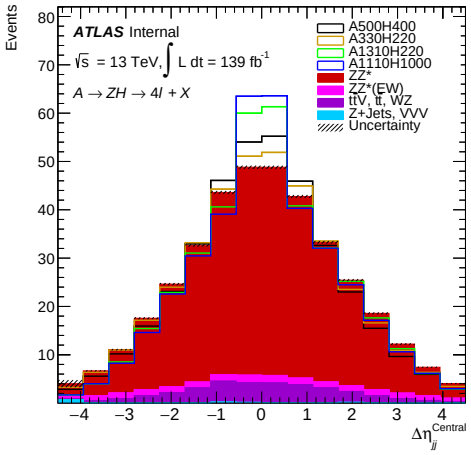


Figure 6.9: Distribution for the $A \to Z(\to X)H(\to 4\ell)$ signal comparing to the different background components of the (a) Four-lepton invariant mass, (b) Four-lepton transverse momentum, (c) Missing transverse energy and (d) $E_{\mathrm{T}}^{\mathrm{miss}}$ significance. Each signal is normalised to the total number of the background.

with 1.12 significance and the rest of the events are moved to the Rest category. The significance of the Low-$E_{\mathrm{T}}^{\mathrm{miss}}$ & $N_{\mathrm{jets}}^{\mathrm{Central}} = 0$ and the Rest categories are 0.28 and 0.21, respectively. The Rest category does not contain any events of interest and are discarded for this study. Also, the Low-$E_{\mathrm{T}}^{\mathrm{miss}}$ & $N_{\mathrm{jets}}^{\mathrm{Central}} = 0$ category is dropped since its significance is very small. The combined significance for the six categories of the $A \to Z(\nu\nu)H(ZZ) \to 4\ell{+}X$ model is 4.15. Table 6.5 summarises



(a) (b)



(c)

Figure 6.10: Distribution for the $A \to Z(\to X)H(\to 4\ell)$ signal comparing to the different background components of the (a) Di-jet transverse momentum, (b) Di-jet invariant mass and (c) Di-jet $\Delta\eta$. Each signal is normalised to the total number of background.

the expected yields per category for the signal and the individual background component. The significance is calculated using equation 6.4 and summarised in Table 6.6. To compare the significance for different signal hypothesis, see tables in Appendix B.3. Since only the background under the signal peak is used, signals with a higher energy gap are underestimated in their significance. The same study is performed using jets instead of central jets. It turns out that using central jets

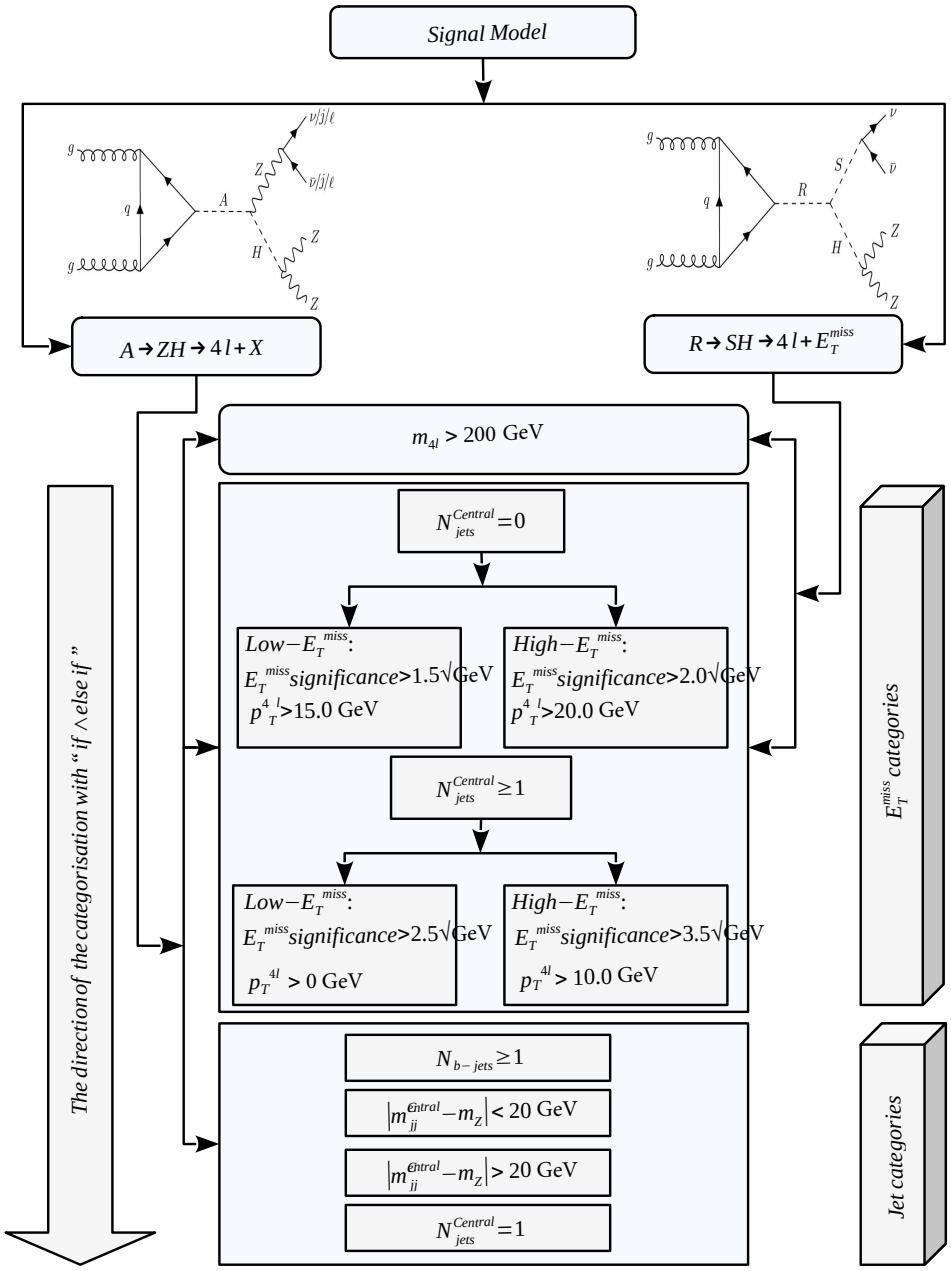


Figure 6.11: Diagram illustrates the categorisation scheme for $A \rightarrow Z(\nu\nu)H(ZZ) \rightarrow 4\ell + X$ and $R \rightarrow SH \rightarrow 4\ell + E_{\mathrm{T}}^{\mathrm{miss}}$ optimisation. Eight orthogonal categories are developed for the $A \rightarrow Z(\nu\nu)H(ZZ) \rightarrow 4\ell + X$ signal and four for $R \rightarrow SH \rightarrow 4\ell + E_{\mathrm{T}}^{\mathrm{miss}}$ signal.

improves the significance by about 6%. Figure 6.11 summarises the categorisation scheme for $A \rightarrow Z(\nu\nu)H(ZZ) \rightarrow 4\ell + X$ and $R \rightarrow SH \rightarrow 4\ell + E_{\mathrm{T}}^{\mathrm{miss}}$ optimisation.

6.4.2 Signal acceptance

The signal acceptance is calculated using simulated events for both $R \to SH \to 4\ell + E_{\mathrm{T}}^{\mathrm{miss}}$ and $A \to Z(\nu\nu)H(ZZ) \to 4\ell + X$ signals. The acceptance is evaluated with the ratio of the reconstructed events after selection requirements to the events after pre-selections. Table B.3 summarises the $R \to SH \to 4\ell + E_{\mathrm{T}}^{\mathrm{miss}}$ signal acceptances for four categories. The $A \to Z(\to X)H(\to 4\ell)$ and $A \to Z(\to 2\ell)H(\to 2\ell + X)$ signals and acceptances for seven categories are shown in Tables 6.8 and B.4. These tables show the acceptances for the H mass of 220 and 250 GeV. The background estimation for this study is documented in Appendix B.4.

6.5 Signal and background parametrisation

Monte Carlo simulation is used to parametrise the constructed four leptons invariant mass distribution of both background and signal shapes. This section explains the signal and background modelling.

6.5.1 Signal modelling

The signal line shapes are taken directly from the MC simulation. However, since a few mass points are generated as described in Section 6.2, for $R \to SH \to 4\ell + E_{\mathrm{T}}^{\mathrm{miss}}$ and $A \to Z(\nu\nu)H(ZZ) \to 4\ell + X$ signals, interpolation is needed to cover the entire ($m_{R/A}$, m_H) parameter-space. A linear interpolation method described in Ref. [167] is used to get signal shapes in between the generated masses in the ($m_{R/A}$, m_H) plane. Since the signal depends on the A and H masses, interpolating the signal must be done in two steps. The first step is to fix the H mass and interpolate the energy gap or the A mass. For example, Figure 6.12 shows the interpolated $A \to Z(\to X)H(\to 4\ell)$ signal with the mass of the H fixed to 500 GeV and 100 different values for the A mass. This is achieved by considering the formula for generating the mass points and varying the A mass by 10 GeV. The new 100 mass points are illustrated in Figure 6.12 using the gradient colour. In addition, three signals (blue, green and cyan) with different energy gaps used during the interpolation, are compared to the interpolated signals.

The interpolated signals along A mass are input for a second interpolation step where the A mass is fixed, and the H mass is varied by 10 GeV. The output

Table 6.7: The signal acceptance times efficiencies for the $R \to SH \to 4\ell + E_{\mathrm{T}}^{\mathrm{miss}}$ signal taken from fully simulated MC samples. The S mass is fixed to 160 GeV, and the H and R masses are varied with $m_R = m_S + m_H + m_{\mathrm{Gap}}$. The m_{Gap} is set to be 10, 20, 30, 40, 50, 100, 200, 500, and 1000 GeV, to generate different signals. The table shows the acceptance times efficiencies for signals with H masses of 220 and 250 GeV.

(m_R, m_H) GeV	$N_{\mathrm{jets}}^{\mathrm{Central}} = 0$		$N_{\mathrm{jets}}^{\mathrm{Central}} \geq 1$	
	High-$E_{\mathrm{T}}^{\mathrm{miss}}$	Low-$E_{\mathrm{T}}^{\mathrm{miss}}$	High-$E_{\mathrm{T}}^{\mathrm{miss}}$	Low-$E_{\mathrm{T}}^{\mathrm{miss}}$
390, 220	12.33%	3.64%	9.34%	5.85%
450, 220	19.02%	0.39%	20.40%	2.83%
800, 220	17.25%	0.03%	32.59%	0.46%
400, 220	16.49%	1.85%	12.35%	5.41%
410, 220	17.73%	1.07%	14.61%	4.87%
420, 220	18.14%	0.77%	16.70%	4.24%
430, 220	18.56%	0.59%	18.22%	3.70%
480, 220	18.93%	0.26%	22.84%	2.08%
580, 220	18.68%	0.10%	27.21%	1.15%
880, 220	17.24%	0.02%	33.83%	0.39%
1380, 220	14.04%	0.00%	38.19%	0.14%
450, 250	18.07%	0.84%	17.27%	4.52%
1500, 250	14.53%	0.00%	40.72%	0.14%
420, 250	12.52%	3.76%	9.07%	6.17%
430, 250	16.29%	1.78%	12.38%	5.91%
440, 250	17.71%	1.19%	14.92%	5.41%
460, 250	18.67%	0.62%	18.99%	3.95%
510, 250	19.13%	0.30%	23.82%	2.31%
610, 250	18.96%	0.10%	28.55%	1.18%
910, 250	17.12%	0.02%	35.22%	0.40%
1410, 250	14.46%	0.01%	40.44%	0.12%

$A \to Z(\to X)H(\to 4\ell)$ signal along H mass can be seen in Figure 6.13, where the A mass is fixed to 500 GeV. Similarly, the $A \to Z(\to 2\ell)H(\to 2\ell + X)$ signal shapes are interpolated, as shown in Appendix B.6, Figures B.12 and B.13. The final $A \to Z(\nu\nu)H(ZZ) \to 4\ell + X$ signal is constructed by merging the interpolated $A \to Z(\to X)H(\to 4\ell)$ and $A \to Z(\to 2\ell)H(\to 2\ell + X)$ signals, as shown in Appendix B.6, Figure B.14. The same interpolating procedures are used for the $R \to SH \to 4\ell + E_{\mathrm{T}}^{\mathrm{miss}}$ signal to get the mass points between the generated samples, as demonstrated in Appendix B.6, Figures B.15 and B.16.

Table 6.8: The signal acceptance times efficiencies for the $A \to Z(\to X)H(\to 4\ell)$ signal taken from the fully simulated MC samples. The Z boson mass is fixed to 90 GeV, and the H and A masses are varied with $m_A = m_Z + m_H + m_{\text{Gap}}$. The m_{Gap} is set to be 10, 20, 30, 40, 50, 100, 200, 500, and 1000 GeV, to generate different signals. The table shows the acceptance times efficiencies for signals with H masses of 220 and 250 GeV.

(m_A, m_H) GeV	$N_{\text{jets}}^{\text{Central}} = 0$		$N_{\text{jets}}^{\text{Central}} \geq 1$		$N_{b\text{-jets}} \geq 1$	$\lvert m_{\text{jj}}^{\text{Central}} - m_Z \rvert < 20\,\text{GeV}$	$\lvert m_{\text{jj}}^{\text{Central}} - m_Z \rvert > 20\,\text{GeV}$	$N_{\text{jets}}^{\text{Central}} = 1$
	High-$E_{\text{T}}^{\text{miss}}$	Low-$E_{\text{T}}^{\text{miss}}$	High-$E_{\text{T}}^{\text{miss}}$	Low-$E_{\text{T}}^{\text{miss}}$				
320, 220	3.46%	1.84%	1.66%	3.17%	6.02%	4.56%	8.82%	9.27%
330, 220	4.38%	1.29%	2.21%	3.32%	6.51%	4.78%	9.22%	9.04%
340, 220	4.76%	0.96%	2.78%	3.31%	6.96%	4.96%	9.66%	8.70%
350, 220	4.88%	0.77%	3.33%	3.22%	7.31%	5.17%	10.14%	8.30%
360, 220	4.94%	0.66%	3.78%	3.10%	7.62%	5.40%	10.49%	7.92%
410, 220	4.92%	0.47%	5.14%	2.58%	8.63%	6.69%	11.53%	6.44%
510, 220	4.68%	0.37%	6.49%	2.14%	9.93%	8.75%	12.12%	4.88%
810, 220	4.11%	0.25%	8.38%	1.59%	11.99%	12.04%	12.29%	3.68%
1310, 220	3.46%	0.19%	9.71%	1.59%	12.86%	3.65%	17.72%	6.75%
350, 250	3.36%	1.89%	1.53%	3.21%	6.39%	4.87%	9.76%	10.08%
360, 250	4.38%	1.34%	2.12%	3.46%	6.89%	5.02%	10.20%	9.72%
370, 250	4.71%	0.99%	2.75%	3.41%	7.37%	5.24%	10.68%	9.14%
380, 250	4.85%	0.79%	3.35%	3.31%	7.72%	5.42%	11.05%	8.67%
390, 250	4.88%	0.67%	3.83%	3.14%	7.98%	5.73%	11.39%	8.20%
440, 250	4.90%	0.46%	5.33%	2.63%	9.10%	6.91%	12.39%	6.48%
540, 250	4.73%	0.36%	6.73%	2.13%	10.43%	9.06%	12.83%	4.92%
840, 250	4.14%	0.26%	8.71%	1.67%	12.43%	12.26%	12.80%	3.76%
1340, 250	3.55%	0.20%	10.25%	1.76%	13.47%	3.62%	18.63%	7.11%

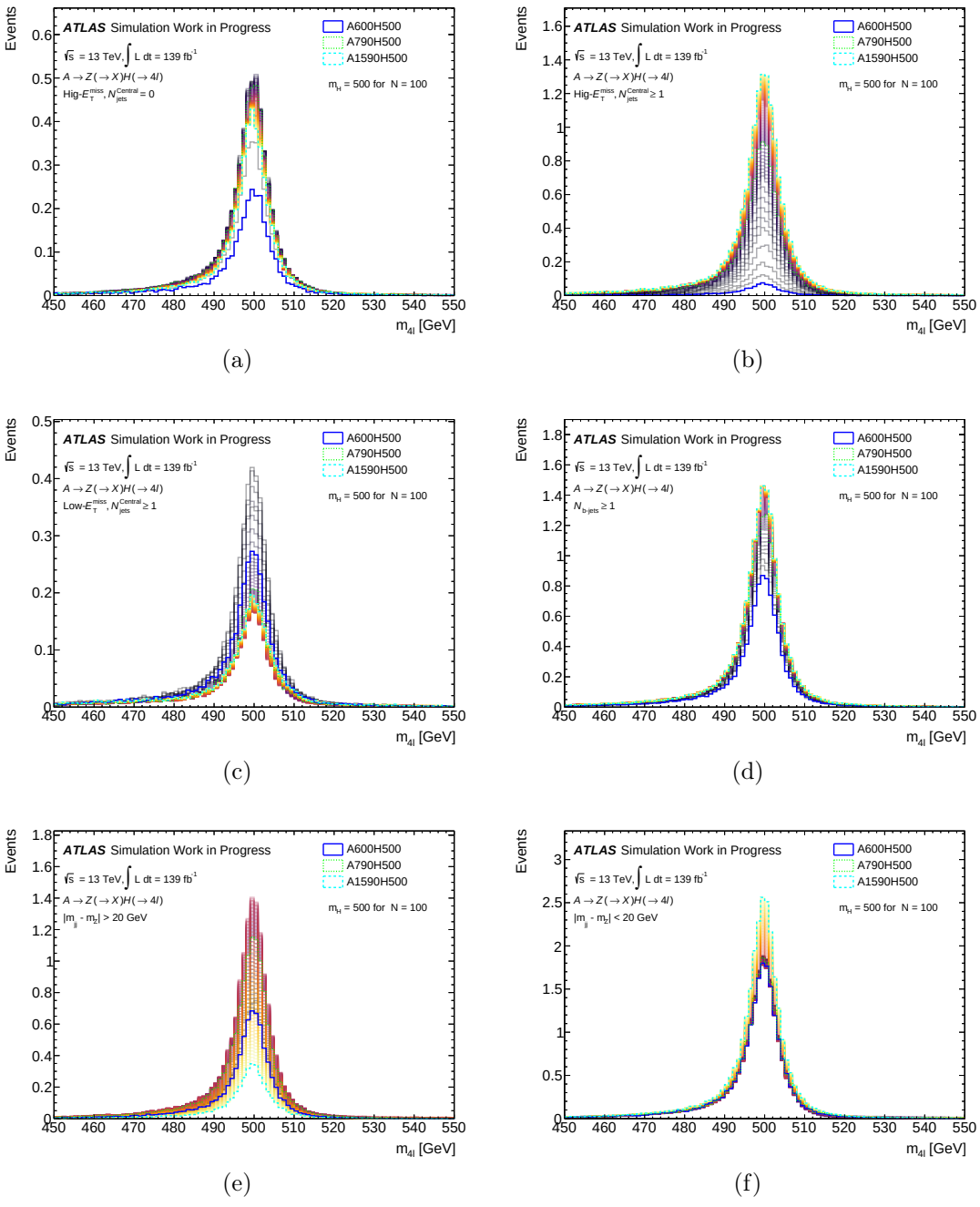


Figure 6.12: The invariant mass of the four leptons of the interpolated $A \to Z(\to X)H(\to 4\ell)$ signal shape with H mass fixed to 500 GeV and A mass varied by 10 GeV. The blue, green and cyan histogram are the original histograms used in the input for different categories.

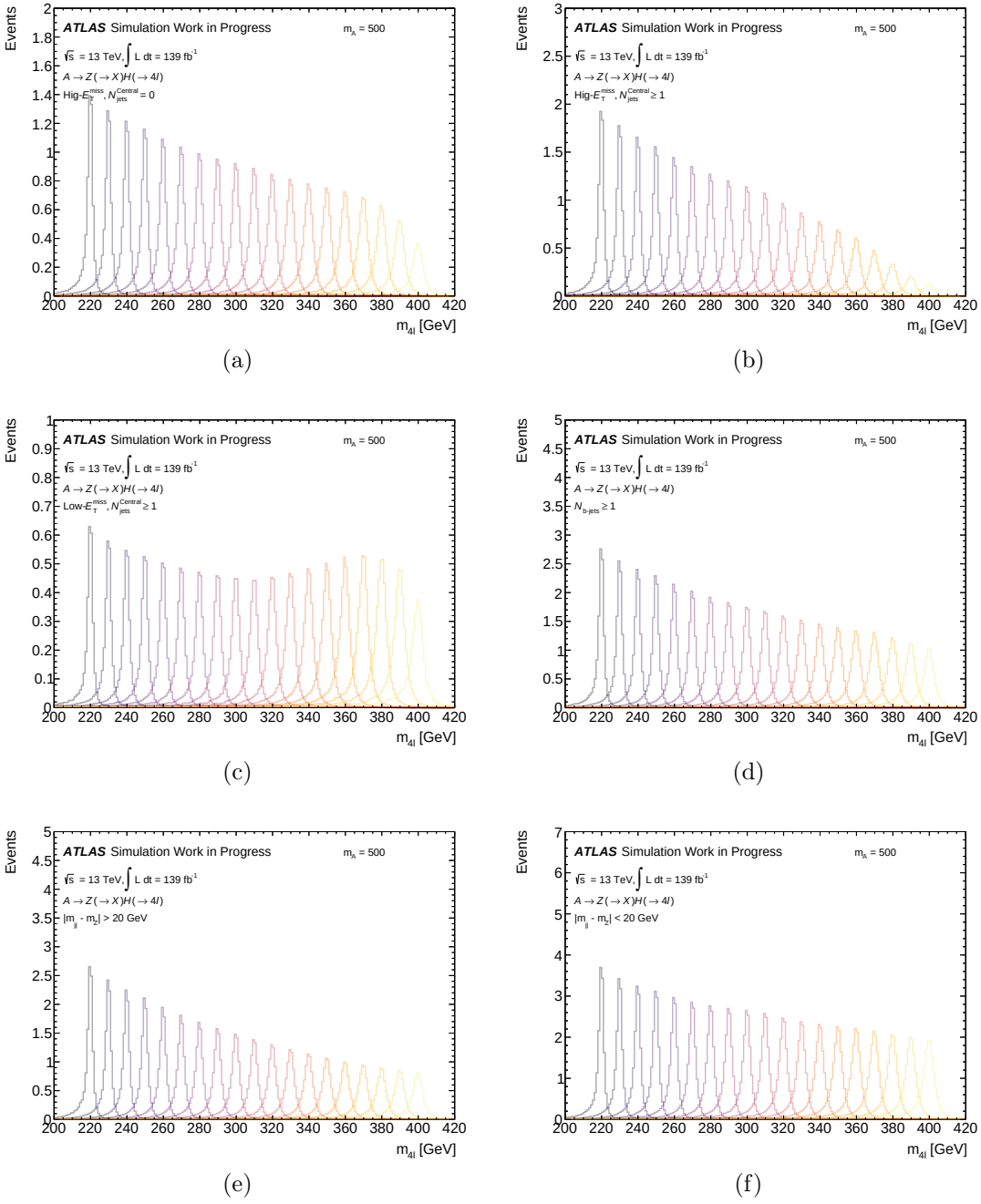


Figure 6.13: The invariant mass of the four leptons of the interpolated $A \to Z(\to X)H(\to 4\ell)$ signal shape with A mass fixed to 500 GeV and H mass varied by 10 GeV.

6.5.2 Background modelling

The $m_{4\ell}$ shape of the backgrounds is obtained from the MC simulation and parametrised using an empirical function in order to decrease statistical uncertainties originating from the limited number of simulated events. Four background templates are used: $qqZZ$, $ggZZ$, VVV and others. The VVV has a different shape from the rest of the backgrounds, therefore it is kept on a separate template. Backgrounds such as $qqZZ$(EW), $t\bar{t}V$, $t\bar{t}$, Z+jets and WZ are combined together in the "others" template. Each of the background templates is fitted with an analytical function for $m_{4\ell}$ between $200 - 1200\,\text{GeV}$, as follows:

$$f(m_{4\ell}) = H(m_0 - m_{4\ell}) f_1(m_{4\ell})\, C_1 + H(m_{4\ell} - m_0) f_2(m_{4\ell})\, C_2, \tag{6.5}$$

where:

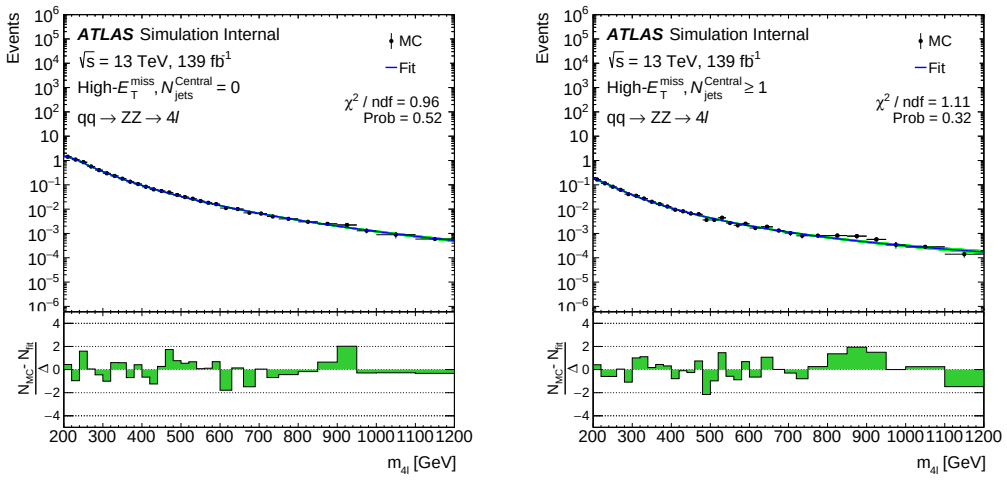
$$f_1(m_{4\ell}) = \frac{a_1 \cdot m_{4\ell} + a_2 \cdot m_{4\ell}^2}{1 + \exp\left(\frac{m_{4\ell} - a_1}{a_3}\right)} \tag{6.6}$$

$$f_2(m_{4\ell}) = \left(1 - \frac{m_{4\ell}}{n_C}\right)^{b_1} \cdot \left(\frac{m_{4\ell}}{n_C}\right)^{\left(b_2 + b_3 \cdot \ln\left(\frac{m_{4\ell}}{n_C}\right)\right)} \tag{6.7}$$

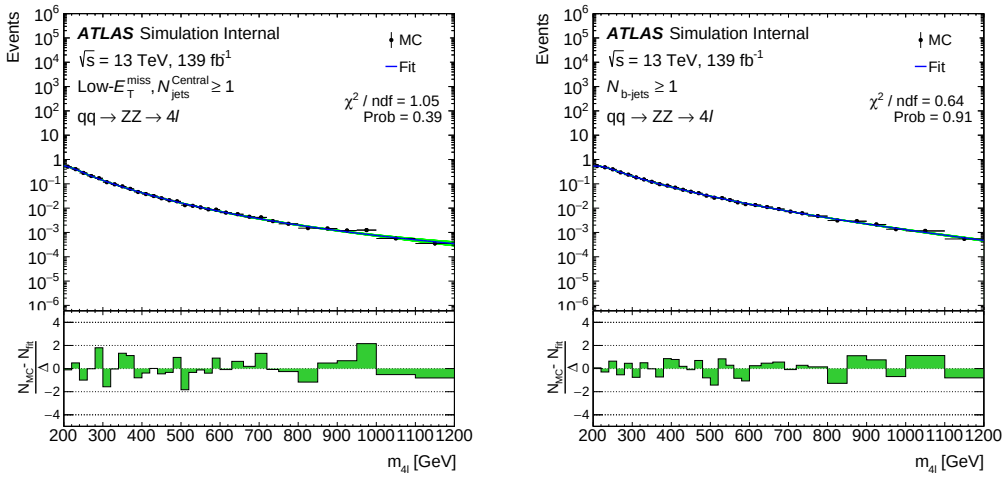
$$C_1 = \frac{1}{f_1(m_0)}, \qquad C_2 = \frac{1}{f_2(m_0)}.$$

The f_1 parameter models the ZZ threshold around $2m_Z$ and f_2 describes the high mass tail. The transition between f_1 and f_2 functions is performed by the Heaviside step function $H(x)$ around m_0, where m_0 is fixed to 260, 240, 250 and 230 for $qqZZ$, $ggZZ$, VVV, and others backgrounds, respectively. The transition point is determined by optimising the function's smoothness. The $m_{4\ell}$ is scaled by a constant $n_C = 13$ GeV in the high mass region. C_1 and C_2 are used to ensure the continuity of the function around the m_0 correspond to f_1 and f_2. Figures 6.14 and 6.15 show $qqZZ$ MC simulation fitted by equation 6.5. Figures for the $ggZZ$, VVV and others MC simulations are shown in Appendix B.7. Table 6.9 summaries the χ^2 values over the number of degrees of freedom (ndof) for each category of the background templates. The a_i and b_i, are shape parameters obtained by fitting the $m_{4\ell}$ distribution for each category. The extracted parameters from the fit for the $qqZZ$, $ggZZ$, VVV and others are shown in Tables 6.10, B.10, B.11

and B.12. The integral error calculated from the fit function is considered a source of systematic uncertainty and is treated as a nuisance parameter during the final fit.



(a) High-$E_{\mathrm{T}}^{\mathrm{miss}}$& $N_{\mathrm{jets}}^{\mathrm{Central}} = 0$ (b) High-$E_{\mathrm{T}}^{\mathrm{miss}}$& $N_{\mathrm{jets}}^{\mathrm{Central}} \geq 1$



(c) Low-$E_{\mathrm{T}}^{\mathrm{miss}}$ & $N_{\mathrm{jets}}^{\mathrm{Central}} \geq 1$ (d) $N_{b-\mathrm{jets}} \geq 1$

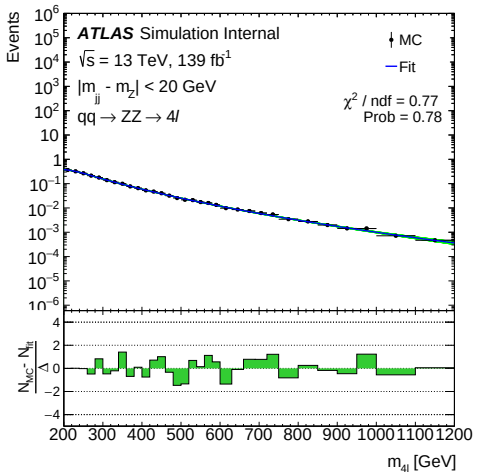
Figure 6.14: The 4ℓ invariant mass distributions for the analytical function fit to $qqZZ$ background in different signal regions.

Table 6.9: Summary of χ^2/ndof values for Equation 6.5 fitted to different background templates. The χ^2/ndof values are shown for Figure 6.14 and Figures shown in Appendices B.17, B.18 and B.19.

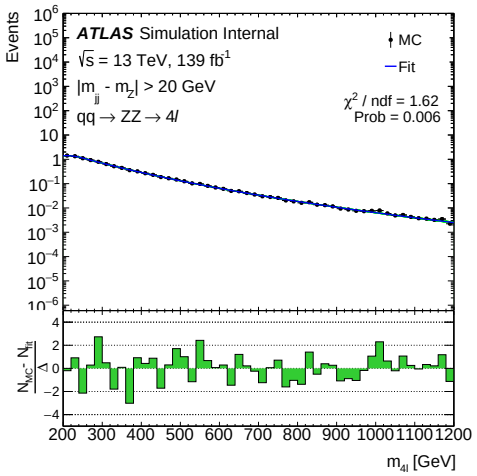
Background source	χ^2/ndof						
	$N_{\text{jets}}^{\text{Central}} = 0$	$N_{\text{jets}}^{\text{Central}} \geq 1$		$N_{b-\text{jets}} \geq 1$	$\lvert m_{\text{jj}} - m_Z \rvert < 20$ GeV	$\lvert m_{\text{jj}} - m_Z \rvert > 20$ GeV	$N_{\text{jets}}^{\text{Central}} = 1$
	High-$E_{\text{T}}^{\text{miss}}$	High-$E_{\text{T}}^{\text{miss}}$	Low-$E_{\text{T}}^{\text{miss}}$				
$qqZZ$	0.96	1.11	1.05	0.64	0.77	1.62	0.81
$ggZZ$	1.29	0.95	0.80	1.35	1.01	0.91	1.57
VVV	0.82	0.45	0.82	1.10	1.12	0.98	0.98
others	0.81	1.02	1.01	0.50	1.19	0.88	1.39

Table 6.10: The extracted parameters after fitting $qqZZ$ MC using Equation 6.5. The m_0 parameter values are fixed during the fit to improve the fit stability.

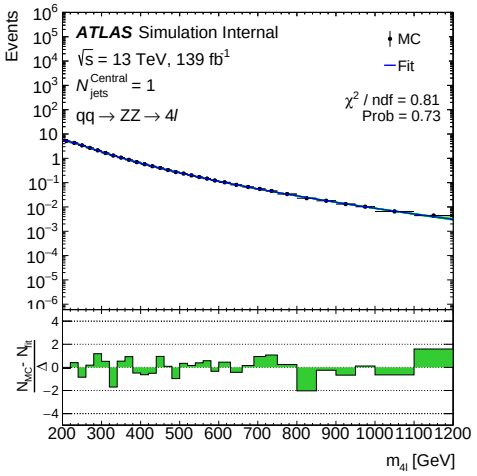
Parameter	High-$E_{\text{T}}^{\text{miss}}$, $N_{\text{jets}}^{\text{Central}} = 0$	High-$E_{\text{T}}^{\text{miss}}$, $N_{\text{jets}}^{\text{Central}} \geq 1$	Low-$E_{\text{T}}^{\text{miss}}$, $N_{\text{jets}}^{\text{Central}} \geq 1$	$\lvert m_{jj}^{\text{Central}} - m_Z \rvert < 20$ GeV	$\lvert m_{jj}^{\text{Central}} - m_Z \rvert > 20$ GeV	$N_{b\text{-jets}} \geq 1$	$N_{\text{jets}}^{\text{Central}} = 1$
N	0.661 ± 0.010	0.0728 ± 0.0025	0.241 ± 0.009	14.04 ± 0.08	1.018 ± 0.009	0.338 ± 0.005	3.02 ± 0.04
a_1	$(-3.85 \pm 0.27)e+05$	$(0.1 \pm 1.0)e+06$	$(-4 \pm 8)e+02$	216 ± 7	$(-1.1 \pm 0.7)e+03$	$(4.6 \pm 0.6)e+06$	-3 ± 6
a_2	$(1.25 \pm 0.09)e+03$	$(0 \pm 4)e+02$	3 ± 5	-0.608 ± 0.021	7 ± 5	$(-2.8 \pm 0.4)e+04$	0.03 ± 0.05
a_3	$(1.6 \pm 0.5)e+02$	49 ± 13	33 ± 6	93 ± 8	41.2 ± 2.3	35.6 ± 3.2	43 ± 5
b_1	-11.4 ± 2.1	-19 ± 5	$(-3 \pm 5)e+01$	10 ± 5	-1 ± 10	28.0 ± 2.6	13 ± 11
b_2	-7.86 ± 0.09	-5.2 ± 0.5	-11 ± 8	-6.4 ± 1.0	-9.8 ± 1.8	-3.33 ± 0.20	-6.9 ± 2.0
b_3	-0.414 ± 0.012	-0.05 ± 0.06	-0.9 ± 1.0	-0.36 ± 0.11	-0.92 ± 0.21	-0.069 ± 0.025	-0.49 ± 0.24
m_0	260.0 ± 0	260.0 ± 0	260.0 ± 0	260.0 ± 0	260.0 ± 0	260.0 ± 0	260.0 ± 0



(a) $|m_{\mathrm{jj}}^{\mathrm{Central}} - m_{\mathrm{Z}}| < 20\,\mathrm{GeV}$



(b) $|m_{\mathrm{jj}}^{\mathrm{Central}} - m_{\mathrm{Z}}| > 20\,\mathrm{GeV}$



(c) $N_{\mathrm{jets}}^{\mathrm{Central}} = 1$

Figure 6.15: The 4ℓ invariant mass distributions for the analytical function fit to the $qqZZ$ background in different signal regions.

6.6 Systematic uncertainties

This section discusses the causes of the systematic uncertainties addressed in this study. These include experimental and theoretical uncertainties in the signal and background processes. Statistical uncertainties regarding the limitation of the generation of MC events are also considered. Uncertainties extracted from the fitting of the data accounts for the unreliability generated by modelling the back-

ground shape. Each systemic component was counted as a nuisance parameter (NP) and profiled into the fit results. The systematic uncertainties are evaluated using the $m_{4\ell}$ as a discriminant.

6.6.1 Experimental systematic uncertainties

Experimental uncertainties such as object reconstruction and identification, trigger efficiencies and energy scale and resolution, are calculated for both signal and background processes. The systematic experimental uncertainties are evaluated using the ratio between the integral of the $m_{4\ell}$ of the interested NP in which the weight modified by one standard deviation and the $m_{4\ell}$ using the nominal weight. The results are shown in percentages for NPs with upward, and downward variation corresponds to $\pm 1\sigma$.

Signal samples are divided into three regions depending on the quantity of the missing transverse energy to simplify estimating the signal's experimental systematic uncertainties. The regions are with Low-$E_{\mathrm{T}}^{\mathrm{miss}}$ ($E_{\mathrm{T}}^{\mathrm{miss}} < 500\,\mathrm{GeV}$), Medium-$E_{\mathrm{T}}^{\mathrm{miss}}$ ($500 > E_{\mathrm{T}}^{\mathrm{miss}} < 700\,\mathrm{GeV}$) and High-$E_{\mathrm{T}}^{\mathrm{miss}}$ ($E_{\mathrm{T}}^{\mathrm{miss}} > 1300\,\mathrm{GeV}$) regions, as illustrated in Figure 6.3 for the $R \to SH \to 4\ell + E_{\mathrm{T}}^{\mathrm{miss}}$ samples. These ranges are lower for $A \to Z(\nu\nu)H(ZZ) \to 4\ell + X$ signal samples. The systematic uncertainties are then evaluated for three signal mass points from each region,for both signals hypotheses. Each result is combined by calculating the mean of three samples per region, for the Low-$E_{\mathrm{T}}^{\mathrm{miss}}$ samples for the $R \to SH \to 4\ell + E_{\mathrm{T}}^{\mathrm{miss}}$ and $A \to Z(\nu\nu)H(ZZ) \to 4\ell + X$ signal, as shown in Appendix B.10.1. The experimental uncertainties on signal shapes are shown in Appendix B.8.1.

6.6.2 Theoretical systematic uncertainties

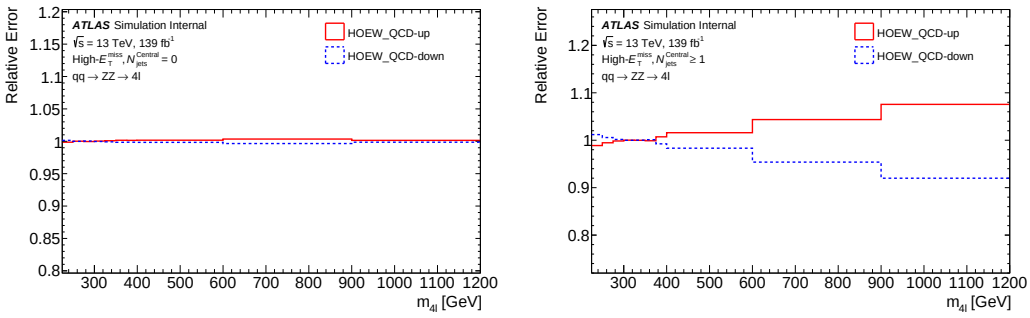
Theoretical uncertainties for the signal processes

The effects of scale, PDF+α_S, multi-parton interactions (MPI), parton showering (PS) and hadronization uncertainties on the migration of the events in each category are evaluated as theoretical uncertainties. The theoretical scale uncertainties on the signal samples are evaluated by varying the factorization and renormalisation scales up and down from their nominal values by a factor of two in each category. The largest deviation in each category divided by the inclusive selections, are considered as the scale uncertainty. The PDF+α_S uncertainties are estimated using the SysCalc [168] package associated with MadGraph. The

uncertainties in the migration of each category are estimated by varying the parameters of the `NNPDF3.0lo` PDF set and taking the maximum change. The ISR, PS and hadronization uncertainties are evaluated by varying the eigen-variables in PYTHIA for signal and by comparing HERWIG 7.1.3 [169] with PYTHIA for the signal samples. All the theoretical uncertainties are summarized in Tables B.14 and B.15, for a few signal samples with up to 48% uncertainties by comparing the PYTHIA with HERWIG, where the $E_{\mathrm{T}}^{\mathrm{miss}}$ is low. For most samples the uncertainties are below 10%.

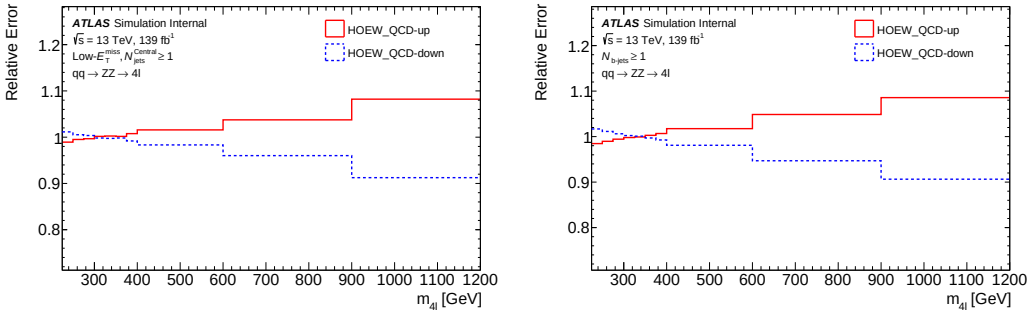
Theoretical uncertainties for the SM background

PDF and QCD scale uncertainties are considered for the $qqZZ$ and $ggZZ$ backgrounds. These systematic uncertainties influence the shape of the $m_{4\ell}$ distribution. A high-order electro-weak correction (HOEW) uncertainty on the $m_{4\ell}$ shape is considered for $qqZZ$ background (see Figure 6.16) in addition to the PDF and QCD scale uncertainties. The scale uncertainties for both $qqZZ$ and $ggZZ$ backgrounds are shown in Appendix B.9. It is estimated to be within 10% for both $qqZZ$ and $ggZZ$ in all categories. Appendix B.9, Figures B.28 and B.30 show a PDF uncertainty of less than 25% for the $qqZZ$ process and about 30% for the $ggZZ$ background respectively.



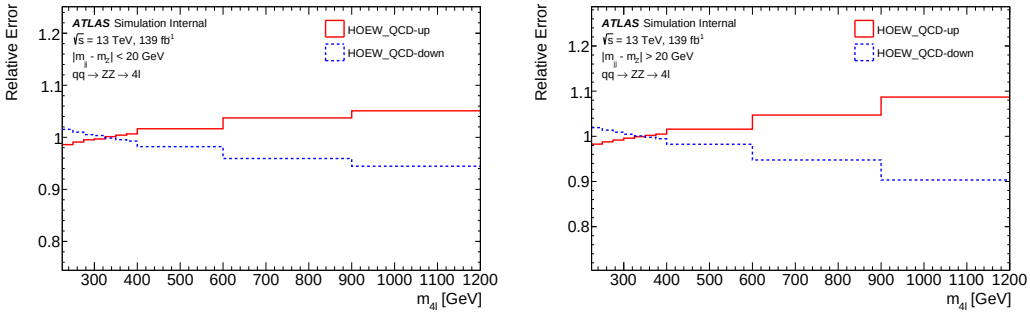
(a) High-$E_{\mathrm{T}}^{\mathrm{miss}}$& $N_{\mathrm{jets}}^{\mathrm{Central}} = 0$

(b) High-$E_{\mathrm{T}}^{\mathrm{miss}}$& $N_{\mathrm{jets}}^{\mathrm{Central}} \geq 1$



(c) Low-$E_{\mathrm{T}}^{\mathrm{miss}}$ & $N_{\mathrm{jets}}^{\mathrm{Central}} \geq 1$

(d) $N_{b-\mathrm{jets}} \geq 1$



(e) $|m_{\mathrm{jj}}^{\mathrm{Central}} - m_{\mathrm{Z}}| < 20\,\mathrm{GeV}$

(f) $|m_{\mathrm{jj}}^{\mathrm{Central}} - m_{\mathrm{Z}}| > 20\,\mathrm{GeV}$

Figure 6.16: The shape uncertainties as a function of the $m_{4\ell}$ of the HOEW correction for the $qqZZ$ background in different signal regions.

6.7 Statistical procedure and results

The $m_{4\ell}$ is employed as a discriminant to examine the null and alternative hypothesis by using the profile likelihood ratio and CL_s techniques.

6.7.1 Statistical procedure

The profile likelihood method [170] is used to indicate new physics versus the likelihood of the SM-only hypothesis. It is defined by the probability of observing n events multiplied by the product sum of the weighted signal and background events, as shown below:

$$\mathcal{L}(m^1_{4\ell},\ldots,m^n_{4\ell}|\sigma_M) = \mathrm{Pois}(n|S_M+B)\left[\prod_{i=1}^{n}\frac{S_M f_{S_M}(m^i_{4\ell})+B f_B(m^i_{4\ell})}{S_M+B}\right]. \quad (6.8)$$

The dependency on the analysis category for each event is implied into the product by the probability distribution functions (PDFs) $f_{S_M}(m_{4\ell})$ and $f_B(m_{4\ell})$ for signals and backgrounds, as outlined in Sections 6.5.1 and 6.5.2, where S_M and B are the expected signal and background yields. The M label could either be RSH or AZH for $R \to SH \to 4\ell + E_{\mathrm{T}}^{\mathrm{miss}}$ or $A \to Z(\nu\nu)H(ZZ) \to 4\ell + X$ signal hypothesis, respectively. Factors B and $f_B(m_{4\ell})$ combine different background contributions, each has different yields, and PDFs are also implicit into the likelihood function. The parameter of interest (POI) is incorporated within the likelihood into the expected signal yields S_M as follows:

$$S_M = \sigma_M \times \mathrm{BR}(A/R \to ZH/SH) \times \mathrm{BR}(H \to ZZ \to 4\ell) \times (\mathrm{A}\times\mathrm{E}) \times \int L\,\mathrm{d}t, \quad (6.9)$$

where A × E is the acceptance times efficiency, discussed in Section 6.4.2, and $\int L\,\mathrm{d}t = 139\ \mathrm{fb}^{-1}$ is the integrated luminosity of the data. The branching ratio of the gluon-fusion to A (R) times the branching ration of the H to four leptons times the cross section, $\sigma_M \times \mathrm{BR}(A/R \to ZH/SH) \times \mathrm{BR}(H \to ZZ \to 4\ell)$, is the fitted POI value. It represents a factor that balances the whole signal distribution. The POI, σ_M[2], regarded as signal strength and it is a free parameter that depends on the signal model. For example, σ_{RSH} and σ_{AZH} to represent $R \to SH \to 4\ell + E_{\mathrm{T}}^{\mathrm{miss}}$ and $A \to Z(\nu\nu)H(ZZ) \to 4\ell + X$ models, respectively. A

[2] σ_M is taken as the POI for simplicity, but it should remembered that it is actually $\sigma_M \times \mathrm{BR}(A/R \to HZ/SH) \times \mathrm{BR}(H \to ZZ \to 4\ell)$.

collection of nuisance parameters (NP) θ_i is introduced to describe how systematic uncertainties influence the predicted number of signal and background events and the shape of the PDFs. These NPs are constrained to their nominal values within the calculated uncertainties using Gaussian constraints. When any nuisance parameter is displaced from its nominal value, additional terms are added to increase the negative log-likelihood. Therefore, the likelihood becomes as a function of the σ_{RSH} or σ_{AZH}, $m_{4\ell}$ and θ_i, $\mathcal{L}(\sigma_{\text{RSH}}/\sigma_{\text{AZH}}, m_{4\ell}, \theta_i)$. The normalisation of the $qqZZ$ and $ggZZ$ backgrounds is floated using the μ_{ZZ} parameter. Fixing or floating the normalisation does not affect the upper limit, as demonstrated in Appendix B.11. The benefit of releasing the ZZ background normalisation is to reduce the background dependency on the theory and other systematic uncertainties. The fit is performed on the invariant mass of the 4ℓ system between 200 and 1200 GeV with 0.5 GeV as a step for the bin. A binned maximum-likelihood fit is used to fit either background only or signal-plus-background data. The background templates used are as follows:

- $qqZZ$: the normalisation is set to be free (μ_{ZZ})
- $ggZZ$: with the same normalisation used for $qqZZ$
- VVV: the normalisation is fixed to the SM measurement
- others: the normalisation is fixed to the SM measurement

The normalisation parameter is made so that it depends on the category, as seen in Appendix B.11. Systematic uncertainties that affect the $qqZZ$ and $ggZZ$ shape are included for $qqZZ$ and $ggZZ$ backgrounds. In addition, the relative acceptance systematic uncertainty between $qqZZ$ and $ggZZ$ is added because these backgrounds have the same normalisation. This relative systematic is calculated as follows:

$$\Delta R\left(\frac{A_{qqZZ}}{A_{ggZZ}}\right) = \left(\Delta A_{qqZZ}^{\text{up/down}} - \Delta A_{ggZZ}^{\text{up/down}}\right)\Big|_{\max(\text{up, down})}, \tag{6.10}$$

where ΔR is the relative systematic uncertainty, and $\Delta A_{qqZZ}^{\text{up/down}}$ and $\Delta A_{ggZZ}^{\text{up/down}}$ are the systematic on the $qqZZ$ and $ggZZ$ yield, respectively. The VVV and others backgrounds are very small compared to the ZZ processes, hence no shape uncertainties are included. Only uncertainties on the $m_{4\ell}$ normalisation are considered. A simultaneous fit is performed on three $R \to SH \to 4\ell + E_{\text{T}}^{\text{miss}}$ categories and seven $A \to Z(\nu\nu)H(ZZ) \to 4\ell + X$ categories. NPs are profiled with Gaus-

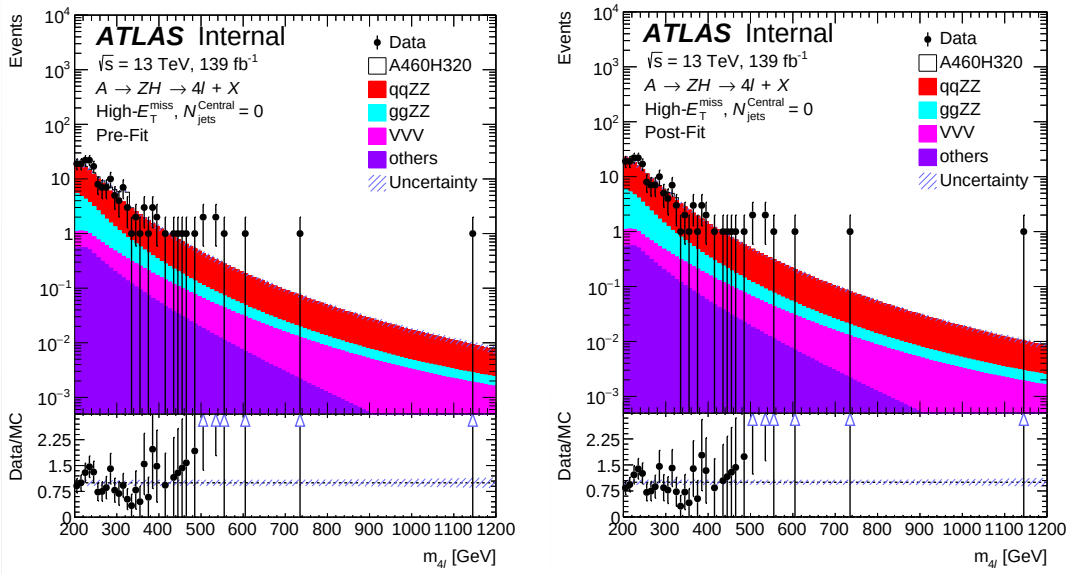
sian constraints during the fit. The shape and the normalisation systematic are pruned by 0.5% and 0.1%, respectively, to remove weaker NPs.

6.7.2 Results

Table 6.11 shows the yields for each of the seven signal regions described in Section 6.4. The observed and expected numbers of events in each signal region were obtained using a simulated binned maximum-likelihood fit, assuming the background-only hypothesis. Signal-plus-background binned maximum-likelihood fits were performed on the $m_{4\ell}$ distribution to search for potential excesses beyond the expected SM backgrounds. The fit model is based on the statistical framework discussed in Section 6.7.1. Figures 6.17 and 6.18 show the results for the Pre-fit and Post-fit of the $m_{4\ell}$ distributions for both the $A \to Z(\nu\nu)H(ZZ)$ and the $R \to SH \to 4\ell + E_{\mathrm{T}}^{\mathrm{miss}}$ models respectively. The $A \to Z(\nu\nu)H(ZZ) \to 4\ell + X$ is fitted with a signal at $(m_A, m_H) = (460, 320)\,\mathrm{GeV}$ for different categories after signal-plus-background fit to data based on the background templates discussed in Section 6.5.2. The $R \to SH \to 4\ell + E_{\mathrm{T}}^{\mathrm{miss}}$ is fitted with a signal at $(m_R, m_H) = (420, 250)\,\mathrm{GeV}$. Figure 6.19 shows the best fit values of the signal strength modifiers μ with their 68% expected confidence intervals (error bars). It shows μ values for seven categories considered in the $A \to Z(\nu\nu)H(ZZ) \to 4\ell + X$ model for $(m_A, m_H) = (460, 320)$, and μ values for three categories considered in the $R \to SH \to 4\ell + E_{\mathrm{T}}^{\mathrm{miss}}$ model for $(m_R, m_H) = (420, 250)$. The effect of NPs on the $\sigma(gg \to A)$ and $\sigma(gg \to R)$ are shown in Figure 6.20 and shows that nuisance parameters are well constrained within $\pm 1\sigma$.

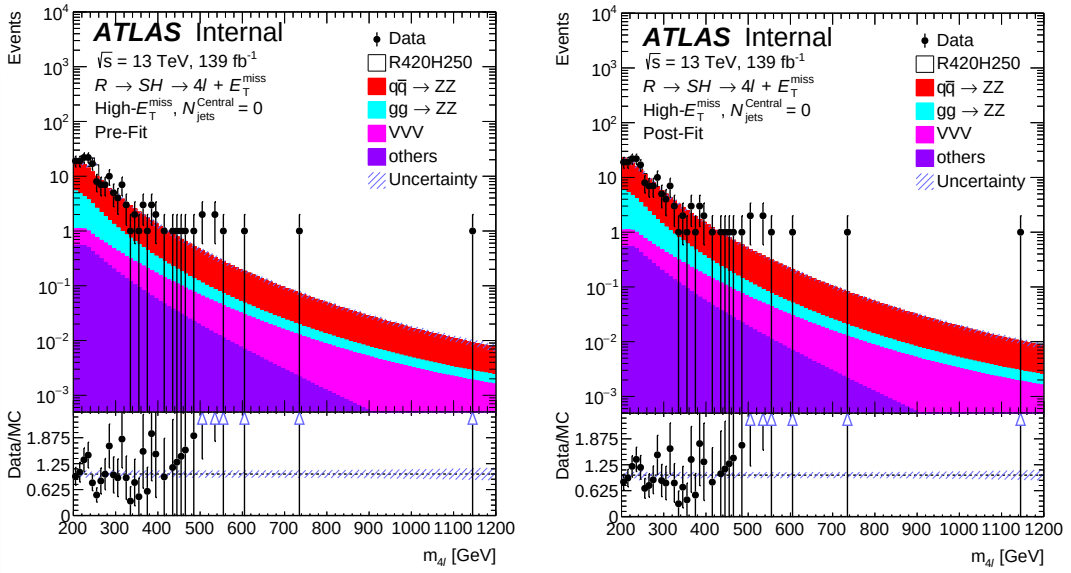
Table 6.11: Observed and expected post-fit event yields for $m_{4\ell} > 200$ GeV with their uncertainties. The expected yields and their uncertainties are obtained from a simultaneous fit to data under the background-only hypothesis on all seven signal regions discussed in Section 6.7.1. The μ^{ZZ}_{norm} is the normalisation factor for $q\bar{q} \to ZZ$ and $gg \to ZZ$ backgrounds which is considered during the fit. The others background include $q\bar{q} \to ZZ$ (EW), $t\bar{t}V$, $t\bar{t}$, Z+jets and WZ processes.

	High-$E_{\text{T}}^{\text{miss}}$, $N_{\text{jets}}^{\text{Central}} = 0$	High-$E_{\text{T}}^{\text{miss}}$, $N_{\text{jets}}^{\text{Central}} \geq 1$	Low-$E_{\text{T}}^{\text{miss}}$, $N_{\text{jets}}^{\text{Central}} \geq 1$	$\lvert m_{jj}^{\text{Central}} - m_Z \rvert < 20$ GeV	$\lvert m_{jj}^{\text{Central}} - m_Z \rvert > 20$ GeV	$N_{b\text{-jets}} \geq 1$	$N_{\text{jets}}^{\text{Central}} \geq 1$
$q\bar{q} \to ZZ$	132.2 ± 12	17.1 ± 6	42 ± 6.8	39.8 ± 6.5	156.2 ± 12.7	86.3 ± 11.6	549 ± 69.4
$gg \to ZZ$	31.9 ± 5.9	3.2 ± 3.1	8.3 ± 3.1	6.6 ± 2.5	22.1 ± 3.5	9.4 ± 4.5	102.1 ± 71.5
VVV	7.5 ± 0.4	4.8 ± 0.3	1.5 ± 0.2	0.2 ± 0	1.1 ± 0.1	0.5 ± 0.1	1.6 ± 0.1
others	5.5 ± 0.9	7.1 ± 0.8	3.6 ± 0.9	2.5 ± 0.3	17.5 ± 0.9	37.6 ± 2.4	11.3 ± 0.8
μ^{ZZ}_{norm}	1.1 ± 0.1	1.3 ± 0.6	1 ± 0.2	0.9 ± 0.2	0.8 ± 0.1	1.4 ± 0.3	1 ± 0.1
Total background	177.1 ± 13.3	32.2 ± 5.6	55.3 ± 7.4	49 ± 7	196.9 ± 14	133.8 ± 11.6	664 ± 26.3
Observed	177	32	55	49	197	135	664



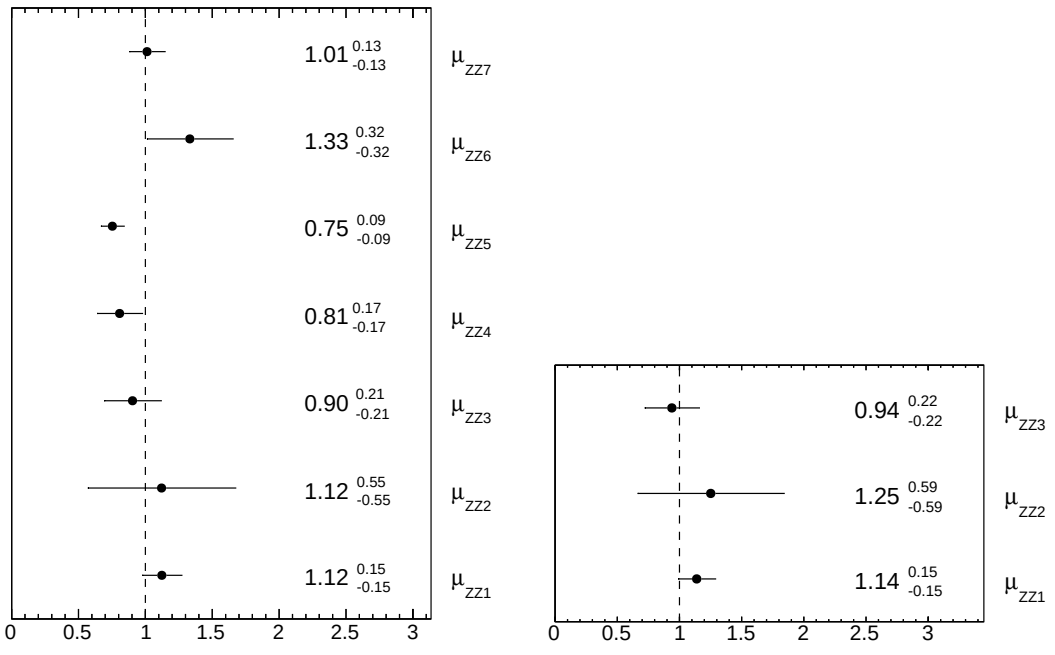
(a) Pre-fit (b) Post-fit

Figure 6.17: The Pre-fit and Post-fit results of the $m_{4\ell}$ distributions for the $A \to Z(\nu\nu)H(ZZ) \to 4\ell + X$ signal with $(m_A, m_H) = (460, 320)\,\text{GeV}$. A blue arrow indicates that the ratio is off-scale.



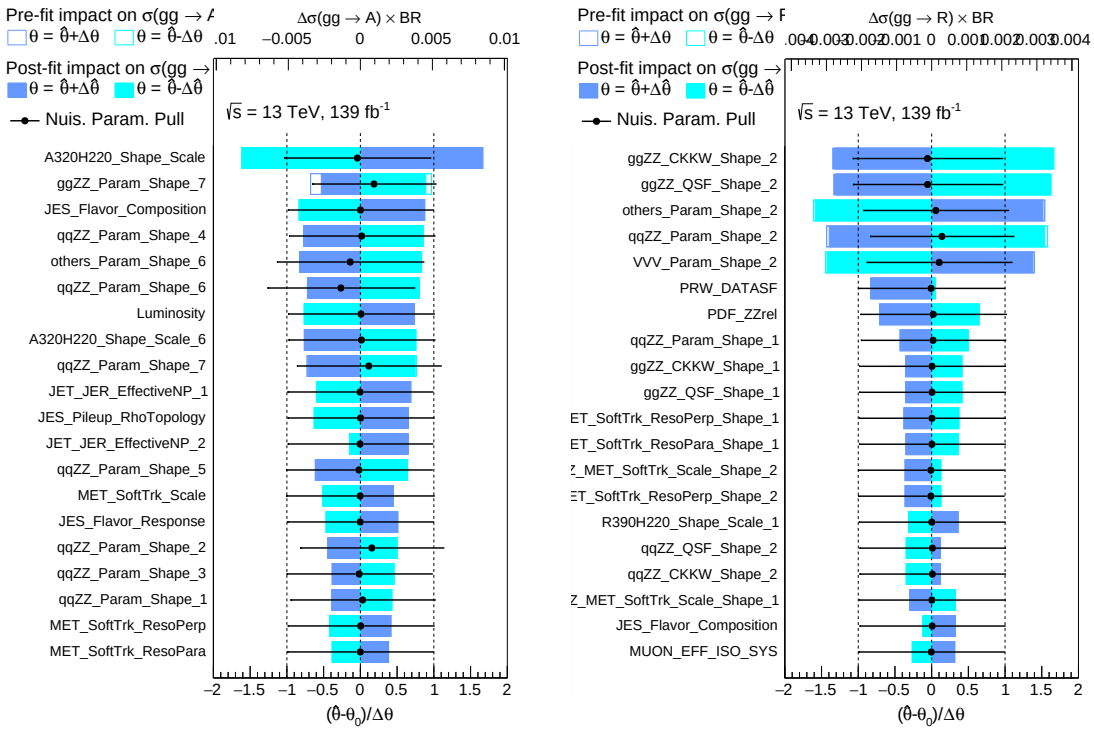
(a) Pre-fit (b) Post-fit

Figure 6.18: The Pre-fit and Post-fit results of the $m_{4\ell}$ distributions for the $R \to SH \to 4\ell + E_{\text{T}}^{\text{miss}}$ signal with $(m_R, m_H) = (420, 250)\,\text{GeV}$. A blue arrow indicates that the ratio is off-scale.



(a) $A \to Z(\nu\nu)H(ZZ) \to 4\ell + X$ (b) $R \to SH \to 4\ell + E_{\mathrm{T}}^{\mathrm{miss}}$

Figure 6.19: Best fit values of the signal strength modifiers μ with their 68% expected confidence intervals (error bars).

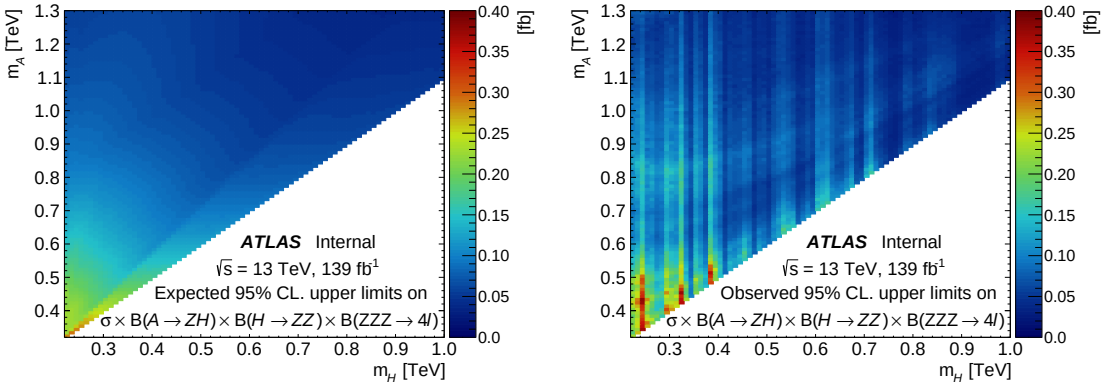


(a) $A \to Z(\nu\nu)H(ZZ) \to 4\ell + X$ (b) $R \to SH \to 4\ell + E_{\mathrm{T}}^{\mathrm{miss}}$

Figure 6.20: The impact of nuisance parameters on (a) $A \to Z(\nu\nu)H(ZZ) \to 4\ell + X$ signal sensitivity (σ_{AZH}) and (b) $R \to SH \to 4\ell + E_{\mathrm{T}}^{\mathrm{miss}}$ (σ_{RSH}), are performed for different mass hypotheses. (a) shows $(m_A, m_H) = (320, 220)$ and (b) shows $(m_R, m_H) = (390, 220)$.

Upper limits

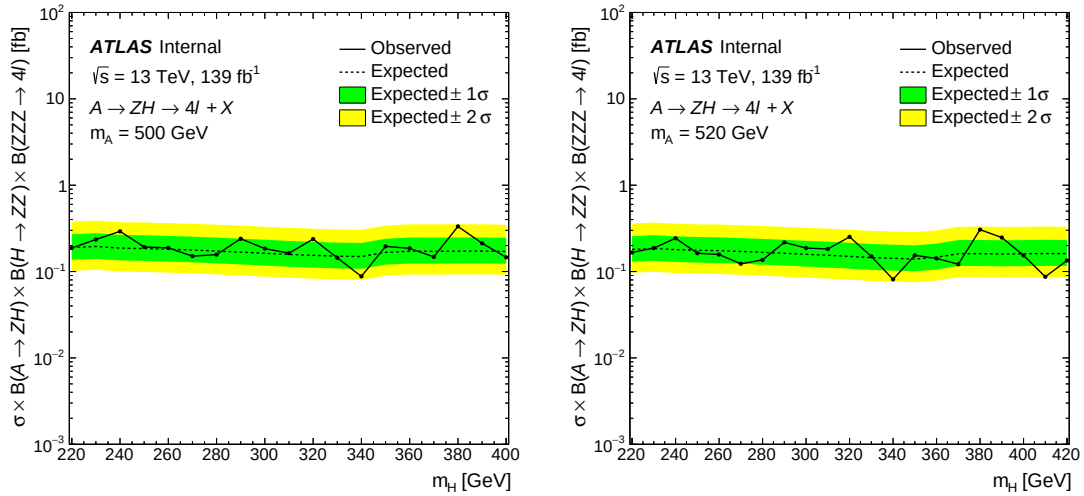
The CL$_s$ approach in the asymptotic approximation [170, 171] was used to calculate upper limits at 95% confidence level on the explored phase space. Setting the H mass parameter to a constant value and maximising the probability function with respect to nuisance parameters, gives the upper limit for the $\sigma(gg \to A/R) \times \mathrm{BRs} \times \mathrm{A} \times \mathrm{E}$ for a given mass hypothesis. Figures 6.21 and 6.23 show the limits in the (m_A, m_H) and (m_R, m_H) planes respectively, where the z-axis displays the $\sigma(gg \to A/R) \times \mathrm{BR}(A/R \to ZH/SH) \times \mathrm{BR}(H \to ZZ \to 4\ell) \times \mathrm{A} \times \mathrm{E}$ in the unit of fb. In Figure 6.22, the expected (observed) upper limit for $A \to Z(\nu\nu)H(ZZ) \to 4\ell + X$ are in the range of 0.028–0.289 (0.023–0.378) fb for $(m_A, m_H) = (320, 220)$ GeV to $(m_A, m_H) = (1300, 1000)$ GeV. The expected (observed) upper limits for the $R \to SH \to 4\ell + E_{\mathrm{T}}^{\mathrm{miss}}$ are in the range of 0.037–0.321 (0.034–0.532) fb for $(m_R, m_H) = (320, 220)$ GeV to



(a) (b)

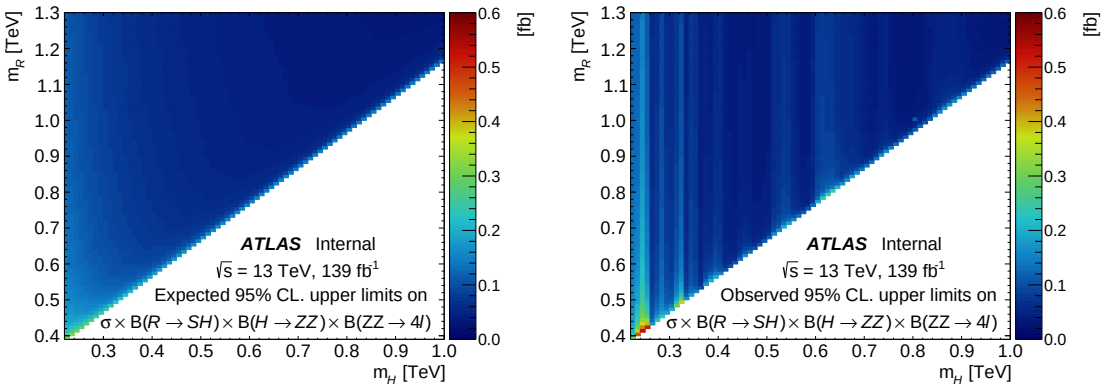
Figure 6.21: The (a) expected and (b) observed upper limits at 95% confidence level on the $\sigma(gg \to A) \times \mathrm{BR}(A \to ZH) \times \mathrm{BR}(H \to ZZ \to 4\ell) \times \mathrm{A} \times \mathrm{E}$ on (m_H, m_A) planes.

$(m_R, m_H) = (1300, 1000)\,\mathrm{GeV}$ as seen in Figure 6.24. The observed upper limits for both, the $A \to Z(\nu\nu)H(ZZ) \to 4\ell + X$ and the $R \to SH \to 4\ell + E_{\mathrm{T}}^{\mathrm{miss}}$ model were within the expected 1σ and 2σ bands.



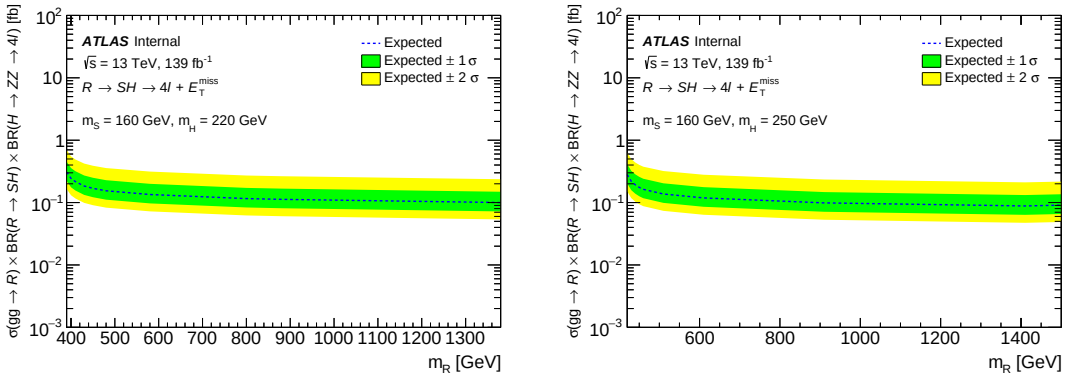
(a) $m_H = 500\,\mathrm{GeV}$ (b) $m_H = 520\,\mathrm{GeV}$

Figure 6.22: The expected and observed 1D upper limits at 95% confidence level on the $\sigma(gg \to A) \times \mathrm{BR}(A \to ZH) \times \mathrm{BR}(H \to ZZ \to 4\ell) \times \mathrm{A} \times \mathrm{E}$ for different m_A mass while fixing m_H to be 500 and 520 GeV for $A \to Z(\nu\nu)H(ZZ) \to 4\ell + X$.



(a) (b)

Figure 6.23: The (a) expected and (b) observed upper limits at 95% confidence level on the $\sigma(gg \to R) \times \mathrm{BR}(R \to SH) \times \mathrm{BR}(H \to ZZ \to 4\ell) \times \mathrm{A} \times \mathrm{E}$ on (m_H, m_R) planes.



(a) $m_H = 220\,\mathrm{GeV}$ (b) $m_H = 250\,\mathrm{GeV}$

Figure 6.24: The expected and observed 1D upper limits at 95% confidence level on the $\sigma(gg \to R) \times \mathrm{BR}(R \to SH) \times \mathrm{BR}(H \to ZZ \to 4\ell) \times \mathrm{A} \times \mathrm{E}$ for different m_R mass while fixing m_H to be 220 and 250 GeV for the $R \to SH \to 4\ell + E_{\mathrm{T}}^{\mathrm{miss}}$ model.

Chapter 7

Conclusions

During the LS2 period (2019–2021), the TileCal underwent the maintenance and Phase-I upgrades, in preparation for the Run 3 (2022–2025) data-taking period. As part of the ATLAS Phase-I upgrades, TileCal upgraded its local legacy TTC system with the ALTI module. The ALTI module integrates the functionalities of four legacy TTC modules: LTP, LTPi, TTCvi and the TTCex. The TileCal Online software was modified in order to integrate the ALTI functionalities by the author. A new TileTTC class was developed, to provide access to the TTCvi and other functionalities. The upgrade required a total of six out of twenty nine TileCal Online software packages to be modified. The OKS database has been modified to include new variables for the TileTTC class. C++ was the main programming language with GitLab used as the source code repository. The author tested and validated the software using the B175 test bench. The TileCal ALTI Online software was deployed in P1 and the OKS database adapted for the ALTI configuration by the author. Five ALTI modules were installed and configured for physics and calibration runs, in the counting room in ATLAS USA15 cavern. The TTC system was further validated for the ATLAS detector and fined tuned for data taking during milestone weeks and the pilot run. The upgraded TTC system participated in the first Run 3 stable beam collisions (July 2022), recording events at $\sqrt{s} = 13.6\,\text{TeV}$. Additionally, the TileCal TTC system for the test beam area at the CERN SPS North area has also been upgraded to use the ALTI module. The upgrade required a different configuration to the test bench and the P1 TileCal TTC system. The upgraded TTC system successfully participated in the November 2022 Phase-II test-beam campaign, recording data for kaons, pions, and electrons. The new TTC systems in the test bench, ATLAS counting

room USA15 and the test beam area, will be replaced by the Phase-II off-detector electronics during the LS3 period (2026–2028), in preparation for the HL-LHC data-taking period.

In parallel to the detector work conducted, the author contributed to a search for the presence of a new heavy resonance produced via gluon-gluon fusion and decaying to the 4ℓ (where $\ell = e$ or μ) final state, in association with $E_{\mathrm{T}}^{\mathrm{miss}}$ or jets, is conducted. The search is motivated by the multi-lepton anomalies observed at the LHC. The search uses pp collision data at $\sqrt{s} = 13\,\mathrm{TeV}$ collected with the ATLAS detector from 2015 to 2018 at the LHC. The data corresponds to a total integrated luminosity of 139 fb^{-1}. The data is interpreted in terms of two models, the $R \to SH \to 4\ell + E_{\mathrm{T}}^{\mathrm{miss}}$ and the $A \to Z(\nu\nu)H(ZZ) \to 4\ell + X$ model. The mass range for the hypothetical resonance spans between 390 (320) GeV and 2160 (2090) GeV for the R (A) boson. And the heavy boson H mass considered is between 220 GeV to 1000 GeV. The results are translated into upper limits on the $\sigma \times \mathrm{BR}(R(A) \to SH(ZH)) \times \mathrm{BR}(H \to ZZ) \times \mathrm{B}(ZZ(ZZZ) \to 4\ell) \times \mathrm{A} \times \mathrm{E}$ at 95% confidence level. The expected (observed) upper limits of the $R \to SH \to 4\ell + E_{\mathrm{T}}^{\mathrm{miss}}$ model are in the range of 0.037–0.321 (0.034–0.532) fb for (m_R, m_H) = (390, 220) GeV to (m_R, m_H) = (1300, 1000) GeV. For the $A \to Z(\nu\nu)H(ZZ) \to 4\ell + X$ model, the expected (observed) upper limits are in the range of 0.028–0.289 (0.023–0.378) fb for (m_A, m_H) = (320, 220) GeV to (m_A, m_H) = (1300, 1000) GeV. The observed upper limits for both, the $A \to Z(\nu\nu)H(ZZ) \to 4\ell + X$ and the $R \to SH \to 4\ell + E_{\mathrm{T}}^{\mathrm{miss}}$ model were within the expected 1σ and 2σ bands.

Appendices

Appendix A

Integration of the ALTI Module in the TileCal

A.1 ALTI modules installed in P1 TTC crates

The ALTI modules were installed in the TileCal TTC crates located above the ROD crates in the BE electronics. Figure A.1 shows ALTI modules located in LBA, LBC, EBA and EBC TTC crates. One additional ALTI module was installed in the Laser crate.

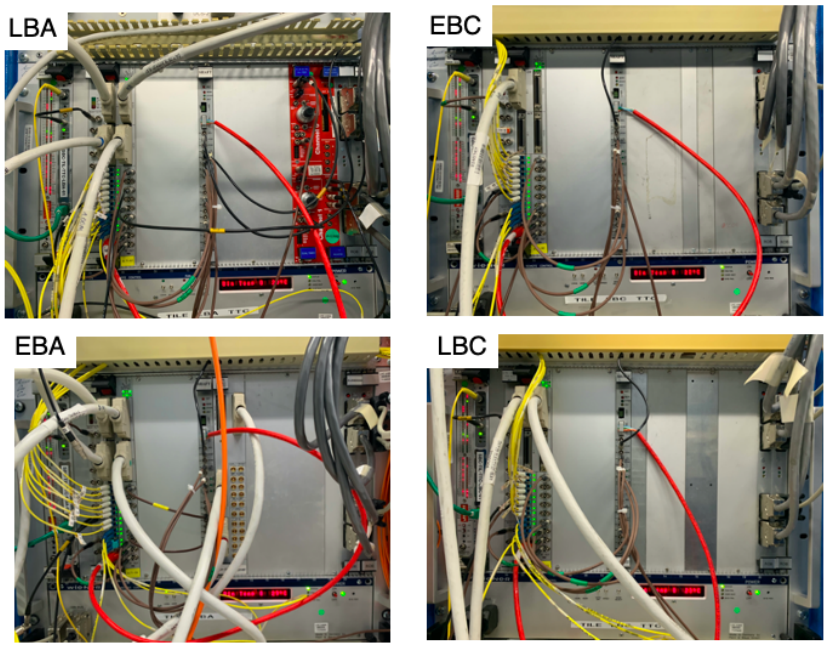


Figure A.1: Four TTC partitions.

A.2 Schematics for Laser, physics and CIS runs at the TB area

The connection schemes allow for the use of three pattern generators for the three run types, laser, physics and CIS runs. Figure A.2 shows the configuration for laser runs, while Figure A.3 shows the configuration for physics runs, and Figure A.4 shows the configuration for CIS runs.

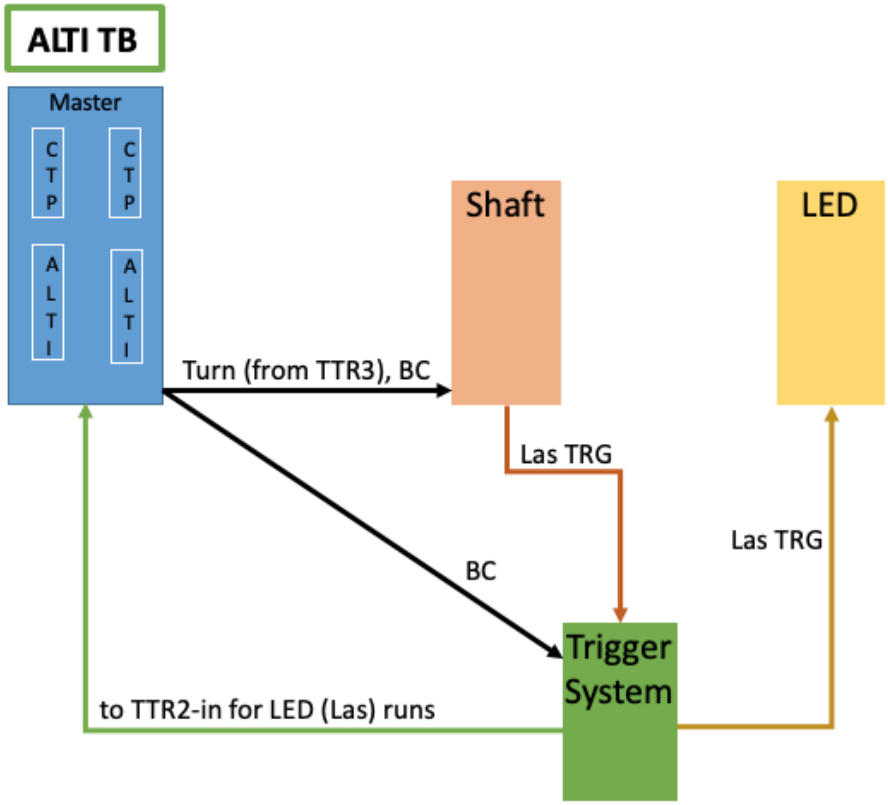


Figure A.2: Schematic of the laser runs at test beam.

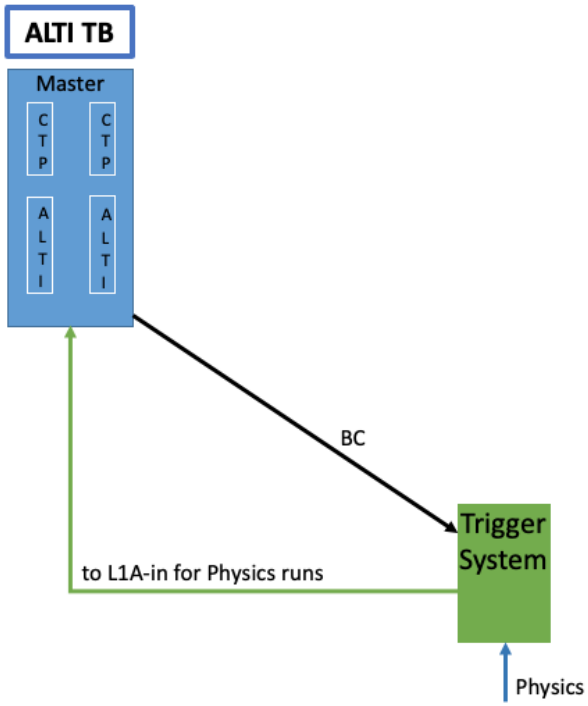


Figure A.3: Schematic of the physics runs at test beam.

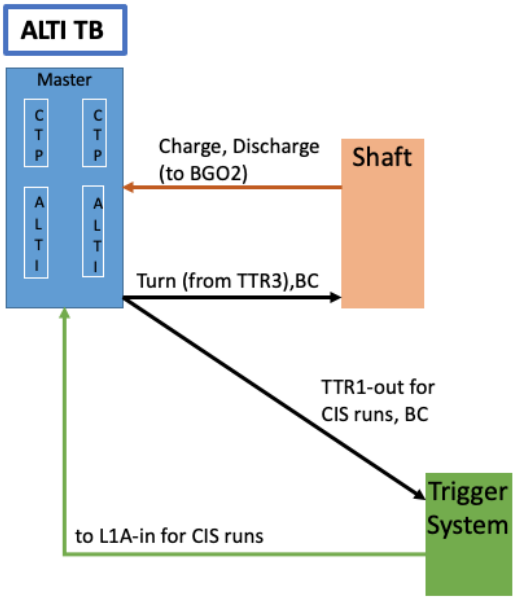


Figure A.4: Schematic of the CIS runs at test beam.

Appendix B

The search for heavy resonances in the 4ℓ final state in association with $E_{\mathrm{T}}^{\mathrm{miss}}$

B.1 S mass scan with different energy gaps

The choice of the S mass does not affect the kinematics of the $R \to SH \to 4\ell + E_{\mathrm{T}}^{\mathrm{miss}}$ signal significantly if it is less than 200 GeV. Figures B.1 and B.2 show the missing transverse energy and the $p_{\mathrm{T}}^{4\ell}$ for different S mass and energy gap at particle level, respectively.

B.2 Object vs Event based $E_{\mathrm{T}}^{\mathrm{miss}}$ significance in signal optimisation

Figures B.3 and B.4 compare the performance of the event-based $E_{\mathrm{T}}^{\mathrm{miss}}$ significance vs $p_{\mathrm{T}}^{4\ell}$ and object-based $E_{\mathrm{T}}^{\mathrm{miss}}$ significance vs the $p_{\mathrm{T}}^{4\ell}$ in a 2D scan. The scan was done similar to the one shown in Section 6.4 with the z-axis represents the significance ($Z_{\mathrm{Sig_1}}$) as shown in equation 6.4. The optimal cuts in x- and y-axis is determined by the z-axis. For instance, the optimal points in Figure B.3a is shown by the black dot as ($p_{\mathrm{T}}^{4\ell}$, event-based $E_{\mathrm{T}}^{\mathrm{miss}}$ significance, $s/\sqrt{b}$) = (30.0 GeV, 2.0, 3.10). Figure B.5 shows the 2D scan of the $p_{\mathrm{T}}^{4\ell}$ and $E_{\mathrm{T}}^{\mathrm{miss}}$ significance for the $R \to SH \to 4\ell + E_{\mathrm{T}}^{\mathrm{miss}}$ signal in the zero central jets region. The z-axis shows the significance calculated using $s/\sqrt{b}$ (top) and $s/\sqrt{s+b}$ (bottom).

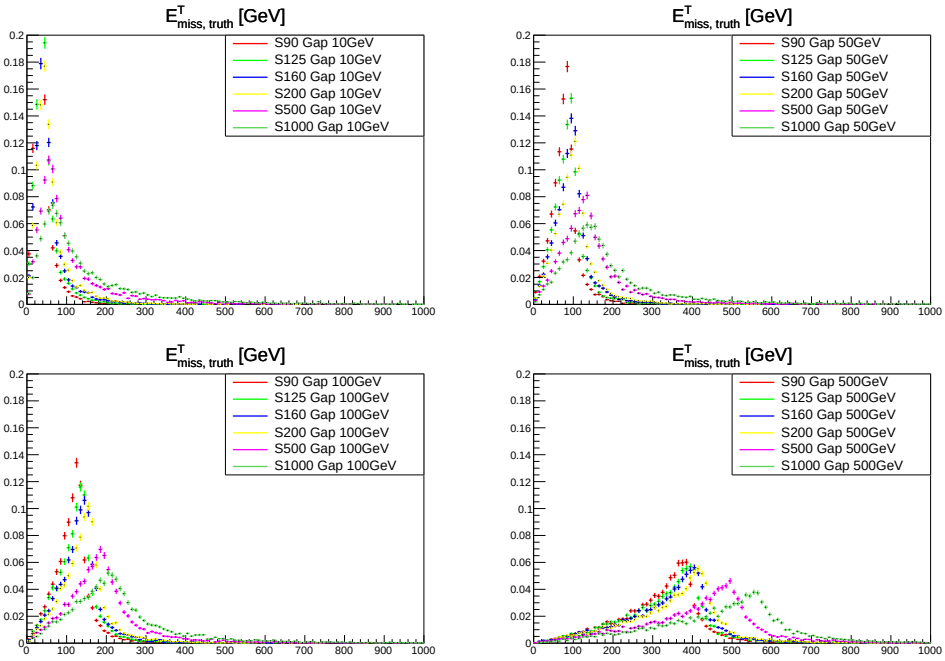


Figure B.1: The missing transverse energy of the four-lepton system at particle level of the $R \to SH \to 4\ell + E_{\mathrm{T}}^{\mathrm{miss}}$ signal for different m_S values.

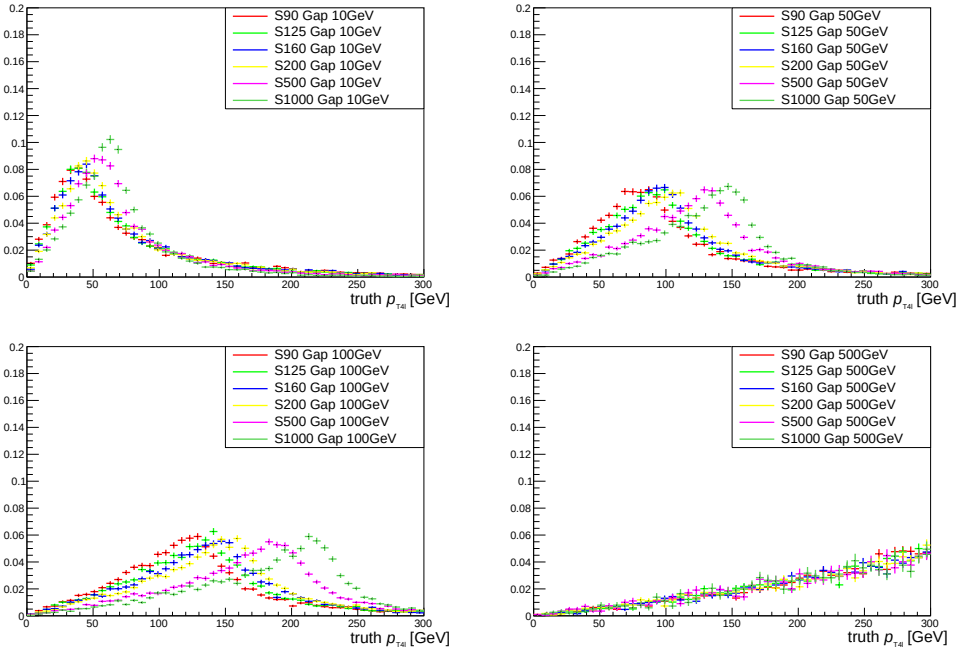


Figure B.2: The transverse momentum of the four-lepton system at particle level of the $R \to SH \to 4\ell + E_{\mathrm{T}}^{\mathrm{miss}}$ signal for different m_S values.

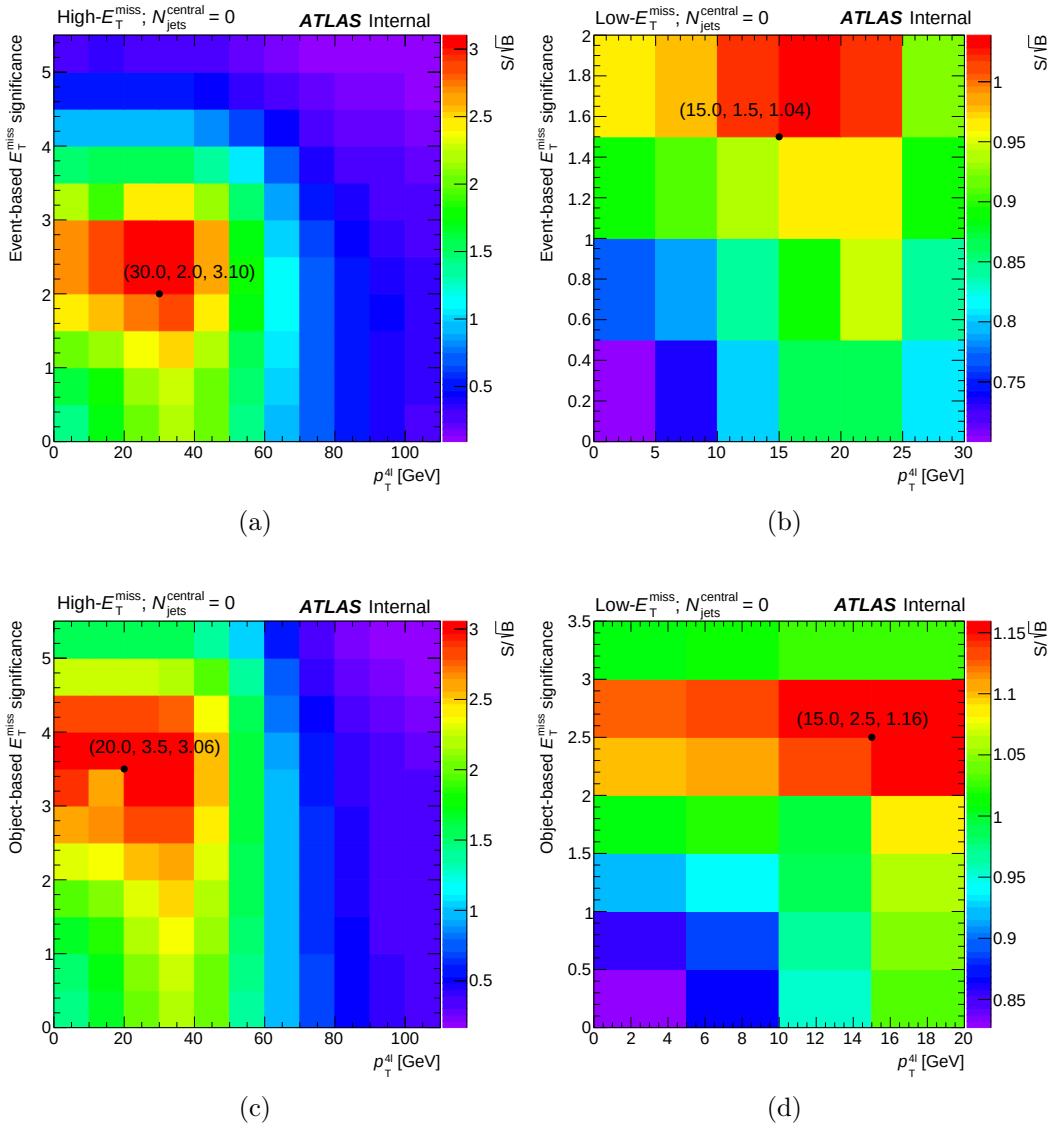


Figure B.3: 2D scan of the $p_{\mathrm{T}}^{4\ell}$ and $E_{\mathrm{T}}^{\mathrm{miss}}$ significance for the $R \to SH \to 4\ell + E_{\mathrm{T}}^{\mathrm{miss}}$ signal. The Event-based $E_{\mathrm{T}}^{\mathrm{miss}}$ significance is shown in (a) and (b) and Object-based $E_{\mathrm{T}}^{\mathrm{miss}}$ significance in (c) and (d) for High- and Low-$E_{\mathrm{T}}^{\mathrm{miss}}$ of the zero central jet.

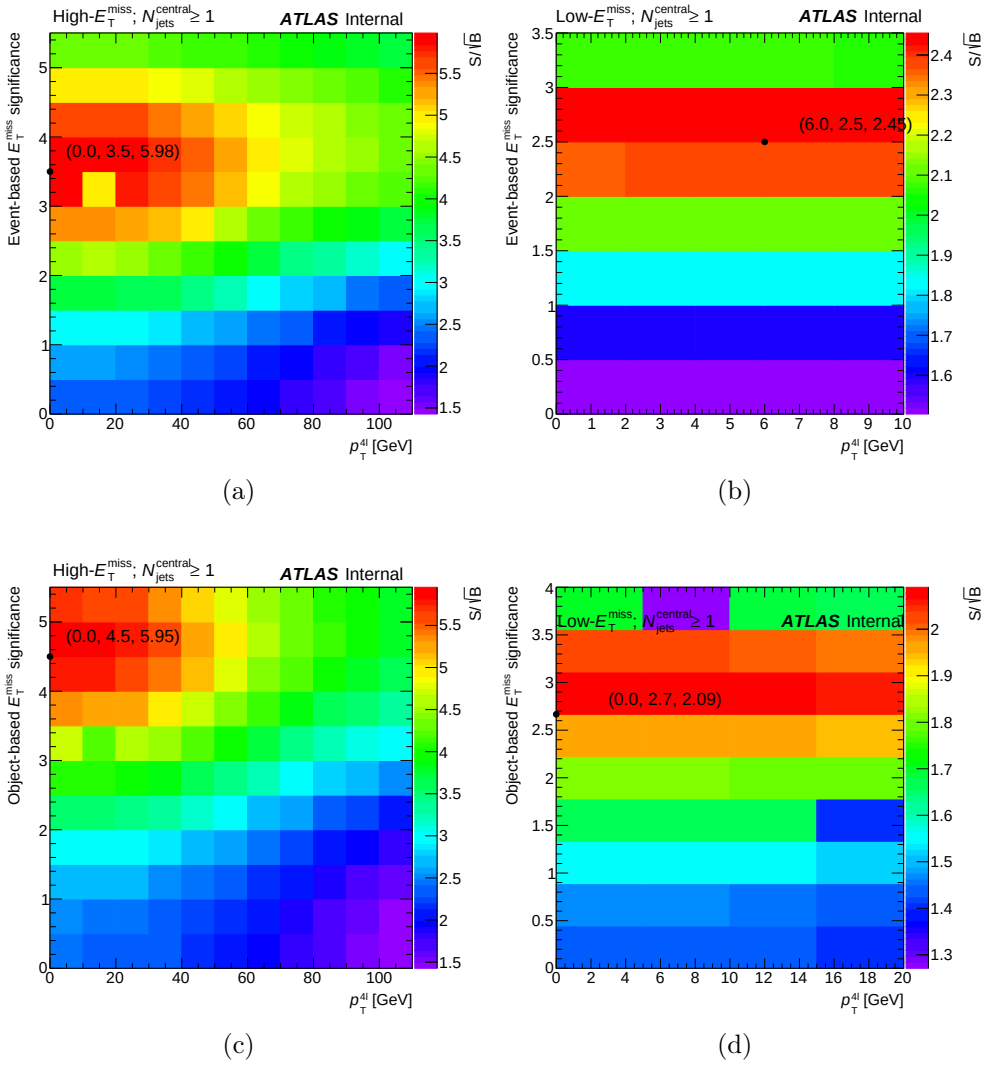


Figure B.4: Two-dimensional scan of the $p_{\mathrm{T}}^{4\ell}$ and $E_{\mathrm{T}}^{\mathrm{miss}}$ significance for the $R \to SH \to 4\ell + E_{\mathrm{T}}^{\mathrm{miss}}$ signal. The Event-based $E_{\mathrm{T}}^{\mathrm{miss}}$ significance is shown in (a) and (b), and Object-based $E_{\mathrm{T}}^{\mathrm{miss}}$ significance in (c) and (d) for High- and Low-$E_{\mathrm{T}}^{\mathrm{miss}}$ of the one central jet.

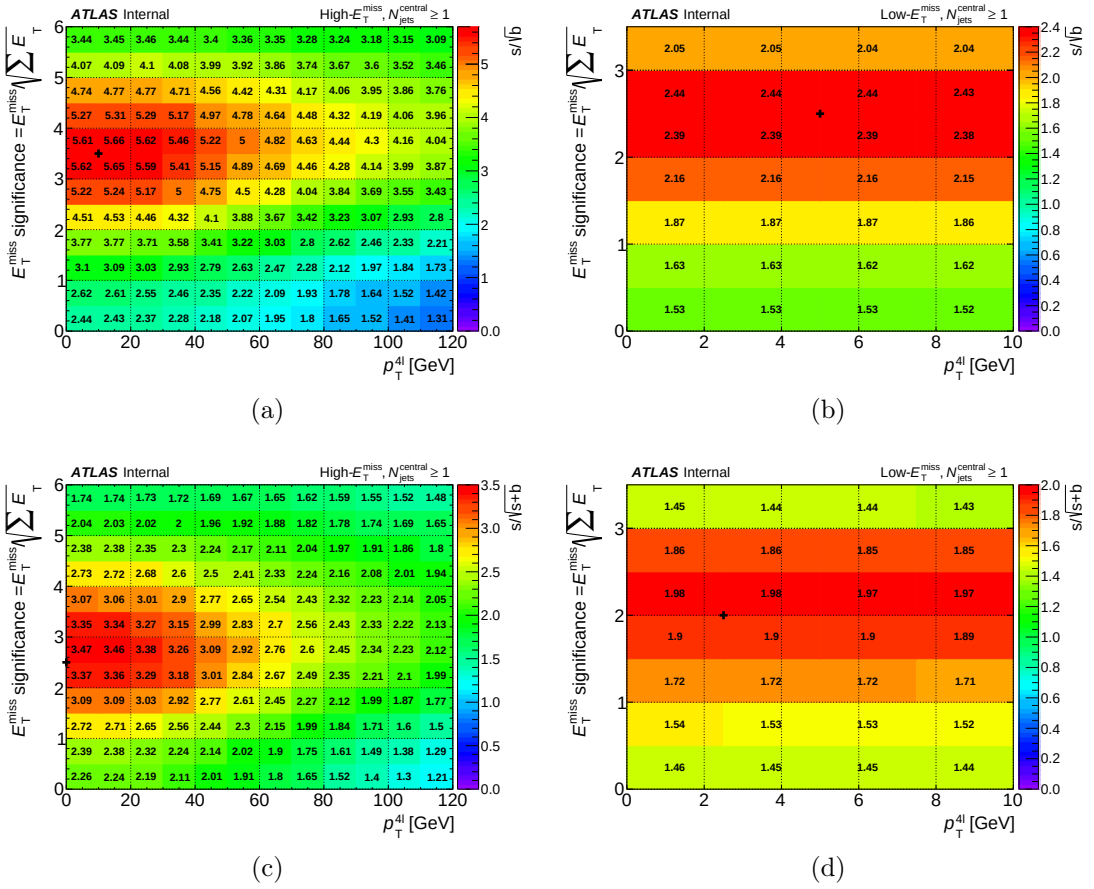


Figure B.5: 2D scan of the $p_{\mathrm{T}}^{4\ell}$ and $E_{\mathrm{T}}^{\mathrm{miss}}$ significance for the $R \to SH \to 4\ell + E_{\mathrm{T}}^{\mathrm{miss}}$ signal in the zero central jets region. The High-$E_{\mathrm{T}}^{\mathrm{miss}}$ scans are shown in (a) and (c), and Low-$E_{\mathrm{T}}^{\mathrm{miss}}$ on (b) and (d).

B.3 Cut-flows and signal acceptances

This appendix summarises the yields, significances and the acceptances for all the generated $A \to Z(\nu\nu)H(ZZ) \to 4\ell + X$ and $R \to SH \to 4\ell + E_{\mathrm{T}}^{\mathrm{miss}}$ mass points in each signal region. Tables B.1 and B.2 show the yields for $R \to SH \to 4\ell + E_{\mathrm{T}}^{\mathrm{miss}}$ and $A \to Z(\nu\nu)H(ZZ) \to 4\ell + X$ signal. The total number of background in each category are also included in the tables.

Table B.1: Yields and significance for $R \to SH \to 4\ell + E_{\mathrm{T}}^{\mathrm{miss}}$ signal taken from fully simulated MC samples. The S mass is fixed to 160 GeV , and the H and R masses are varied with $m_R = m_S + m_H + m_{\mathrm{Gap}}$. The m_{Gap} is set to be 10, 20, 30, 40, 50, 100, 200, 500, and 1000 GeVs to generate different signals. The table shows event yields and significances for signals with H masses of 220 and 250 GeVs for different categories. The significance is calculated using Z_{Sig_1} and Z_{Sig_2} defined in Equation 6.4. The $R \to SH \to 4\ell + E_{\mathrm{T}}^{\mathrm{miss}}$ signal cross section is assumed to be 1 fb.

(m_R, m_H) GeV	$N_{\mathrm{jets}}^{\mathrm{Central}} = 0$						$N_{\mathrm{jets}}^{\mathrm{Central}} \geq 1$					
	High-$E_{\mathrm{T}}^{\mathrm{miss}}$			Low-$E_{\mathrm{T}}^{\mathrm{miss}}$			High-$E_{\mathrm{T}}^{\mathrm{miss}}$			Low-$E_{\mathrm{T}}^{\mathrm{miss}}$		
	Yields	Z_{Sig_1}	Z_{Sig_2}	Yields	Z_{Sig_1}	Z_{Sig_2}	Yields	Z_{Sig_1}	Z_{Sig_2}	Yields	Z_{Sig_1}	Z_{Sig_2}
390, 220	17.37	3.13	2.50	5.11	0.78	0.74	13.26	5.87	3.09	8.30	2.48	1.88
450, 220	26.66	4.81	3.52	0.55	0.08	0.08	29.02	12.84	4.97	4.02	1.20	1.03
800, 220	24.18	4.36	3.26	0.04	0.01	0.01	46.15	20.42	6.45	0.67	0.20	0.20
400, 220	23.15	4.18	3.15	2.59	0.40	0.39	17.48	7.73	3.68	7.70	2.31	1.77
410, 220	24.88	4.49	3.34	1.52	0.23	0.23	20.78	9.20	4.08	6.96	2.08	1.64
420, 220	25.48	4.60	3.40	1.09	0.17	0.17	23.75	10.51	4.42	6.01	1.80	1.45
430, 220	26.09	4.71	3.46	0.84	0.13	0.13	25.92	11.47	4.65	5.27	1.58	1.30
480, 220	26.58	4.79	3.51	0.36	0.06	0.06	32.44	14.35	5.29	2.94	0.88	0.78
580, 220	26.18	4.72	3.47	0.14	0.02	0.02	38.68	17.11	5.84	1.62	0.49	0.45
880, 220	24.09	4.34	3.25	0.02	0.00	0.00	47.90	21.19	6.58	0.55	0.16	0.16
1380, 220	19.55	3.53	2.76	0.01	0.00	0.00	53.85	23.82	7.01	0.21	0.06	0.06
450, 250	25.39	5.66	3.76	1.18	0.22	0.22	24.50	13.41	4.64	6.45	2.39	1.74
1500, 250	20.16	4.50	3.18	0.00	0.00	0.00	57.44	31.44	7.37	0.20	0.07	0.07
420, 250	17.54	3.91	2.86	5.28	1.00	0.92	12.89	7.06	3.20	8.73	3.23	2.18
430, 250	22.86	5.10	3.49	2.49	0.47	0.45	17.65	9.66	3.85	8.44	3.12	2.13
440, 250	24.87	5.55	3.71	1.64	0.31	0.30	21.30	11.65	4.29	7.68	2.84	1.98
460, 250	26.15	5.83	3.85	0.90	0.17	0.17	26.97	14.76	4.90	5.59	2.07	1.56
510, 250	26.83	5.99	3.92	0.41	0.08	0.08	33.91	18.56	5.56	3.35	1.24	1.03
610, 250	26.63	5.94	3.90	0.14	0.03	0.03	40.54	22.18	6.12	1.66	0.61	0.55
910, 250	23.94	5.34	3.61	0.03	0.01	0.01	49.91	27.31	6.84	0.57	0.21	0.20
1410, 250	20.14	4.49	3.17	0.01	0.00	0.00	57.14	31.27	7.35	0.17	0.06	0.06
Total Backgrounds	153.70			212.31			25.54			55.77		

Table B.2: Yields and significance for $A \to Z(\to X)H(\to 4\ell)$ signal taken from fully simulated MC samples. The Z boson mass is fixed to 90 GeV, and the H and A masses are varied with $m_A = m_Z + m_H + m_{\mathrm{Gap}}$. The m_{Gap} is set to be 10, 20, 30, 40, 50, 100, 200, 500, and 1000 GeVs to generate different signals. The table shows event yields and significances for signals with H masses of 220 and 250 GeVs for different categories. The significance is calculated using Z_{Sig_1} and Z_{Sig_2} defined in Equation 6.4. The $A \to Z(\to X)H(\to 4\ell)$ signal cross section is assumed to be 1 fb.

(m_A, m_H) GeV	$N_{\mathrm{jets}}^{\mathrm{Central}} = 0$						$N_{\mathrm{jets}}^{\mathrm{Central}} \geq 1$						$N_{b\text{-jets}} \geq 1$			$\lvert m_{\mathrm{jj}}^{\mathrm{Central}} - m_Z \rvert < 20$			$\lvert m_{\mathrm{jj}}^{\mathrm{Central}} - m_Z \rvert > 20$			$N_{\mathrm{jets}}^{\mathrm{Central}} = 1$		
	High-$E_{\mathrm{T}}^{\mathrm{miss}}$			Low-$E_{\mathrm{T}}^{\mathrm{miss}}$			High-$E_{\mathrm{T}}^{\mathrm{miss}}$			Low-$E_{\mathrm{T}}^{\mathrm{miss}}$														
	Yields	Z_{Sig_1}	Z_{Sig_2}	Yields	Z_{Sig_1}	Z_{Sig_2}	Yields	Z_{Sig_1}	Z_{Sig_2}	Yields	Z_{Sig_1}	Z_{Sig_2}	Yields	Z_{Sig_1}	Z_{Sig_2}	Yields	Z_{Sig_1}	Z_{Sig_2}	Yields	Z_{Sig_1}	Z_{Sig_2}	Yields	Z_{Sig_1}	Z_{Sig_2}
320, 220	4.88	0.88	0.82	2.59	0.40	0.39	2.36	1.05	0.86	4.51	1.35	1.14	8.02	1.69	1.45	6.44	1.97	1.56	12.61	1.83	1.63	13.09	1.17	1.11
330, 220	6.15	1.11	1.01	1.82	0.28	0.27	3.16	1.40	1.10	4.74	1.42	1.19	8.66	1.83	1.55	6.77	2.07	1.62	13.19	1.91	1.69	12.74	1.14	1.08
340, 220	6.66	1.20	1.09	1.35	0.21	0.20	3.98	1.76	1.32	4.70	1.41	1.18	9.19	1.94	1.64	7.03	2.15	1.67	13.82	2.00	1.76	12.31	1.10	1.05
350, 220	6.85	1.24	1.12	1.08	0.17	0.16	4.72	2.09	1.50	4.57	1.37	1.15	9.70	2.05	1.71	7.35	2.25	1.73	14.49	2.10	1.84	11.73	1.05	1.00
360, 220	6.96	1.25	1.13	0.93	0.14	0.14	5.38	2.38	1.66	4.41	1.32	1.12	10.02	2.12	1.76	7.68	2.35	1.79	15.05	2.18	1.90	11.21	1.00	0.96
410, 220	6.91	1.25	1.13	0.66	0.10	0.10	7.28	3.22	2.07	3.69	1.10	0.96	11.27	2.38	1.94	9.54	2.92	2.12	16.60	2.41	2.07	9.17	0.82	0.79
510, 220	6.58	1.19	1.08	0.52	0.08	0.08	9.18	4.06	2.43	3.06	0.92	0.81	12.76	2.70	2.15	12.51	3.83	2.60	17.61	2.55	2.18	6.93	0.62	0.60
810, 220	5.75	1.04	0.95	0.35	0.05	0.05	11.88	5.25	2.88	2.31	0.69	0.63	15.00	3.17	2.45	17.38	5.32	3.28	17.82	2.58	2.20	5.21	0.47	0.46
1310, 220	4.82	0.87	0.81	0.27	0.04	0.04	13.73	6.08	3.16	2.34	0.70	0.64	15.61	3.30	2.53	5.31	1.63	1.33	25.91	3.76	3.02	9.67	0.86	0.83
350, 250	4.77	1.06	0.96	2.66	0.51	0.48	2.17	1.19	0.93	4.56	1.69	1.32	8.52	2.23	1.77	6.91	2.62	1.86	13.96	2.50	2.08	14.21	1.57	1.45
360, 250	6.17	1.38	1.20	1.89	0.36	0.35	3.01	1.64	1.19	4.91	1.82	1.41	9.16	2.39	1.88	7.11	2.69	1.89	14.56	2.61	2.15	13.71	1.51	1.40
370, 250	6.62	1.48	1.28	1.40	0.27	0.26	3.91	2.14	1.45	4.84	1.79	1.39	9.72	2.54	1.97	7.44	2.82	1.96	15.29	2.74	2.24	12.95	1.43	1.33
380, 250	6.84	1.53	1.32	1.12	0.21	0.21	4.75	2.60	1.67	4.70	1.74	1.36	10.17	2.66	2.04	7.69	2.91	2.01	15.83	2.84	2.31	12.25	1.35	1.26
390, 250	6.87	1.53	1.32	0.94	0.18	0.17	5.44	2.98	1.84	4.48	1.66	1.31	10.53	2.75	2.10	8.16	3.09	2.10	16.30	2.92	2.37	11.62	1.28	1.20
440, 250	6.89	1.54	1.33	0.65	0.12	0.12	7.58	4.15	2.29	3.74	1.39	1.13	11.86	3.10	2.30	9.87	3.74	2.40	17.80	3.19	2.55	9.23	1.02	0.97
540, 250	6.64	1.48	1.28	0.50	0.10	0.09	9.51	5.21	2.65	3.04	1.13	0.95	13.39	3.50	2.53	12.98	4.92	2.91	18.56	3.33	2.63	6.98	0.77	0.74
840, 250	5.78	1.29	1.14	0.37	0.07	0.07	12.32	6.74	3.11	2.41	0.89	0.77	15.54	4.06	2.83	17.74	6.72	3.57	18.59	3.33	2.64	5.31	0.59	0.57
1340, 250	4.94	1.10	0.99	0.28	0.05	0.05	14.50	7.94	3.43	2.59	0.96	0.82	16.31	4.26	2.93	5.23	1.98	1.50	27.25	4.89	3.57	10.19	1.13	1.06
Total Backgrounds	153.70			212.31			25.54			55.77			111.91			53.34			237.90			627.44		

Table B.3: The signal acceptance times efficiencies for the $R \to SH \to 4\ell + E_{\mathrm{T}}^{\mathrm{miss}}$ signal taken from fully simulated MC samples. The S mass is fixed to 160 GeV, and the H and R masses are varied with $m_R = m_S + m_H + m_{\mathrm{Gap}}$. The m_{Gap} is set to be 10, 20, 30, 40, 50, 100, 200, 500, and 1000 GeVs to generate different signals. The table shows the acceptance times efficiencies for signals with H masses of 600, 800, and 1000 GeVs.

(m_R, m_H) GeV	$N_{\mathrm{jets}}^{\mathrm{Central}} = 0$		$N_{\mathrm{jets}}^{\mathrm{Central}} \geq 1$	
	High-$E_{\mathrm{T}}^{\mathrm{miss}}$	Low-$E_{\mathrm{T}}^{\mathrm{miss}}$	High-$E_{\mathrm{T}}^{\mathrm{miss}}$	Low-$E_{\mathrm{T}}^{\mathrm{miss}}$
770, 600	8.31%	4.78%	4.23%	7.67%
780, 600	13.68%	2.68%	8.08%	10.85%
790, 600	15.88%	1.74%	13.05%	10.84%
800, 600	17.00%	1.16%	17.57%	9.73%
810, 600	17.13%	0.90%	21.29%	8.05%
860, 600	17.74%	0.39%	30.55%	3.74%
960, 600	17.62%	0.14%	35.52%	1.71%
1260, 600	16.24%	0.03%	40.57%	0.58%
1760, 600	14.10%	0.01%	44.33%	0.19%
970, 800	6.85%	4.66%	3.13%	7.11%
980, 800	11.60%	3.23%	6.07%	11.09%
990, 800	14.27%	1.94%	10.78%	12.80%
1000, 800	15.13%	1.37%	15.59%	12.14%
1010, 800	16.04%	1.04%	19.86%	10.37%
1060, 800	17.16%	0.44%	31.59%	4.83%
1160, 800	16.50%	0.16%	38.07%	2.01%
1460, 800	15.23%	0.06%	42.65%	0.60%
1960, 800	13.77%	0.01%	45.52%	0.21%
1500, 1000	15.31%	0.08%	42.34%	1.13%
1170, 1000	5.80%	4.28%	2.56%	6.44%
1180, 1000	10.03%	3.38%	5.04%	10.77%
1190, 1000	12.68%	2.20%	8.95%	13.31%
1200, 1000	13.92%	1.46%	13.55%	13.74%
1210, 1000	14.58%	1.08%	18.24%	12.33%
1260, 1000	15.78%	0.47%	31.80%	5.81%
1360, 1000	15.85%	0.17%	39.30%	2.38%
1660, 1000	14.86%	0.04%	43.88%	0.71%
2160, 1000	13.19%	0.03%	46.66%	0.26%

Table B.4: The signal acceptance times efficiencies for the $A \to Z(\to 2\ell)H(\to 2\ell + X)$ signal taken from the fully simulated MC samples. The Z boson mass is fixed to 90 GeV, and the H and A masses are varied with $m_A = m_Z + m_H + m_{\text{Gap}}$. The m_{Gap} is set to be 10, 20, 30, 40, 50, 100, 200, 500, and 1000 GeV to generate different signals. The table shows the acceptance times efficiencies for signals with H masses of 220 and 250 GeV.

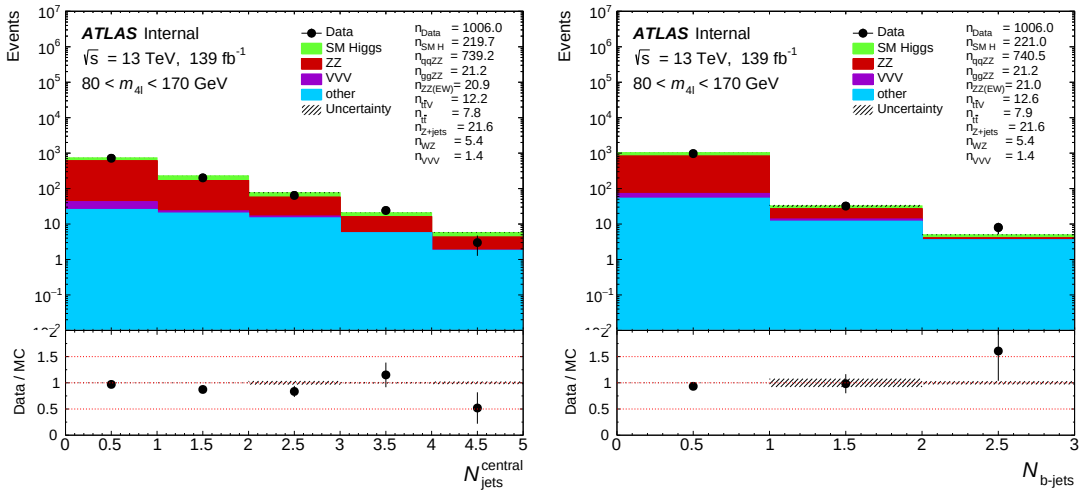
(m_A, m_H) GeV	$N_{\text{jets}}^{\text{Central}} = 0$		$N_{\text{jets}}^{\text{Central}} \geq 1$		$N_{b\text{-jets}} \geq 1$	$\lvert m_{\text{jj}}^{\text{Central}} - m_Z \rvert < 20$	$\lvert m_{\text{jj}}^{\text{Central}} - m_Z \rvert > 20$	$N_{\text{jets}}^{\text{Central}} = 1$
	High-$E_{\text{T}}^{\text{miss}}$	Low-$E_{\text{T}}^{\text{miss}}$	High-$E_{\text{T}}^{\text{miss}}$	Low-$E_{\text{T}}^{\text{miss}}$				
320, 220	1.89	0.46	1.01	1.41	2.71	2.01	4.01	3.80
330, 220	2.77	0.70	1.65	2.13	4.28	2.96	6.19	5.60
340, 220	3.24	0.72	2.01	2.53	5.18	3.66	7.81	6.69
350, 220	3.61	0.81	2.43	2.73	6.00	4.24	9.02	7.55
360, 220	3.91	0.84	2.65	2.78	6.71	4.73	9.71	8.18
410, 220	4.55	0.70	3.78	3.04	8.42	5.76	12.65	9.29
510, 220	4.49	0.56	4.54	2.87	9.41	6.59	14.57	8.38
810, 220	4.36	0.28	7.12	2.46	10.30	7.14	16.35	6.26
1310, 220	3.91	0.17	9.95	2.30	9.07	5.17	15.19	4.65
350, 250	3.03	0.32	2.30	1.95	4.56	3.08	6.44	5.04
360, 250	3.54	0.40	2.76	2.27	5.46	3.69	7.98	6.10
370, 250	3.95	0.45	2.95	2.52	6.13	4.26	9.04	6.63
380, 250	4.10	0.50	3.28	2.66	6.71	4.53	9.84	7.12
390, 250	4.23	0.52	3.47	2.63	7.09	4.91	10.62	7.47
440, 250	4.71	0.57	4.28	2.99	8.71	6.17	13.22	8.23
540, 250	4.57	0.52	4.89	2.72	9.75	7.10	15.38	7.98
840, 250	4.27	0.30	6.88	2.45	11.02	8.13	17.37	6.37
1340, 250	3.61	0.14	9.41	2.39	10.75	6.13	17.19	4.74

B.4 Background estimation

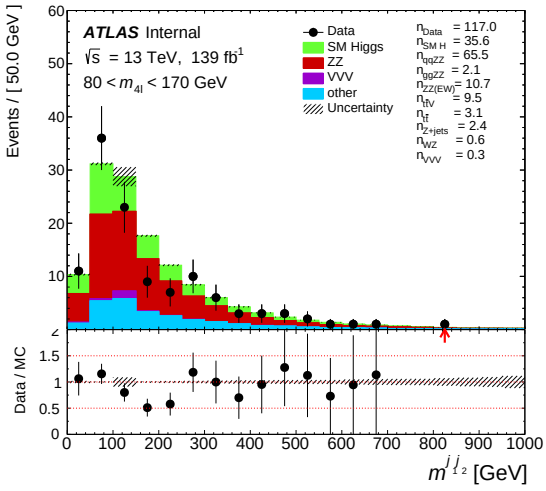
The main background in this study emerges from the Z boson leptonic decay. The quark-antiquark annihilation, $qqZZ$, is estimated to be 84.60% of the total expected background events and approximately 11.70% from the gluon-initiated, $ggZZ$, process. Only 1% accounts for EW vector-boson scattering, $q\bar{q} \to ZZ$ (EW), process. All other background processes such as $t\bar{t}V$, Zjets, $t\bar{t}$, WZ and VVV are estimated to be nearly 2.60% from the whole background events.

The control region (CR) is defined by $80 < m_{4\ell} < 170$ GeV to determine the compatibility of the data to the SM prediction. Table B.5 shows the number of events in the CR for data and background processes. The number of events for the signal regions in the CR are shown in Table B.6. Figure B.6 displays the number of jets, b-tagged jets, and invariant mass of the di-jets. The 4ℓ kinematic distributions are shown in Figure B.7 for the invariant mass, transverse momentum, pseudorapidity and rapidity of the 4ℓ final states. Distributions of the invariant mass of the 2ℓ system for the first, m_{Z_1}, and second, m_{Z_2}, lepton pairs and the $E_{\text{T}}^{\text{miss}}$ significance are shown in Appendix B.5, Figure B.9. Appendix B.5,

Figure B.10 shows the momentum of individual leptons, $p_T^{\ell_1}$, $p_T^{\ell_2}$, $p_T^{\ell_3}$ and $p_T^{\ell_4}$.



(a) (b)



(c)

Figure B.6: Kinematic distributions of the (a) number of central jets, (b) number of b-tagged jets and (c) di-jet invariant mass. The data at integrated luminosity of 139 fb^{-1} are compared to the SM prediction in the control region of $80 < m_{4\ell} < 170$ GeV.

Table B.5: The expected and observed events in a control region of $80 < m_{4\ell} < 170\,\text{GeV}$. The data used corresponds to an integrated luminosity of 139 fb^{-1}.

	SM Higgs	$q\bar{q} \to ZZ$	$gg \to ZZ$	$q\bar{q} \to ZZ$(EW)	$t\bar{t}V$	VVV	Z+jets	WZ	$t\bar{t}$	Expected	Observed
$2\mu 2e$	99.87±0.11	283.19±1.03	9.40±0.10	9.67±0.12	5.71±0.12	0.67±0.02	12.34±2.16	2.62±0.23	5.98±0.26	429.44±2.43	417.00±20.42
$4e$	39.18±0.07	128.02±0.75	3.97±0.07	3.76±0.07	2.67±0.08	0.27±0.02	2.70±0.16	1.66±0.18	0.76±0.10	182.99±0.81	178.00±13.34
4μ	81.53±0.10	328.41±1.27	7.81±0.09	7.61±0.12	4.31±0.10	0.46±0.02	6.55±0.25	1.07±0.15	1.18±0.10	438.93±1.32	411.00±20.27
Total ($4\ell = 4\mu + 4e + 2\mu 2e$)	220.59±0.17	739.61±1.80	21.18±0.15	21.03±0.19	12.69±0.17	1.40±0.04	21.59±2.18	5.35±0.33	7.92±0.30	1051.36±2.88	1006.00±31.72

[H]

Table B.6: The expected and observed events for the signal regions in a control region of $80 < m_{4\ell} < 170\,\text{GeV}$. The data used corresponds to an integrated luminosity of 139 fb^{-1}.

	SM Higgs	$q\bar{q} \to ZZ$	$gg \to ZZ$	$q\bar{q} \to ZZ$(EW)	$t\bar{t}V$	VVV	Z+jets	WZ	$t\bar{t}$	Expected	Observed
Preselection	220.59±0.17	739.61±1.80	21.18±0.15	21.03±0.19	12.69±0.17	1.40±0.04	21.59±2.18	5.35±0.33	7.92±0.30	1051.36±2.88	1006.00±31.72
High-$E_{\text{T}}^{\text{miss}}$ & $N_{\text{jets}}^{\text{Central}} = 0$	24.76±0.06	57.39±0.55	3.82±0.07	1.10±0.04	0.55±0.05	0.63±0.02	3.23±0.17	2.26±0.21	1.64±0.12	95.38±0.64	93.00±9.64
Low-$E_{\text{T}}^{\text{miss}}$ & $N_{\text{jets}}^{\text{Central}} = 0$	18.95±0.05	50.34±0.54	2.26±0.05	0.64±0.04	0.02±0.01	0.05±0.01	3.70±1.21	0.35±0.08	0.17±0.04	76.48±1.33	91.00±9.54
High-$E_{\text{T}}^{\text{miss}}$ & $N_{\text{jets}}^{\text{Central}} \geq 1$	3.05±0.02	7.41±0.16	0.53±0.03	0.55±0.03	1.60±0.07	0.39±0.02	0.26±0.05	1.01±0.14	1.65±0.15	16.44±0.28	16.00±4.00
Low-$E_{\text{T}}^{\text{miss}}$ & $N_{\text{jets}}^{\text{Central}} \geq 1$	6.79±0.03	18.19±0.26	0.76±0.03	1.34±0.05	0.46±0.04	0.09±0.01	0.54±0.07	0.45±0.10	0.41±0.06	29.04±0.30	31.00±5.57
$N_{b\text{-jets}} \geq 1$	6.73±0.02	13.39±0.24	0.28±0.02	0.91±0.04	9.43±0.14	0.03±0.01	1.76±1.26	0.18±0.06	3.29±0.20	36.01±1.31	40.00±6.32
$\lvert m_{jj}^{\text{Central}} - m_Z \rvert < 20$	4.66±0.02	8.31±0.11	0.28±0.02	1.62±0.05	0.06±0.01	0.01±0.00	0.15±0.04	0.04±0.03	0.05±0.02	15.18±0.13	14.00±3.74
$\lvert m_{jj}^{\text{Central}} - m_Z \rvert > 20$	15.88±0.04	32.16±0.21	0.87±0.03	5.27±0.09	0.26±0.03	0.04±0.01	0.30±0.05	0.14±0.05	0.18±0.04	55.09±0.25	36.00±6.00
$N_{\text{jets}}^{\text{Central}} = 1$	50.85±0.07	113.14±0.77	3.53±0.06	7.60±0.12	0.25±0.03	0.07±0.01	2.10±0.13	0.61±0.11	0.33±0.05	178.49±0.81	154.00±12.41
Rest	88.93±0.11	439.28±1.36	8.86±0.10	1.98±0.06	0.06±0.01	0.07±0.01	9.54±1.28	0.32±0.08	0.22±0.04	549.26±1.88	531.00±23.04

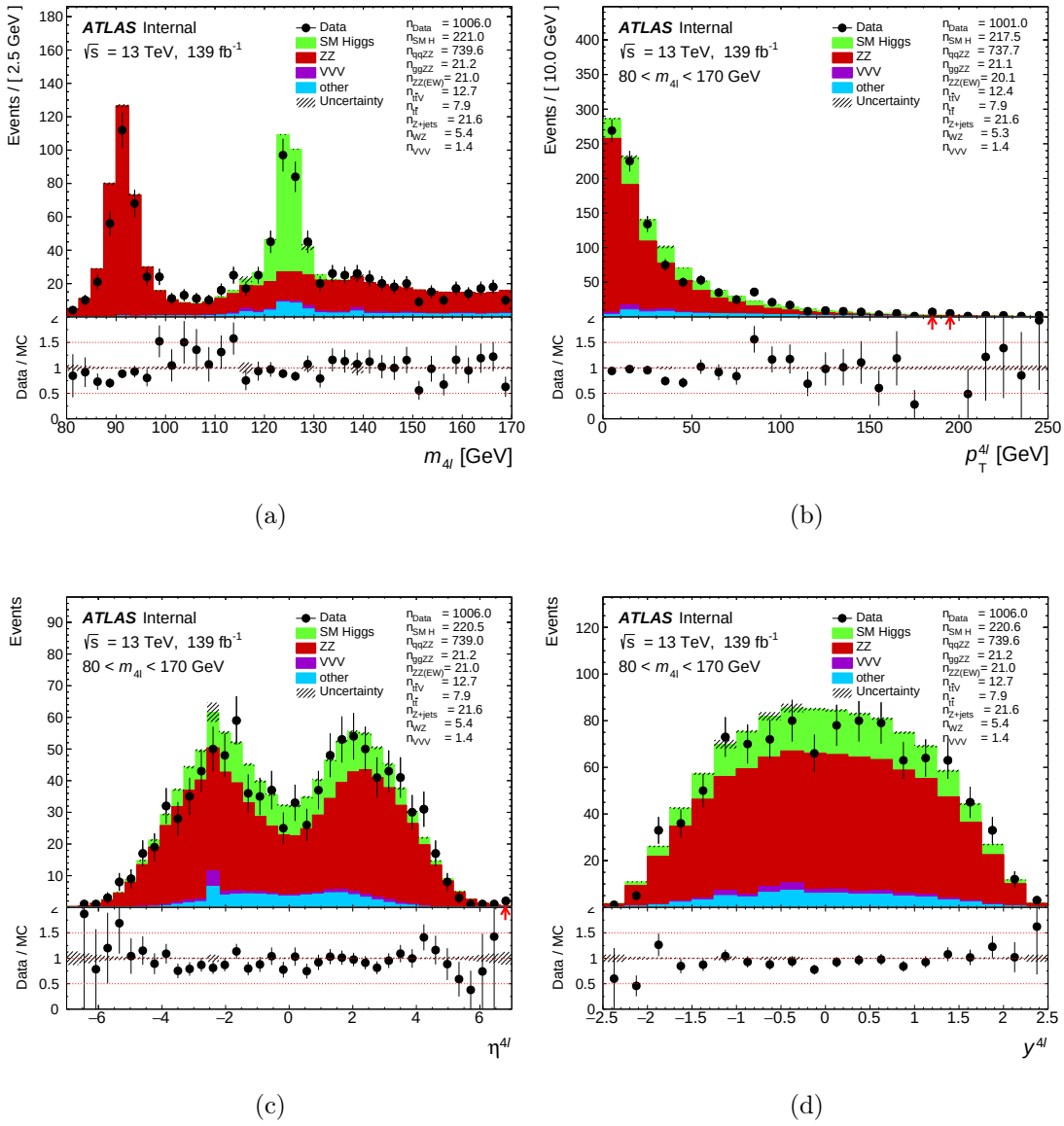


Figure B.7: Kinematic distributions of (a) the $m_{4\ell}$, (b) $p_T^{4\ell}$, (c) $\eta^{4\ell}$, and (d) $y^{4\ell}$. The data at integrated luminosity of 139 fb^{-1} are compared to the SM prediction in the control region of $80 < m_{4\ell} < 170$ GeV.

Since the CR is defined to be $m_{4\ell} < 2m_Z$, it is applicable to check the Data/MC comparisons for non-discriminative distributions in the signal region. A normali-

sation factor (μ_{ZZ}) for $qqZZ$ and $ggZZ$ processes is calculated using:

$$\mu_{ZZ} = \frac{\left(N^{\text{data}} - N_{\text{MC}}^{\text{non-}(qqZZ,\, ggZZ)}\right)}{N_{\text{MC}}^{(qqZZ,\, ggZZ)}}, \tag{B.1}$$

where N^{data} is the number of the data. $N_{\text{MC}}^{\text{non-}(qqZZ,\, ggZZ)}$ and $N_{\text{MC}}^{(qqZZ,\, ggZZ)}$ are the number of MC without and with the $qqZZ$ and $ggZZ$ processes, respectively. $\mu_{ZZ} = 1.11$ is used to scale the $qqZZ$ and $ggZZ$ as shown in Figure B.8. The misidentification of leptons is a critical source of background in events with multiple leptons. In this study, events with at least one jet misidentified as a lepton are fake lepton events. However, the fake lepton in the $m_{4\ell} > 200$ GeV range is negligible. These events emerge from $t\bar{t}V$ ($V = W/Z$), $t\bar{t}$, Z+jets and WZ background processes which are less than 3% of the total number of the background. Table B.7 shows the expected yields for events with fake leptons in the signal regions.

Table B.7: The expected yields for $t\bar{t}Z$, $t\bar{t}Z$, $Z+jets$, WZ and $t\bar{t}$ backgrounds from the MC simulation with an integrated luminosity of 139 fb^{-1}. The uncertainties included on the table are statistical uncertainty only. The expected events at the preselection are after the selection discussed in Section 6.3.

	$t\bar{t}Z$	$t\bar{t}W$	$Z+jets$	WZ	$t\bar{t}$
Preselection	37.02±0.42	0.16±0.03	3.85±1.15	4.89±0.31	2.80±0.19
High-$E_{\text{T}}^{\text{miss}}$ & $N_{\text{jets}}^{\text{Central}} = 0$	1.17±0.06	0.02±0.01	0.58±0.07	1.73±0.19	0.64±0.08
Low-$E_{\text{T}}^{\text{miss}}$ & $N_{\text{jets}}^{\text{Central}} = 0$	0.09±0.01	0.00±0.00	0.33±0.03	0.45±0.08	0.06±0.02
High-$E_{\text{T}}^{\text{miss}}$ & $N_{\text{jets}}^{\text{Central}} \geq 1$	3.90±0.14	0.04±0.01	0.05±0.02	0.75±0.12	0.58±0.07
Low-$E_{\text{T}}^{\text{miss}}$ & $N_{\text{jets}}^{\text{Central}} \geq 1$	1.28±0.08	0.00±0.01	0.11±0.03	0.32±0.08	0.20±0.07
$N_{b-\text{jets}} \geq 1$	28.51±0.37	0.08±0.02	0.12±0.03	0.14±0.05	0.95±0.13
$\lvert m_{jj}^{\text{Central}} - m_Z \rvert < 20$	0.22±0.03	0.00±0.00	0.00±0.00	0.04±0.03	0.01±0.01
$\lvert m_{jj}^{\text{Central}} - m_Z \rvert > 20$	1.08±0.08	0.01±0.01	0.80±0.73	0.31±0.08	0.08±0.02
$N_{\text{jets}}^{\text{Central}} = 1$	0.67±0.05	0.00±0.00	0.24±0.05	0.69±0.12	0.17±0.04
Rest	0.11±0.02	0.00±0.00	1.61±0.89	0.45±0.11	0.12±0.03

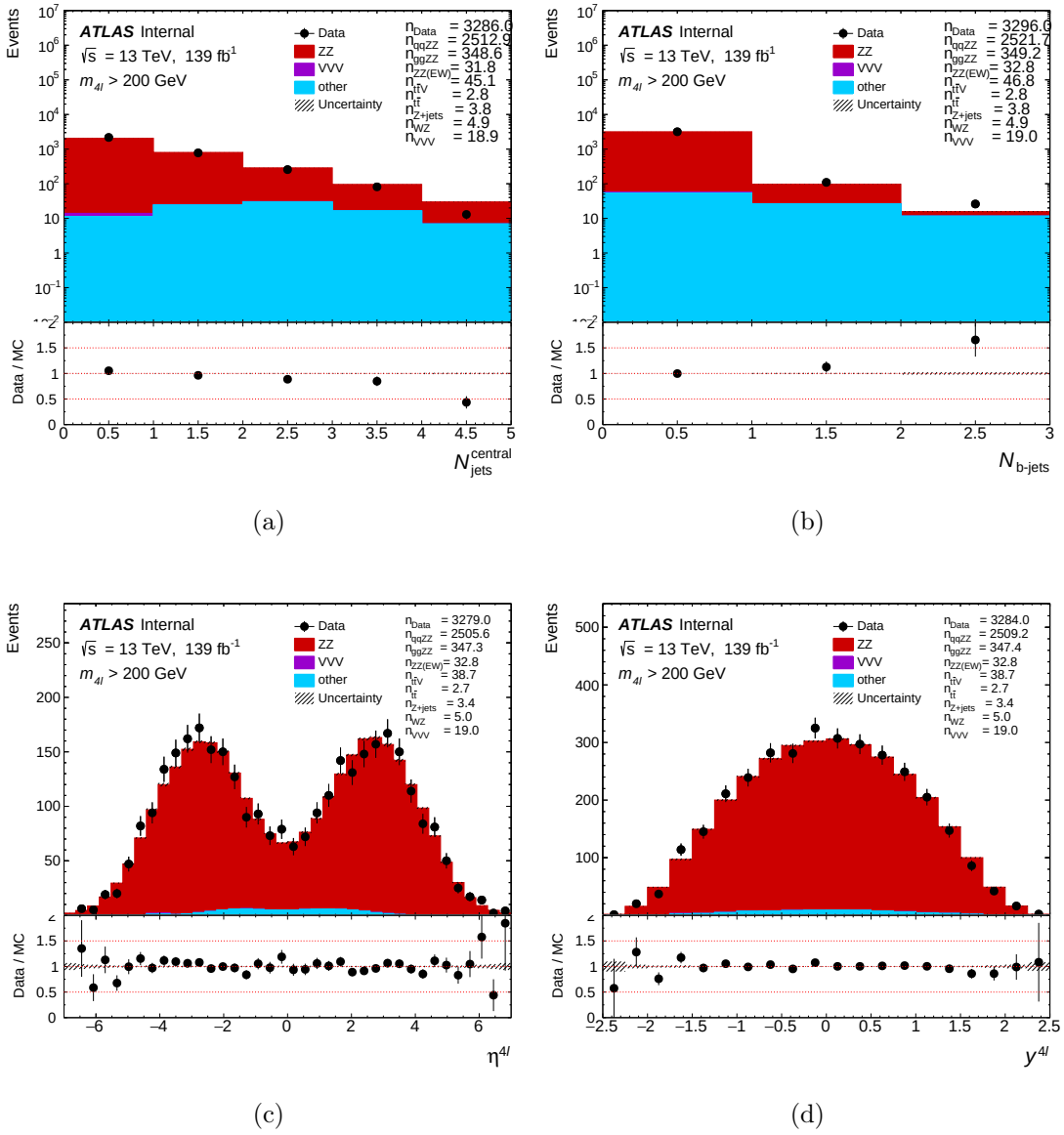
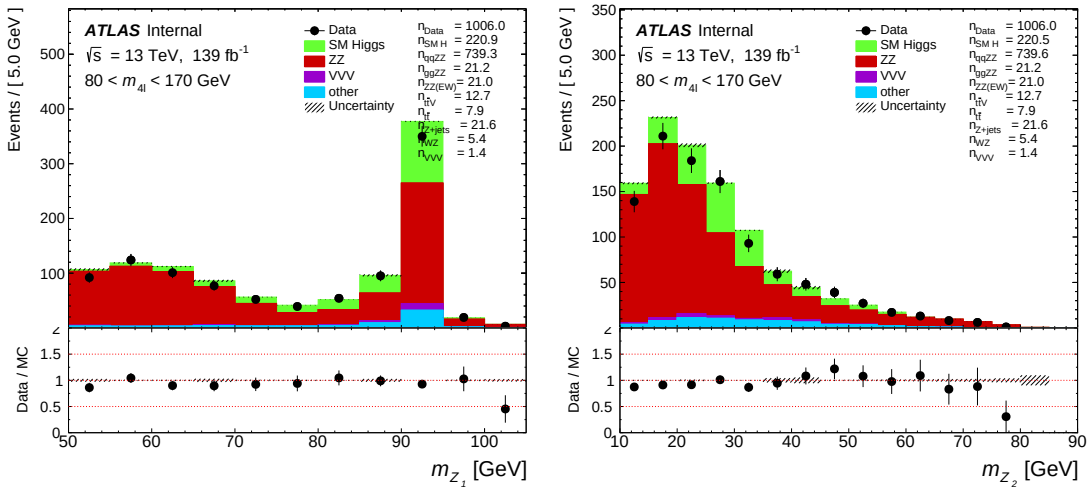


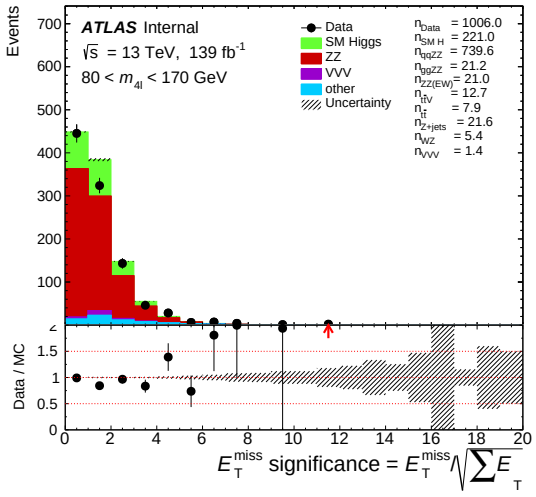
Figure B.8: Non-discriminative kinematic distributions of the (a) $N_{\text{jets}}^{\text{Central}}$, (b) $N_{b\text{-jets}}$, (c) $\eta^{4\ell}$, and (d) $y^{4\ell}$. The data corresponding to an integrated luminosity of 139 fb^{-1}, are compared to the SM prediction in the $m_{4\ell} > 200$ GeV region.

B.5 Kinematic distributions

Figures B.9 and B.10 show the kinematic distributions in the control region of $80 < m_{4\ell} < 170$ GeV.



(a) (b)



(c)

Figure B.9: Kinematic distributions of (a) the m_{Z_1}, (b), m_{Z_2} and (c) $E_{\mathrm{T}}^{\mathrm{miss}}$ significance. The date at integrated luminosity of 139 fb^{-1} are compared to the SM prediction in the control region of $80 < m_{4\ell} < 170$ GeV.

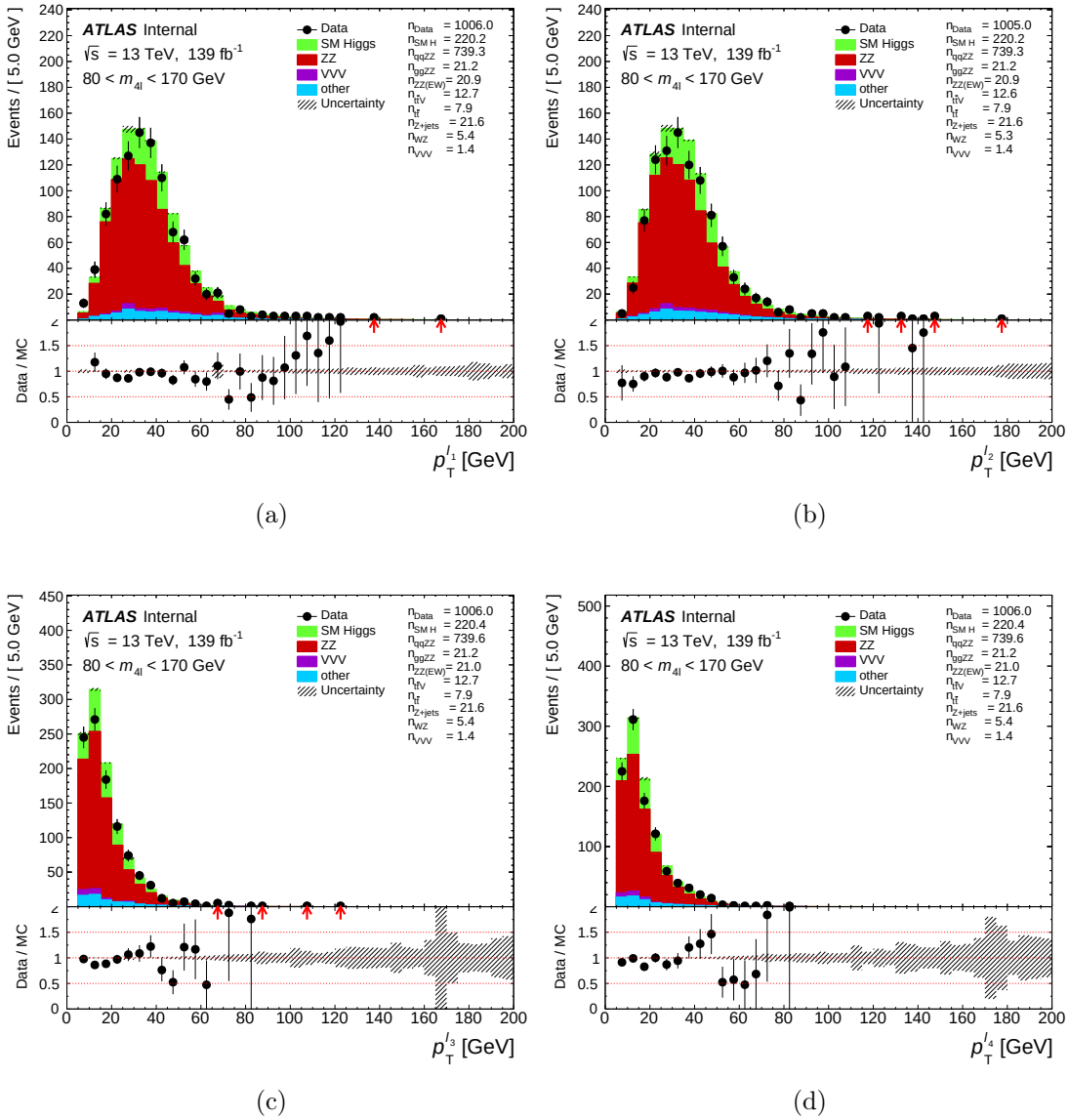


Figure B.10: Kinematic distributions of (a) the $p_{\mathrm{T}}^{\ell_1}$, (b) $p_{\mathrm{T}}^{\ell_2}$, (c) $p_{\mathrm{T}}^{\ell_3}$, and (d) $p_{\mathrm{T}}^{\ell_4}$. The date at integrated luminosity of 139 fb^{-1} are compared to the SM prediction in the control region of $80 < m_{4\ell} < 170\,\mathrm{GeV}$.

B.6 Signal modelling

The narrow-width signal models of $R \to SH \to 4\ell + E_{\mathrm{T}}^{\mathrm{miss}}$ and $A \to Z(\to X)H(\to 4\ell)$ signals are modelled using a double-sided Crystal ball ($\mathcal{DSCB}$) [172] plus Gaussian ($\mathcal{G}$) functions. The sum of these functions is described as:

$$P_{\mathrm{signal}}(m_{4\ell}) = f \times \mathcal{DSCB}(m_{4\ell}; \mu, \sigma, \alpha_1, n_1, \alpha_2, n_2) + (1-f) \times \mathcal{G}(m_{4\ell}; \mu, \sigma_{\mathcal{G}}), \quad \text{(B.2)}$$

where;

$$\mathcal{DSCB}(m_{4\ell}; \mu, \sigma, \alpha_1, n_1, \alpha_2, n_2) = \begin{cases} e^{-\frac{1}{2}\frac{m_{4\ell}-\mu}{\sigma}}; & \text{if } -\alpha_1 \leq \frac{m_{4\ell}-\mu}{\sigma} < \alpha_2 \\ \frac{e^{-\frac{1}{2}\alpha_1^2}}{\left[\frac{|\alpha_1|}{n_1}\left(\frac{n_1}{|\alpha_1|} - \left|\alpha_1 + \frac{m_{4\ell}-\mu}{\sigma}\right|\right)\right]^{n_1}}; & \text{if } \frac{m_{4\ell}-\mu}{\sigma} < \alpha_1 \\ \frac{e^{-\frac{1}{2}\alpha_2^2}}{\left[\frac{|\alpha_2|}{n_2}\left(\frac{n_2}{|\alpha_2|} - \left|\alpha_2 + \frac{m_{4\ell}-\mu}{\sigma}\right|\right)\right]^{n_2}}; & \text{if } \frac{m_{4\ell}-\mu}{\sigma} \geq \alpha_2 \end{cases} \quad \text{(B.3)}$$

Both $\mathcal{DSCB}$ and $\mathcal{G}$ functions peak at a mean value of $m_{4\ell}(\mu) = m_H$ which is the reconstructed 4-lepton invariant mass of (m_R, m_H) or (m_A, m_H) signal mass points. The resolution of the $m_{4\ell}$ distribution is contorted by σ and $\sigma_{\mathcal{G}}$ parameters. The power-law low-end (high-end) tail position of the non-Gaussian distribution is adjusted using the α_1 (α_2) parameter, while its slope is handled by the n_1 (n_2) parameter. The relative normalisation between the Gaussian and $\mathcal{DSCB}$ functions is taking care of by f parameter. The $P_{\mathrm{signal}}(m_{4\ell})$ function is fitted to simulated signal samples to determine the values of the function's parameters.

The MC samples used are from mc16a, mc16d and mc16e campaigns which add-up to 139 fb^{-1} luminosity of Run 2 dataset. The $\mathcal{DSCB} + \mathcal{G}$ PDF is fitted to the MC of individual 4μ, $4e$, $2\mu 2e$ channels to extract the parameter showing in equation B.2. Figure B.11 shows the $\mathcal{CB} + \mathcal{G}$ PDF fit to $R \to SH \to 4\ell + E_{\mathrm{T}}^{\mathrm{miss}}$ signals with $m_H = 220$ GeV and different m_R masses. The values of χ^2/ndof illustrates the goodness of the PDF fit. Tables B.8 and B.9 show χ^2/ndof values result from fitting $\mathcal{CB} + \mathcal{G}$ PDF to different $R \to SH \to 4\ell + E_{\mathrm{T}}^{\mathrm{miss}}$ and $A \to Z(\to X)H(\to 4\ell)$ signals. More plots and tables are included in appendix B.6 for all the considered mass points.

Table B.8: Summary of χ^2/ndof values from fitting $\mathcal{CB}+\mathcal{G}$ PDF of equation B.2 to m_H (m_A) between $220-250$ GeV ($390-1500$) GeV of the $R \to SH \to 4\ell + E_{\mathrm{T}}^{\mathrm{miss}}$ model.

(m_A, m_H) GeV	$N_{\mathrm{jets}}^{\mathrm{Central}} = 0$	$N_{\mathrm{jets}}^{\mathrm{Central}} \geq 1$	
	High-$E_{\mathrm{T}}^{\mathrm{miss}}$	High-$E_{\mathrm{T}}^{\mathrm{miss}}$	Low-$E_{\mathrm{T}}^{\mathrm{miss}}$
390, 220	1.26	1.74	1.80
400, 220	1.78	1.55	1.99
410, 220	1.47	1.95	1.88
420, 220	1.99	1.73	1.92
430, 220	1.97	1.86	1.76
450, 220	1.45	1.50	1.83
480, 220	1.54	1.96	1.11
580, 220	1.75	1.80	1.64
800, 220	1.94	2.22	1.76
880, 220	1.44	2.25	1.81
1380, 220	1.63	1.97	1.90
420, 250	1.49	1.65	1.98
430, 250	1.43	1.51	1.84
440, 250	1.91	1.58	1.79
450, 250	1.41	1.64	1.47
460, 250	1.86	0.83	1.85
510, 250	1.35	1.76	1.64
610, 250	1.87	1.89	1.39
910, 250	1.22	2.87	1.97
1410, 250	1.50	1.98	1.84
1500, 250	2.83	1.97	1.37

Table B.9: Summary of χ^2/ndof values from fitting $\mathcal{CB}+\mathcal{G}$ PDF of equation B.2 to m_H (m_A) between $220-400$ GeV ($320-1490$) GeV of the $A \to Z(\to X)H(\to 4\ell)$ model.

(m_A, m_H) GeV	$N_{\text{jets}}^{\text{Central}} = 0$	$N_{\text{jets}}^{\text{Central}} \geq 1$		$N_{b\text{-jets}} \geq 1$	$\lvert m_{jj}^{\text{Central}} - m_Z \rvert < 20$	$\lvert m_{jj}^{\text{Central}} - m_Z \rvert > 20$	$N_{\text{jets}}^{\text{Central}} = 1$
	High-$E_{\text{T}}^{\text{miss}}$	High-$E_{\text{T}}^{\text{miss}}$	Low-$E_{\text{T}}^{\text{miss}}$				
320, 220	1.95	1.79	2.28	1.75	1.96	1.86	2.00
330, 220	1.89	1.35	2.10	1.72	1.71	1.49	1.87
340, 220	1.94	1.64	2.80	1.90	1.82	1.47	1.52
350, 220	1.59	1.73	2.60	1.60	1.56	1.52	1.59
360, 220	1.90	1.41	2.58	1.41	1.43	1.48	0.94
410, 220	1.45	1.91	2.80	1.80	1.94	1.70	1.94
510, 220	1.41	1.58	1.67	1.18	1.53	1.34	2.06
810, 220	2.61	1.73	2.12	1.85	2.06	1.81	0.72
1310, 220	1.96	1.78	1.60	2.09	1.80	1.56	1.96
350, 250	1.20	1.13	2.15	1.84	1.61	1.17	1.90
360, 250	1.37	1.35	2.68	1.30	1.33	1.22	1.81
370, 250	2.04	1.63	2.52	1.65	1.52	1.27	1.04
380, 250	1.96	1.41	2.79	1.97	1.85	2.31	1.96
390, 250	1.97	1.51	2.83	1.38	1.68	1.71	2.28
440, 250	1.85	1.44	2.36	1.27	1.70	1.42	1.47
540, 250	1.86	1.34	2.30	2.06	1.72	1.39	1.42
840, 250	1.24	1.47	2.93	1.80	2.02	1.34	1.48
1340, 250	1.69	1.85	1.52	1.50	0.87	1.48	0.83
400, 300	1.72	1.51	2.86	1.62	1.56	2.44	3.00
410, 300	2.00	1.78	1.78	1.48	2.06	1.31	2.31
420, 300	1.95	1.70	2.46	1.19	1.89	1.37	1.92
430, 300	1.61	1.19	1.97	1.97	1.78	1.84	1.78
440, 300	1.93	1.78	1.93	1.61	1.73	2.28	1.91
490, 300	1.39	1.98	2.08	1.96	1.53	1.91	1.36
590, 300	1.79	1.76	1.84	1.76	2.56	2.92	1.58
890, 300	2.53	2.07	2.49	2.38	1.46	1.72	1.11
1390, 300	1.70	1.59	2.43	1.87	1.56	2.42	1.26
500, 400	0.96	1.33	2.79	1.15	1.52	1.97	1.54
510, 400	1.50	1.41	2.82	2.10	1.45	1.54	1.19
520, 400	1.99	1.04	2.95	1.56	1.87	1.68	1.28
530, 400	2.13	1.20	2.26	1.62	1.58	1.08	1.23
540, 400	1.40	1.93	2.73	1.68	2.30	1.47	2.40
590, 400	1.78	1.78	1.87	2.10	1.59	1.93	1.28
690, 400	2.82	2.22	1.67	2.01	1.80	1.75	1.78
990, 400	2.79	2.01	1.71	2.21	1.96	1.87	1.38
1490, 400	1.82	1.86	1.93	1.89	0.80	1.77	1.46

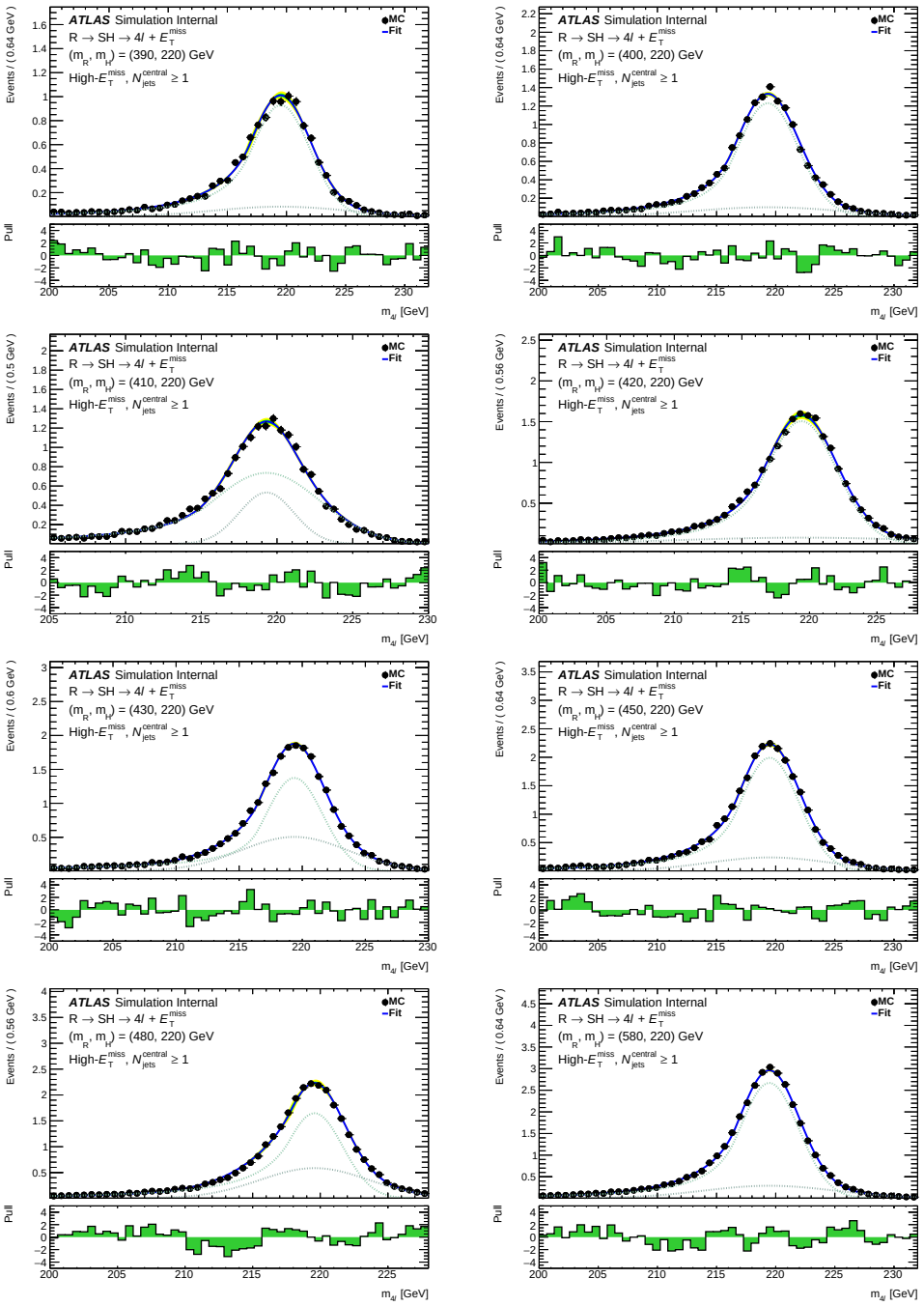


Figure B.11: Distributions of the four-lepton invariant mass for fitting the $\mathcal{CB}+\mathcal{G}$ PDF of equation B.2 to $R \to SH \to 4\ell + E_{\mathrm{T}}^{\mathrm{miss}}$ signal with $m_H = 220\,\mathrm{GeV}$ and different m_R masses. The fit is performed using MC simulation with statistics equivalent to integrated luminosity of $139\,\mathrm{fb}^{-1}$. The ratio plot in each figure shows the pull distribution. The plots are shown for the High-$E_{\mathrm{T}}^{\mathrm{miss}}$ and $N_{\mathrm{jets}}^{\mathrm{Central}} \geq 1$ signal region.

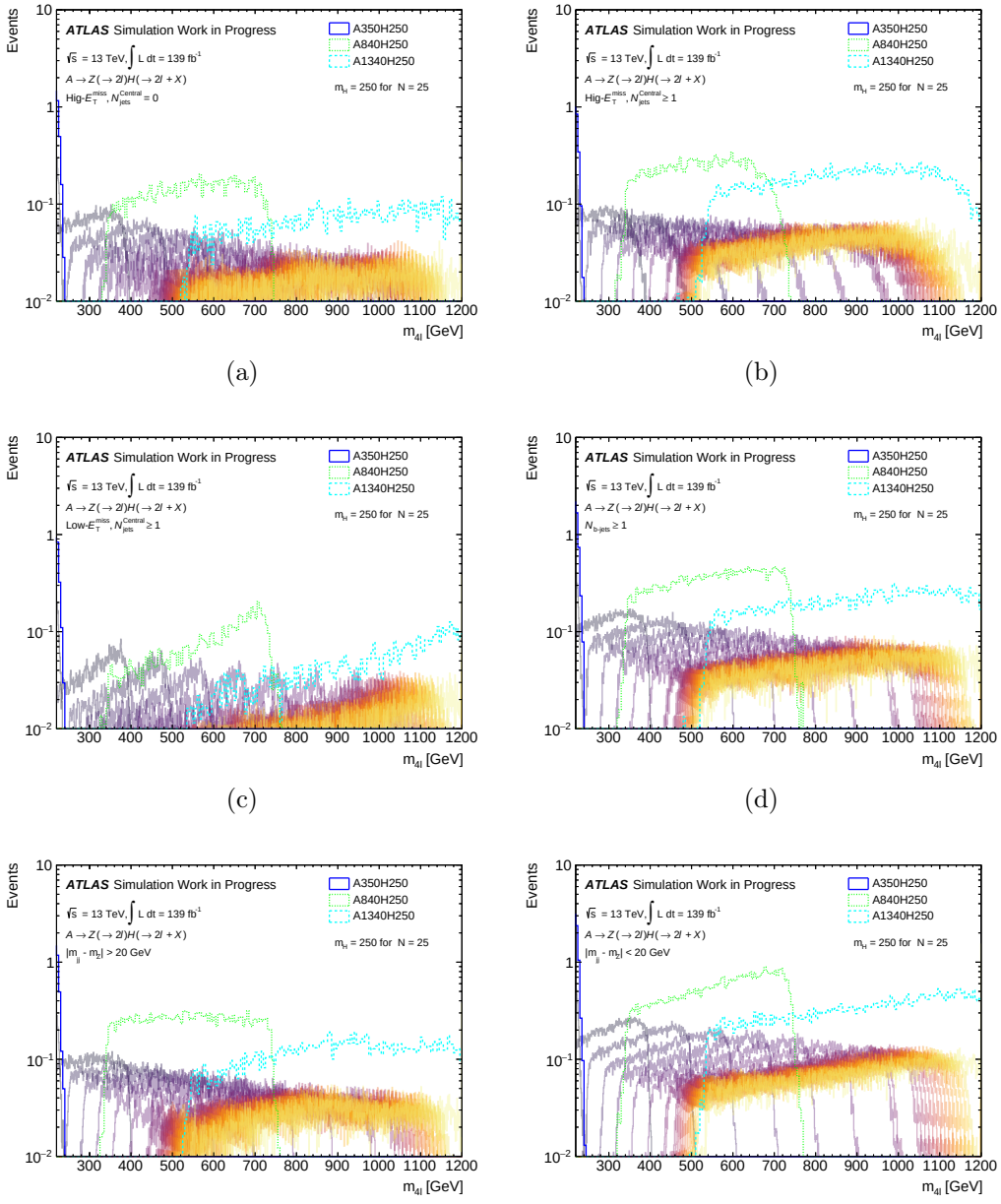


Figure B.12: The invariant mass of the four leptons of the interpolated $A \rightarrow Z(\rightarrow 2\ell)H(\rightarrow 2\ell + X)$ signal shape with H mass fixed to 250 GeV and A mass varied by 10 GeV. Because the signal doesn't peak on the H mass, a few mass points ($N = 25$) are shown as an example to get a better view of the interpolated samples. The blue, green and cyan histogram are the original histograms used in the input for different categories.

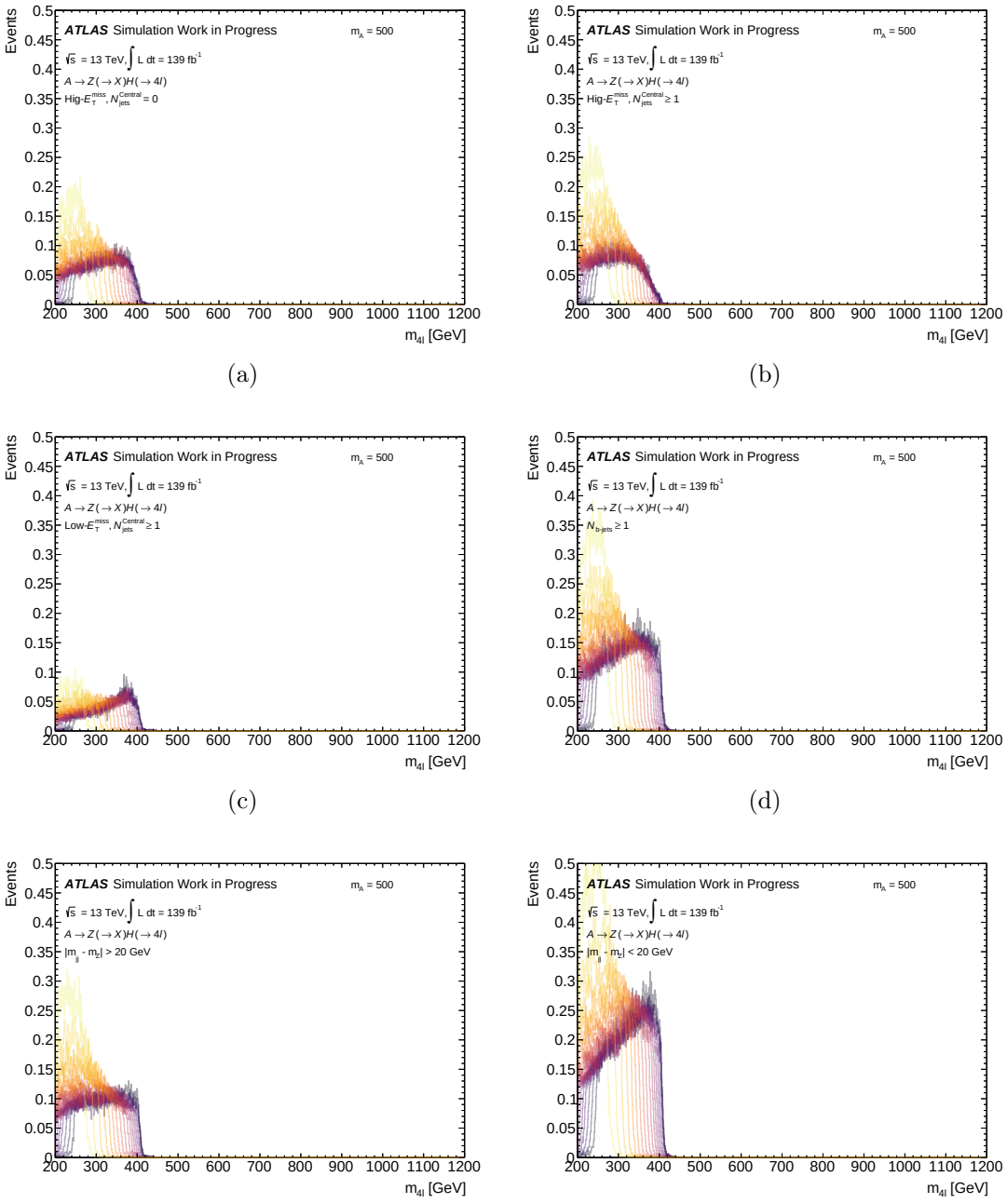


Figure B.13: The invariant mass of the four leptons of the interpolated $A \to Z(\to 2\ell)H(\to 2\ell + X)$ signal shape with A mass fixed to 500 GeV and H mass varied by 10 GeV.

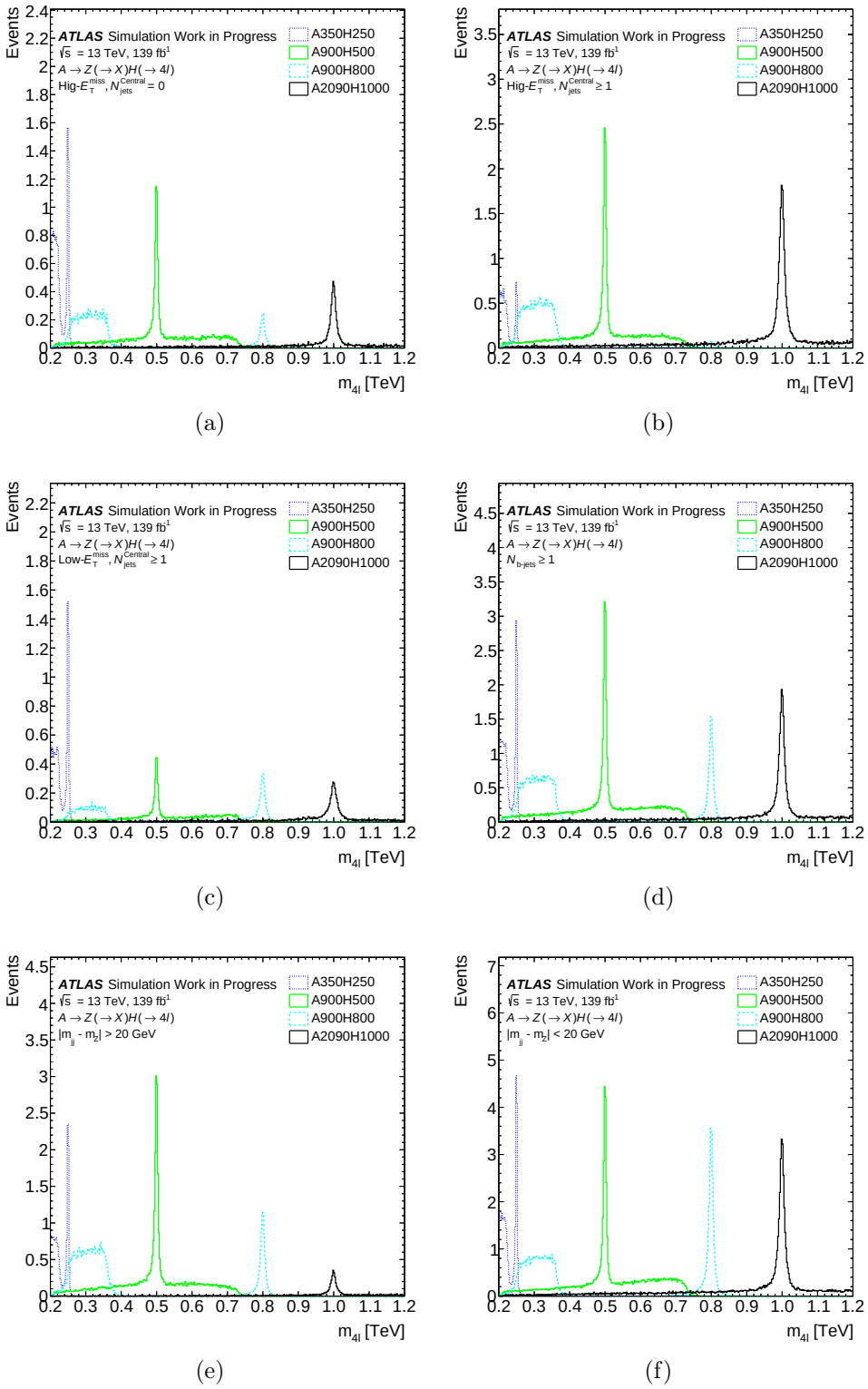


Figure B.14: The invariant mass of the four leptons of the $A \to ZH \to 4\ell + X$ for all the signal regions with varies mass points.

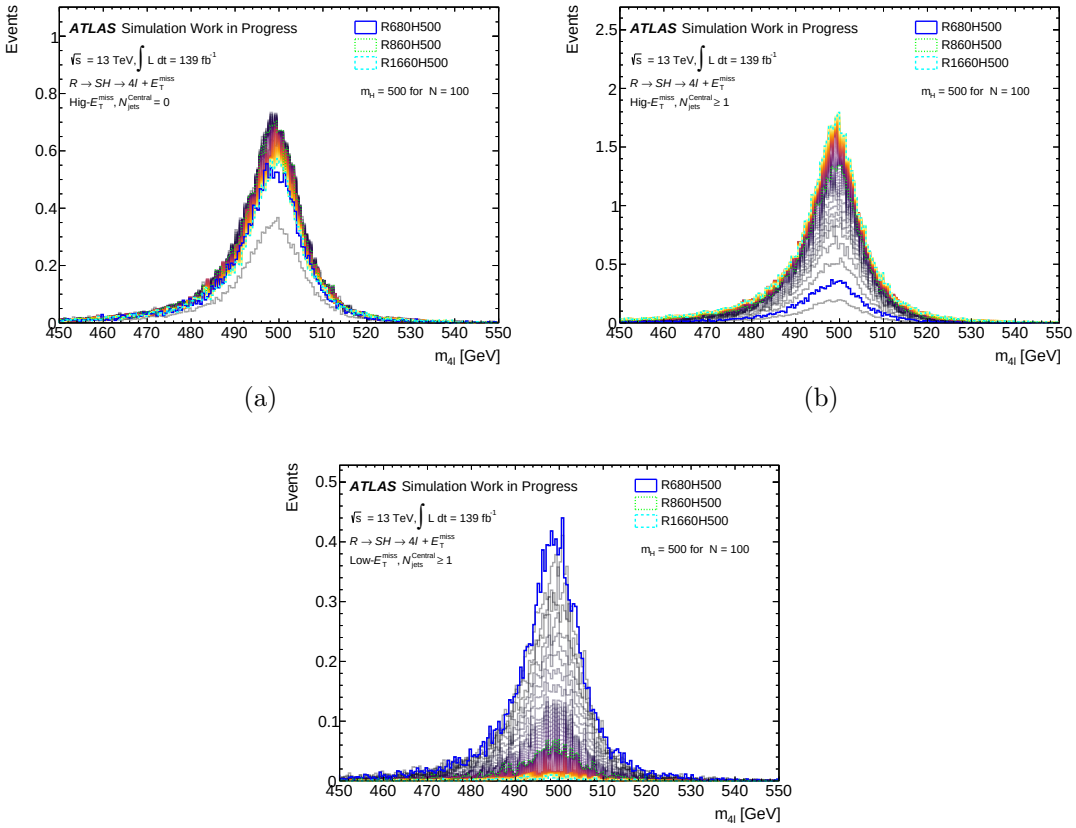
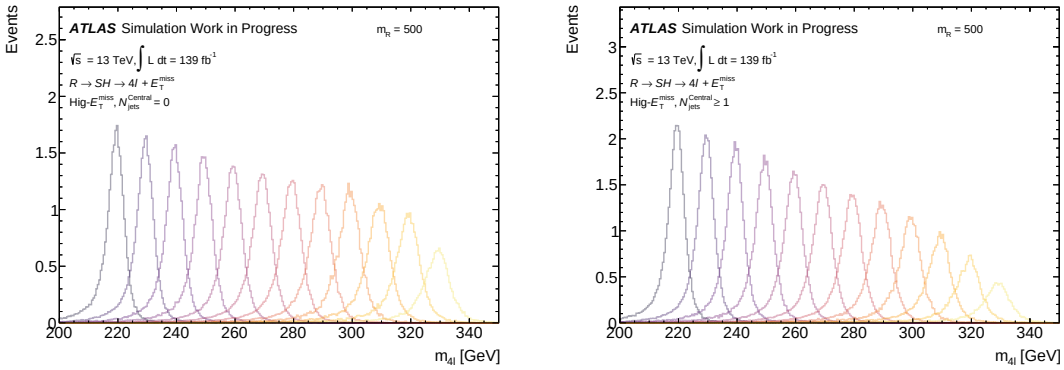
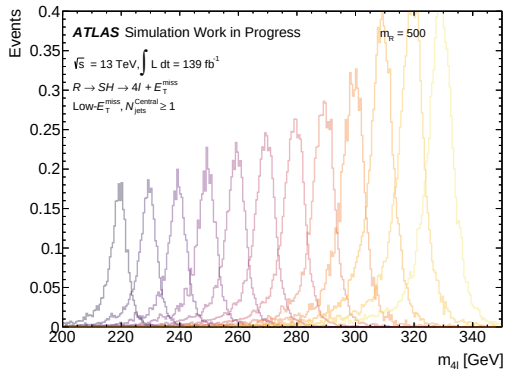


Figure B.15: The invariant mass of the four leptons of the interpolated $R \to SH \to 4\ell + E_{\mathrm{T}}^{\mathrm{miss}}$ signal shape with H mass fixed to 500 GeV and R mass varied by 10 GeV. The blue, green and cyan histogram are the original histograms used in the input for different categories.



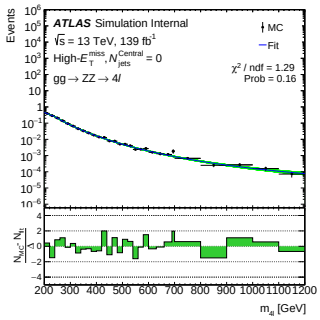
(a) (b)



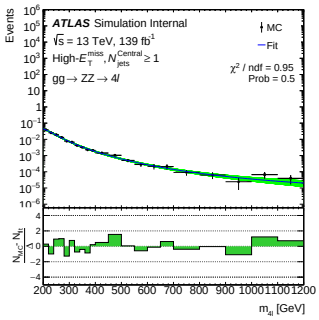
(c)

Figure B.16: The invariant mass of the four leptons of the interpolated $R \to SH \to 4\ell + E_{\mathrm{T}}^{\mathrm{miss}}$ signal shape with R mass fixed to 500 GeV and H mass varied by 10 GeV.

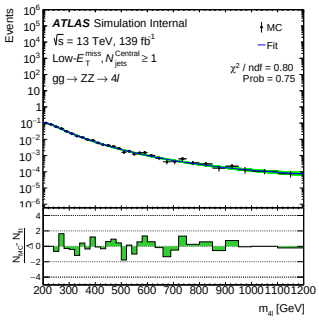
B.7 Background modelling



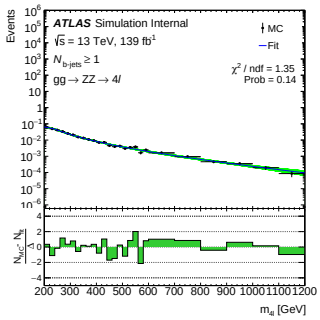
(a) High-$E_{\mathrm{T}}^{\mathrm{miss}}$& $N_{\mathrm{jets}}^{\mathrm{Central}} = 0$



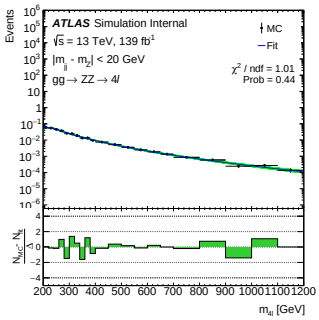
(b) High-$E_{\mathrm{T}}^{\mathrm{miss}}$& $N_{\mathrm{jets}}^{\mathrm{Central}} \geq 1$



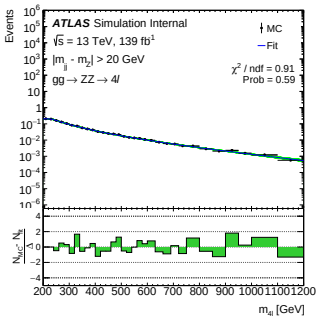
(c) Low-$E_{\mathrm{T}}^{\mathrm{miss}}$ & $N_{\mathrm{jets}}^{\mathrm{Central}} \geq 1$



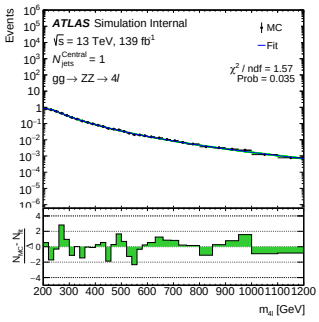
(d) $N_{b-\mathrm{jets}} \geq 1$



(e) $|m_{\mathrm{jj}}^{\mathrm{Central}} - m_{\mathrm{Z}}| < 20\,\mathrm{GeV}$

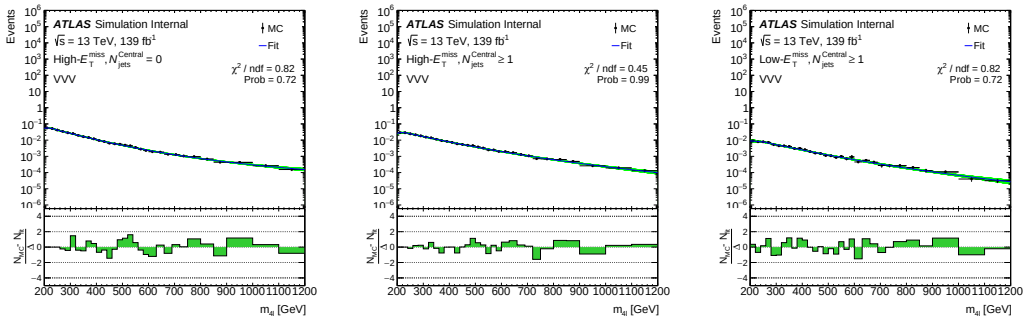


(f) $|m_{\mathrm{jj}}^{\mathrm{Central}} - m_{\mathrm{Z}}| > 20\,\mathrm{GeV}$

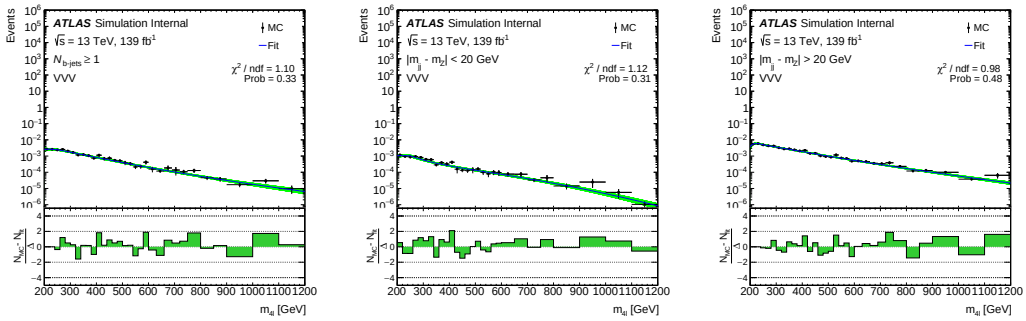


(g) $N_{\mathrm{jets}}^{\mathrm{Central}} = 1$

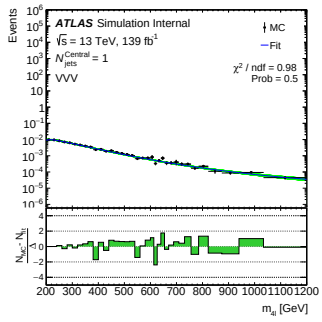
Figure B.17: The four-lepton invariant mass distributions for the analytical function fit to $ggZZ$ background in different signal regions.



(a) High-$E_{\mathrm{T}}^{\mathrm{miss}}$& $N_{\mathrm{jets}}^{\mathrm{Central}} = 0$ (b) High-$E_{\mathrm{T}}^{\mathrm{miss}}$& $N_{\mathrm{jets}}^{\mathrm{Central}} \geq 1$ (c) Low-$E_{\mathrm{T}}^{\mathrm{miss}}$ & $N_{\mathrm{jets}}^{\mathrm{Central}} \geq 1$

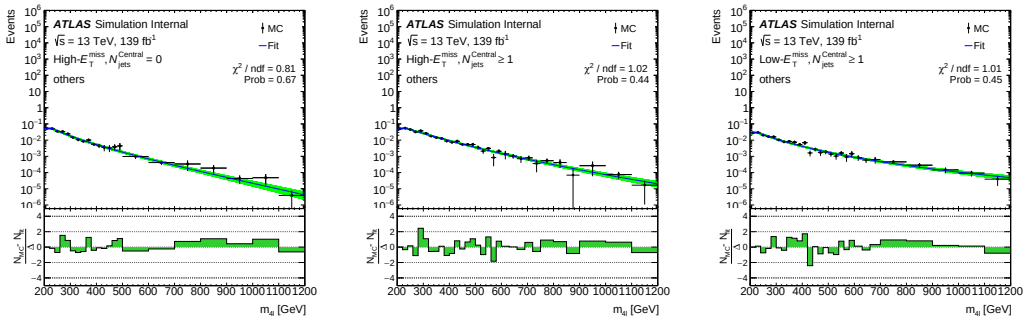


(d) $N_{b-\mathrm{jets}} \geq 1$ (e) $|m_{\mathrm{jj}}^{\mathrm{Central}} - m_{\mathrm{Z}}| < 20\,\mathrm{GeV}$ (f) $|m_{\mathrm{jj}}^{\mathrm{Central}} - m_{\mathrm{Z}}| > 20\,\mathrm{GeV}$

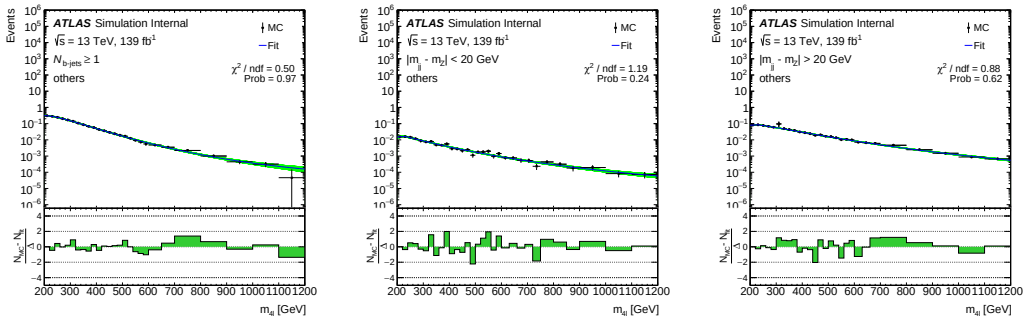


(g) $N_{\mathrm{jets}}^{\mathrm{Central}} = 1$

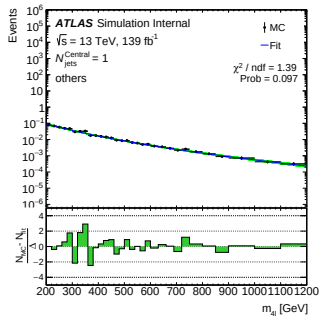
Figure B.18: The four-lepton invariant mass distributions for the analytical function fit to VVV background in different signal regions.



(a) High-$E_{\mathrm{T}}^{\mathrm{miss}}$& $N_{\mathrm{jets}}^{\mathrm{Central}} = 0$ (b) High-$E_{\mathrm{T}}^{\mathrm{miss}}$& $N_{\mathrm{jets}}^{\mathrm{Central}} \geq 1$ (c) Low-$E_{\mathrm{T}}^{\mathrm{miss}}$ & $N_{\mathrm{jets}}^{\mathrm{Central}} \geq 1$



(d) $N_{b-\mathrm{jets}} \geq 1$ (e) $|m_{\mathrm{jj}}^{\mathrm{Central}} - m_{\mathrm{Z}}| < 20\,\mathrm{GeV}$ (f) $|m_{\mathrm{jj}}^{\mathrm{Central}} - m_{\mathrm{Z}}| > 20\,\mathrm{GeV}$



(g) $N_{\mathrm{jets}}^{\mathrm{Central}} = 1$

Figure B.19: The four-lepton invariant mass distributions for the analytical function fit to others ($qqZZ$(EW), $t\bar{t}V$, $t\bar{t}$ and WZ) background in different signal regions.

Table B.10: The extracted parameters after fitting $ggZZ$ MC using Equation 6.5. The m_0 parameter values are fixed during the fit to improve the fit stability.

Parameter	High-E_T^{miss}, $N_{jets}^{Central} = 0$	High-E_T^{miss}, $N_{jets}^{Central} \geq 1$	Low-E_T^{miss}, $N_{jets}^{Central} \geq 1$	$\lvert m_{jj} - m_Z \rvert < 20$ GeV	$\lvert m_{jj} - m_Z \rvert > 20$ GeV	$N_{b\text{-jets}} \geq 1$	$N_{jets}^{Central} = 1$
N	0.252 ± 0.004	0.0221 ± 0.0010	0.0726 ± 0.0018	0.0523 ± 0.0013	0.184 ± 0.004	0.0477 ± 0.0020	0.665 ± 0.006
a_1	$(0.8 \pm 2.6)e+03$	$(0 \pm 8)e+07$	$(-6.7 \pm 0.9)e+04$	$(0 \pm 9)e+04$	$(-0.4 \pm 1.1)e+05$	$(0 \pm 5)e+09$	$(3 \pm 9)e+02$
a_2	0.2 ± 2.4	$(0.0 \pm 2.1)e+04$	229 ± 32	$(-0 \pm 5)e+01$	$(3 \pm 7)e+02$	$(0.0 \pm 1.3)e+06$	0.0 ± 0.6
a_3	50 ± 7	44 ± 15	$(0.2 \pm 1.9)e+04$	$(1.0 \pm 1.2)e+02$	43 ± 17	$(8 \pm 7)e+01$	81 ± 13
b_1	-47 ± 18	-37 ± 13	-77 ± 6	18 ± 4	45 ± 21	$(5 \pm 6)e+01$	20 ± 8
b_2	-12.0 ± 2.8	-7.8 ± 1.1	-16.7 ± 0.5	-3.16 ± 0.24	2 ± 4	3 ± 11	-2.1 ± 1.4
b_3	-0.73 ± 0.32	-0.26 ± 0.12	-1.36 ± 0.06	-0.031 ± 0.031	0.5 ± 0.4	0.7 ± 1.3	0.20 ± 0.16
m_0	240.0 ± 0	240.0 ± 0	240.0 ± 0	240.0 ± 0	240.0 ± 0	240.0 ± 0	240.0 ± 0

Table B.11: The extracted parameters after fitting VVV MC using Equation 6.5. The m_0 parameter values are fixed during the fit to improve the fit stability.

Parameter	High-E_T^{miss}, $N_{jets}^{Central} = 0$	High-E_T^{miss}, $N_{jets}^{Central} \geq 1$	Low-E_T^{miss}, $N_{jets}^{Central} \geq 1$	$\lvert m_{jj} - m_Z \rvert < 20$ GeV	$\lvert m_{jj} - m_Z \rvert > 20$ GeV	$N_{b\text{-jets}} \geq 1$	$N_{jets}^{Central} = 1$
N	0.0416 ± 0.0009	0.0245 ± 0.0007	0.0077 ± 0.0004	0.00104 ± 0.00011	0.00493 ± 0.00028	0.00247 ± 0.00024	0.0082 ± 0.0004
a_1	$(-3.7 \pm 2.9)e+03$	$(-0.9 \pm 1.1)e+04$	$(0.0 \pm 1.4)e+06$	$(0.0 \pm 1.6)e+07$	$(-5 \pm 9)e+04$	$(-0 \pm 8)e+04$	$(-1 \pm 4)e+05$
a_2	21 ± 17	$(5 \pm 6)e+01$	$(-0 \pm 4)e+02$	$(-0 \pm 9)e+03$	$(3 \pm 5)e+02$	$(0 \pm 6)e+02$	$(0.5 \pm 2.4)e+03$
a_3	33 ± 4	38 ± 9	$(1.2 \pm 2.3)e+02$	$(2 \pm 7)e+02$	31 ± 9	$(0.6 \pm 1.7)e+02$	41 ± 17
b_1	-61 ± 27	-17 ± 34	$(-1 \pm 6)e+01$	246 ± 13	$(2 \pm 5)e+01$	$(0.0 \pm 1.1)e+02$	$(-8 \pm 4)e+01$
b_2	-19 ± 5	-13 ± 6	-11 ± 11	33.3 ± 1.2	-8 ± 9	-12 ± 20	-23 ± 8
b_3	-2.0 ± 0.6	-1.3 ± 0.7	-1.2 ± 1.3	4.06 ± 0.14	-0.8 ± 1.1	-1.3 ± 2.4	-2.6 ± 0.9
x_0	250.0 ± 0	250.0 ± 0	250.0 ± 0	250.0 ± 0	250.0 ± 0	250.0 ± 0	250.0 ± 0

Table B.12: The extracted parameters after fitting others MC using Equation 6.5. The m_0 parameter values are fixed during the fit to improve the fit stability.

Parameter	High-E_T^{miss}, $N_{jets}^{Central} = 0$	High-E_T^{miss}, $N_{jets}^{Central} \geq 1$	Low-E_T^{miss}, $N_{jets}^{Central} \geq 1$	$\lvert m_{jj} - m_Z \rvert < 20$ GeV	$\lvert m_{jj} - m_Z \rvert > 20$ GeV	$N_{b\text{-jets}} \geq 1$	$N_{jets}^{Central} = 1$
N	0.052 ± 0.005	0.056 ± 0.004	0.0290 ± 0.0021	0.0162 ± 0.0009	0.0849 ± 0.0022	0.283 ± 0.007	0.0697 ± 0.0025
a_1	$(-0.8 \pm 1.7)e+04$	$(-0 \pm 9)e+05$	$(0.1 \pm 1.8)e+04$	$(1 \pm 7)e+04$	$(2 \pm 7)e+02$	$(0.2 \pm 1.3)e+02$	$(-0.9 \pm 2.8)e+03$
a_2	$(0.7 \pm 2.1)e+02$	$(-0.1 \pm 3.4)e+03$	$(0.2 \pm 1.6)e+02$	$(-0.1 \pm 1.2)e+02$	-0.1 ± 0.7	-0.06 ± 0.35	17 ± 10
a_3	$(0.7 \pm 1.7)e+02$	$(1 \pm 8)e+03$	$(1.2 \pm 1.6)e+02$	$(0 \pm 6)e+04$	$(0.4 \pm 1.1)e+03$	$(0 \pm 6)e+03$	59 ± 20
b_1	$(1.0 \pm 1.6)e+02$	19 ± 8	1 ± 11	-35 ± 22	-28 ± 11	$(-1.4 \pm 0.4)e+02$	17 ± 14
b_2	3 ± 28	-10.21 ± 0.31	-5.7 ± 1.0	-14 ± 4	-15.0 ± 2.0	-38 ± 7	-5.3 ± 2.4
b_3	0.7 ± 3.2	-0.99 ± 0.04	-0.29 ± 0.12	-1.4 ± 0.4	-1.65 ± 0.23	-4.2 ± 0.8	-0.41 ± 0.28
m_0	230.0 ± 0	230.0 ± 0	230.0 ± 0	230.0 ± 0	230.0 ± 0	230.0 ± 0	230.0 ± 0

B.8 Systematic uncertainties

Table B.13: Summary of all systematic uncertainties considered as nuisance parameters in this analysis. The variables with brackets at the end, for example [1-7], represents different independent number variables.

Uncertainty source			NP name
Luminosity			LUMI
Pile-up reweighing			PRW_DATASF
Electron	Energy Resolution		EG_RESOLUTION_ALL
	Energy scale		EG_SCALE_ALL
	Efficiencies	Identification	EL_EFF_ID_CorrUncertaintyNP[0-15]
			EL_EFF_ID_SIMPLIFIED_UncorrUncertaintyNP[0-17]
		Isolation	EL_EFF_Iso_TOTAL_1NPCOR_PLUS_UNCOR
		Reconstruction	EL_EFF_Reco_TOTAL_1NPCOR_PLUS_UNCOR
Muon	ID Track Smearing		MUON_ID
	MS Track Smearing		MUON_MS
	Momentum Scale		MUON_SCALE
	Sagitta Correction		MUON_SAGITTA_RESBIAS
			MUON_SAGITTA_RHO
	Efficiencies	TTVA	MUON_EFF_TTVA_SYS
			MUON_EFF_TTVA_STAT
		Isolation	MUON_EFF_ISO_STAT
			MUON_EFF_ISO_SYS
		Reconstruction	MUON_EFF_RECO_SYS
			MUON_EFF_RECO_STAT
			MUON_EFF_RECO_STAT_LOWPT
			MUON_EFF_RECO_SYS_LOWPT
Jet	Energy Scale		JES_EffectiveNP_Statistical[1-6]
			JES_EffectiveNP_Detector[1-2]
			JES_EffectiveNP_Modelling1[1-4]
			JES_EffectiveNP_Mixed[1-3]
			JES_EtaIntercalibration_Modelling
			JES_EtaIntercalibration_NonClosure_2018data
			JES_EtaIntercalibration_NonClosure_highE
			JES_EtaIntercalibration_NonClosure_negEta
			JES_EtaIntercalibration_NonClosure_posEta
			JES_EtaIntercalibration_TotalStat
			JES_BJES_Response
			JES_Flavor_Composition
			JES_Flavor_Response
			JES_Pileup_PtTermET_Pileup_RhoTopology
			JES_Pileup_OffsetMu
			JES_Pileup_OffsetNPV
			JES_PunchThrough_MC16(_AFFII for signals)
			JES_SingleParticle_HighPt
	Energy Resolution		JET_JER_DataVsMC_MC16(_AFII for signals)
			JET_JER_EffectiveNP[1-11]
			JET_JER_EffectiveNP_12restTerm
	Efficiencies	Flavour Tagging	FT_EFF_Eigen_B_[0-2]
			FT_EFF_Eigen_C_[0-3]
			FT_EFF_Eigen_Light_[0-4]
		JVT	JET_JvtEfficiency
E_T^{miss}soft track	E_T^{miss} Offset		MET_SoftTrk_Scale
	Resolution		MET_SoftTrk_ResoPara
			MET_SoftTrk_ResoPerp

B.8.1 Experimental systematic uncertainties

Pile-up reweighting

Systematic uncertainty introduced by rescaling the simulated pile-up to the data is considered. The data scale factor is calculated using data to MC comparisons which comes with uncertainty. For the current MC, the nominal value is 1.0/1.03, which is scaled upward by 1.0/0.99 and downward by 1.0/1.07 to account for the pile-up reweighting uncertainty [173]. It is estimated to be 14.75% for the $R \to SH \to 4\ell + E_{\mathrm{T}}^{\mathrm{miss}}$ signal, 1.10% for the $A \to Z(\nu\nu)H(ZZ) \to 4\ell + X$ signal and 3.29% for the $qqZZ$ background.

Lepton efficiency

The lepton reconstruction, identification, and isolation efficiency uncertainties are evaluated using the scale factor's efficiency variation. Different sources are varied up and down by $\pm 1\sigma$ to get the efficiency uncertainty. Electrons (muons) have a total efficiency uncertainty of 1.71% (3.22%) for the $R \to SH \to 4\ell + E_{\mathrm{T}}^{\mathrm{miss}}$ signal, 2.27% (5.04%) for the $A \to Z(\nu\nu)H(ZZ) \to 4\ell + X$ signal and 1.08% (1.99%) $qqZZ$ the backgrounds.

Muon track-to-vertex association efficiency

Matching the muon track to vertex introduces uncertainty on the calculated efficiency. This uncertainty is accounted for by the muon track-to-vertex association uncertainty (TTVA). The calculated value for this uncertainty is 0.27% for the $R \to SH \to 4\ell + E_{\mathrm{T}}^{\mathrm{miss}}$ signal, 0.45% for the $A \to Z(\nu\nu)H(ZZ) \to 4\ell + X$ signal, and 1.33% for $qqZZ$ background.

Lepton energy scale and resolution

The experimental systematic uncertainties related to leptons arise mainly from the efficiency measurements which are necessary for modelling the detector acceptance, the lepton energy scale and the resolution, and from the estimation of misidentified lepton background yields. The effects on the electron and muon energy scale arising from correlated effects are evaluated. The uncertainties due to the electron energy scale and resolution is 0.15% for $R \to SH \to 4\ell + E_{\mathrm{T}}^{\mathrm{miss}}$ signal, 0.2% for the $A \to Z(\nu\nu)H(ZZ) \to 4\ell + X$ signal and 0.33% for the backgrounds.

Jet energy scale and resolution

Migration of events among categories occurs owing to changes in object energies/momenta, due mostly to misreconstruction of jets and $E_{\mathrm{T}}^{\mathrm{miss}}$. Although no direct jet selection is used in the analysis, the jet energy scale and resolution impact the calculation of $E_{\mathrm{T}}^{\mathrm{miss}}$. The impact of the uncertainties in jet energy scale and resolution using FullJER(13NPs) and CategoryReductionJES(30NPs) is estimated by varying each of these quantities by the amount of each component of the uncertainties independently of the other components, and recalculating $E_{\mathrm{T}}^{\mathrm{miss}}$ for each variation. $E_{\mathrm{T}}^{\mathrm{miss}}$ soft terms, MET_SoftTrk_ResoPara, MET_SoftTrk_ResoPerp, MET_SoftTrk_Scale, are evaluated independently by using the method described in Ref. [174]. The uncertainties due to the jet energy resolution is 1.5% for the $R \to SH \to 4\ell + E_{\mathrm{T}}^{\mathrm{miss}}$ signal, 2.68% for the $A \to Z(\nu\nu)H(ZZ) \to 4\ell + X$ signal and 6.77% for the backgrounds.

Jet flavour tagging

Flavour tagging uncertainties due to the disagreement in selecting the jet flavour are calculated by altering the uncertainty of the tagged jet flavour efficiency by $\pm 1\sigma$. The total estimated flavour tagging uncertainty is 5.03%, 9.26% and 15.04% for the $R \to SH \to 4\ell + E_{\mathrm{T}}^{\mathrm{miss}}$ and $A \to Z(\nu\nu)H(ZZ) \to 4\ell + X$ signals and the $qqZZ$ background, respectively.

Missing transverse energy

The $E_{\mathrm{T}}^{\mathrm{miss}}$ is reconstructed using a signal associated to hard objects: muons, electrons, photon, hadronically decaying taus and jets. Objects not related to the hard ones are referred to as soft objects. Uncertainties on the $E_{\mathrm{T}}^{\mathrm{miss}}$ measurement are considered on the soft track term (TST) [175], and are estimated using the three components:

- The $E_{\mathrm{T}}^{\mathrm{miss}}$-scale uncertainty is calculated by the mean value of the soft objects momenta projection along the hard objects momenta. It is evaluated to be 0.89% for the $R \to SH \to 4\ell + E_{\mathrm{T}}^{\mathrm{miss}}$ signal and 6.14% for the $(A \to Z(\nu\nu)H(ZZ) \to 4\ell + X)$ signal. For the $qqZZ$ background the $E_{\mathrm{T}}^{\mathrm{miss}}$-scale is 12.11%.

- The $E_{\mathrm{T}}^{\mathrm{miss}}$ TST parallel and perpendicular are calculated by the RMS of soft objects momenta projection parallel and perpendicular to hard objects

momenta. Each component is considered to have up and down variation. The combined resolution uncertainty for $R \to SH \to 4\ell + E_{\mathrm{T}}^{\mathrm{miss}}$ signal is 1.79%. Also, 7.73% and 15.72% are estimated for the $A \to Z(\nu\nu)H(ZZ) \to 4\ell + X$ signal and $qqZZ$ background, respectively.

The effect of the experimental uncertainties on signal shapes

The DSCB parameters, explained in Appendix B.6, are used to estimate the systematic on the signal shape. First, the mean for the scale (up/down) and RMS for the resolution (up/down) samples are calculated. Hence, to get the scale, μ is modified by the calculated mean from the samples. And similarly, to get the variation for the resolution, σ is varied (up/down) by the RMS estimated from the samples. Figure B.20 shows the systematic variation for the scale and resolution for $A \to Z(\to X)H(\to 4\ell)$ and $R \to SH \to 4\ell + E_{\mathrm{T}}^{\mathrm{miss}}$ signals.

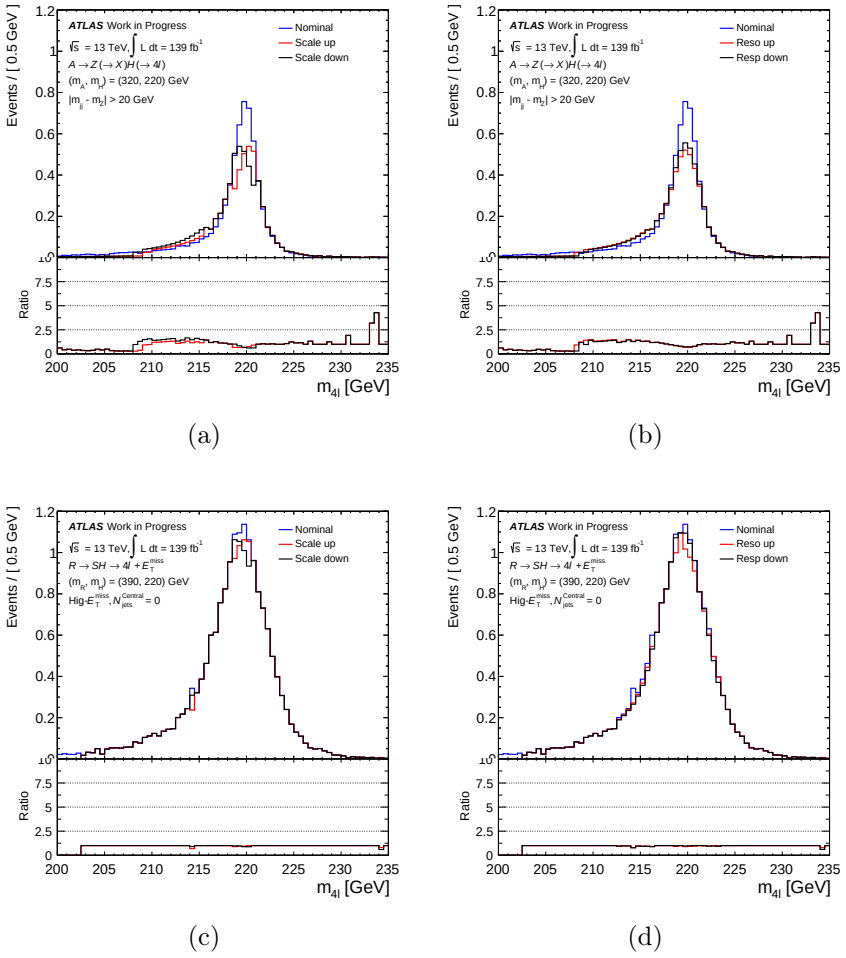


Figure B.20: Systematic uncertainties on the $A \to Z(\to X)H(\to 4\ell)$ shape (top) and $R \to SH \to 4\ell + E_{\mathrm{T}}^{\mathrm{miss}}$ shape (bottom).

Other systematic uncertainties

A global uncertainty of ±1.7% [176] on the total integrated luminosity of the data reported between 2015 and 2018 is considered.

B.8.2 Systematic uncertainties on background shapes modelling

This uncertainty is accounted for due to the bias introduced by the analytical function discussed in Section 6.5. Figures B.21 and B.22 show the shape uncertainties for the $qqZZ$ background.

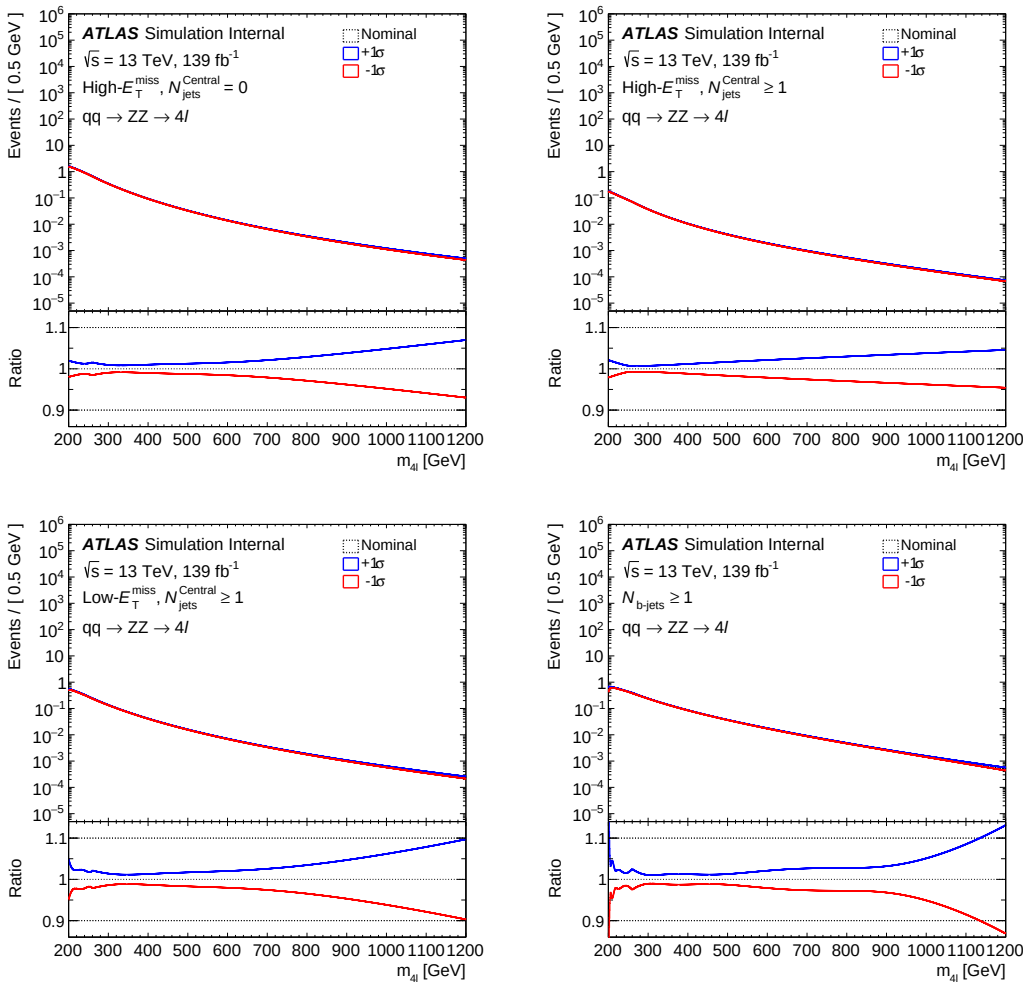


Figure B.21: Shape systematic uncertainties due to $qqZZ$ background parametrisation in the invariant mass of the four leptons.

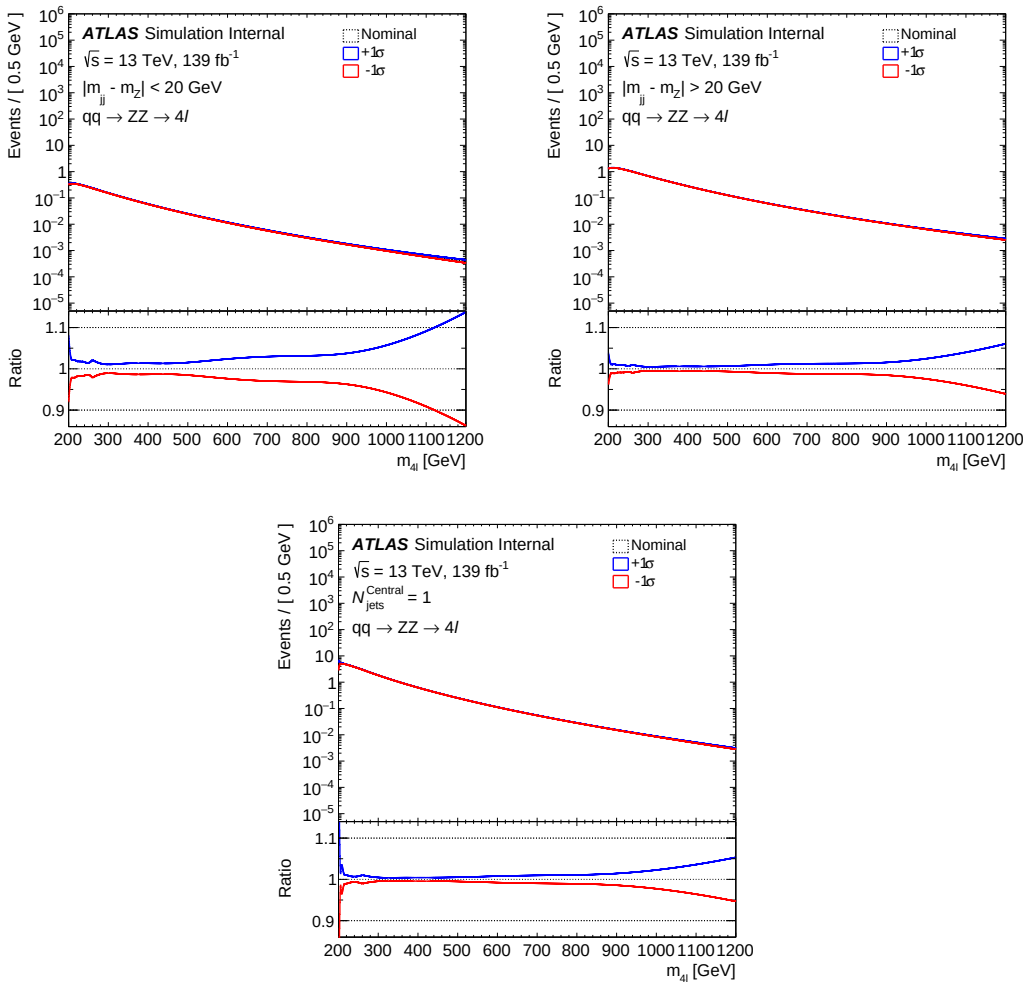


Figure B.22: Shape systematic uncertainties due to $qqZZ$ background parametrisation in the invariant mass of the four leptons.

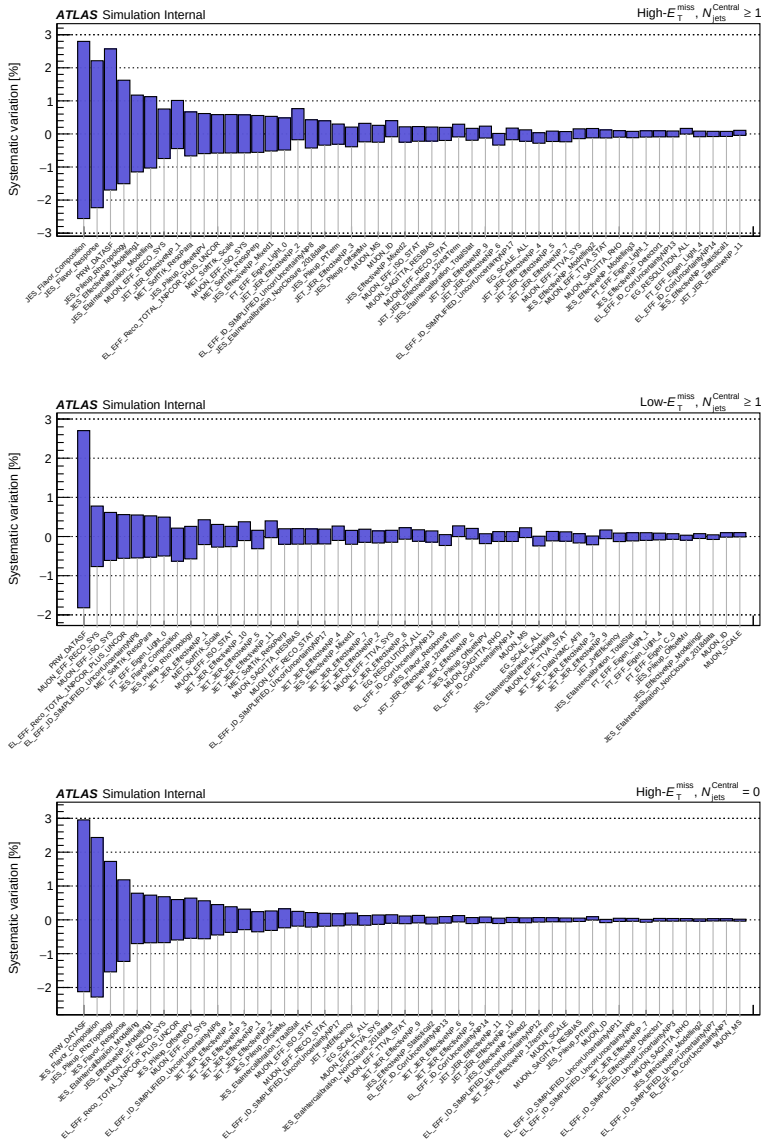


Figure B.23: The mean value for systematic uncertainties in the $m_{4\ell}$ normalisation calculated from the (390, 220), (790, 600) and (1190, 1000) mass points with $m_R - m_H \leq 200\,\text{GeV}$ for the $R \to SH \to 4\ell + E_{\text{T}}^{\text{miss}}$ signal. Top (bottom) two plots represent the High- and Low-$E_{\text{T}}^{\text{miss}}$ of the $N_{\text{jets}}^{\text{Central}} \geq 1$ ($N_{\text{jets}}^{\text{Central}} = 0$) categories, respectively. Up and Down variations are shown in descending order only for the first 50 nuisance parameters.

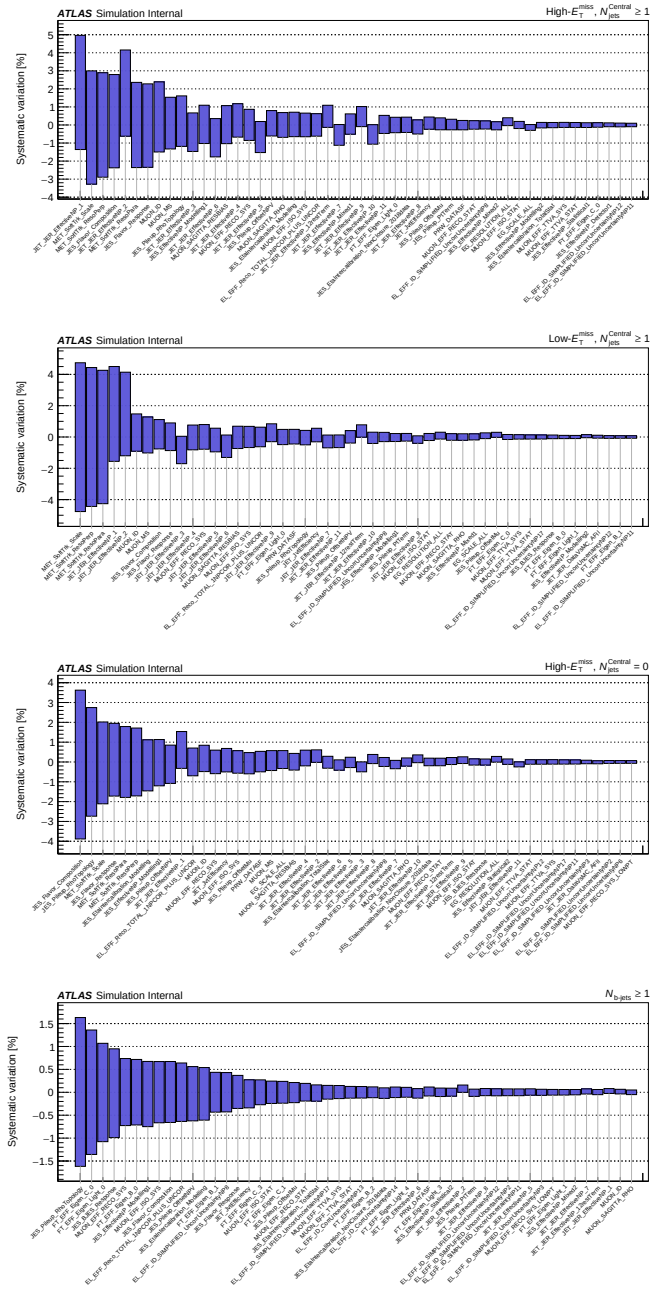


Figure B.24: The mean value for systematic uncertainties in the $m_{4\ell}$ normalisation calculated from the (330, 220), (700, 600) and (1100, 1000) mass points with $m_A - m_H \leq 100\,\text{GeV}$ for the $A \to Z(\nu\nu)H(ZZ) \to 4\ell + X$ signal. Top two plots represent the High- and Low-$E_{\text{T}}^{\text{miss}}$ of the $N_{\text{jets}}^{\text{Central}} \geq 1$ category, respectively. The bottom plots show High-$E_{\text{T}}^{\text{miss}}$ of $N_{\text{jets}}^{\text{Central}} = 0$ and $N_{b-\text{jets}} \geq 1$ categories, respectively. Up and Down variations are shown in descending order only for the first 50 nuisance parameters.

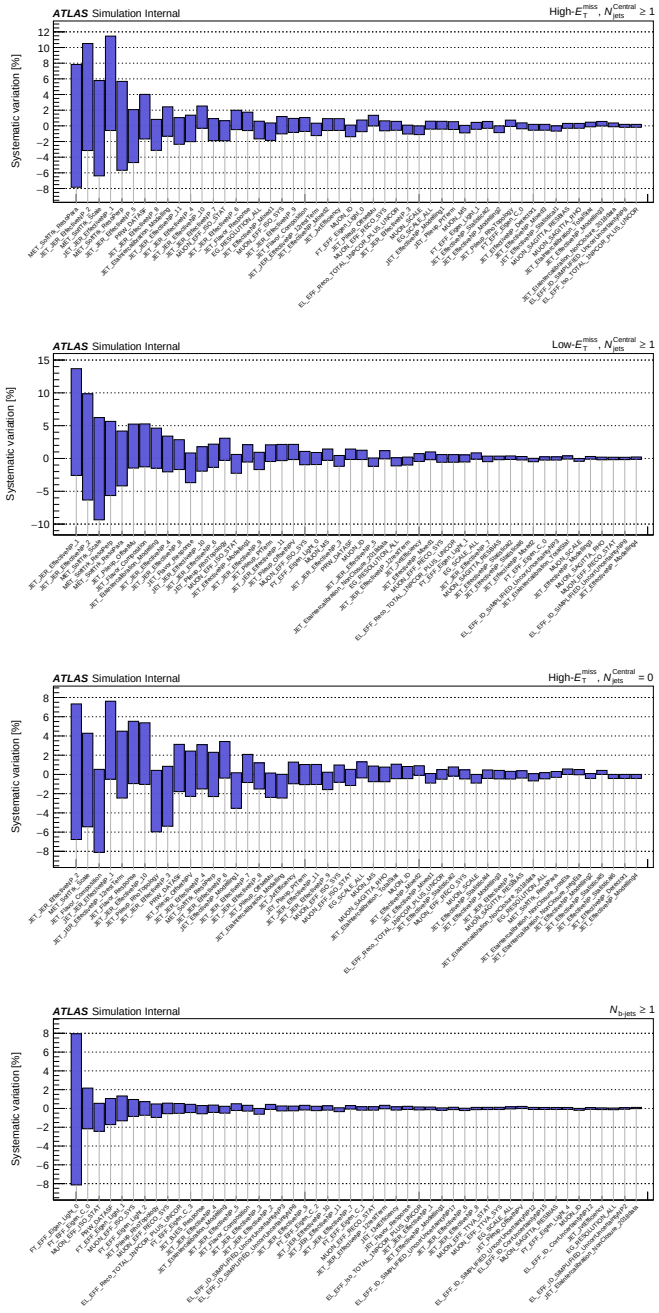


Figure B.25: The experimental systematic uncertainties on the normalisation of the $m_{4\ell}$ distribution for the other backgrounds. Top two plots represent the High- and Low-$E_{\mathrm{T}}^{\mathrm{miss}}$ of the $N_{\mathrm{jets}}^{\mathrm{Central}} \geq 1$ category, respectively. The bottom plots show High-$E_{\mathrm{T}}^{\mathrm{miss}}$ of $N_{\mathrm{jets}}^{\mathrm{Central}} = 0$ and $N_{b-\mathrm{jets}} \geq 1$ categories, respectively. Up and Down variations are shown in descending order only for the first 50 nuisance parameters.

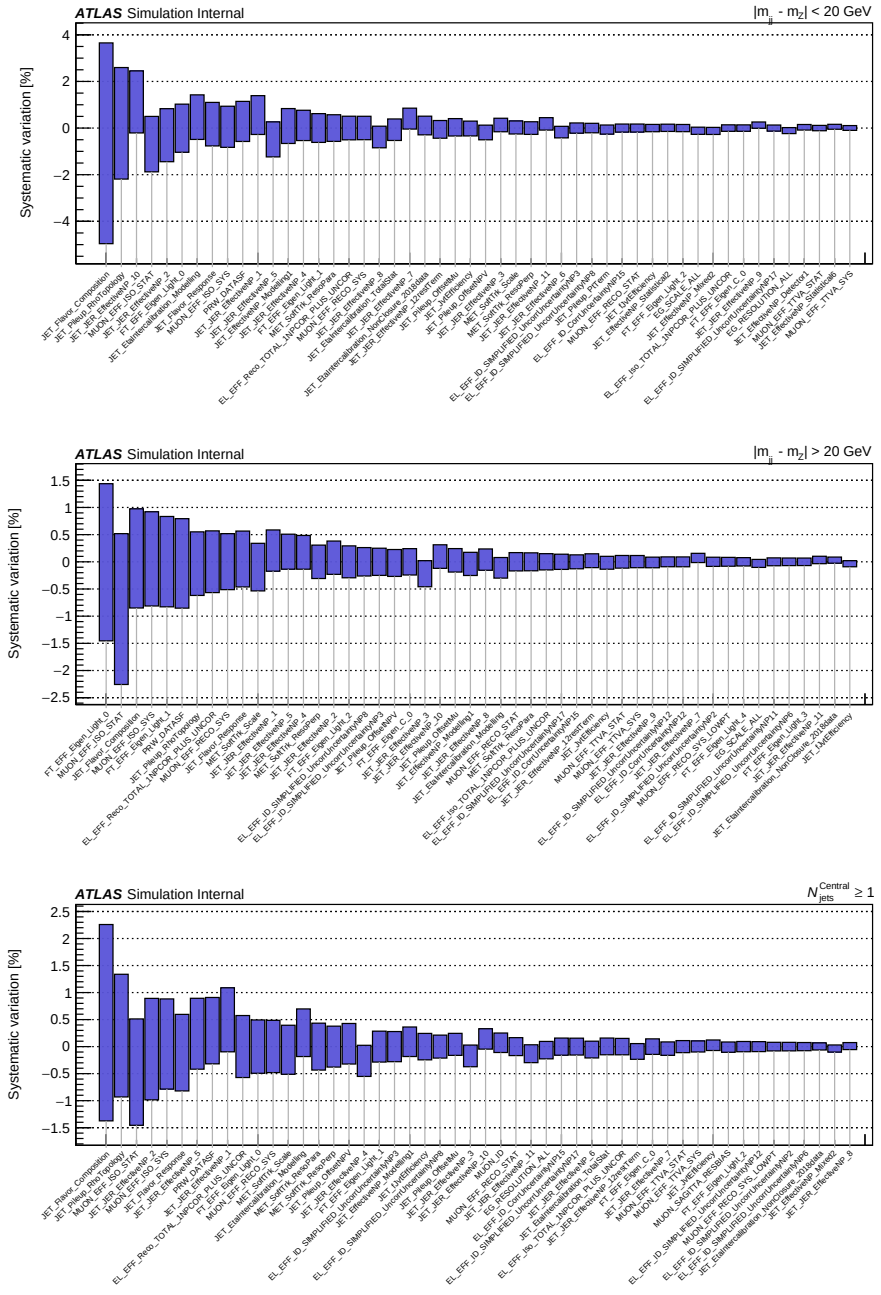
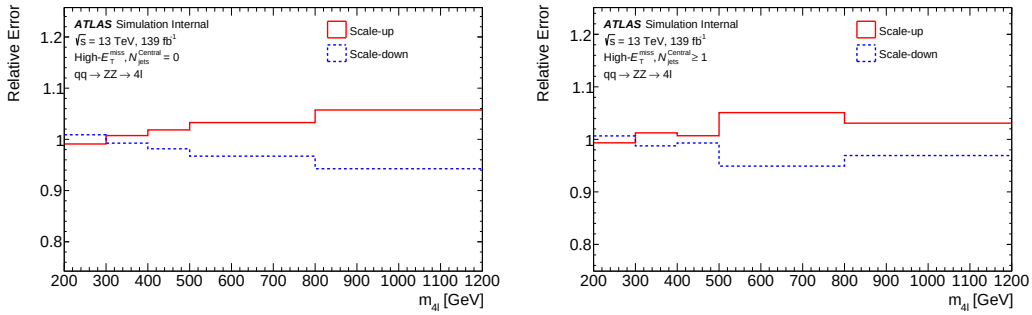


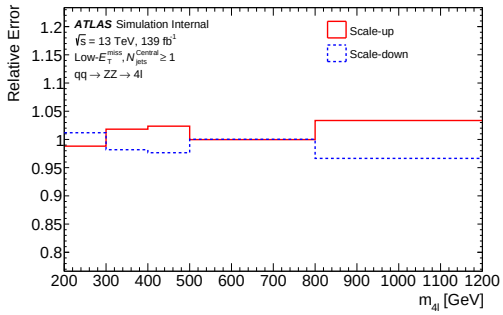
Figure B.26: The experimental systematic uncertainties on the normalisation of the $m_{4\ell}$ distribution for the other backgrounds. Top (bottom) two plots represent the $|m_{\mathrm{jj}} - m_Z| < 20\,\mathrm{GeV}$ and $|m_{\mathrm{jj}} - m_Z| > 20\,\mathrm{GeV}$ $(N_{\mathrm{jets}}^{\mathrm{Central}} = 1)$ categories, respectively. Up and Down variations are shown in descending order only for the first 50 nuisance parameters.

B.9 Shape uncertainties

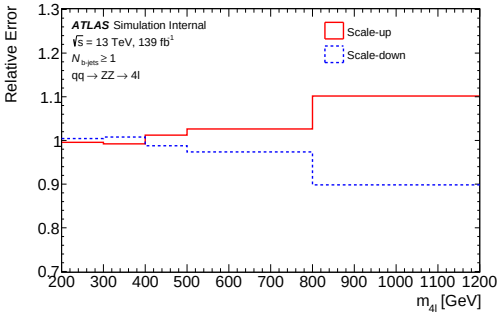


(a) High-$E_{\mathrm{T}}^{\mathrm{miss}}$& $N_{\mathrm{jets}}^{\mathrm{Central}} = 0$

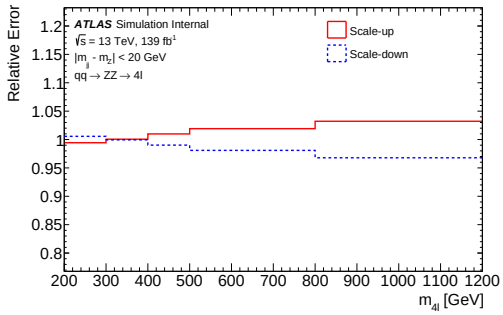
(b) High-$E_{\mathrm{T}}^{\mathrm{miss}}$& $N_{\mathrm{jets}}^{\mathrm{Central}} \geq 1$



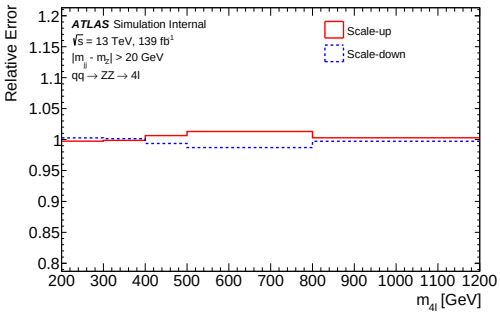
(c) Low-$E_{\mathrm{T}}^{\mathrm{miss}}$ & $N_{\mathrm{jets}}^{\mathrm{Central}} \geq 1$



(d) $N_{b-\mathrm{jets}} \geq 1$

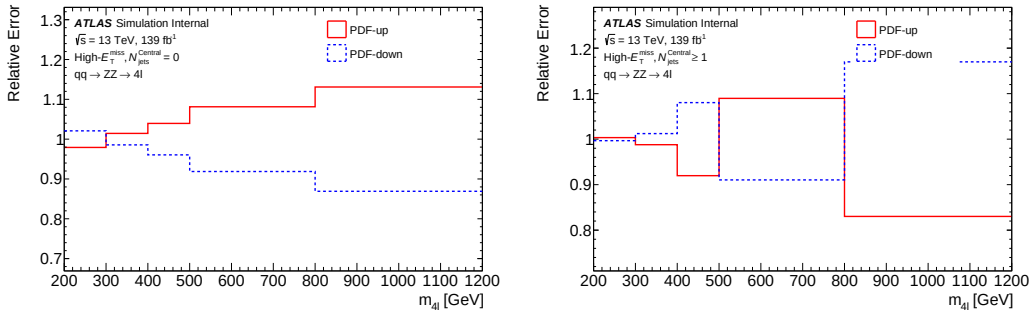


(e) $|m_{\mathrm{jj}}^{\mathrm{Central}} - m_{\mathrm{Z}}| < 20\,\mathrm{GeV}$



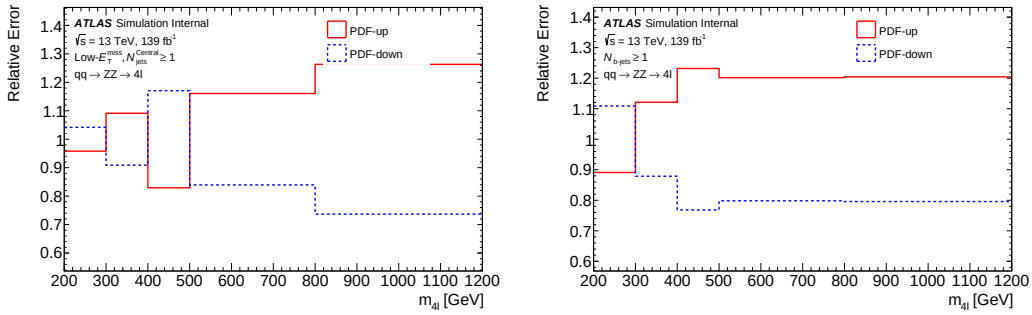
(f) $|m_{\mathrm{jj}}^{\mathrm{Central}} - m_{\mathrm{Z}}| > 20\,\mathrm{GeV}$

Figure B.27: The shape uncertainties as a function of the invariant mass of the four leptons of the QCD scale variations for the $qqZZ$ background in different signal regions.



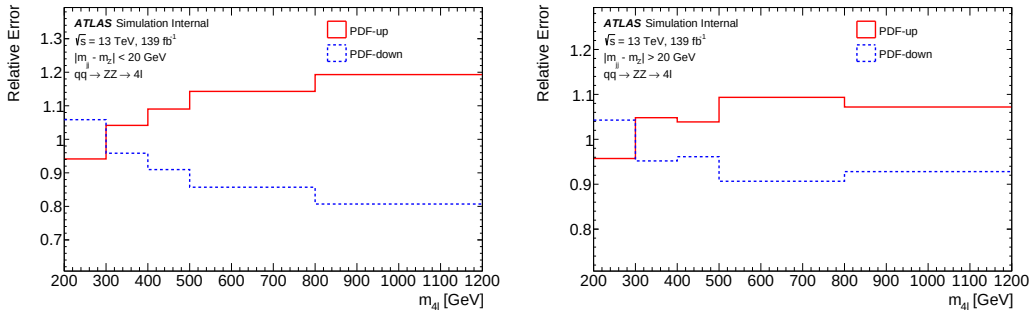
(a) High-$E_{\mathrm{T}}^{\mathrm{miss}}$& $N_{\mathrm{jets}}^{\mathrm{Central}} = 0$

(b) High-$E_{\mathrm{T}}^{\mathrm{miss}}$& $N_{\mathrm{jets}}^{\mathrm{Central}} \geq 1$



(c) Low-$E_{\mathrm{T}}^{\mathrm{miss}}$ & $N_{\mathrm{jets}}^{\mathrm{Central}} \geq 1$

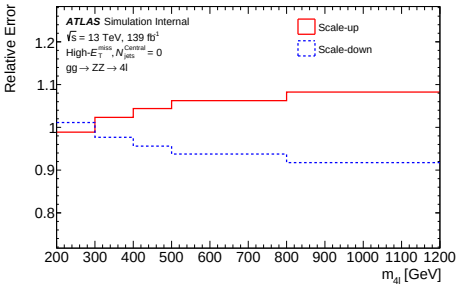
(d) $N_{b-\mathrm{jets}} \geq 1$



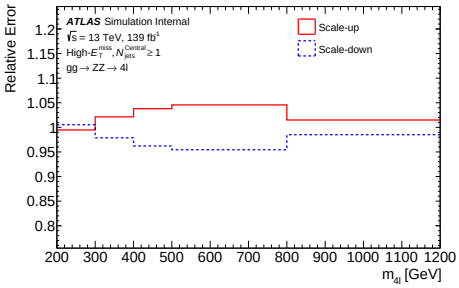
(e) $|m_{\mathrm{jj}}^{\mathrm{Central}} - m_{\mathrm{Z}}| < 20\,\mathrm{GeV}$

(f) $|m_{\mathrm{jj}}^{\mathrm{Central}} - m_{\mathrm{Z}}| > 20\,\mathrm{GeV}$

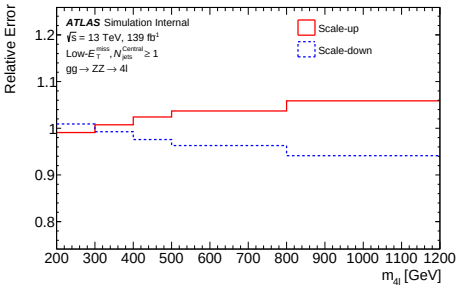
Figure B.28: The shape uncertainties as a function of the invariant mass of the four leptons PDF variations for the $qqZZ$ background in different signal regions.



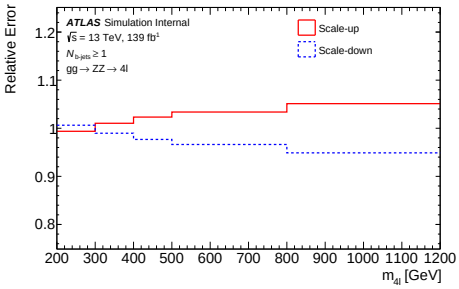
(a) High-$E_{\mathrm{T}}^{\mathrm{miss}}$& $N_{\mathrm{jets}}^{\mathrm{Central}} = 0$



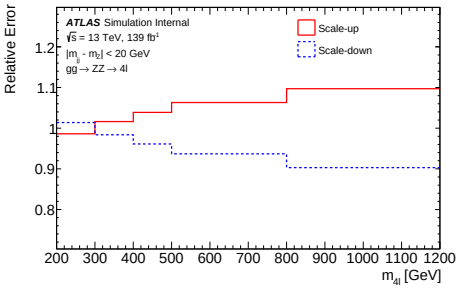
(b) High-$E_{\mathrm{T}}^{\mathrm{miss}}$& $N_{\mathrm{jets}}^{\mathrm{Central}} \geq 1$



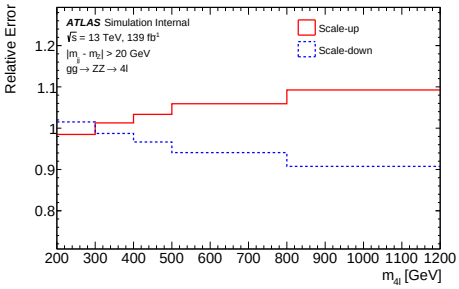
(c) Low-$E_{\mathrm{T}}^{\mathrm{miss}}$ & $N_{\mathrm{jets}}^{\mathrm{Central}} \geq 1$



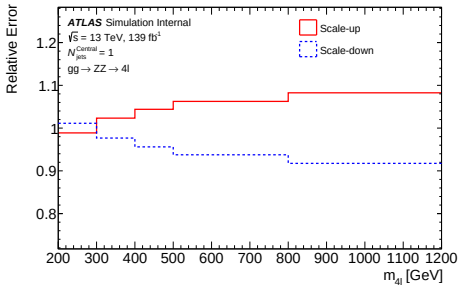
(d) $N_{b-\mathrm{jets}} \geq 1$



(e) $|m_{\mathrm{jj}}^{\mathrm{Central}} - m_{\mathrm{Z}}| < 20\,\mathrm{GeV}$

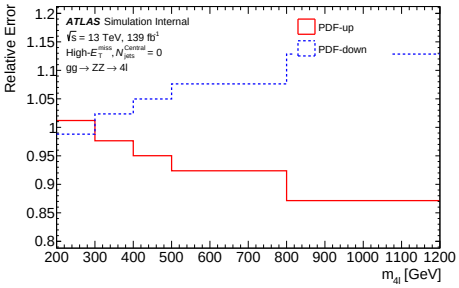


(f) $|m_{\mathrm{jj}}^{\mathrm{Central}} - m_{\mathrm{Z}}| > 20\,\mathrm{GeV}$

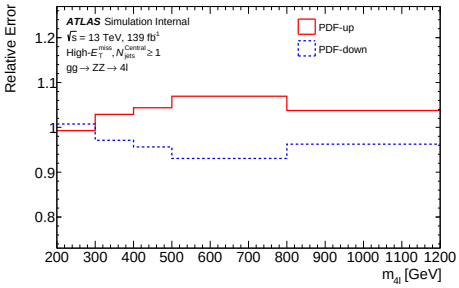


(g) $N_{\mathrm{jets}}^{\mathrm{Central}} = 1$

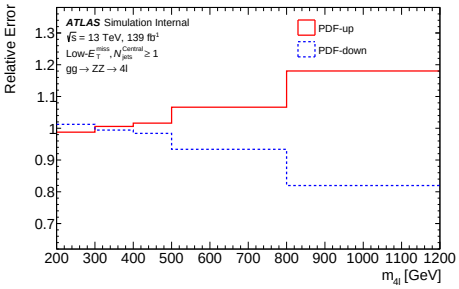
Figure B.29: The shape uncertainties as a function of the invariant mass of the four leptons of the QCD scale variations for the $ggZZ$ background in different signal regions.



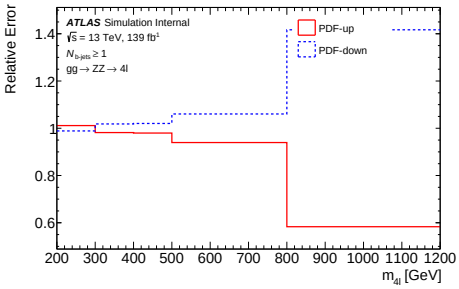
(a) High-$E_{\mathrm{T}}^{\mathrm{miss}}$& $N_{\mathrm{jets}}^{\mathrm{Central}} = 0$



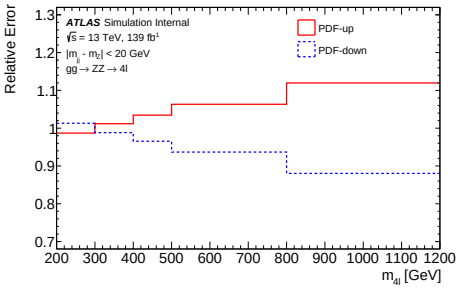
(b) High-$E_{\mathrm{T}}^{\mathrm{miss}}$& $N_{\mathrm{jets}}^{\mathrm{Central}} \geq 1$



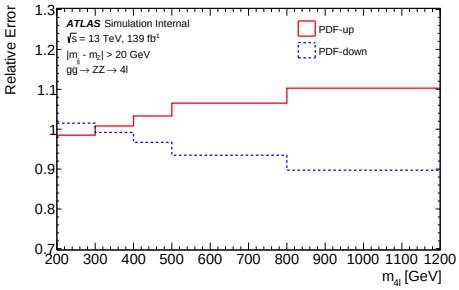
(c) Low-$E_{\mathrm{T}}^{\mathrm{miss}}$ & $N_{\mathrm{jets}}^{\mathrm{Central}} \geq 1$



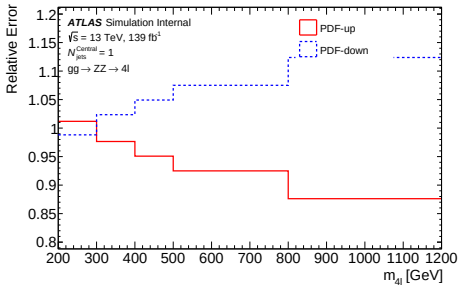
(d) $N_{b-\mathrm{jets}} \geq 1$



(e) $|m_{\mathrm{jj}}^{\mathrm{Central}} - m_{\mathrm{Z}}| < 20\,\mathrm{GeV}$



(f) $|m_{\mathrm{jj}}^{\mathrm{Central}} - m_{\mathrm{Z}}| > 20\,\mathrm{GeV}$



(g) $N_{\mathrm{jets}}^{\mathrm{Central}} = 1$

Figure B.30: The shape uncertainties as a function of the invariant mass of the four leptons PDF variations for the $ggZZ$ background in different signal regions.

B.10 Systematic uncertainty breakdown

A summary of the experimental and theory systematic uncertainties is discussed in this section. The nuisance parameters considered in the study are organised in a table shown in Appendix B.8. A quadrature sum is calculated for the uncertainty source with more than one nuisance parameter. Tables B.14 and B.15 provide a summary of the uncertainty for $R \to SH \to 4\ell + E_{\mathrm{T}}^{\mathrm{miss}}$ and $A \to Z(\nu\nu)H(ZZ) \to 4\ell + X$ signals, respectively. The backgrounds uncertainty on the $m_{4\ell}$ normalisation are shown in Table B.16 for $qqZZ$ and in Appendix B.10.1 for the $ggZZ$, VVV and others backgrounds. The shape uncertainties due to background parametrisation are shown in Table B.17 and the shape systematics in the $m_{4\ell}$ for $qqZZ$ and $ggZZ$ are shown in Tables B.18 and B.19. These systematics are extracted from the experimental NPs and the theoretical systematic uncertainties. For the experimental NPs, only NPs with an effect above 5% is taken for the up or down variable.

Table B.14: Summary of the systematic uncertainties estimated from different sources in percentage on the $R \to SH \to 4\ell + E_{\mathrm{T}}^{\mathrm{miss}}$ signal.

Uncertainty source			$N_{\mathrm{jets}}^{\mathrm{Central}} = 0$	$N_{\mathrm{jets}}^{\mathrm{Central}} \geq 1$	
			High-$E_{\mathrm{T}}^{\mathrm{miss}}$	High-$E_{\mathrm{T}}^{\mathrm{miss}}$	Low-$E_{\mathrm{T}}^{\mathrm{miss}}$
Luminosity			±1.70%	±1.70%	±1.70%
Pile-up reweighing			±2.54%	±2.13%	±2.26%
Electron	Energy Resolution		±0.02%	±0.09%	±0.15%
	Energy scale		±0.14%	±0.17%	±0.12%
	Efficiencies	Identification	±0.52%	±0.50%	±0.62%
		Isolation	±0.00%	±0.00%	±0.00%
		Reconstruction	±0.60%	±0.58%	±0.56%
Muon	ID Track Smearing		±0.05%	±0.24%	±0.06%
	MS Track Smearing		±0.03%	±0.26%	±0.12%
	Momentum Scale		±0.06%	±0.05%	±0.06%
	Sagitta Correction		±0.06%	±0.24%	±0.23%
	Efficiencies	TTVA	±0.18%	±0.19%	±0.19%
		Isolation	±0.65%	±0.62%	±0.67%
		Reconstruction	±0.71%	±0.78%	±0.80%
Jet	Energy Scale		±3.35%	±4.26%	±0.69%
	Energy Resolution		±0.67%	±1.01%	±0.67%
	Efficiencies	Flavour Tagging	±0.00%	±0.51%	±0.52%
		JVT	±0.18%	±0.05%	±0.11%
$E_{\mathrm{T}}^{\mathrm{miss}}$soft track	$E_{\mathrm{T}}^{\mathrm{miss}}$ Offset		±0.01%	±0.58%	±0.29%
	Resolution		±0.01%	±0.87%	±0.56%
Theory	ISR/FSR		±0.13%	±0.02%	±0.04%
	QCD Scale		±0.0%	±0.20%	±0.20%
	PDF		±1.0%	±1.0%	±1.0%
	MPI/Hadronization		±5.0% ± 7.7%	±10.0% ± 48%	±5.7% ± 2.7%
Total Experimental			±4.44%	±5.19%	±2.94%
Total Theory/Excluding MPI/Hadronization			±1.01%	±1.02%	±1.02%

Table B.15: Summary of the systematic uncertainties estimated from different sources in percentage on the $A \to Z(\nu\nu)H(ZZ) \to 4\ell + X$ signal.

Uncertainty source			$N_{jets}^{Central} = 0$	$N_{jets}^{Central} \geq 1$		$N_{b-jets} \geq 1$	$\lvert m_{jj} - m_Z \rvert < 20$ GeV	$\lvert m_{jj} - m_Z \rvert > 20$ GeV	$N_{jets}^{Central} = 1$
			High-E_T^{miss}	High-E_T^{miss}	Low-E_T^{miss}				
Luminosity			±1.70%	±1.70%	±1.70%	±1.70%	±1.70%	±1.70%	±1.70%
Pile-up reweighing			±0.56%	±0.18%	±0.39%	±0.08%	±0.46%	±0.17%	±0.68%
Electron	Energy Resolution		±0.14%	±0.23%	±0.19%	±0.01%	±0.03%	±0.03%	±0.06%
	Energy scale		±0.50%	±0.16%	±0.23%	±0.05%	±0.05%	±0.07%	±0.06%
	Efficiencies	Identification	±0.74%	±0.70%	±0.94%	±1.38%	±1.31%	±1.55%	±1.38%
		Isolation	±0.00%	±0.00%	±0.00%	±0.00%	±0.00%	±0.00%	±0.00%
		Reconstruction	±0.55%	±0.50%	±0.51%	±0.53%	±0.54%	±0.53%	±0.55%
Muon	ID Track Smearing		±0.68%	±1.92%	±1.23%	±0.05%	±0.16%	±0.24%	±0.24%
	MS Track Smearing		±0.49%	±1.45%	±1.15%	±0.02%	±0.18%	±0.18%	±0.19%
	Momentum Scale		±0.02%	±0.03%	±0.06%	±0.02%	±0.00%	±0.03%	±0.03%
	Sagitta Correction		±0.02%	±0.09%	±0.09%	±0.01%	±0.03%	±0.05%	±0.02%
	Efficiencies	TTVA	±0.16%	±0.20%	±0.20%	±0.19%	±0.18%	±0.19%	±0.18%
		Isolation	±2.07%	±2.61%	±3.00%	±3.48%	±3.35%	±3.64%	±2.91%
		Reconstruction	±0.63%	±0.90%	±0.82%	±0.76%	±0.69%	±0.77%	±0.69%
Jet	Energy Scale		±1.42%	±0.76%	±0.17%	±0.56%	±0.83%	±0.70%	±0.82%
	Energy Resolution		±1.19%	±4.74%	±4.32%	±0.28%	±1.86%	±0.47%	±0.67%
	Pileup		±3.03%	±1.55%	±0.66%	±1.59%	±2.52%	±1.54%	±2.14%
	Efficiencies	Flavour Tagging	±4.32%	±3.64%	±1.92%	±4.10%	±3.64%	±3.33%	±3.01%
		JVT/fJVT	±0.60%	±0.35%	±0.44%	±0.29%	±0.44%	±0.16%	±0.21%
E_T^{miss}soft track	E_T^{miss}Offset		±2.08%	±3.19%	±4.72%	±0.00%	±0.53%	±0.50%	±0.64%
	Resolution		±2.50%	±3.73%	±6.17%	±0.00%	±0.64%	±0.64%	±0.83%
Theory	ISR/FSR		±0.13%	±0.02%	±0.04%	±0.02%	±0.04%	±0.04%	±0.01%
	QCD Scale		±0.0%	±0.20%	±0.20%	±0.30%	±0.10%	±0.10%	±0.20%
	PDF		±1.0%	±1.0%	±1.0%	±1.0%	±1.0%	±1.0%	±1.0%
	MPI/Hadronization		±5.0% ± 7.7%	±10.0% ± 48%	±5.7% ± 2.7%	±2.4%	±1.9%	±2.7%	±2.7%
Total Experimental			±7.31%	±9.03%	±9.97%	±6.17%	±6.50%	±5.91%	±5.61%
Total Theory/Excluding MPI/Hadronization			±1.01%	±1.02%	±1.02%	±1.04%	±1.01%	±1.01%	±1.02%

Table B.16: Summary of the systematic uncertainties for the $m_{4\ell}$ normalisation estimated from different sources in percentage on the $qqZZ$ background.

Uncertainty source			$N_{jets}^{Central} = 0$	$N_{jets}^{Central} \geq 1$		$N_{b-jets} \geq 1$	$\lvert m_{jj} - m_Z \rvert < 20$ GeV	$\lvert m_{jj} - m_Z \rvert > 20$ GeV	$N_{jets}^{Central} = 1$
			High-E_T^{miss}	High-E_T^{miss}	Low-E_T^{miss}				
Luminosity			±1.70%	±1.70%	±1.70%	±1.70%	±1.70%	±1.70%	±1.70%
Pile-up reweighing			±0.50%	±2.46%	±2.03%	±0.23%	±0.47%	±0.17%	±0.34%
Electron	Energy Resolution		±0.17%	±0.76%	±0.10%	±0.20%	±0.29%	±0.02%	±0.07%
	Energy scale		±0.57%	±0.49%	±0.34%	±0.19%	±0.24%	±0.10%	±0.10%
	Efficiencies	Identification	±0.45%	±0.48%	±0.44%	±0.44%	±0.45%	±0.45%	±0.44%
		Isolation	±0.13%	±0.14%	±0.13%	±0.14%	±0.14%	±0.14%	±0.14%
		Reconstruction	±0.54%	±0.56%	±0.53%	±0.57%	±0.56%	±0.56%	±0.56%
Muon	ID Track Smearing		±0.29%	±0.56%	±0.34%	±0.16%	±0.30%	±0.04%	±0.07%
	MS Track Smearing		±0.19%	±0.48%	±0.29%	±0.19%	±0.21%	±0.04%	±0.08%
	Momentum Scale		±0.20%	±0.69%	±0.18%	±0.20%	±0.25%	±0.06%	±0.09%
	Sagitta Correction		±0.94%	±6.06%	±2.75%	±0.77%	±0.43%	±0.13%	±0.79%
	Efficiencies	TTVA	±0.12%	±0.13%	±0.13%	±1.29%	±0.14%	±0.15%	±0.14%
		Isolation	±1.28%	±1.39%	±1.31%	±0.51%	±1.30%	±1.42%	±1.14%
		Reconstruction	±0.49%	±0.53%	±0.51%	±0.51%	±0.52%	±0.54%	±0.49%
Jet	Energy Scale		±0.49%	±1.99%	±2.35%	±0.70%	±1.48%	±1.30%	±0.42%
	Energy Resolution		±2.47%	±7.60%	±11.09%	±1.06%	±2.17%	±0.81%	±0.47%
	Pileup		±1.62%	±5.01%	±5.46%	±1.75%	±3.98%	±2.77%	±1.06%
	Efficiencies	Flavour Tagging	±2.54%	±7.62%	±7.77%	±6.61%	±5.93%	±4.38%	±1.84%
		JVT/fJVT	±0.87%	±0.63%	±0.33%	±0.17%	±0.40%	±0.25%	±0.11%
E_T^{miss}soft track	E_T^{miss} Offset		±4.97%	±9.41%	±5.70%	±0.09%	±0.61%	±0.50%	±0.45%
	Resolution		±5.77%	±12.62%	±7.29%	±0.13%	±0.66%	±0.82%	±0.60%
Total Experimental			±9.05%	±21.16%	±18.05%	±7.43%	±8.20%	±6.34%	±3.38%

Table B.17: Summary of the systematic uncertainties on the $m_{4\ell}$ shape due to background parametrisation in percentage for the $qqZZ$, $ggZZ$, VVV and others backgrounds. The numbers are organised to represent the effect on low and higher $m_{4\ell}$ regions such as $m_{4\ell}[200-700]$ GeV and $m_{4\ell}[700-1200]$ GeV, respectively.

Uncertainty source		$N_{\text{jets}}^{\text{Central}}=0$	$N_{\text{jets}}^{\text{Central}}\geq 1$		$N_{b\text{-jets}}\geq 1$	$\lvert m_{\text{jj}}-m_Z\rvert<20$ GeV	$\lvert m_{\text{jj}}-m_Z\rvert>20$ GeV	$N_{\text{jets}}^{\text{Central}}=1$
		High-$E_{\text{T}}^{\text{miss}}$	High-$E_{\text{T}}^{\text{miss}}$	Low-$E_{\text{T}}^{\text{miss}}$				
Parametrisation	$q\bar{q}\to ZZ$	±2.0% - ±8.0%	±2.0% - ±4.5%	±5.0% - ±10.0%	±10.0% - ±13.0%	±8.0% - ±14.0%	±4.0% - ±6.0%	±20.0% - ±2.0%
	$gg\to ZZ$	±20.0% - ±22.50%	±10.0% - ±12.50%	±5.0% - ±30.0%	±15.0% - ±12.5%	±15.0% - ±22.50%	±5.0% - ±10.0%	±2.50% - ±9.0%
	VVV	±6.0% - ±10.0%	±10.0% - ±15.0%	±4.0% - ±4.0%	±15.0% - ±20.0%	±17.5% - ±22.5%	±8.0% - ±8.5%	±12.0% - ±11.0%
	others	±7.5% - ±30.0%	±25.0% - ±45.0%	±40.0% - ±30.0%	±2.0% - ±16.0%	±45.0% - ±25.0%	±20.0% - ±17.50%	±10.0% - ±13.0%

Table B.18: Summary of the systematic uncertainties on the $m_{4\ell}$ shape estimated from different sources in percentage for the $qqZZ$ background.

Uncertainty source		$N_{\text{jets}}^{\text{Central}}=0$	$N_{\text{jets}}^{\text{Central}}\geq 1$		$N_{b\text{-jets}}\geq 1$	$\lvert m_{\text{jj}}-m_Z\rvert<20$ GeV	$\lvert m_{\text{jj}}-m_Z\rvert>20$ GeV	$N_{\text{jets}}^{\text{Central}}=1$
		High-$E_{\text{T}}^{\text{miss}}$	High-$E_{\text{T}}^{\text{miss}}$	Low-$E_{\text{T}}^{\text{miss}}$				
PRW_DATAS		±3.97%	±2.67%	±2.07%	±1.11%	±1.33%	±0.80%	±1.26%
MET_SoftTrk_ResoPara		±0.92%	±8.39%	±0.75%	±0.65%	±0.72%	±0.49%	±0.47%
MET_SoftTrk_ResoPerp		±1.58%	±8.18%	±1.40%	±0.65%	±1.00%	±0.60%	±0.60%
MET_SoftTrk_Scale		±1.45%	±7.91%	±1.45%	±0.81%	±0.71%	±0.36%	±0.47%
JET_JER_EffectiveNP_1		±1.84%	±9.72%	±3.45%	±0.94%	±1.72%	±1.13%	±0.42%
JET_JER_EffectiveNP_2		±1.48%	±4.87%	±3.83%	±0.64%	±1.54%	±0.81%	±0.61%
JET_JER_EffectiveNP_3		±1.34%	±3.57%	±6.94%	±1.01%	±3.94%	±0.39%	±0.61%
JET_JER_EffectiveNP_4		±1.17%	±4.68%	±5.81%	±1.15%	±2.16%	±0.68%	±0.64%
JET_JER_EffectiveNP_5		±2.16%	±3.11%	±5.46%	±0.75%	±2.30%	±0.60%	±0.22%
JET_JER_EffectiveNP_6		±1.54%	±5.02%	±3.89%	±0.89%	±2.46%	±0.46%	±0.33%
Theory	HOEW QCD	±1.0%	±6.66%	±8.0%	±9.0%	±5.0%	±9.0%	±3.0%
	QCD scale	±6.0%	±5.0%	±3.50%	±10.0%	±3.0%	±1.50%	±6.0%
	PDF	±13.0%	±17.0%	±26.0%	±23.0%	±19.0%	±9.0%	±9.0%

Table B.19: Summary of the systematic uncertainties on the $m_{4\ell}$ shape estimated from different sources in percentage for the $ggZZ$ background.

Uncertainty source		$N_{\text{jets}}^{\text{Central}}=0$	$N_{\text{jets}}^{\text{Central}}\geq 1$		$N_{b\text{-jets}}\geq 1$	$\lvert m_{\text{jj}}-m_Z\rvert<20$ GeV	$\lvert m_{\text{jj}}-m_Z\rvert>20$ GeV	$N_{\text{jets}}^{\text{Central}}=1$
		High-$E_{\text{T}}^{\text{miss}}$	High-$E_{\text{T}}^{\text{miss}}$	Low-$E_{\text{T}}^{\text{miss}}$				
PRW_DATAS		±2.68%	±11.15%	±6.66%	±8.22%	±3.50%	±1.83%	±1.56%
MET_SoftTrk_ResoPara		±1.30%	±10.10%	±0.81%	±2.38%	±1.46%	±0.27%	±1.00%
MET_SoftTrk_ResoPerp		±0.98%	±11.09%	±3.31%	±2.38%	±1.06%	±0.47%	±0.37%
MET_SoftTrk_Scale		±1.18%	±11.19%	±1.52%	±3.58%	±0.81%	±0.52%	±0.30%
JET_JER_EffectiveNP_1		±4.78%	±11.08%	±10.43%	±2.07%	±1.92%	±1.19%	±1.05%
JET_JER_EffectiveNP_2		±7.06%	±12.50%	±7.31%	±1.32%	±8.08%	±1.41%	±0.87%
JET_JER_EffectiveNP_3		±3.58%	±16.80%	±4.38%	±4.87%	±3.07%	±1.25%	±1.55%
JET_JER_EffectiveNP_4		±2.39%	±11.87%	±6.72%	±4.05%	±4.05%	±2.14%	±1.92%
JET_JER_EffectiveNP_5		±1.50%	±9.57%	±11.79%	±1.49%	±9.69%	±1.22%	±0.63%
JET_JER_EffectiveNP_6		±5.16%	±13.79%	±2.14%	±3.27%	±4.48%	±0.69%	±1.06%
Theory	QCD scale	±8.0%	±4.5%	±6.0%	±5.0%	±10.0%	±9.50%	±8.0%
	PDF	±13.0%	±7.0%	±18.0%	±42.5%	±12.0%	±10.0%	±12.5%

B.10.1 Systematic uncertainties on the normalisation of the $m_{4\ell}$ distribution

Table B.20: Summary of the systematic uncertainties for the $m_{4\ell}$ normalisation estimated from different sources in percentage on the $ggZZ$ background.

Uncertainty source			$N_{\text{jets}}^{\text{Central}} = 0$	$N_{\text{jets}}^{\text{Central}} \geq 1$		$N_{b-\text{jets}} \geq 1$	$\lvert m_{\text{jj}} - m_Z \rvert < 20$ GeV	$\lvert m_{\text{jj}} - m_Z \rvert > 20$ GeV	$N_{\text{jets}}^{\text{Central}} = 1$
			High-$E_{\text{T}}^{\text{miss}}$	High-$E_{\text{T}}^{\text{miss}}$	Low-$E_{\text{T}}^{\text{miss}}$				
Luminosity			±1.70%	±1.70%	±1.70%	±1.70%	±1.70%	±1.70%	±1.70%
Pile-up reweighing			±0.14%	±1.95%	±2.37%	±0.33%	±0.65%	±0.20%	±0.45%
Electron	Energy Resolution		±0.19%	±0.04%	±0.18%	±0.07%	±0.05%	±0.01%	±0.03%
	Energy scale		±0.45%	±0.15%	±0.55%	±0.14%	±0.01%	±0.06%	±0.07%
	Efficiencies	Identification	±0.47%	±0.47%	±0.47%	±0.48%	±0.48%	±0.47%	±0.47%
		Isolation	±0.13%	±0.12%	±0.12%	±0.14%	±0.14%	±0.14%	±0.14%
		Reconstruction	±0.59%	±0.52%	±0.56%	±0.58%	±0.58%	±0.56%	±0.59%
Muon	ID Track Smearing		±0.14%	±0.25%	±0.34%	±0.04%	±0.19%	±0.07%	±0.04%
	MS Track Smearing		±0.13%	±0.32%	±0.11%	±0.03%	±0.09%	±0.05%	±0.03%
	Momentum Scale		±0.22%	±0.21%	±0.14%	±0.11%	±0.05%	±0.10%	±0.07%
	Sagitta Correction		±0.04%	±0.54%	±0.07%	±0.03%	±0.04%	±0.02%	±0.01%
	Efficiencies	TTVA	±0.13%	±0.13%	±0.13%	±0.15%	±0.15%	±0.15%	±0.14%
		Isolation	±1.22%	±1.43%	±1.30%	±1.31%	±1.32%	±1.42%	±1.16%
		Reconstruction	±0.45%	±0.50%	±0.48%	±0.48%	±0.49%	±0.51%	±0.47%
Jet	Energy Scale		±1.52%	±2.21%	±1.22%	±1.03%	±1.77%	±1.87%	±0.64%
	Energy Resolution		±1.37%	±9.20%	±7.80%	±1.53%	±1.93%	±1.30%	±0.45%
	Pileup		±2.20%	±5.50%	±3.97%	±2.20%	±4.53%	±4.11%	±1.30%
	Efficiencies	Flavour Tagging	±3.48%	±9.40%	±5.82%	±8.18%	±6.48%	±6.87%	±2.02%
		JVT/fJVT	±0.42%	±0.46%	±0.30%	±0.23%	±0.42%	±0.32%	±0.14%
$E_{\text{T}}^{\text{miss}}$soft track	$E_{\text{T}}^{\text{miss}}$ Offset		±4.56%	±10.68%	±5.54%	±0.00%	±0.72%	±0.61%	±0.63%
	Resolution		±5.98%	±13.66%	±6.64%	±0.00%	±1.11%	±0.76%	±0.75%
Total Experimental			±9.17%	±22.88%	±14.16%	±9.03%	±8.97%	±8.90%	±3.60%

Table B.21: Summary of the systematic uncertainties for the $m_{4\ell}$ normalisation estimated from different sources in percentage on the VVV background.

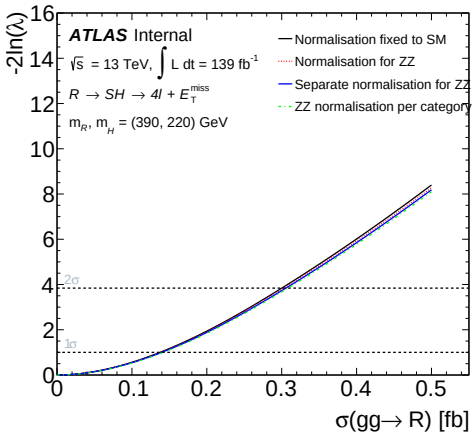
Uncertainty source			$N_{\text{jets}}^{\text{Central}} = 0$	$N_{\text{jets}}^{\text{Central}} \geq 1$		$N_{b-\text{jets}} \geq 1$	$\lvert m_{\text{jj}} - m_Z \rvert < 20$ GeV	$\lvert m_{\text{jj}} - m_Z \rvert > 20$ GeV	$N_{\text{jets}}^{\text{Central}} = 1$
			High-$E_{\text{T}}^{\text{miss}}$	High-$E_{\text{T}}^{\text{miss}}$	Low-$E_{\text{T}}^{\text{miss}}$				
Luminosity			±1.70%	±1.70%	±1.70%	±1.70%	±1.70%	±1.70%	±1.70%
Pile-up reweighing			±0.56%	±0.67%	±1.32%	±1.50%	±1.73%	±0.40%	±0.90%
Electron	Energy Resolution		±0.04%	±0.02%	±0.24%	±0.10%	±0.15%	±0.08%	±0.20%
	Energy scale		±0.16%	±0.16%	±0.21%	±0.16%	±0.21%	±0.26%	±0.13%
	Efficiencies	Identification	±0.47%	±0.51%	±0.50%	±0.47%	±0.47%	±0.49%	±0.46%
		Isolation	±0.16%	±0.17%	±0.15%	±0.16%	±0.15%	±0.16%	±0.15%
		Reconstruction	±0.61%	±0.62%	±0.57%	±0.58%	±0.55%	±0.56%	±0.59%
Muon	ID Track Smearing		±0.04%	±0.03%	±0.36%	±0.19%	±0.60%	±0.11%	±0.29%
	MS Track Smearing		±0.02%	±0.02%	±0.24%	±0.08%	±0.17%	±0.18%	±0.18%
	Momentum Scale		±0.04%	±0.07%	±0.12%	±0.14%	±0.12%	±0.26%	±0.12%
	Sagitta Correction		±0.10%	±0.04%	±0.07%	±0.93%	±0.08%	±0.43%	±0.05%
	Efficiencies	TTVA	±0.15%	±0.16%	±0.15%	±0.17%	±0.17%	±0.16%	±0.15%
		Isolation	±1.87%	±1.55%	±1.25%	±1.74%	±1.41%	±1.84%	±1.28%
		Reconstruction	±0.51%	±0.55%	±0.53%	±0.57%	±0.52%	±0.59%	±0.54%
Jet	Energy Scale		±0.59%	±0.61%	±0.39%	±0.52%	±2.89%	±0.58%	±0.56%
	Energy Resolution		±0.55%	±1.11%	±2.91%	±1.39%	±2.93%	±1.29%	±1.84%
	Pileup		±1.24%	±1.53%	±1.16%	±1.41%	±7.00%	±1.22%	±0.56%
	Efficiencies	Flavour Tagging	±1.88%	±2.75%	±0.11%	±8.49%	±8.88%	±2.75%	±0.74%
		JVT/fJVT	±0.18%	±0.11%	±1.51%	±0.23%	±0.41%	±0.16%	±0.05%
$E_{\text{T}}^{\text{miss}}$soft track	$E_{\text{T}}^{\text{miss}}$ Offset		±0.05%	±0.22%	±0.09%	±0.00%	±0.73%	±0.58%	±0.32%
	Resolution		±0.02%	±0.19%	±0.95%	±0.00%	±0.54%	±0.58%	±0.89%
Total Experimental			±3.69%	±4.33%	±4.57%	±9.31%	±12.03%	±4.41%	±3.47%

Table B.22: Summary of the systematic uncertainties for the $m_{4\ell}$ normalisation estimated from different sources in percentage on the others backgrounds.

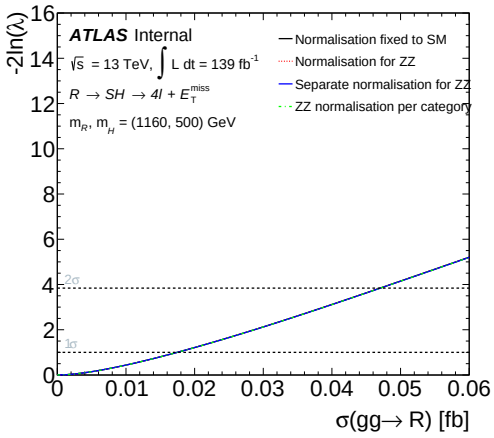
Uncertainty source			$N_{\text{jets}}^{\text{Central}} = 0$	$N_{\text{jets}}^{\text{Central}} \geq 1$		$N_{b-\text{jets}} \geq 1$	$\lvert m_{\text{jj}} - m_Z \rvert < 20$ GeV	$\lvert m_{\text{jj}} - m_Z \rvert > 20$ GeV	$N_{\text{jets}}^{\text{Central}} = 1$
			High-$E_{\text{T}}^{\text{miss}}$	High-$E_{\text{T}}^{\text{miss}}$	Low-$E_{\text{T}}^{\text{miss}}$				
Luminosity			±1.70%	±1.70%	±1.70%	±1.70%	±1.70%	±1.70%	±1.70%
Pile-up reweighing			±2.46%	±2.85%	±0.80%	±1.39%	±0.86%	±0.82%	±0.61%
Electron	Energy Resolution		±0.32%	±1.13%	±0.62%	±0.09%	±0.13%	±0.01%	±0.16%
	Energy scale		±0.84%	±0.51%	±0.48%	±0.12%	±0.15%	±0.07%	±0.02%
	Efficiencies	Identification	±0.43%	±0.35%	±0.46%	±0.46%	±0.42%	±0.47%	±0.47%
		Isolation	±0.10%	±0.19%	±0.14%	±0.16%	±0.14%	±0.15%	±0.15%
		Reconstruction	±0.50%	±0.57%	±0.58%	±0.52%	±0.51%	±0.57%	±0.57%
Muon	ID Track Smearing		±0.63%	±0.74%	±0.71%	±0.10%	±0.10%	±0.05%	±0.18%
	MS Track Smearing		±0.81%	±0.48%	±0.87%	±0.04%	±0.08%	±0.05%	±0.05%
	Momentum Scale		±0.45%	±0.56%	±0.22%	±0.05%	±0.02%	±0.02%	±0.06%
	Sagitta Correction		±0.85%	±0.44%	±0.34%	±0.11%	±0.04%	±0.02%	±0.11%
	Efficiencies	TTVA	±0.15%	±0.17%	±0.16%	±0.17%	±0.15%	±0.16%	±0.15%
		Isolation	±1.23%	±1.69%	±1.76%	±1.74%	±1.48%	±1.64%	±1.29%
		Reconstruction	±0.51%	±0.66%	±0.63%	±0.60%	±0.53%	±0.55%	±0.52%
Jet	Energy Scale		±1.55%	±1.92%	±3.13%	±0.38%	±1.14%	±0.20%	±0.03%
	Energy Resolution		±10.64%	±10.55%	±12.48%	±0.85%	±2.35%	±0.79%	±1.38%
	Pileup		±4.30%	±0.95%	±4.13%	±0.73%	±2.45%	±0.67%	±1.21%
	Efficiencies	Flavour Tagging	±5.40%	±1.76%	±4.25%	±8.51%	±4.58%	±2.01%	±2.04%
		JVT/fJVT	±1.15%	±0.77%	±0.60%	±0.20%	±0.35%	±0.13%	±0.26%
$E_{\text{T}}^{\text{miss}}$soft track	$E_{\text{T}}^{\text{miss}}$ Offset		±4.87%	±6.08%	±7.79%	±0.00%	±0.28%	±0.44%	±0.45%
	Resolution		±2.32%	±9.68%	±7.03%	±0.00%	±0.63%	±0.35%	±0.58%
Total Experimental			±14.58%	±16.46%	±17.96%	±9.09%	±6.46%	±3.56%	±3.79%

B.11 Effect of ZZ background normalisation on the upper limits

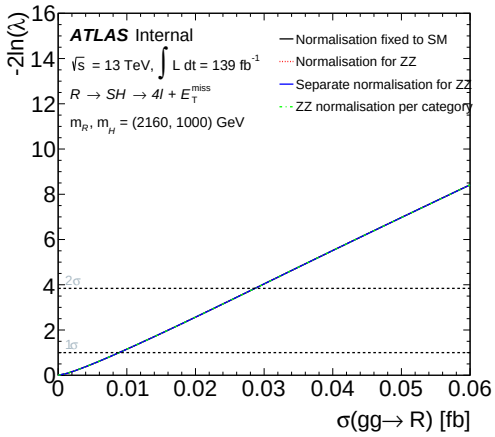
This study was conducted to test the effect of fixing or floating the background normalisation on the expected upper limits. Three $R \to SH \to 4\ell + E_{\text{T}}^{\text{miss}}$ and $A \to Z(\nu\nu)H(ZZ) \to 4\ell + X$ signal samples with low, medium and high missing transverse energy were selected for the study.



(a) $(m_R,\, m_H) = (390,\, 220)\,\text{GeV}$

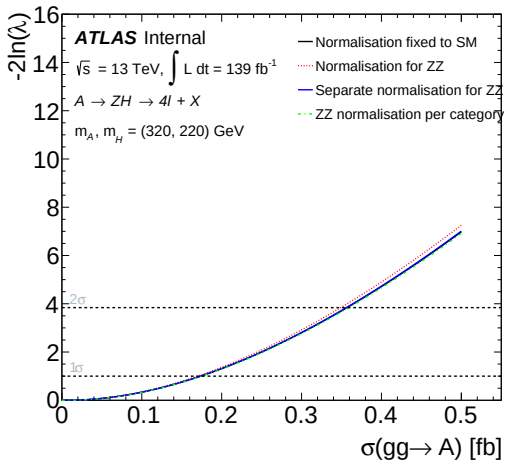


(b) $(m_R,\, m_H) = (1160,\, 500)\,\text{GeV}$

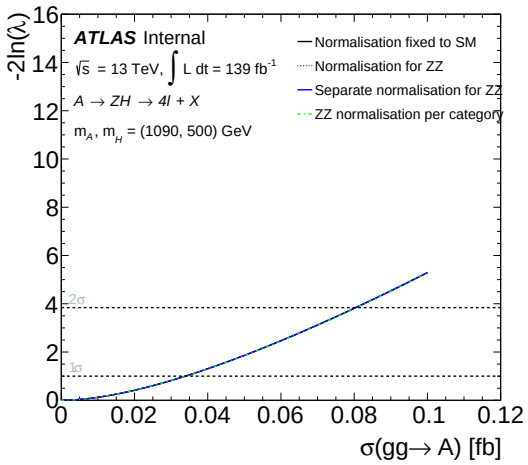


(c) $(m_R,\, m_H) = (2160,\, 1000)\,\text{GeV}$

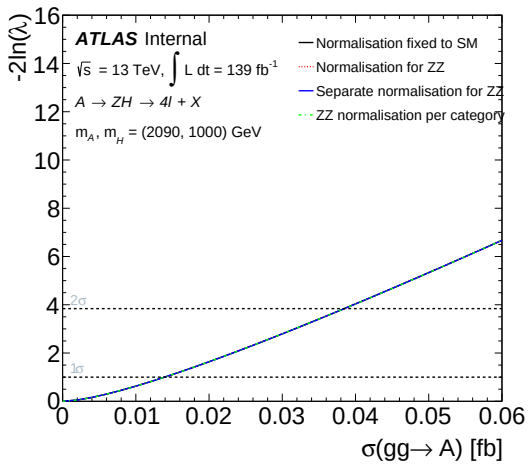
Figure B.31: The likelihood profile as function of the $\sigma(gg \to R) \times \text{BR}(R \to SH) \times \text{BR}(H \to ZZ \to 4\ell)$ for the $R \to SH \to 4\ell + E_{\text{T}}^{\text{miss}}$ signal. The 2σ level represents the upper limit at 95% CL.



(a) $(m_A, m_H) = (320, 220)$ GeV



(b) $(m_A, m_H) = (1090,500)$ GeV

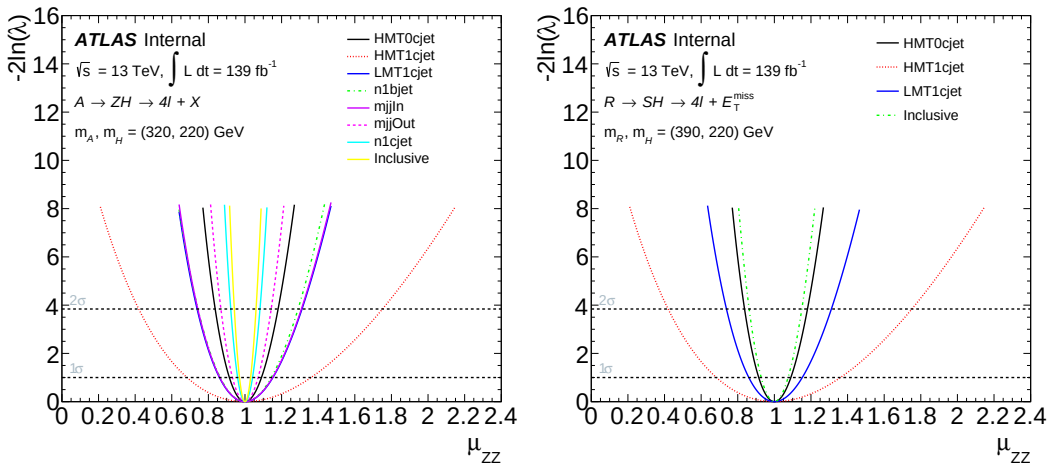


(c) $(m_A, m_H) = (2090, 1000)$ GeV

Figure B.32: The likelihood profile as function of the $\sigma(gg \to A) \times \mathrm{BR}(A \to ZH) \times \mathrm{BR}(H \to ZZ \to 4\ell)$ for the $A \to Z(\nu\nu)H(ZZ) \to 4\ell + X$ signal. The 2σ level represents the upper limit at 95% CL.

The negative log-likelihood as a function of the $\sigma(gg \to R)$ scan for different mass point is shown in Figure B.31 for the $R \to SH \to 4\ell + E_{\mathrm{T}}^{\mathrm{miss}}$. A similar scan is shown in Figure B.32 for $A \to Z(\nu\nu)H(ZZ) \to 4\ell + X$ signal. The effect is within 2% for samples with low $E_{\mathrm{T}}^{\mathrm{miss}}$ for both models. However, the difference disappears for samples with medium and high $E_{\mathrm{T}}^{\mathrm{miss}}$. Figure B.33 shows the negative log-likelihood as function of the zz background normalisation scan for

$A \to Z(\nu\nu)H(ZZ) \to 4\ell + X$ and $R \to SH \to 4\ell + E_{\mathrm{T}}^{\mathrm{miss}}$ models. The scan is compared when the normalisation depends on the category and the inclusive case where the normalisation doesn't depend on the categories.



(a) $A \to Z(\nu\nu)H(ZZ) \to 4\ell + X$ (b) $R \to SH \to 4\ell + E_{\mathrm{T}}^{\mathrm{miss}}$

Figure B.33: The likelihood profile as function of the $qqZZ$ and $ggZZ$ normalisation (μ_{ZZ}). The normalisation scan is shown per category and inclusively.

Bibliography

[1] von Buddenbrock S, Chakrabarty N, Cornell A S, Kar D, Kumar M, Mandal T, Mellado B, Mukhopadhyaya B, Reed R G and Ruan X 2016 *Eur. Phys. J. C* **76** 580 (*Preprint* 1606.01674)

[2] Buddenbrock S, Cornell A S, Fang Y, Fadol Mohammed A, Kumar M, Mellado B and Tomiwa K G 2019 *JHEP* **10** 157 (*Preprint* 1901.05300)

[3] Glashow S L 1961 *Nuclear Physics* **22** 579–588 ISSN 0029-5582 URL https://www.sciencedirect.com/science/article/pii/0029558261904692

[4] Weinberg S 1967 *Phys. Rev. Lett.* **19**(21) 1264–1266 URL https://link.aps.org/doi/10.1103/PhysRevLett.19.1264

[5] Salam A 1968 *Conf. Proc. C* **680519** 367–377

[6] Halzen F and Martin A D 1984 *Quarks and Leptons, an introduction course in modern particle physics* (J. Wiley & Sons)

[7] Gell-Mann M 1964 *Phys. Lett.* **8** 214–215

[8] Zweig G 1964 *An SU(3) model for strong interaction symmetry and its breaking. Version 2* (Developments in the Quark Theory of Hadrons) pp 22–101

[9] Arnison G *et al.* 1983 *Physics Letters B* **122** 103–116 ISSN 0370-2693 URL https://www.sciencedirect.com/science/article/pii/0370269383911772

[10] Bagnaia P *et al.* 1983 *Physics Letters B* **129** 130–140 ISSN 0370-2693 URL https://www.sciencedirect.com/science/article/pii/037026938390744X

[11] ALEPH Collaboration, DELPHI Collaboration, L3 Collaboration, OPAL Collaboration and the LEP Working Group for Higgs Boson Searches 2003 *Physics Letters B* **565** 61–75 ISSN 0370-2693 URL https://www.sciencedirect.com/science/article/pii/S0370269303006142

[12] The CDF, D0 Collaborations, the Tevatron New Phenomena, and the Higgs Working Group 2011 Combined cdf and d0 upper limits on standard model higgs boson production with up to 8.6 fb-1 of data URL https://arxiv.org/abs/1107.5518

[13] Aad G *et al.* (ATLAS) 2020 *Eur. Phys. J. C* **80** 942 (*Preprint* 2004.03969)

[14] Sirunyan A M *et al.* (CMS) 2021 *Eur. Phys. J. C* **81** 488 (*Preprint* 2103.04956)

[15] Aad G *et al.* (ATLAS Collaboration and CMS Collaboration) 2015 *Phys. Rev. Lett.* **114**(19) 191803 URL https://link.aps.org/doi/10.1103/PhysRevLett.114.191803

[16] Womersley J 2000 QCD at the Tevatron: Status and Prospects URL https://arxiv.org/abs/hep-ex/0012061

[17] Georgi H M, Glashow S L, Machacek M E and Nanopoulos D V 1978 *Phys. Rev. Lett.* **40** 692

[18] Graudenz D, Spira M and Zerwas P M 1993 *Phys. Rev. Lett.* **70** 1372–1375

[19] Actis S, Passarino G, Sturm C and Uccirati S 2008 *Phys. Lett. B* **670** 12–17 (*Preprint* 0809.1301)

[20] Ciccolini M, Denner A and Dittmaier S 2008 *Phys. Rev. D* **77** 013002 (*Preprint* 0710.4749)

[21] Han T and Willenbrock S 1991 *Physics Letters B* **273** 167–172 ISSN 0370-2693 URL https://www.sciencedirect.com/science/article/pii/0370269391905728

[22] Dawson S, Jackson C, Orr L H, Reina L and Wackeroth D 2003 *Physical Review D* **68** URL https://doi.org/10.1103%2Fphysrevd.68.034022

[23] Tanabashi M *et al.* (Particle Data Group) 2018 *Phys. Rev. D* **98**(3) 030001 URL https://link.aps.org/doi/10.1103/PhysRevD.98.030001

[24] CERN 2017 Cern yellow reports: Monographs, vol 2 (2017): Handbook of lhc higgs cross sections: 4. deciphering the nature of the higgs sector URL https://e-publishing.cern.ch/index.php/CYRM/issue/view/32

[25] Overduin J and Wesson P 1997 *Physics Reports* **283** 303–378 URL https://doi.org/10.1016%2Fs0370-1573%2896%2900046-4

[26] Terning J 2005 *Modern Supersymmetry: Dynamics and Duality* (Oxford University Press) ISBN 9780198567639 URL https://doi.org/10.1093/acprof:oso/9780198567639.001.0001

[27] Planck Collaboration *et al.* 2014 *A&A* **571** A1 URL https://doi.org/10.1051/0004-6361/201321529

[28] Ahmad Q R *et al.* (SNO) 2002 *Phys. Rev. Lett.* **89** 011301 (*Preprint* nucl-ex/0204008)

[29] Ashie Y *et al.* (Super-Kamiokande) 2004 *Phys. Rev. Lett.* **93** 101801 (*Preprint* hep-ex/0404034)

[30] Riotto A 1998 *ICTP Summer School in High-Energy Physics and Cosmology* pp 326–436 (*Preprint* hep-ph/9807454)

[31] von Buddenbrock S, Chakrabarty N, Cornell A S, Kar D, Kumar M, Mandal T, Mellado B, Mukhopadhyaya B and Reed R G 2015 The compatibility of lhc run 1 data with a heavy scalar of mass around 270 gev URL https://arxiv.org/abs/1506.00612

[32] von Buddenbrock S, Cornell A S, Kumar M and Mellado B 2017 *J. Phys. Conf. Ser.* **889** 012020 (*Preprint* 1709.09419)

[33] Aad G *et al.* (ATLAS) 2014 *Journal of High Energy Physics* **2014** URL https://doi.org/10.1007%2Fjhep09%282014%29112

[34] Aad G *et al.* (ATLAS) 2014 *Physics Letters B* **738** 234–253 URL https://doi.org/10.1016%2Fj.physletb.2014.09.054

[35] Khachatryan V *et al.* (CMS) 2016 *The European Physical Journal C* **76** URL https://doi.org/10.1140%2Fepjc%2Fs10052-015-3853-3

[36] Khachatryan V *et al.* (CMS) 2016 *Journal of High Energy Physics* **2016** URL https://doi.org/10.1007%2Fjhep04%282016%29005

[37] Aad G *et al.* (ATLAS) 2015 *Physical Review D* **92** URL https://doi.org/10.1103%2Fphysrevd.92.092004

[38] Khachatryan V *et al.* (CMS) 2016 *Physical Review D* **94** URL https://doi.org/10.1103%2Fphysrevd.94.052012

[39] Khachatryan V *et al.* (CMS) 2016 *Physical Review D* **755** 217–244 URL https://doi.org/10.1016%2Fj.physletb.2016.01.056

[40] Khachatryan V *et al.* (CMS) 2014 *Phys. Rev. D* **90**(11) 112013 URL https://link.aps.org/doi/10.1103/PhysRevD.90.112013

[41] Aad G *et al.* (ATLAS) 2015 *Physics Letters B* **740** 222–242 URL https://doi.org/10.1016%2Fj.physletb.2014.11.049

[42] Aad G *et al.* (ATLAS) 2015 *Physics Letters B* **749** 519–541 URL https://doi.org/10.1016%2Fj.physletb.2015.07.079

[43] Aad G *et al.* (ATLAS) 2015 *The European Physical Journal C* **75** URL https://doi.org/10.1140%2Fepjc%2Fs10052-015-3543-1

[44] Khachatryan V *et al.* (CMS) 2014 *Journal of High Energy Physics* **2014** URL https://doi.org/10.1007%2Fjhep09%282014%29087

[45] Aad G *et al.* (ATLAS) 2016 *Journal of High Energy Physics* **2016** URL https://doi.org/10.1007%2Fjhep01%282016%29032

[46] Aad G *et al.* (ATLAS) 2016 *The European Physical Journal C* **76** URL https://doi.org/10.1140%2Fepjc%2Fs10052-015-3820-z

[47] Khachatryan V *et al.* (CMS) 2015 *Journal of High Energy Physics* **2015** URL https://doi.org/10.1007%2Fjhep10%282015%29144

[48] Kumar M, von Buddenbrook S, Chakrabarty N, Cornell A S, Kar D, Mandal T, Mellado B, Mukhopadhyaya B and Reed R G 2017 *Journal of Physics: Conference Series* **802** 012007 URL https://doi.org/10.1088%2F1742-6596%2F802%2F1%2F012007

[49] von Buddenbrock S, Cornell A S, Fadol A, Kumar M, Mellado B and Ruan X 2017 Multi-lepton signatures of additional scalar bosons beyond the standard model at the lhc URL https://arxiv.org/abs/1711.07874

[50] von Buddenbrock S, Cornell A S, Fang Y, Mohammed A F, Kumar M, Mellado B and Tomiwa K G 2019 *Journal of High Energy Physics* **2019** URL https://doi.org/10.1007%2Fjhep10%282019%29157

[51] CERN 1999 Dipole and quadripole magnets in the LEP tunnel. Les aimants dipoles and quadrupoles dans le tunnel LEP aC multimedia documents URL https://cds.cern.ch/record/41673

[52] Wenninger J 2016 *CERN Yellow Reports* **2** 377 [Online, Accessed September 11, 2022] URL https://e-publishing.cern.ch/index.php/CYR/article/view/242

[53] Mobs E 2018 The CERN accelerator complex - August 2018. Complexe des accélérateurs du CERN - Août 2018 general Photo URL http://cds.cern.ch/record/2636343

[54] Boccali T 2022 *Nuclear Instruments and Methods in Physics Research Section A: Accelerators, Spectrometers, Detectors and Associated Equipment* **1043** 167434 ISSN 0168-9002 URL https://www.sciencedirect.com/science/article/pii/S0168900222007264

[55] Aad G *et al.* (ATLAS) 2008 *JINST* **3** S08003 URL https://iopscience.iop.org/article/10.1088/1748-0221/3/08/S08003

[56] Chatrchyan S *et al.* (CMS) 2008 *JINST* **3** S08004

[57] Aamodt K *et al.* (ALICE) 2008 *JINST* **3** S08002

[58] Szumlak T (LHCb) 2010 *Acta Phys. Polon. B* **41** 1661–1668

[59] Acharya B *et al.* 2022 *2022 Snowmass Summer Study* (*Preprint* 2209.03988)

[60] Abreu H *et al.* (FASER) 2022 The FASER Detector (*Preprint* 2207.11427)

[61] Acampora G *et al.* (SND@LHC) 2022 SND@LHC: The Scattering and Neutrino Detector at the LHC (*Preprint* 2210.02784)

[62] Robichaud-Véronneau A 2009 The ATLAS detector at the LHC cERN

[63] Pequenao J 2008 Computer generated image of the whole ATLAS detector general Photo URL https://cds.cern.ch/record/1095924

[64] Aad G *et al.* 2017 *The European Physical Journal C* **77** 490 ISSN 1434-6052 URL https://doi.org/10.1140/epjc/s10052-017-5004-5

[65] Patrignani C and Particle Data Group 2016 *Chinese Physics C* **40** 100001 URL http://stacks.iop.org/1674-1137/40/i=10/a=100001

[66] de Andrade Filho L M *et al.* 2012 *Computer Physics Communications* **183** 245 – 250 ISSN 0010-4655 URL http://www.sciencedirect.com/science/article/pii/S0010465511003092

[67] The ATLAS Collaboration 2010 *The European Physical Journal C* **70** 1193–1236 ISSN 1434-6052 URL https://doi.org/10.1140/epjc/s10052-010-1508-y

[68] Aaboud M *et al.* (ATLAS) 2017 *Eur. Phys. J.* **C77** 317 (*Preprint* 1611.09661)

[69] The ATLAS Collaboration (ATLAS) 2018 Trigger Menu in 2017 Tech. Rep. ATL-DAQ-PUB-2018-002 CERN Geneva URL http://cds.cern.ch/record/2625986

[70] Abolins M *et al.* (ATLAS TDAQ) 2016 *JINST* **11** P06008 URL http://stacks.iop.org/1748-0221/11/i=06/a=P06008

[71] Spiwoks R *et al.* 2005 *11th Workshop on Electronics for LHC and Future Experiments (LECC 2005)* p 47

[72] Stelzer J and the ATLAS collaboration 2011 *Journal of Physics: Conference Series* **331** 022026 URL http://stacks.iop.org/1742-6596/331/i=2/a=022026

[73] Jenni P *et al.* (ATLAS Collaboration) 2003 *ATLAS high-level trigger, data-acquisition and controls: Technical Design Report* Technical Design Report ATLAS (Geneva: CERN) URL https://cds.cern.ch/record/616089

[74] van der Bij H C *et al.* 1996 *1996 IEEE Nuclear Science Symposium. Conference Record* vol 1 pp 465–469 vol.1 ISSN 1082-3654

[75] Vazquez J G 2014 The ATLAS Data Acquisition System: from Run 1 to Run 2 Tech. Rep. ATL-DAQ-PROC-2014-035 CERN Geneva URL https://cds.cern.ch/record/1954156

[76] Cranfield R *et al.* 2008 *JINST* **3** T01002 URL https://iopscience.iop.org/article/10.1088/1748-0221/3/01/T01002

[77] ATLAS Collaboration (ATLAS) 2005 *ATLAS Computing: technical design report* Technical design report. ATLAS (Geneva: CERN) URL https://cds.cern.ch/record/837738

[78] ATLAS Collaboration 2012 Letter of Intent for the Phase-II Upgrade of the ATLAS Experiment Tech. Rep. CERN-LHCC-2012-022. LHCC-I-023 CERN Geneva draft version for comments URL https://cds.cern.ch/record/1502664

[79] Hrynevich A (ATLAS) 2017 *JINST* **12** C06021

[80] The ATLAS Collaboration 2008 *Journal of Instrumentation* **3** S08003–S08003 URL https://doi.org/10.1088%2F1748-0221%2F3%2F08%2Fs08003

[81] Cuciuc M (ATLAS Tile Calorimeter System) 2012 *2012 IEEE Nuclear Science Symposium and Medical Imaging Conference and 19th Workshop on Room-Temperature Semiconductor X-ray and Gamma-ray Detectors* pp 948–950

[82] Martins F (ATLAS) 2016 *2016 IEEE Nuclear Science Symposium and Medical Imaging Conference* p 8069837

[83] Dawson J W, Francis D J, Haberichter W N and Schlereth J L 2001 TTCPR: a PMC receiver for TTC cERN URL https://cds.cern.ch/record/529413

[84] Valero A *et al.* 2007 *JINST* **2** P05003 URL https://iopscience.iop.org/article/10.1088/1748-0221/2/05/P05003

[85] Ciodaro T, de Seixas J M and Cerqueira A 2014 *IEEE Trans. Nucl. Sci.* **61** 1047–1055

[86] Marjanovic M (ATLAS) 2019 *IEEE Trans. Nucl. Sci.* **66** 1228–1235 (*Preprint* 1806.09156)

[87] Aad G *et al.* (ATLAS) 2013 *Eur. Phys. J. C* **73** 2518 (*Preprint* 1302.4393)

[88] Blanchot G *et al.* 2020 *JINST* **15** P03017 (*Preprint* 2002.12800)

[89] Almeida J *et al.* 2008 *Journal of Physics: Conference Series* **119** 022004 URL http://stacks.iop.org/1742-6596/119/i=2/a=022004

[90] The ATLAS Collaboration (ATLAS) 1998 ATLAS level-1 trigger: Technical Design Report Tech. Rep. CERN-LHCC-98-14. ATLAS-TDR-12 CERN final version presented to December 2013 LHCC.

[91] Solans C A 2010 *Implementation of the ROD Crate DAQ Software for the ATLAS Tile Calorimeter and a Search for a MSSM Higgs Boson decaying into Tau pairs* Ph.D. thesis Valencia U., IFIC

[92] Barczyk M *et al.* 2003 *eConf* **C0303241** TUGP005 (*Preprint* hep-ex/0305106)

[93] Haas S *et al.* 2018 ALTI specification review and preliminary design review URL https://indico.cern.ch/event/735376/attachments/1673160/2684944/ALTI-Specification_Rev_1_2.pdf

[94] Ask S *et al.* 2008 *JINST* **3** P08002

[95] Billereau W *et al.* 2017 EDA-03627 ALTI - Atlas LTrg Interface URL https://edms.cern.ch/ui/#!master/navigator/project?P:1844187571:1844187571:subDocs

[96] Samtec 2022 0.5 mm Q Strip High-Speed Ground Plane QSH/QTH series connectors URL http://suddendocs.samtec.com/catalog_english/qsh.pdf

[97] Texas Instruments 2022 DS10CP154A – 1.5 Gbps 4×4 LVDS Crosspoint Switch URL https://www.ti.com/lit/ds/symlink/ds10cp154a.pdf

[98] Analog Devices 2022 Triple Differential Receiver with Adjustable Line Equalization URL http://www.analog.com/media/en/technical-documentation/data-sheets/AD8123.pdf

[99] Analog Devices 2022 Rail-to-Rail, Very Fast, 2.5 V to 5.5 V, Single-Supply LVDS Comparators URL https://www.analog.com/media/en/technical-documentation/data-sheets/ADCMP604_605.pdf

[100] Analog Devices 2022 2.5 V to 5.5 V, 500 μA, 2-Wire Interface Quad Voltage Output, 8-/10-/12-Bit DACs URL https://www.analog.com/media/en/technical-documentation/data-sheets/AD5305_5315_5325.pdf

[101] W-Optics 2022 Small Form Factor Pluggable Dual Optical Transmitter Duplex LC Receptacle 1250 Mbit/s URL https://indico.cern.ch/event/735376/attachments/1671862/2682296/W-Optics_SAA-1AF1-111SFP_2T_GbE_SM_10km_V04.pdf

[102] Finisar 2022 RoHS Compliant Pluggable SFP Transceiver URL https://ii-vi.com/product-category/products/optical-communications/optical-transceivers/page/1/

[103] Cypress 2022 16-Mbit (1M×16) Static RAM URL https://www.infineon.com/dgdl/Infineon-CY7C10612G_CY7C10612GE_16-Mbit_%281_M_16%29_Static_RAM-DataSheet-v07_00-EN.pdf?fileId=8ac78c8c7d0d8da4017d0ec3fea63963&utm_source=cypress&utm_medium=referral&utm_campaign=202110_globe_en_all_integration-datasheet

[104] Analog Devices 2022 MAXM17515 – 5A High-Efficiency Power Module URL https://www.analog.com/en/products/maxm17515.html

[105] Traco Power 2022 THN15-221: DC/DC Converters, THN 15 Series, 15 Watt URL https://www.tracopower.com/products/thn15.pdf

[106] Linear Technology 2022 LTC2991: Octal I^2C Voltage, Current, and Temperature Monitor URL https://www.analog.com/media/en/technical-documentation/data-sheets/2991ff.pdf

[107] Maxim Integrated 2022 MAX1617A: Remote/Local Temperature Sensor with SMBus Serial Interface URL https://www.analog.com/media/en/technical-documentation/data-sheets/max1617a.pdf

[108] XILINX 2022 QuickBoot Method for FPGA Design Remote Update URL https://docs.xilinx.com/v/u/en-US/xapp1081-quickboot-remote-update

[109] Analog Devices 2022 ADN2814: Continuous Rate 10 Mb/s to 675 Mb/s Clock and Data Recovery IC with Integrated Limiting Amp

URL https://www.analog.com/media/en/technical-documentation/data-sheets/ADN2814.pdf

[110] Kittelmann T H, Tsulaia V, Boudreau J and Moyse E 2010 *J. Phys. Conf. Ser.* **219** 032012

[111] Bianchi R M, Boudreau J, Konstantinidis N, Martyniuk A C, Moyse E, Thomas J, Waugh B M and Yallup D P (ATLAS) 2017 *J. Phys. Conf. Ser.* **898** 072014

[112] Carrió F, Moreno P and Valero A (ATLAS Tile Calorimeter System) 2016 *JINST* **11** C03047

[113] Valdes Santurio E (ATLAS Tile Calorimeter System) 2017 *J. Phys. Conf. Ser.* **928** 012024

[114] Di Girolamo B, Dotti A, Giangiobbe V, Johansson P, Pribyl L and Volpi M 2005 Beamline instrumentation in the 2004 combined ATLAS testbeam Tech. rep. CERN

[115] Spanggaard J 1998 Delay Wire Chambers - A Users Guide Tech. rep. CERN Geneva URL https://cds.cern.ch/record/702443

[116] The ATLAS collaboration (ATLAS) 2010 Performance of the ATLAS Silicon Pattern Recognition Algorithm in Data and Simulation at $\sqrt{s} = 7$ TeV Tech. rep. CERN

[117] The ATLAS collaboration (ATLAS) 2012 Performance of the ATLAS Inner Detector Track and Vertex Reconstruction in the High Pile-Up LHC Environment Tech. rep. CERN

[118] Fruhwirth R 1987 *Nucl. Instrum. Meth. A* **262** 444–450

[119] The ATLAS collaboration (ATLAS) 2014 *Journal of Instrumentation* **9** P09009–P09009 URL https://doi.org/10.1088%2F1748-0221%2F9%2F09%2Fp09009

[120] The ATLAS collaboration (ATLAS) 2010 Performance of primary vertex reconstruction in proton-proton collisions at $\sqrt{s}$ =7 TeV in the ATLAS experiment Tech. rep. CERN

[121] Galea C F (ATLAS) 2017 *Nucl. Part. Phys. Proc.* **287-288** 111–114

[122] Neutelings I (ATLAS, CMS) 2021 *PoS* **LHCP2020** 045

[123] Aaboud M *et al.* (ATLAS) 2019 *Eur. Phys. J. C* **79** 639 (*Preprint* 1902.04655)

[124] Cornelissen T G, Elsing M, Gavrilenko I, Laporte J F, Liebig W, Limper M, Nikolopoulos K, Poppleton A and Salzburger A 2008 *J. Phys. Conf. Ser.* **119** 032013

[125] The ATLAS collaboration (ATLAS) 2014 Electron efficiency measurements with the ATLAS detector using the 2012 LHC proton-proton collision data Tech. rep. CERN

[126] Frühwirth R 2003 *Computer Physics Communications* **154** 131–142 ISSN 0010-4655 URL https://www.sciencedirect.com/science/article/pii/S0010465503002923

[127] Aaboud M *et al.* (ATLAS) 2019 *JINST* **14** P03017 (*Preprint* 1812.03848)

[128] Illingworth J and Kittler J 1988 *Computer Vision, Graphics, and Image Processing* **44** 87–116 ISSN 0734-189X URL https://www.sciencedirect.com/science/article/pii/S0734189X88800331

[129] Aad G *et al.* (ATLAS) 2016 *Eur. Phys. J. C* **76** 292 (*Preprint* 1603.05598)

[130] The ATLAS collaboration 2017 *The European Physical Journal C* **77** URL https://doi.org/10.1140%2Fepjc%2Fs10052-017-5004-5

[131] Cacciari M, Salam G P and Soyez G 2008 *JHEP* **04** 063 (*Preprint* 0802.1189)

[132] Cacciari M, Salam G P and Soyez G 2012 *Eur. Phys. J. C* **72** 1896 (*Preprint* 1111.6097)

[133] The ATLAS collaboration (ATLAS) 2015 Expected performance of missing transverse momentum reconstruction for the ATLAS detector at $\sqrt{s} =$ 13 TeV Tech. rep. CERN

[134] Adams D *et al.* 2014 Recommendations of the Physics Objects and Analysis Harmonisation Study Groups 2014 Tech. rep. CERN Geneva URL https://cds.cern.ch/record/1700874

[135] Branco G C, Ferreira P M, Lavoura L, Rebelo M N, Sher M and Silva J P 2012 *Phys. Rept.* **516** 1–102 (*Preprint* 1106.0034)

[136] Lee T D 1973 *Phys. Rev. D* **8** 1226–1239

[137] Aaboud M *et al.* (ATLAS) 2018 *Phys. Lett. B* **783** 392–414 (*Preprint* 1804.01126)

[138] Sirunyan A M *et al.* (CMS) 2020 *JHEP* **03** 055 (*Preprint* 1911.03781)

[139] Aad G *et al.* (ATLAS) 2021 *Eur. Phys. J. C* **81** 332 (*Preprint* 2009.14791)

[140] von Buddenbrock S, Chakrabarty N, Cornell A S, Kar D, Kumar M, Mandal T, Mellado B, Mukhopadhyaya B, Reed R G and Ruan X 2016 *Eur. Phys. J. C* **76** 580 (*Preprint* 1606.01674)

[141] Muhlleitner M, Sampaio M O P, Santos R and Wittbrodt J 2017 *JHEP* **03** 094 (*Preprint* 1612.01309)

[142] Dorsch G, Huber S, Mimasu K and No J 2014 *Phys. Rev. Lett.* **113** 211802 (*Preprint* 1405.5537)

[143] von Buddenbrock S, Cornell A S, Fadol A, Kumar M, Mellado B and Ruan X 2018 *J. Phys. G* **45** 115003 (*Preprint* 1711.07874)

[144] ATLAS Collaboration 2014 *JINST* **9** P08009 (*Preprint* 1404.7473)

[145] ATLAS Collaboration 2014 *JINST* **9** P07024 (*Preprint* 1405.3768)

[146] ATLAS Collaboration 2015 Selection of jets produced in 13 TeV proton–proton collisions with the ATLAS detector ATLAS-CONF-2015-029 URL https://cds.cern.ch/record/2037702

[147] Gleisberg T *et al.* 2009 *JHEP* **02** 007 (*Preprint* 0811.4622)

[148] Höche S, Krauss F, Schumann S and Siegert F 2009 *JHEP* **05** 053 (*Preprint* 0903.1219)

[149] Gleisberg T and Höche S 2008 *JHEP* **12** 039 (*Preprint* 0808.3674)

[150] Ball R D *et al.* (NNPDF) 2015 *JHEP* **04** 040 (*Preprint* 1410.8849)

[151] Schumann S and Krauss F 2008 *JHEP* **03** 038 (*Preprint* 0709.1027)

[152] Höche S, Krauss F, Schönherr M and Siegert F 2013 *JHEP* **04** 027 (*Preprint* 1207.5030)

[153] Biedermann B, Denner A, Dittmaier S, Hofer L and Jäger B 2016 *Phys. Rev. Lett.* **116** 161803 (*Preprint* 1601.07787)

[154] Biedermann B, Denner A, Dittmaier S, Hofer L and Jager B 2017 *JHEP* **01** 033 (*Preprint* 1611.05338)

[155] Cascioli F *et al.* 2014 *JHEP* **01** 046 (*Preprint* 1309.0500)

[156] Cascioli F, Maierhofer P and Pozzorini S 2012 *Phys. Rev. Lett.* **108** 111601 (*Preprint* 1111.5206)

[157] Denner A, Dittmaier S and Hofer L 2014 *PoS* **LL2014** 071 (*Preprint* 1407.0087)

[158] Alwall J, Herquet M, Maltoni F, Mattelaer O and Stelzer T 2011 *JHEP* **06** 128 (*Preprint* 1106.0522)

[159] Sjöstrand T, Ask S, Christiansen J R, Corke R, Desai N, Ilten P, Mrenna S, Prestel S, Rasmussen C O and Skands P Z 2015 *Comput. Phys. Commun.* **191** 159 (*Preprint* 1410.3012)

[160] Alioli S, Nason P, Oleari C and Re E 2010 *JHEP* **06** 043 (*Preprint* 1002.2581)

[161] Higgs bsm 2hdm recommendations https://twiki.cern.ch/twiki/bin/view/AtlasProtected/HiggsBSM2HDMRecommendations accessed: 2021-10-27

[162] Aaboud M *et al.* (ATLAS) 2018 *Eur. Phys. J. C* **78** 293 (*Preprint* 1712.06386)

[163] Kostyukhin V 2003 VKalVrt - package for vertex reconstruction in ATLAS. Tech. rep. CERN Geneva revised version number 1 submitted on 2003-09-24 11:10:53 URL https://cds.cern.ch/record/685551

[164] Abidi S H *et al.* 2018 Event selection and background estimation in the $H \to ZZ \to 4\ell$ channel at $\sqrt{s}$=13TeV - Final Run 2 Analysis Tech. rep. CERN Geneva URL https://cds.cern.ch/record/2651267

[165] ATLAS Collaboration 2012 Reconstruction of collinear final-state-radiation photons in Z decays to muons in sqrts=7 TeV proton-proton collisions. ATLAS-CONF-2012-143 URL https://cds.cern.ch/record/1491697

[166] ATLAS Collaboration 2018 Object-based missing transverse momentum significance in the ATLAS Detector ATLAS-CONF-2018-038 URL https://cds.cern.ch/record/2630948

[167] Read A L 1999 *Nucl. Instrum. Meth. A* **425** 357–360

[168] Kalogeropoulos A and Alwall J 2018 The syscalc code: A tool to derive theoretical systematic uncertainties (*Preprint* 1801.08401)

[169] Bellm J *et al.* 2016 *Eur. Phys. J. C* **76** 196 (*Preprint* 1512.01178)

[170] Cowan G, Cranmer K, Gross E and Vitells O 2011 *Eur. Phys. J. C* **71** 1554 (*Preprint* 1007.1727)

[171] Read A L 2002 *J. Phys. G* **28** 2693

[172] Oreglia M 1980 A Study of the Reactions $\psi' \to \gamma\gamma\psi$ URL https://www.slac.stanford.edu/cgi-wrap/getdoc/slac-r-236.pdf

[173] Buttinger W 2015 Using Event Weights to account for differences in Instantaneous Luminosity and Trigger Prescale in Monte Carlo and Data Tech. Rep. ATL-COM-SOFT-2015-119 CERN Geneva URL https://cds.cern.ch/record/2014726

[174] Aaboud M *et al.* (ATLAS) 2018 *Eur. Phys. J. C* **78** 903 (*Preprint* 1802.08168)

[175] Tolley E *et al.* 2017 $E_{\mathrm{T}}^{\mathrm{miss}}$ performance in the ATLAS detector using 2015-2016 LHC p-p collisions Tech. Rep. ATL-COM-PHYS-2017-1732 CERN Geneva URL https://cds.cern.ch/record/2294891

[176] ATLAS Collaboration 2019 Luminosity determination in pp collisions at $\sqrt{s} = 13\,\mathrm{TeV}$ using the ATLAS detector at the LHC ATLAS-CONF-2019-021 URL https://cds.cern.ch/record/2677054